Study of Magnetic and Dielectric Properties of Rare Earth Iron Garnets

A Thesis Submitted

By

Aakansha

Roll Number: 146121022

In Partial Fulfillment of the Requirements for the Award of the Degree of

Doctor of Philosophy in Physics

Department of Physics

Indian Institute of Technology Guwahati

Guwahati-781039, India

December, 2019

Statement

The work contained in the thesis entitled "**Study of Magnetic and Dielectric Properties of Rare Earth Iron Garnets"** has been carried out by me under the supervision of Prof. S. Ravi, Department of Physics, Indian Institute of Technology Guwahati. This work has not been submitted elsewhere for the award of any degree.

December, 2019

Aakansha
Department of Physics
Indian Institute of Technology Guwahati
Guwahati – 781039, India

Certificate

It is certified that the work contained in the thesis entitled **"Study of Magnetic and Dielectric Properties of Rare Earth Iron Garnets"** by Ms. Aakansha, a Ph.D. student of the Department of Physics, Indian Institute of Technology Guwahati for the award of the degree of *Doctor of Philosophy* has been carried out under my supervision. This work has not been submitted elsewhere for the award of any degree.

December, 2019

Dr. S. Ravi
Professor, Department of Physics
Indian Institute of Technology Guwahati
Guwahati – 781 039, India

Dedicated

To

My Mother and Bhabhi

Acknowledgements

Life is nothing without experience, and I was fortunate enough to possess that wonderful five-year-long memory in IIT Guwahati during my Ph.D. thesis stay. Not to mention, it would have been impossible for me to achieve the accomplishment within time without any kind of support and assistance from several souls around me. Though the journey of researchers is a never-ending process, I would like to have immense pleasure to finally show my gratitude towards those persons at the important milestone of my research life.

At the foremost, I would like to express thankfulness to Department of Physics, IIT Guwahati for giving me an opportunity to fulfil my dreams. This place had been my home for the last few years and provided me with a lesson to be confident and expressive. The campus is indeed beautiful and gave me a delightful as well as a brilliant environment to study.

Firstly, I wish to convey my sincere gratitude and respect to my thesis supervisor Prof. S. Ravi, Department of Physics, IIT Guwahati, for providing me with a well-established experimental lab to conduct my research under his valuable guidance. His humbleness, caring nature and gentle behaviour inspired me to be motivated. His encouragements worked as pillars of confidence every time I faced difficulties in my research work. Moreover, his valuable insights on numerous technical ideas and his colossal experiences in this field guided me to sort out problems arose during the experiments.

I would like to offer my sincere gratefulness to my doctoral committee (DC) members Prof. A. Perumal (chairperson), Prof. Dilip pal and Prof. V. Manivannan for their thoughtful suggestions and encouragement to comprehend and improve my thesis work from various outlook. Moreover, I would like to acknowledge Dr. D. Pamu for giving me access to his lab instruments.

I am very much thankful to present Head of the Department (HoD) of Physics, Prof. S. Ghosh and former HoDs of Physics, Prof. Poulose and Prof. S. Basu for providing instrument facilities and their cooperation during the tenure of my Ph.D. thesis. I am thankful to all the faculty members and other staff members of the Department of Physics as well.

My special thanks to Dr. Sidananda Sarma for assisting me to carry out experiments. I am grateful to present (Prof. M Qureshi) and former (Prof. G. Krishnamoorthy) head of the Central Instrumental Facility (CIF), IIT Guwahati, and all the scientific officers and technical staff of CIF, IIT Guwahati, for enabling me to perform the experiments using various sophisticated instruments during my Ph.D. tenure.

I would like to acknowledge my lab-mates Pratap, Mahananda, Ritupan and Pushpanjali for their support, helpful nature and maintaining a peaceful environment in the lab. I am appreciative to my seniors Dr. Tribedi Bora, Dr. T. Ranganatha, Dr. Junmoni Barman, Dr. Bipul Deka, Dr. Bhibhuti Bhusan Dash and post-doctoral fellow Dr. Vishwajit Manohar Gaikwad for lots of discussions and technical help.

"A friend in need is a friend indeed", without friends the journey of life is incomplete. I honestly thank my friends Dinesh, Mriganka, Monika, Kritika, Indukalpa, Vikesh, Priyanka, Robin, for their encouragement. My heartiest gratitude to Dolly Taparia and Ankan Bhattacharya for their continuous inspiration and care. Without their care and motivation, I could not be able to finish my thesis on time.

I would like to give my sincere respect and gratitude to my elder brother Sanjay, for his support and blessing throughout my life. I am extremely thankful to my father and my siblings (Shweta, Abhishek and Priya) for their love, help and active support to follow up my dreams.

Last but not the least, I acknowledge the Department of Science and Technology (DST), Fund for Improvement of S&T Infrastructure (FIST), New Delhi for providing the facilities of Vibrating sample magnetometer, TTRAX III X-ray diffractometer, Physical properties measurements system. Moreover, my special gratitude to DST for providing the travelling grant for international conference. I express my sincere thanks to the Ministry of Human Resource and Development (MHRD) and Indian Institute of Technology Guwahati for providing the financial assistance through institute fellowship during my Ph.D. tenure.

Finally, my heartiest gratitude to the almighty God for giving me the strength and courage to face all the difficulties in life to pursue my dreams and move ahead in the beautiful journey of life.

Aakansha

IIT Guwahati

Abstract

Magnetic ceramics, or ferrites, are a very well-established class of magnetic materials. In the last 50 years, research activity on ferrites has led to the establishment of many theories, complementing models and new materials for applications. Magnetic ceramics participate effectively almost in every application area such as telecommunication, optical isolators, memory storage, energy storage devices, etc. Since then, ferrites have become a reference material, but innovations and improvements continue to take place; many new and exciting applications, theories and preparation technologies are currently under development. Ferrites are complex in nature, because they are the combination of magnetic phenomena and ceramic microstructures. The approach to ferrites, their synthesis, crystal structure, magnetic and physical properties are interrelated. They draw the major attention towards the application in microwave and energy storage devices due to their attractive magnetic and dielectric properties.

Ferrites are mainly composed of ferric oxide and α-Fe_2O_3 as originally reported by *Néel* in 1948. Ferrites are mainly categorized into three subcategories based on their crystal structure: spinels, garnets and hexaferrites. Among these ferrites, garnets are the potential and primary choice for microwave devices due to their low dielectric loss, high resistivity, low resonance line width, etc. Rare earth iron garnet forms at a high annealing temperature of ~ 1673 K to avoid impurity phases such as $YFeO_3$ and α-Fe_2O_3. The presence of Fe^{2+} ions in rare earth iron garnet leads to photo-induced phenomena and changes in various properties, particularly in electrical conductivity. Rare earth iron garnets exhibit magneto-electric (ME), magneto-dielectric (MD) and relaxor ferroelectric type behaviours, which provide potential applications in memory storage and energy efficient devices. As per the literature survey and knowledge, the magnetic and dielectric properties can be studied in detail in order to enhance their functional properties. So, we have chosen yttrium and gadolinium iron garnet to study in detail.

Both Yttrium iron garnet (YIG) and Gadolinium iron garnet (GIG) are cubic in nature with 8 formula units per unit cell having $Ia\bar{3}d$ space group. They exhibit ferrimagnetic ordering because of the antiferromagnetic coupling of $3Fe^{3+}$ (up spin) ions in tetrahedral site and $2Fe^{3+}$ (down spin) ions in octahedral site, resulting in the net magnetic moment of $1Fe^{3+}$ ion ($5\ \mu_B$). The ferrimagnetic (FIM) transition temperature (T_C) for YIG

is 550 K and for GIG it is 560 K. The FIM T_C is mainly affected by the superexchange interaction between Fe ions at octahedral (*a*) site and tetrahedral (*d*) site through an oxygen ion (Fe(*a*)-O-Fe(*d*)). So, FIM T_C is not much affected by substituting at rare earth site, but it got affected by the substitution at Fe site. Besides FIM T_C, GIG undergoes magnetic compensation at 286 K, which arises due to the weak interaction between Gd ions at dodecahedral (*c*) site and Fe ions at octahedral site. The resultant moment of such interaction becomes equal to that of Fe ions at tetrahedral site, which gives rise to the magnetic compensation. Other than $Gd_3Fe_5O_{12}$, $Dy_3Fe_5O_{12}$, $Ho_3Fe_5O_{12}$ and $Tb_3Fe_5O_{12}$ exhibit magnetic compensation behaviour below the room temperature. In addition to magnetic properties, YIG and GIG exhibit good dielectric properties along with magneto-electric and magneto-dielectric behaviour due to the presence of Fe^{2+} ions. Maxwell-Wagner and Debye type relaxation are activated in these compounds at higher and lower temperature, respectively. Recently, Bi-substitution in YIG gives rise the relaxor ferroelectric behaviour, which leads to multiferroicity, and in GIG it enhances the dielectric constant. Bi-substitution also leads to negative magnetization below magnetic compensation (~ 80 K) in $Tb_3Fe_5O_{12}$ and $Ho_3Fe_5O_{12}$. Therefore, the present thesis focusses on the extensive investigation of magnetic and dielectric properties of parent and impurity substituted YIG and GIG.

The chosen samples for the above study are as follows:

1) $Y_{3-x}Sm_xFe_5O_{12}$ (x = 0 to 3.0)
2) $Y_3Fe_{5-x}Cr_xO_{12}$ (x = 0 to 0.5)
3) $Y_3Fe_{5-x}Mn_xO_{12}$ (x = 0 to 0.2)
4) $Gd_{3-x}Sm_xFe_5O_{12}$ (x = 0 to 3.0)
5) $Gd_{3-x}Bi_xFe_5O_{12}$ (x = 0 to 1.0)
6) $Gd_3Fe_{5-x}Cr_xO_{12}$ (x = 0 to 0.3)

The crystallinity and the phase formation of the above-mentioned samples are characterized by recording X-ray diffraction (XRD) patterns. The microstructure and compositional analyses are carried out by using field emission scanning electron microscope (FESEM) attached with energy dispersive X-ray (EDX) spectrometer. Vibrating sample magnetometer (VSM) equipped with He closed cycle refrigerator and high temperature oven was used to perform the temperature and field variations of

magnetization measurements. LCR meter was used to obtain the impedance data in order to study dielectric properties.

This thesis contains seven chapters:

1. **Introduction**
2. **Experimental Techniques**
3. **Sm-Substituted Yttrium Iron Garnet.**
4. **Magnetic and Dielectric Properties of Y-(Fe, M)-O Compounds (M = Cr, Mn)**
5. **Ferrimagnetic and Relaxor Ferroelectric Properties in Gd-Fe-O series.**
6. **Magnetic and Dielectric Studies in Gd-(Fe, Cr)-O Series**
7. **Conclusion**

Chapter 1 presents the importance of rare earth iron garnets (RIGs) and their applications in various advanced devices. A general introduction to various type of magnetic interactions and their mechanism is given. The influence of different kind of magnetic anisotropy in the overall magnetic properties of a material including negative magnetization is discussed. A brief discussion on ac impedance spectroscopy, dielectric spectroscopy and electric modulus spectroscopy is given with a special emphasis on different dielectric relaxation models. Finally, the crystal structure of yttrium iron garnet (YIG) and gadolinium iron garnet (GIG) along with the literature review on their magnetic and dielectric properties are described.

Chapter 2 covers the experimental techniques followed in material preparation, their characterization and various physical measurements. The sample preparation techniques and the experimental techniques employed for several characterization such as XRD patterns, magnetization, impedance spectroscopy, etc. are presented. The working principle of various sophisticated instruments such as X-ray diffractometer (XRD), field emission scanning electron microscope (FESEM) equipped with energy dispersive X-ray (EDX) spectrometer, vibration sample magnetometer (VSM) and dielectric set-up with LCR meter are discussed.

Chapter 3 describes the sample preparation, characterization and detailed study of structural, magnetic and dielectric properties of Sm-substituted YIG compounds.

Sm-substituted YIG samples were synthesised by solid-state reaction method, XRD analysis unveils the crystallinity and phase purity of these samples. The lattice constant

obtained from the Rietveld refinement of XRD patterns using space group $Ia\bar{3}d$, reveals the increment in lattice constant with Sm-concentration. The dense microstructure with well-defined grains and fine grain boundaries is observed from the FESEM analysis along with the chemical composition close to the desired stoichiometric ratio. Temperature variation of magnetization undergoes the ferrimagnetic (FIM) transition and its T_C, increases from 550 K to 573 K with Sm-substitution. However, Sm-substitution reduces the saturation magnetization (M_S) value from 27.54 emu/g to 22.59 emu/g, which is due to antiferromagnetic coupling of Sm^{3+} (0.71 μ_B) ions having lesser magnetic moment to the net moment of Fe^{3+} (5 μ_B) ions. Both grains and grain boundaries contributions are present in these samples as per the complex impedance analysis plotted in terms of Nyquist plots (-Z'' versus Z'). The Nyquist plots were fitted to an equivalent circuit comprised of resistance, capacitance and constant phase elements of grains and grain boundaries. The relaxation process across grain boundaries takes place at higher temperature due to the long-range motion of charge carriers having large relaxation time. The value of dielectric constant, obtained from impedance data increases with Sm-concentration, i.e., from 22 to 29. Further, the ac conductivity spectra were analyzed using Jonscher power law and the frequency exponent (n) value lies in the range of 0.5 to 1.5. Based on the temperature variation of n value, it is observed that both large and small polarons are contributing towards conduction process. The relaxation time and conductivity data are plotted with respect to inverse of temperature and they follow a linear behaviour. An anomalous behaviour is observed near the ferrimagnetic transition temperature, which is due to the coupling of magnetic and electric polarization known as magneto-electric coupling.

Chapter 4 contains the detailed study of magnetic and dielectric properties of Cr and Mn-substituted yttrium iron garnet.

Polycrystalline samples of $Y_3Fe_{5-x}Cr_xO_{12}$ with x = 0, 0.1, 0.2, 0.3, 0.4 and 0.5 were prepared in single-phase form using solid-state reaction method. XRD patterns are refined using Fullprof software. Cr-substitution lowers the value of obtained structural parameters such as lattice constant and unit cell volume. Raman spectra analysis also verifies the substitution of Cr at Fe site. The thermomagnetic analysis demonstrates the decrease in ferrimagnetic transition temperature from 547 K to 494 K, and it is due to the reduction in bond angle Fe(a)-O-Fe(d) that weakens this superexchange interaction. Room temperature saturation magnetization (M_S) was obtained from the analysis of initial magnetization data

using the law of approach to saturation. The value of M_S increases with Cr-substitution due to its preferential occupation at octahedral site. The dielectric data ε' and ε'' were determined from the impedance data and analyzed using Havriliak – Negami (HN) equation. The obtained value of dielectric constant increases with Cr-concentration, i.e., from 20 to 52 at 300 K for 1 MHz. Such increment is associated to the increase in number of Fe^{2+} ions. The dc conduction loss due to space charge accumulation at grain boundaries results in the linear behaviour in dielectric spectra at higher temperature. Such dc conduction is clearly visible in ac conductivity spectra and follows the Jonscher power law. The conduction mechanism is governed by the small polaron hopping model. The Arrhenius plots of relaxation time and conductivity suggest the presence of electron hopping between Fe^{2+} and Fe^{3+} networks within grains and oxygen vacancies across grain boundaries.

The single-phase samples of $Y_3Fe_{5-x}Mn_xO_{12}$ compound were prepared by sol-gel method. Mn-substitution reduces the lattice constant as per the XRD analysis with Rietveld refinement using space group $Ia\bar{3}d$. The ferrimagnetic transition temperature reduces with Mn-substitution. The Nyquist plots of Mn-substituted samples display the presence of semi-circular arc due to grain boundaries and they were fitted to an equivalent circuit comprised of resistance, capacitance and constant phase element arranged in parallel. Mn-substitution lowers the dielectric constant along with dc conduction loss at lower frequency and higher temperature.

Chapter 5 describes the preparation of Sm and Bi-substituted gadolinium iron garnet and the detailed study of magnetic and dielectric properties of these compounds.

Single-phase samples of $Gd_{3-x}Sm_xFe_5O_{12}$ were prepared by solid-state reaction method. The XRD patterns were analyzed using Rietveld refinement in cubic unit cell with space group $Ia\bar{3}d$. The lattice parameter, bond length and bond angle values are found to increase with Sm-concentration as per the XRD analysis. Such increase is due to larger ionic radii of Sm^{3+} ions compared to that of Gd^{3+} ions. Zero field-cooled (ZFC) magnetization versus temperature data depicts the presence of ferrimagnetic transition (magnetic compensation) above (below) the room temperature. Sm-substitution increases the ferrimagnetic (FIM) transition temperature (T_C) from 567 K to 575 K, while decreases the magnetic compensation temperature (T_{Comp}) from 293 K to 70 K. Field-cooled (FC) measurement of magnetization as a function of temperature for x = 2.0 sample shows a novel magnetization reversal below the T_{Comp}. This phenomenon is originated due to the

enhancement in the magnetic anisotropy, which resists the spin alignment in the direction of applied field and leads to the negative moment. The increment in magnetic anisotropy is also in accordance with the obtained value of anisotropy constant evaluated from the law of approach to saturation (LAS) model. A large increase in the value of saturation magnetization (M_S) is noticed with Sm-substitution. The impedance spectra confirm the dominant behaviour of grains and grain boundaries at lower and higher temperature, respectively as per the analysis of Nyquist plots. The Nyquist plots were fitted to a modelled circuit with a parallel combination of a resistor, capacitor and constant phase elements associated to grain boundaries at high temperature. The resistance value decreases with temperature and it denotes the negative temperature coefficient of resistance. The Arrhenius plots of relaxation time shows an anomaly in the vicinity of ferrimagnetic transition temperature that indicates the presence of magneto-electric coupling. The activation energy of charge carriers lies in the range of 0.41 to 1.19 eV.

Moreover, Bi-substituted GIG ($Gd_{3-x}Bi_xFe_5O_{12}$: x = 0, 0.5 and 1.0) formed in single-phase according to XRD analysis. Bi-substitution increases the lattice constant from 12.4624 Å to 12.5156 Å, due to larger ionic size of Bi^{3+} compared to Gd^{3+}. Ferrimagnetic transition temperature and saturation magnetization values increase with Bi-substitution. The enhancement in the strengthening of superexchange interaction increases the FIM T_C. Besides, the substitution of non-magnetic Bi^{3+} ion lowers the magnetic moment at Gd^{3+} site, resulting in the reduction of the magnetic compensation temperature. The magnitude of resistance increases with Bi-concentration due to decrease in number of charge carriers ascribed to Bi loss and associated Fe^{2+} concentration. The frequency variation of -Z'' plots at different temperature exhibit relaxation peak, and their shifting towards higher frequency side is indicative of the charge activation due to thermal energy. The temperature variation of dielectric constant depicts a broad relaxation peak in the temperature range of 560 K to 600 K. The relaxation peak shifts towards higher temperature side with increase in frequency. Such shifting is attributed to local distortion in the crystal structure, which generates nano-polar region. The ε' plots as a function of temperature were fitted to modified Curie-Weiss law and the obtained diffusiveness constant value is close to 2, suggesting the relaxor ferroelectric behaviour.

Chapter 6 demonstrates the detailed characterization and analysis of Cr-substituted GIG.

Single-phase form of polycrystalline samples of $Gd_3Fe_{5-x}Cr_xO_{12}$ were obtained for x = 0 to 0.3. Cr^{3+} ions having smaller ionic radii substituting at larger Fe^{3+} ions reduce the lattice parameter and unit cell volume. These samples undergo ferrimagnetic transition at lower value than that of parent compound (569 K). Cr^{3+}-substitution leads to decrease in the value of compensation temperature (T_{Comp}) from 294 K to 265 K. The increase in magnetization value from 0.56 emu/g to 2.29 emu/g is ascribed to the favourable occupation of Cr^{3+} ions at octahedral sublattice of Fe^{3+} ions. The dielectric spectra dominated by the dc conduction loss were analyzed by plotting their modulus spectra. The analysis of modulus spectra obtained from the dielectric data is explained using Kohlrausch-Williams-Watts (KWW) function. These spectra contain a relaxation peak, which confirms the short-range movement of charge carriers associated to grains. The obtained exponent β suggests the deviation of relaxation dynamics from the ideal Debye type.

Chapter 7 presents the overall summary of the rare earth and transition metal substituted yttrium and gadolinium iron garnet. All the samples are in single-phase form and were analyzed using Rietveld refinement of the XRD patterns. The substitution of larger (smaller) ionic radii increases (decreases) the lattice constant. The increment (reduction) in bond angle strengthens (weakens) the superexchange interaction, which increases (reduces) the ferrimagnetic (FIM) transition temperature (T_C). The substitution of Cr and Mn at Fe site reduces the FIM T_C, while Sm and Bi-substitution increases the FIM T_C in both YIG and GIG. The minimum value of FIM T_C is found as 494 K for $Y_3Fe_{4.5}Cr_{0.5}O_{12}$ and the maximum value of 596 K is obtained for $Gd_2Bi_1Fe_5O_{12}$. A novel negative magnetization is observed in $Gd_1Sm_2Fe_5O_{12}$ compound due to the enhancement in magnetic anisotropy below the magnetic compensation temperature. Nyquist plots reveal the contribution of grains and grain boundaries at lower temperature while the dominance of grain boundaries at higher temperature. On the other hand, relaxor type ferroelectric behaviour is observed in Bi-substituted GIG compounds and they are explained by modified Curie-Weiss law. The dielectric loss is also reduced sharply up to 0.5 with Bi-substitution. The Kohlrausch-Williams-Watts (KWW) function is used to explain the modulus spectra and they exhibit relaxation peak associated to grains in Cr-substituted GIG compound. A brief write-up of future scope of works has also been mentioned.

List of Abbreviation used in this Thesis

AFM	Antiferromagnetic
CCR	Closed Cycle Refrigerator
CPE	Constant Phase Element
DM	Dzyaloshinskii – Moriya
EDX	Energy Dispersive X-Ray
FC	Field Cooled
FESEM	Field Emission Scanning Electron Microscope
FIM	Ferrimagnetic
FM	Ferromagnetic
G	Grains
GB	Grain Boundaries
GIG	$Gd_3Fe_5O_{12}$ or Gadolinium Iron Garnet
HN	Havriliak-Negami
JPL	Jonscher's Power Law
KWW	Kohlrausch – Williams – Watts
LAS	Law of Approach to Saturation
MR	Magnetization Reversal
$\boldsymbol{M_S}$	Saturation Magnetization
NTCR	Negative Temperature Coefficient of Resistance
OV	Oxygen Vacancies
PPMS	Physical Properties Measurement System
RE	Rare Earth
RIGs	$R_3Fe_5O_{12}$ or Rare Earth Iron Garnet

RKKY	Ruderman – Kittel – Kasuya – Yosida
T_C	Transition Temperature
T_{Comp}	Compensation Temperature
UDR	Universal Dielectric Response
VESTA	Visualization Electronic and Structural Analysis
XPS	X-ray Photoelectron Spectroscopy
XRD	X-ray Diffraction
ZFC	Zero Field Cooled

Table of Contents

List of Figures

Chapter 1

Chapter 2

Chapter 3

Chapter 4

Chapter 5

Chapter 6

List of Tables

Chapter 1

Chapter 3

Chapter 4

Chapter 5

Chapter 6

Chapter 1

Introduction

Since centuries, the magnetic and dielectric materials are being studied to improve their functional properties towards various applications. The tailoring of magnetic and electrical properties of several materials towards applications in memory devices, solid-state devices, sensors, transducers, biomedical devices, etc. is the main focus of several researchers in condensed matter physics [1–6]. Materials exhibiting two or more ferroic ordering such as ferromagnetic (FM), antiferromagnetic (AFM), ferroelectric (FE), ferroelastic (FES), etc. are known as multiferroic materials [1–3]. The coupling between two ferroic ordering leads to an additional functionality known as magneto-electric effect, where in principle electric polarization can be tuned by the magnetic field or the magnetization can be tuned by the electric field. Such magneto-electric coupling would permit the data to be written electrically and read magnetically [3,6,7]. It avoids the problems associated with reading ferroelectric random access memory devices and the requirement of large current or large local magnetic field in writing magnetic storage devices.

Ferrites draw considerable attention towards application in microwave and spintronic devices. Ferrites are mainly composed of ferric oxide, α-Fe_2O_3, and they were initially explained by *Néel* in 1948 [8]. Based on the crystal structure, ferrites are classified into spinels, garnets and hexaferrites. The cubic spinels and more specifically the spinel ferrites have been extensively studied in the literature [9,10]. Hexaferrites exhibit hexagonal crystal structure with relatively large magnetic moment at room temperature [11]. The rare earth iron garnets (RIGs) with cubic structure exhibit interesting magnetic and dielectric properties and they are one of the attractive materials for engineering applications [12–14].

Among all ferrites, RIGs exhibit many interesting properties such as, controllable magnetic, dielectric, ferroelectric, magneto-electric, magneto-dielectric, magneto-caloric, magnetic compensation, negative magnetization and magneto-optical properties [15–18]. Such properties have significant role in many technological applications like oscillators,

optical isolators, sensors, bio-antennas, microwave devices, spintronic devices, phase shifters and electrochemical devices, etc. [19–22]

The present thesis work is dedicated to the study of magnetic and dielectric properties of rare earth based iron garnet. So, this introductory chapter is mainly devoted to some theoretical background of magnetic ordering and electric polarization along with the literature review on Yttrium iron garnet (YIG) and Gadolinium iron garnet (GIG) based materials. We begin with the crystal structure of RIGs.

1.1 Crystal Structure of RIG

For the first time, *Menzer* in 1928 [23] determined the crystal structure of natural garnets, i.e., the silicate minerals having the chemical formula of $Ca_3Al_2(SiO_4)_3$ using the X-ray powder photographs. RIGs also exhibit similar kind of crystal structure as that of silicate and can be represented as $R_3Fe1_2(Fe2O_4)_3$ where R represents rare earth element (R = Gd, Tb, Dy, Ho, Er, Tm, Tb, Lu, Y, etc.), Fe1 and Fe2 represent the Fe ions at octahedral (*a*) and tetrahedral (*d*) site, respectively. *Bertaut* and *Forret* (1956) [24] and *Geller* and *Gilleo* (1957) [25] have found that these synthetic garnets have similar structure like natural garnets. RIGs belong to a cubic centrosymmetric space group (No. 230) O_h^{10}:$Ia\bar{3}d$, i.e., it belongs to a body-centred Bravais lattice. The unit cell here contains eight formula units of $\{R_3\}[Fe1_2](Fe2_3)O_{12}$ with 160 atoms. Here { }, [ ] and ( ) represent three different cationic sublattices such as dodecahedral, octahedral and tetrahedral sites, respectively. These cations are located at the centres of corresponding polyhedrons as shown in Figure 1.1. Thus, R^{3+} ions occupy dodecahedral (Figure 1.1(a)) coordinated sites with Wyckoff position 24*c* (1/8, 0, 1/4), $Fe1^{3+}$ ions are distributed over octahedral (Figure 1.1(b)) sites with Wyckoff positions 16*a* (0, 0, 0) and $Fe2^{3+}$ ions occupy the tetrahedral (Figure 1.1(c)) sites with Wyckoff positions 24*d* (3/8, 0, 1/4). The oxygen ions are at Wyckoff position 96*h* (x, y, z). The arrangement of different polyhedra along with the oxygen ions are given in Figure 1.2 for the garnet structure. The typical crystal structure of RIG is shown in Figure 1.3. The atomic positions of various elements in $R_3Fe_5O_{12}$ are given in Table 1.1. The interaction between $Fe1^{3+}$-O^{2-}-$Fe2^{3+}$ is the strongest one among all the interactions in RIGs, which is negative in nature as explained by *Néel* [8]. The lattice constant of RIGs lies in the range of 12.302 Å ($Yb_3Fe_5O_{12}$) to 12.600Å ($Nd_3Fe_5O_{12}$) [26].

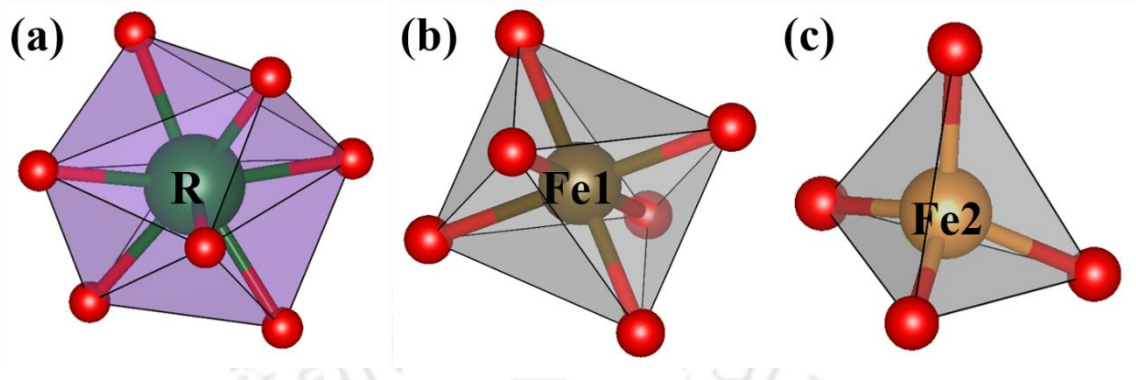

Figure 1.1: Different polyhedral arrangement of cations in RIGs (a) Dodecahedral, (b) Octahedral and (c) Tetrahedral.

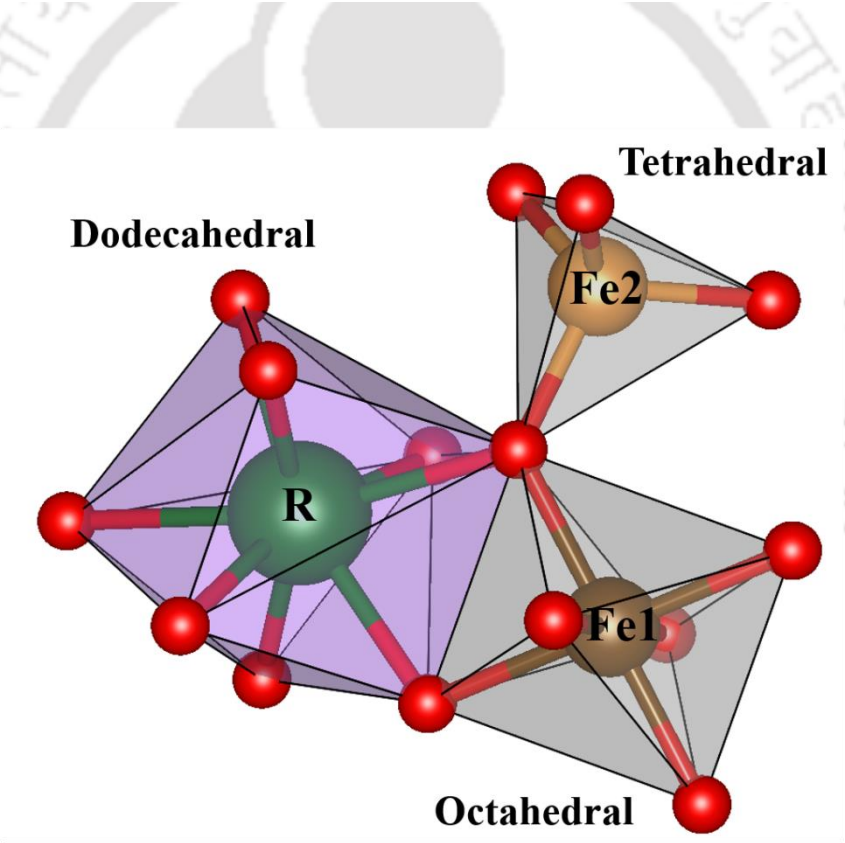

Figure 1.2: The arrangement of different polyhedra together in a unit cell of RIGs.

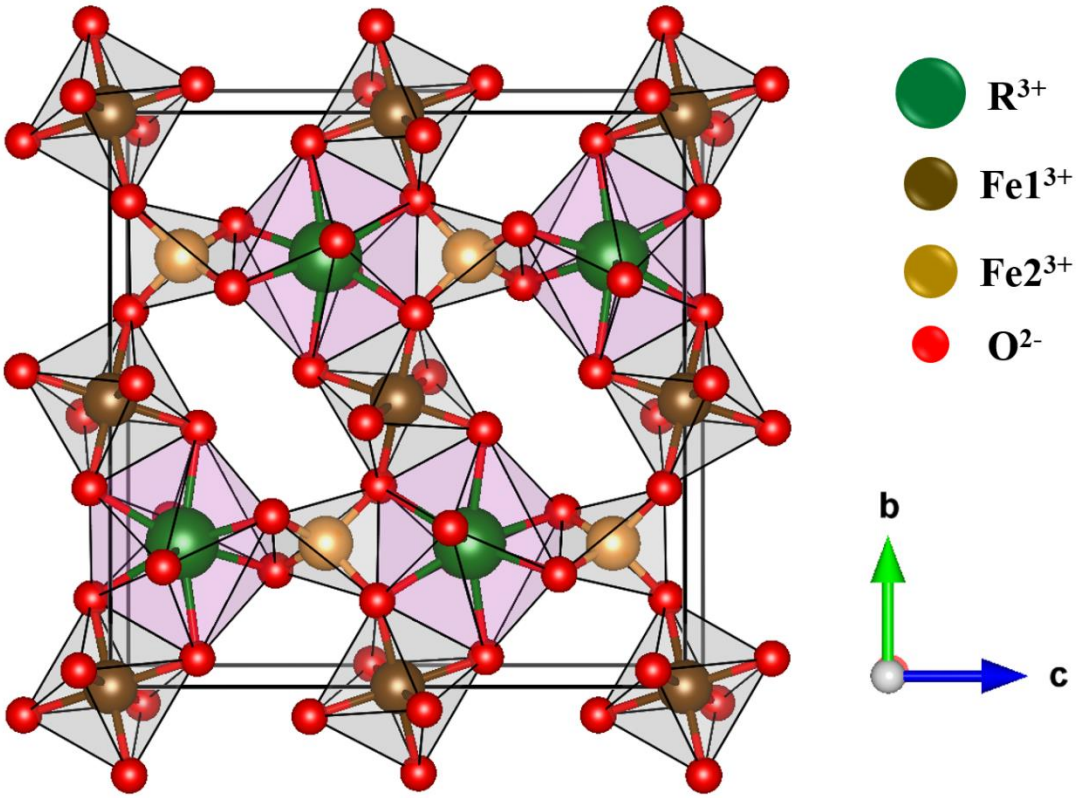

Figure 1.3: The crystal structure of $R_3Fe_5O_{12}$ having eight formula units per unit cell.

Table 1.1: Atomic positions of constituent elements of $R_3Fe_5O_{12}$ as per $Ia\bar{3}d$ space group.

Atoms	Wyckoff position	Coordination to oxygen	(x, y, z)
O	96*h*	-	(-0.029, 0.057, 0.149)
R	24*c*	8	(1/8, 0, 1/4)
Fe1	16*a*	6	(0, 0, 0)
Fe2	24*d*	4	(3/8, 0, 1/4)

1.2 Crystal Field Effect and Orbital Quenching

The crystal field is an average electric field experienced by an atom or ion at a given site due to the neighbouring atoms in the crystal in a solid [27]. The symmetry of the crystal determines the strength and nature of the crystal field. The transition element (Fe) atoms/ions present in RIGs play a major role in its room temperature ferrimagnetism and other interesting magnetic properties. The magnetism in transition elements originate from their unfilled *d*-shell electrons. In general, the *d* orbital has five degenerate energy levels and are divided into t_{2g} and e_g orbitals, where the former one contains three orbitals namely d_{xy}, d_{yz} and d_{zx} and the later one consists of $d_{x^2-y^2}$ and d_{z^2} orbitals as shown in Figure 1.4. The t_{2g} orbitals are oriented in between x, y and z axes, but the e_g orbitals are aligned along the direction of x, y and z axes. In most of the oxides involving transition elements, the 3*d* orbitals of transition elements mostly overlap with 2*p* orbitals of oxygen ions. The three *p* orbitals p_x, p_y and p_z are known to exhibit electronic distribution extending along x, y and z direction, respectively.

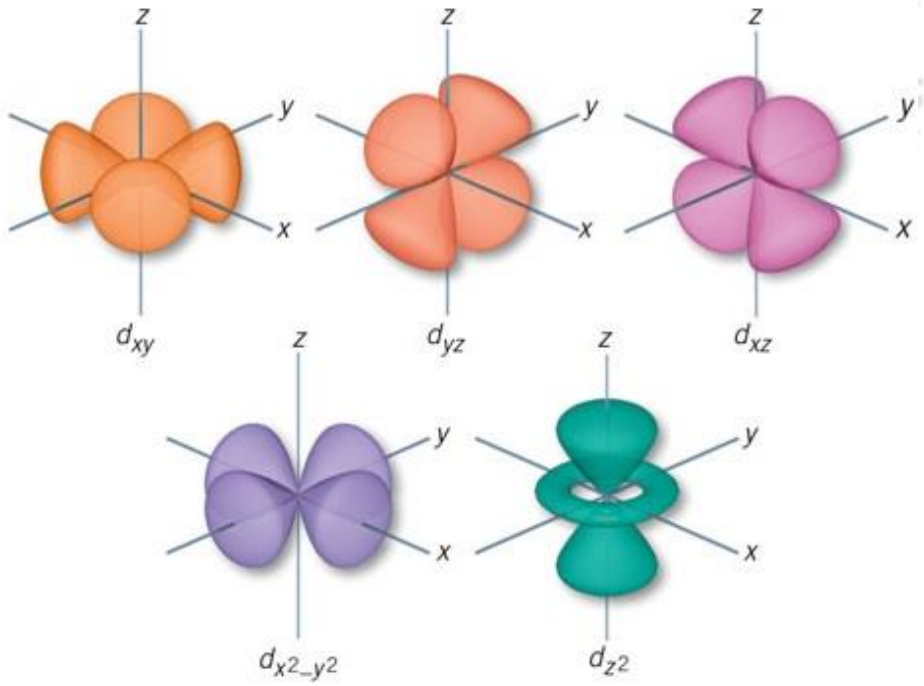

Figure 1.4: The electronic distribution of 3*d* orbitals.

In an octahedral environment, e_g electrons overlap predominantly with neighboring *p* orbitals of oxygen ion compared to that of t_{2g} orbital electrons, which results in lifting of the e_g level with respect to t_{2g} level. The energy level diagram in octahedral environment is shown in Figure 1.5 for the case of CrO_6 [28]. But, in the case of tetrahedral environment,

t_{2g} levels are lifted up because they overlap predominantly with neighboring *p* orbitals as in the case of MnO_4 [27]. The competition between crystal field energy (Δ_o or Δ_t) and the Hund's coupling energy Δ_H plays a role in the arrangement of electrons in 3*d* orbitals leading to either low spin ($\Delta_{o,\,t} > \Delta_H$) or high spin ($\Delta_H > \Delta_{o,\,t}$) state of transition elements in the crystal. So, the crystal field effect influences the magnetic moment of a given transition elements in a solid.

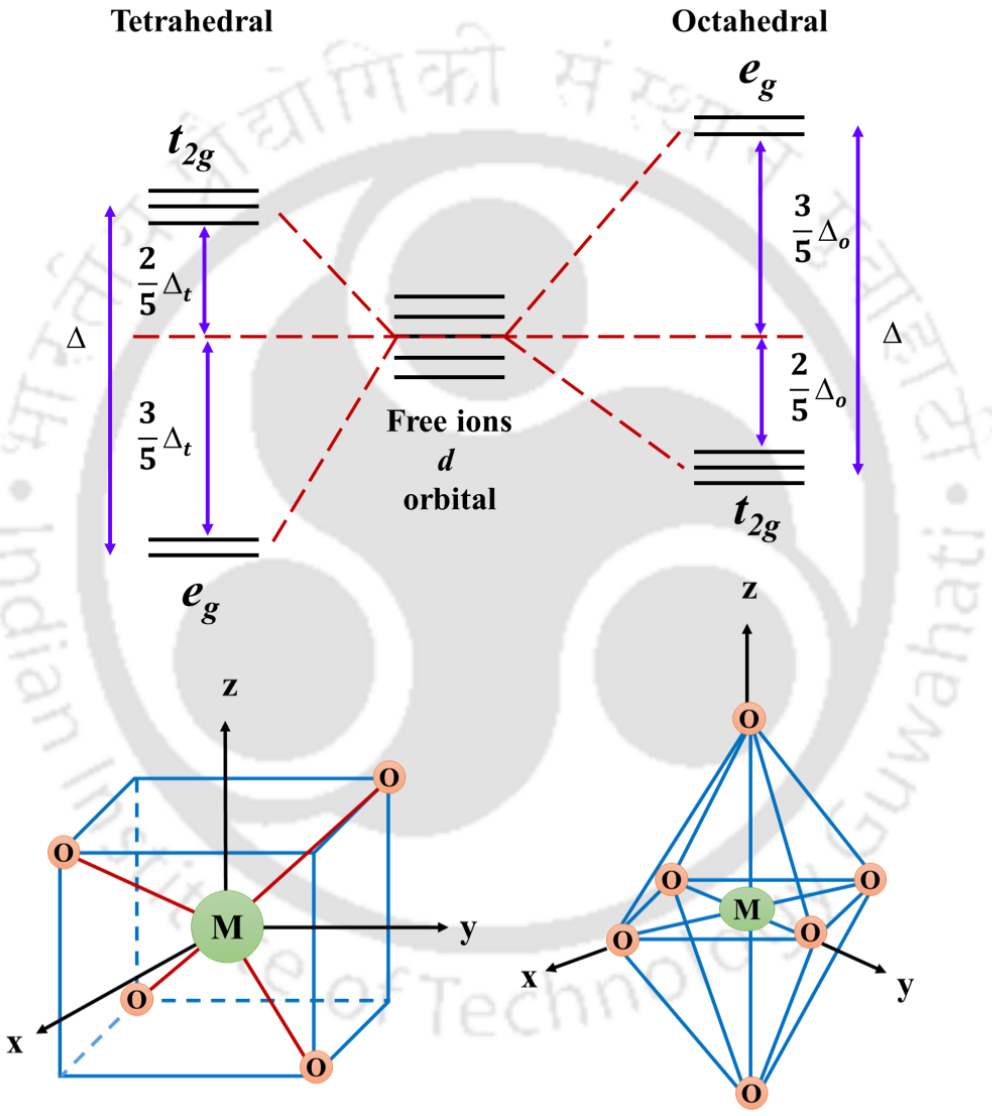

Figure 1.5: Crystal field effect in tetrahedral and octahedral environments.

Even in the absence of strong crystal field, the magnetic moment of a given transition element is affected by a process called orbital quenching ($L = 0$) due to the dominant crystal field energy compared to the Hund's spin-orbit coupling energy. In

general, the effective magnetic moment (μ_{eff}) of an ion can be calculated by using the relation: $\mu_{eff} = g\sqrt{J(J+1)}\,\mu_B$ but it does not match with experimental values for most of the transition elements such as for $3d^5$ and $3d^{10}$ ions. This is due to the above said orbital quenching and the magnetic moment of such system is determined by considering only the spin angular momentum. Hence, μ_{eff} is calculated using the relation: $\mu_{eff} = g\sqrt{S(S+1)}\,\mu_B$. Here *J* and *S* refer the quantum numbers corresponding to total and spin angular momentum of electrons, respectively. The orbital quenching explains the experimentally observed ground state magnetic moment of 3*d* transition metal ions. However, the 4*f*, 4*d*, 5*d* series do not possess such effect. In case of 4*f* ions, the orbital distribution of electrons does not extend far away to get influenced by the electron distributions of neighboring ions since they lie beneath the 5*s* and 5*p* orbitals. So, no crystal field effect comes into picture. For 4*d* and 5*d* series of transition elements, the orbital quenching is less clear-cut since, the effect of crystal field and spin-orbit is comparable.

1.3 Exchange Interaction

The Weiss molecular field is known as exchange field, which is responsible for the alignment of magnetic dipoles in a particular arrangement in such a way that the total energy of the material is minimized [29]. Exchange interaction is a quantum mechanical phenomenon explained by *Heisenberg* in 1928 from the electrostatic interaction between the neighboring atoms. The exchange interaction is guided by the Pauli exclusion principle, applied to the electronic configuration of two neighboring atoms as a whole. This principle states that two electrons can have the same quantum number only if they have opposite spins. According to Heisenberg model, the interaction energy between two atoms *a* and *b* having electron spins S_a and S_b is defined as

$$E_{ex} = -2\sum_{a>b} J_{ab}\left(\overrightarrow{S_a}.\overrightarrow{S_b}\right) \tag{1.1}$$

where, J_{ab} is the exchange integral related to the overlap of the charge distribution of the atoms *a* and *b*. For $J_{ab} > 0$, the E_{ex} would be minimum for the parallel alignment of spin vectors and thus leading to FM. For $J_{ab} < 0$, minimum E_{ex} is obtained for the antiparallel alignment of the spin vectors and it corresponds to AFM or FIM interaction [27]. In this section, some of the important magnetic exchange interactions are briefly described at microscopic scale, which are responsible for long-range magnetic ordering.

1.3.1 Direct Exchange Interaction

In direct exchange interaction, the electrons of the neighbouring magnetic atoms interact directly without any intermediate non-magnetic ion. Due to insufficient overlapping of electron distribution between the two neighbouring atoms, this interaction does not play an important role in controlling the magnetic properties. The Pauli exclusion principle keeps the electrons with parallel spins away from each other to reduce the Coulomb repulsion. So, mostly antiparallel spin configuration is favoured in direct exchange interaction. Therefore, in order to justify magnetism, we have to look for other interactions.

1.3.2 Superexchange Interaction

Superexchange interaction is an indirect long-range exchange interaction, where two magnetic ions interact through an intermediate non-magnetic ion. According to *Kramers'* model [30], the interaction between cations having more(less) than half-filled *d*-shells gives rise to AFM (FM) interaction. Later, *Slater* [31] and, *Goodenough* and *Loeb* [32,33] suggested that the AFM interaction is also allowed among cations having less than half filled *d*-shell.

The superexchange interaction can be understood by taking the example of two Mn^{3+}-3*d* ions separated by an oxygen ion as depict in Figure 1.6. Figure 1.6(a) represents the AFM interaction between Mn^{3+}-O^{2-}-Mn^{3+} network. Here, the core spins of Mn^{3+} cations are aligned antiparallel to each other through an oxygen anion. Such interaction gives rise to AFM, which is assisted by the strong Hund's coupling. Following the Hund's rule, the up spin electron of O-2*p* orbital points towards the Mn^{3+} cation having up spin configuration and the down spin electron points towards the Mn^{3+} cation having down spin configuration. The overlapping of both Mn-3*d* and O-2*p* orbitals support the formation of covalent bond between the Mn-O. The above process suggests the FM spin alignment in cation-anion pair however, the net interaction between two magnetic ions results in AFM ordering.

Besides, Mn^{3+}-O^{2-}-Mn^{3+} networks can exhibit FM interaction as well. As per the Goodenough theory [32], FM prevails if the cation-anion-cation interaction is asymmetric, i.e., covalent bond (*d* and *p* orbitals pointing towards each other) at one side and ionic bond (*d* and *p* orbital points away each other) at another side as shown in Figure 1.6(b). Here, the up spin electron of oxygen anions points towards the up spin electron of Mn^{3+} cation (left side), i.e., via covalent bond. However, another down spin electron of oxygen anion

points away from the right-hand side Mn^{3+} cation, i.e., via ionic bond. The direct exchange between the right-hand side cation and oxygen anion is AFM in nature. Thus, resulting the overall interaction between two Mn-3*d* ions.

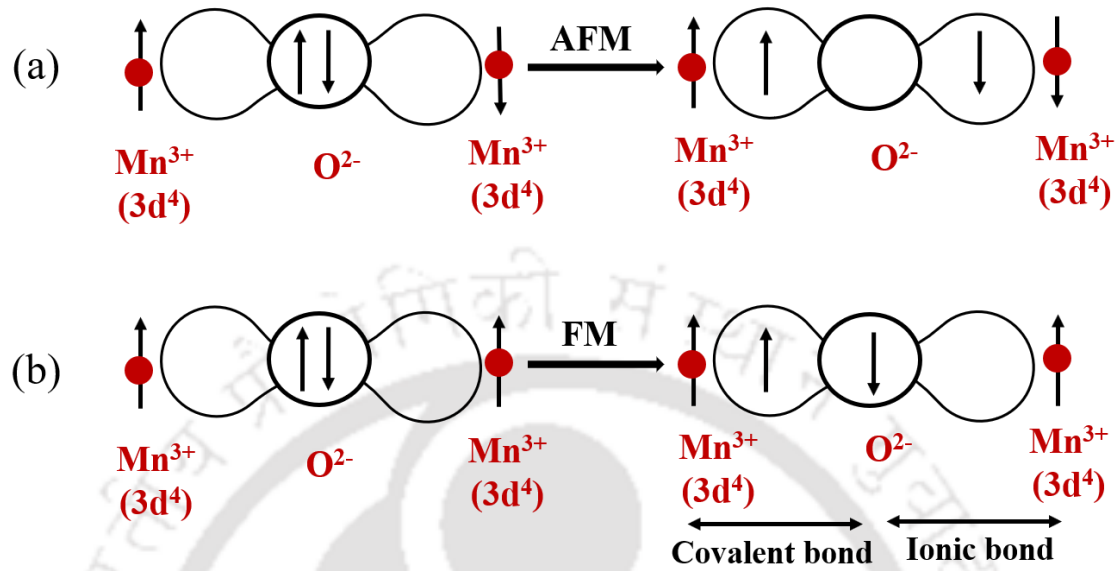

Figure 1.6: Schematic representation of (a) AFM and (b) FM superexchange interaction [32].

The superexchange interaction in RIGs basically originates from the interaction between Fe^{3+} ions situated in octahedral and tetrahedral sites through the intervening oxygen anion, i.e., $Fe^{3+}(a)$-O^{2-}-$Fe^{3+}(d)$ networks [34].

1.3.3 Double Exchange Interaction

It is also an indirect exchange interaction where transfer of an electron from one magnetic ion to another magnetic ion through a non-magnetic intermediate ion takes place and is popularly known as Zener double exchange interaction [35,36]. This interaction occurs in materials where the magnetic ions possess mixed valent states and electron hops from lower valent site of one magnetic ion to higher valent site of another magnetic ion through intermediate oxygen ion only if the core electron spins of the two magnetic ions are parallel. Such interaction always gives rise to FM. Typical example of double exchange interactions between Mn^{3+} and Mn^{4+} ions via an oxygen ion is shown in Figure 1.7(a). Here, O^{2-} gives its up spin electron to Mn^{4+} and this is followed by the transfer of a up spin electron from Mn^{3+} to O^{2-}. At the end of the process Mn^{3+} is oxidized to Mn^{4+} and Mn^{4+} is reduced to Mn^{3+}. Due to these two-step process of exchange of electrons, it is called double exchange interaction. Thus, this interaction leads to FM. If the Mn spins are not parallel, the electron transfer becomes difficult due to the violation of Hund's coupling as shown in

Figure 1.7(b). The electron transfer is also more difficult if the Mn-O-Mn bond is considerably bent away from 180°. The double exchange mechanism is visualized as a second order process proposed by *Anderson* and *Hasegawa* [37], where the electron hopping takes place as per the following sequence; $Mn^{3+}_{1\uparrow} O^{2-}_{2\uparrow,3\downarrow} Mn^{4+}_{\square} \rightarrow Mn^{3+}_{1\uparrow} O^{2-}_{3\downarrow} Mn^{3+}_{2\uparrow} \rightarrow Mn^{4+}_{\square} O^{2-}_{1\uparrow,3\downarrow} Mn^{3+}_{2\uparrow}$. Here 1, 2, 3 and □ are the labelling of electron spins and vacant site, respectively.

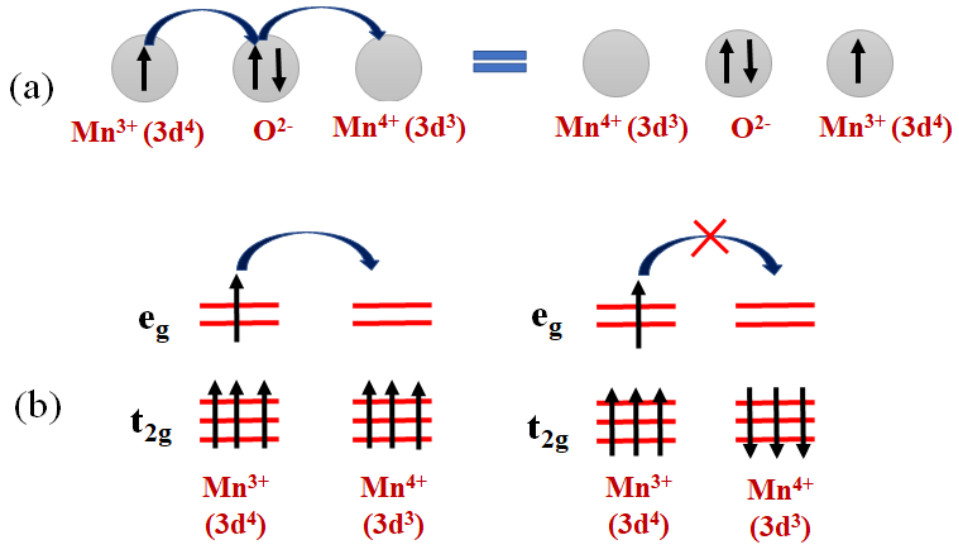

Figure 1.7: Schematic representation of double exchange interaction between Mn^{3+} and Mn^{4+} ions through oxygen ion. (b) The allowed e_g electron transfer for parallel spin arrangement of Mn ions and the forbidden e_g electron transfer for antiparallel spins.

1.3.4 Dzyaloshinskii-Moriya Exchange Interaction

The Dzyaloshinskii-Moriya (DM) exchange interaction is a type of anisotropic exchange interaction. This exchange interaction results in the bending of the antiparallel spins towards each other, which leads to a net magnetic moment. The exchange energy between the magnetic moments at this canted configuration can be written as follow [38,39]:

$$H_{DM} = \vec{D}.\left(\overrightarrow{S_a} \times \overrightarrow{S_b}\right) \qquad (1.2)$$

Here D represents the DM vector. $\overrightarrow{S_a}$ and $\overrightarrow{S_b}$ are the spin of two interacting magnetic ions. If there is an inversion symmetry with respect to the central point connecting the two magnetic ions, the vector D would be zero. The DM interaction tries to align $\overrightarrow{S_a}$ and $\overrightarrow{S_b}$ orthogonal to each other in a plane perpendicular to D. The DM interaction mostly appears

in the AFM materials, which sometimes gives rise to a weak FM interaction. Some of the AFM crystals like α-Fe_2O_3, Cr_2O_3, etc. exhibit such weak FM behaviour [27]. The anti-symmetric exchange interaction is one of the most important factors contributing magnetism induced electric polarization in multiferroic systems.

1.3.5 Ruderman-Kittel-Kasuya-Yosida Interaction

The exchange interaction between the magnetic ions through the conduction electrons is known as Ruderman-Kittel-Kasuya-Yosida (RKKY) interaction. The magnetic moment of a localized spin polarizes the conduction electrons and this polarization couples with another localized magnetic ion at a distance *r* away. This is a long-range interaction, which gives rise to either AFM or FM coupling depending upon the distance between the magnetic ions [27].

1.4 Magnetic Orderings

The magnetism within a material arises from their atomic structure. The net magnetic moment of an atom is the sum of both orbital and spin magnetic moment contributions of each electron as well as considering the cancellation of moment in completely filled orbitals. Based on magnetic exchange interaction among various atoms or ions, the magnetic materials are broadly classified as: diamagnet, paramagnet (PM), ferromagnet (FM), antiferromagnet (AFM) and ferrimagnet (FIM).

1.4.1 Diamagnets

Diamagnetism is an inherent property of all the materials but it is often hidden by the other type of magnetism [29]. Diamagnetic materials do not contain any magnetic dipoles or magnetic ions in the absence of magnetic field due to their completely filled outermost electronic shell. In the presence of an external magnetic field, a magnetic moment is induced which tends to oppose the direction of applied magnetic field in accordance with the Lenz's law. Diamagnetic materials exhibit negative susceptibility, which implies that the induced magnetization is opposite to the applied magnetic field. Some of the examples of diamagnetic materials are the monoatomic rare gases (He, Ne, Ar, etc.), polyatomic gases (H_2, N_2, etc.), metals (Zn, Cu, Au, Ag, Bi, etc.), and many organic compounds [29]. The diamagnetic susceptibility in general is quite weak except a special case of superconductors.

1.4.2 Paramagnets

In paramagnetic (PM) materials, the magnetic dipoles orient in the random direction such that they do not have any net magnetic moment in the absence of magnetic field. In the presence of magnetic field, the magnetic dipoles (atomic moment) try to align along the filed direction such that it gives rise to positive magnetic susceptibility. The degree of alignment increases with increase in applied field as well as decrease in temperature. The susceptibility of a paramagnetic material as a function of temperature can be written as follows as per the *Langevin* classical approach [27].

$$\chi = \frac{N\mu_0\mu^2}{3k_BT} \tag{1.3}$$

Here, N represents the number of magnetic ions (magnetic dipoles) per unit volume each having a magnetic moment μ. μ_0 is the permeability of free space and k_B is the Boltzmann constant. This equation is also known as Curie law, where the magnetic susceptibility is inversely proportional to the temperature [27,29]. The PM susceptibility at low magnetic field, as per the quantum mechanical approach is written as:

$$\chi = \frac{N\mu_0 g^2\mu_B^2 J(J+1)}{3k_BT} \tag{1.4}$$

Where, the Lande's g factor, $g = 1 + \frac{J(J+1)+S(S+1)-L(L+1)}{2J(J+1)}$ (1.5)

Salts of transition elements, salts and oxides of the rare earths and the rare earth elements are the examples of strong paramagnetic substances [27].

1.4.3 Ferromagnets

Ferromagnets (FM) are a class of materials, where they exhibit spontaneous magnetization even in the absence of external magnetic field due to the parallel alignment of magnetic spins. However, in most of the macroscopic materials, such spontaneous magnetization is restricted to small regions known as magnetic domains of the order of a few μm. Such domains are oriented in the random direction leading to net zero magnetic moment in the absence of magnetic field. With the application of external magnetic field, the multi-domains orientated in the random direction and form into a single domain along the direction of applied magnetic field.

The FM behaviour is observed below the transition temperature (T_C) known as Curie temperature [29,40]. For T > T_C they behave like a PM and follow the Curie-Weiss law:

$$\chi = \frac{C}{T - T_C} \tag{1.6}$$

where, C and T_C represent Curie constant and Curie temperature respectively. Here,

$$C = \frac{\mu_0 N g^2 \mu_B^2 J(J+1)}{3k_B} \text{ or } C = \frac{\mu_0 N g^2 \mu^2}{3k_B} \tag{1.7}$$

The most common examples of room temperature ferromagnets are Co, Ni and Fe with typical T_C value of 631 K, 1043 K and 1394 K, respectively [29]. Among the entire rare earth elements, only Gd is ferromagnetic in nature with T_C value of 294 K, i.e., close to the room temperature [41].

1.4.4 Antiferromagnets

Antiferromagnetic material exhibits negative exchange interaction, which leads to the antiparallel alignment of magnetic spins nearest to each other, as a result the net magnetic moment becomes zero. This ordering is active below certain temperature known as Néel temperature (T_N) and above T_N it mostly behaves like a PM with susceptibility:

$$\chi = \frac{C}{T + T_N} \tag{1.8}$$

The typical AFM materials are α-Fe_2O_3, NiO, Cr_2O_3, CoO, FeO, MnO, MnF_2, etc. with their T_N values of 950 K, 568 K, 307 K, 293 K, 198 K, 122 K, and 67 K, respectively.

1.4.5 Ferrimagnets

Ferrimagnetic (FIM) material macroscopically behaves like ferromagnetic material, which possess spontaneous magnetization even in the absence of magnetic field. However, microscopically the spin arrangement is antiparallel to each other similar to AFM. Unlike AFM materials, FIM materials exhibit different magnetic sublattices having different magnetic moment, so they do not cancel each other.

The net magnetic moment of a FIM material is the difference between the moment of the two given sublattices, i.e., $M_{net} = M_A - M_B$ [29]. Figure 1.8(a) shows that, the moment of A sublattice decreases less rapidly with increasing temperature than that of moment of the B sublattice. In result, the net magnetic moment increases with increasing temperature, and goes through a maximum before dropping to zero at T_C. Such behaviour is observed

for the cubic spinel $NiCr_2O_4$ [42]. However, as shown in Figure 1.8(b), sometimes the moment of one sublattice becomes dominant at low temperature compared to that of other sublattice and vice-versa at higher temperature. This may lead to net zero magnetic moment at some intermediate temperature less than T_C, where both the sublattices moment balance each other which is known as magnetic compensation temperature (T_{Comp}), i.e., $M_A = M_B$ at T_{Comp}. Above and below the T_{Comp}, one sublattice moment dominates over the other [40].

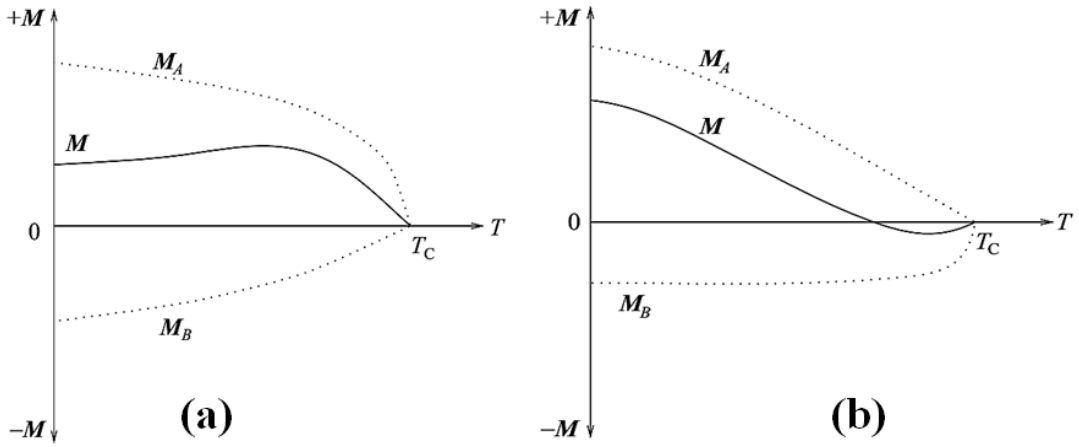

Figure 1.8: The schematic diagram of magnetic moment versus temperature of two magnetic sublattices A and B.

Spinel ferrites, garnets and hexaferrites are the example of FIM. The FIM T_C for various spinel and hexaferrites such as Fe_3O_4, $NiFe_2O_4$, $CoFe_2O_4$, $BaFe_{12}O_{18}$ are 858 K, 858 K, 793 K, 723 K, respectively [29]. RIGs contain three different sublattices, *c*, *a* and *d* denoted for dodecahedral, octahedral and tetrahedral, respectively. Some of these materials exhibit magnetic compensation. For example, gadolinium iron garnet (GIG) exhibits magnetic compensation around 286 K [43]. The magnetic moment as a function temperature of three sublattices are given in Figure 1.9 along with resultant magnetic moment [19]. The moment of '*c*' sublattice decreases rapidly with temperature. However, the moment of '*a*' and '*d*' sublattice is nearly constant with temperature and sharply falls to zero near $T_C \sim 600$ K. Sublattice '*d*' has slightly high magnetic moment that that of '*a*'. At a point below the transition temperature, the net magnetic moment becomes zero, which is known as magnetic compensation point (T_{Comp}) and above T_{Comp} the moment of '*d*' sublattice dominates over the other sublatttices moment and gives rise to the positive moment represented by dashed line in Figure 1.9. The magnetic moment of one '*d*' sublattice is equal to the net magnetization of other two sublattice ($M_c + M_a$) leading to T_{Comp}.

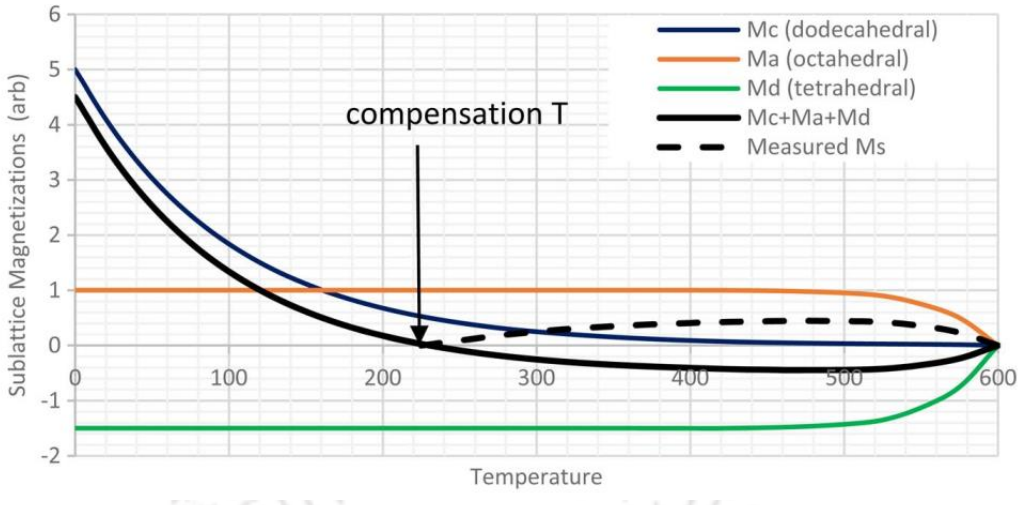

Figure 1.9: Temperature dependence of three different sublattices moment along with resultant magnetic moment [19].

1.5 Magnetic Anisotropy

The magnetic properties of some of the materials depend upon the direction of applied magnetic field with respect to crystallographic orientation, macroscopic dimension, etc., and such variation is attributed to the phenomenon of magnetic anisotropy. The type and the magnitude of magnetic anisotropy affect the coercivity, remanence, saturation magnetization along with the shape of the hysteresis loop. The nature and strongness of anisotropy determine the applicability of the given magnetic material for a specific application. The anisotropy can be either intrinsic in nature due to its crystal structure or extrinsic in nature due to processing condition, macroscopic dimension, etc. The most commonly known magnetic anisotropies are magnetocrystalline anisotropy, shape anisotropy, stress anisotropy and exchange anisotropy.

1.5.1 Magnetocrystalline Anisotropy

The tendency of magnetization to align in the preferred crystallographic direction is defined as magnetocrystalline anisotropy. The easy axis is the preferred direction since in such direction it is easy to magnetize the sample to the saturation with relatively low applied field. The other crystallographic direction is termed as hard axis. The origin of magnetocrystalline anisotropy is spin-orbit coupling [29]. In a crystal, electrons are coupled by various mechanism such as spin-spin, spin-lattice, lattice-orbit and spin-orbit coupling. The spin-spin coupling is quite strong which keep the alignment of neighbouring spins parallel or antiparallel to each other. The orbit-lattice coupling is very strong, where the

orientation of the orbits is fixed with crystal lattice and the orientation cannot change even at very large magnetic field. The spin-orbit coupling is relatively weak, when an external magnetic field is applied the spin and orbital moments try to reorient in the direction of applied field. Generally, orbitals are strongly coupled with lattice so, it resists the spin axis rotation. The energy required to rotate the spins away from the easy axis is known as the anisotropy energy (E), i.e., the energy required to overcome the spin-orbit coupling. In 1929, a Russian physicist *Akulov* [44] expressed *E* in terms of series expansion of direction cosine α_i of saturation magnetization (M_S) with respect to crystal axes as given by:

$$E = K_0 + K_1(\alpha_1^2\alpha_2^2 + \alpha_2^2\alpha_3^2 + \alpha_3^2\alpha_1^2) + K_2(\alpha_1^2\alpha_2^2\alpha_3^2) + \cdots \quad (1.9)$$

Here, K_0, K_1 and K_2 represent the anisotropy constants for a particular crystal at a particular temperature. α_1, α_2 and α_3 are the direction cosines related to M_S in the crystallographic axes a, b and c.

The term K_0 is neglected most of the times because it is angle independent. In case of K_2 = 0, the direction of easy axis is determined by the sign of K_1. If $K_1 > 0$, then $E_{100} < E_{110} < E_{111}$, having <100> as the easy axis. The Fe and Co exhibit <100> easy axis. The value of K_1 for Fe = 4.8×10^4 J/m^3 and for Co = 5×10^5 J/m^3. If $K_1 < 0$, then $E_{111} < E_{110} < E_{100}$ with <111> as the easy axis. Ni is one such example having K_1 = -5.7×10^3 J/m^3. If $K_2 \neq 0$, then easy axis depends upon the value of both K_1 and K_2 [29].

1.5.2 Shape Anisotropy

Generally, most of the materials exhibit magnetocrystalline anisotropy, but in polycrystalline samples, such effect will get averaged due to random orientation of crystals. In the case of spherical sample, applied field can magnetize it to same extent in any direction. But, if the sample is non-spherical in shape, the longer side gets easily magnetized compared to shorter side of the sample. Such property is referred as shape anisotropy. The shape anisotropy is explained in terms of demagnetization field ($H_d = -N_d M$), which is known to be strong along the shorter dimension of the material compared to its longer one. The H_d depends on the magnetization of the material and the dimension dependent demagnetization factor N_d (0 to 1 in SI unit).

1.5.3 Stress Anisotropy

Besides magnetocrystalline and shape anisotropy, stress can also affect the domain structure by creating one or more magnetization easy axis in a material. It is a uniaxial anisotropy and its energy is written as:

$$E_\sigma = K_\sigma sin^2\theta \qquad (1.10)$$

K_σ and θ represent the stress anisotropy constant and the angle between the axis in which the stress is applied and the magnetization [29,40].

1.5.4 Exchange Anisotropy

The exchange anisotropy generally arises due to the exchange interaction between two dissimilar materials such as FM, AFM, etc. at an interface or heterostructure.

1.6 Magnetization Reversal and Negative Magnetization

Magnetization reversal (MR) is a phenomenon of change in the sign of the dc magnetization from positive to negative value as the temperature is varied for the constant positive applied magnetic field. It is quite different from diamagnetism and is generally observed under field-cooled condition. It can be also observed by changing the magnitude of applied field at a given temperature. This phenomenon is explained by considering several intrinsic parameters such as crystal structure, magnetic anisotropy, exchange interactions, and temperature dependence of sublattice magnetization. MR was first studied by *Néel* in FIM material in 1948 [8]. Later, it was extended to other system such as canted AFM [44] as well as FM compounds [45]. During such sign change, magnetization passes through zero value (M = 0) and it is known as magnetic compensation point and the corresponding temperature is called as compensation temperature (T_{Comp}). MR leads to many technological application such as thermally assisted magnetoresistive random access memory (TAMRAM) devices, thermomagnetic switches, spin valve and magnetic tunnel junction, etc. [46–50]

Magnetic compensation has been reported in several RIGs (R = Gd, Tb, Dy, Ho and Er) but without any MR [51]. Here, different temperature dependences of magnetic moments of various sublattices gives rise to magnetic compensation. *Chukalkin* et al. [52] have reported negative magnetization with T_{Comp} = 50 K in polycrystalline $Y_{2.25}Gd_{0.75}Fe_5O_{12}$ compound under field cooled (FC) condition with the cooling field H_{FC} = 15 Oe. They have also explained this phenomenon on the basis of different temperature

dependences of Gd and Fe sublattices moments. On the other hand, magnetic anisotropy also causes MR (under FC condition) as observed in Bi substituted $Tb_3Fe_5O_{12}$ and $Ho_3Fe_5O_{12}$ compounds as shown in Figure 1.10 [16,53]. Here Bi-substitution induces a strong anisotropy due to the strong covalent bonding between Fe(*a*) and Bi ions, such strong anisotropy resists the rotation of Fe^{3+} ions below T_{Comp} and thus leading to MR.

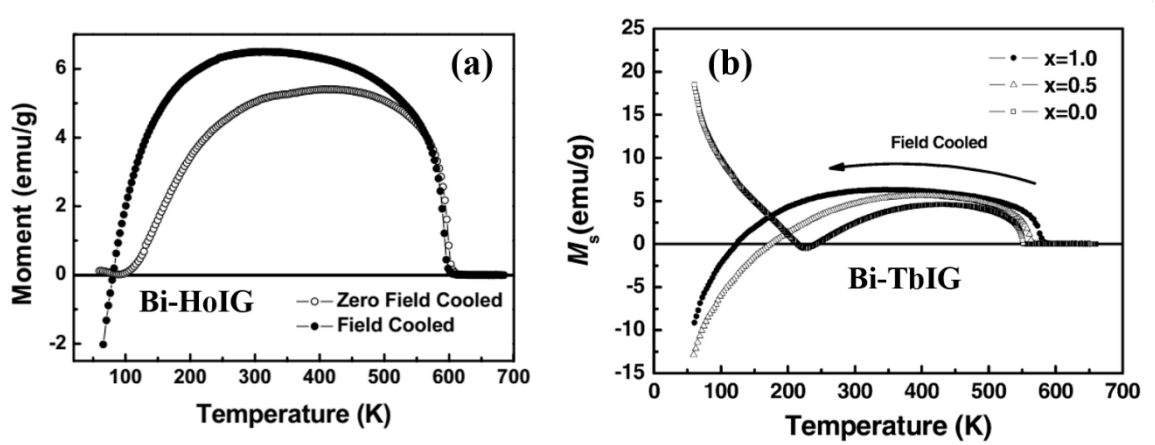

Figure 1.10: Temperature dependence of magnetization in (a) $Ho_2Bi_1Fe_5O_{12}$ (b) $Tb_{3-x}Bi_xFe_5O_{12}$ under FC condition at H_{FC} = 100 Oe [16,53].

Other systems such as spinel ferrites, spinel chromites, orthochromites, manganties, molecular magnets, etc. are also known to show MR due to several reasons. *Menyuk* et al. [54] reported MR in Co_2VO_4 with T_{Comp} = 70 K as per Néel hypothesis of different temperature dependence of sublattice magnetization. In spinel ferrites and chromites, they are mainly explained in terms of different temperature dependences of sublattice magnetization [42,55,56]. In orthoferrites ($RFeO_3$) and orthochromites ($RCrO_3$), the competition between weak ferromagnetic moment due to spin canting and the paramagnetic moment under the negative internal field gives rise to magnetization reversal [57–60]. In intermetallic alloys, it is mostly attributed to different temperature dependence of spin and orbital moments of rare earth elements and due to significant moment of polarized conduction electrons [61,62].

1.7 Dielectric Properties

Dielectric materials have potential application in power, industrial and commercial equipment. Materials having the capacity to store electric charge but cannot conduct electricity are generally known as dielectrics. The bound charges form electric dipoles and their orientation under an electric field E causes a macroscopic dipole moment *p*, which is

measured in terms of polarization [63]. For a linear isotropic and uniform dielectric, the polarization P depends on the strength of the electric field E,

$$P = \varepsilon_0 \chi E \tag{1.11}$$

where ε_0 is dielectric permittivity of free space (8.854×10^{-12} F/m) and χ is dielectric susceptibility. The relative dielectric permittivity (ε_r) or dielectric constant is the ratio of permittivity of the given medium (ε) to the permittivity of free space as given below:

$$\varepsilon_r = \frac{\varepsilon}{\varepsilon_0} \tag{1.12}$$

The chemical structure and the imperfections (defects) of the material, as well as on other physical parameters including temperature and pressure, etc. affect the dielectric permittivity.

The polarization process is divided into five different categories such as (i) electronic, (ii) ionic/atomic, (iii) orientation, (iv) space-charge and (v) hopping polarization. They are explained as follows.

The process of shifting of positive and negative centre of charges with respect to each other in an atom due to the applied electric field gives rise to induced displacement. Such displacement is known as electronic polarization as given in Figure 1.11(a)**.** The time required for electronic polarization is about 10^{-15} sec [63].

In a polyatomic molecule, the ions or atoms displaced relative to each other under an applied electric field gives rise to ionic/atomic polarization as shown in Figure 1.11(b).

The orientation polarization mainly occurs only in materials having permanent dipole moment and the application of electric field causes the reorientation of the dipoles toward the direction of the field as shown in Figure 1.11(c)**.** The material with asymmetric bonding structure having the centre of positive and negative charges not coinciding with each other gives rise to net polarization. Here, the system has permanent dipole moment and the examples are H_2O, NH_3, HF, etc. The time required for orientation polarization is about 10^{-10} sec.

The space charge polarization generally occurs in polycrystalline or amorphous materials having some trapped charge carriers (electron, hole or ions, etc.). These charge carriers are generally trapped at the interface or the electrode of the material due to the carrier injection by electric current. The interfacial polarization occurs at the interface of two phases having different conductivities and permittivity. Unlike other polarization

mechanism, no dipole displacement is involved in interfacial polarization as shown in Figure 1.11(d).

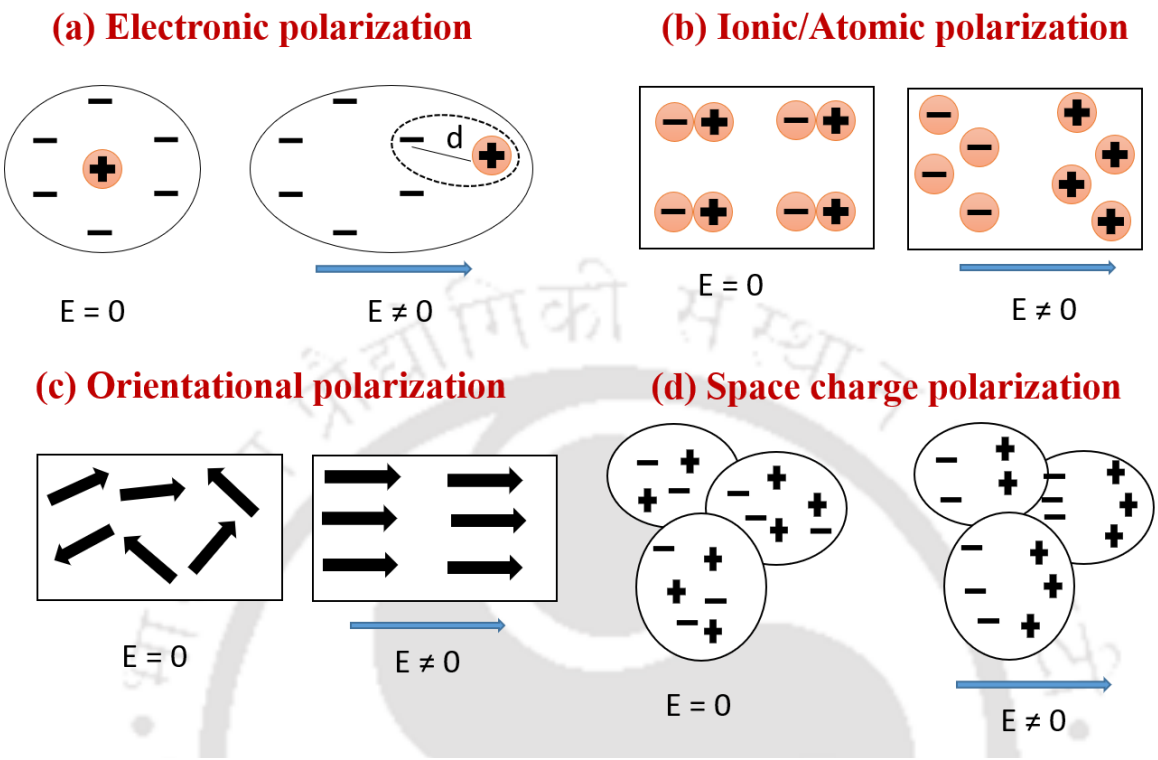

Figure 1.11: Pictorial representation of several types of electric polarization such as, (a) electronic, (b) ionic/atomic, (c) orientational and (d) space-charge polarization.

Hopping polarization occurs due to the hopping of charge carriers from one site to another site and associated potential barrier for such hopping.

There are two approaches for the polarization mechanism: one is time domain and another one is frequency domain. In the time-domain approach, the time dependent polarization is measured immediately after the application of electric field or, the system is brought back to its initial state after removal of electric field. This decay is generally referred to as dielectric relaxation. In the frequency-domain approach, the dielectric constant is measured at different frequencies of alternating excitation fields. Both approaches should be connected to each other and in principle, yields the same result [63].

The polarization can be divided into resonance and relaxation type behaviour. Both the electronic polarization and the ionic polarization are mainly due to the elastic displacement of electron clouds and lattice vibration within the atoms or molecules. Resonance occurs when the natural frequency of the oscillations of the system is nearly close to the frequency of applied electric field. Their interaction is an intramolecular

phenomenon, and the restoring field against the displacement is relatively insensitive to temperature, so electronic and ionic polarization processes are only slightly dependent on temperature. In contrast, orientation polarization is a rotational process, the rotation of a dipole in a material is like a small ball, or any body, rotating in a viscous fluid. Under an external electric field, it tends to change from its original equilibrium state to a new dynamic equilibrium state, and after removing the electric field, it relaxes back to its original equilibrium state. This process is generally referred to as the relaxation process. This polarization involves the inelastic movement of particles, and its interaction is an intermolecular phenomenon; hence, orientational polarizability is strongly temperature-dependent.

1.7.1 Complex Impedance Spectroscopy

Impedance spectroscopy (IS) is a comparatively new and powerful method of characterizing many of the electrical properties of materials and their interfaces with electronically conducting electrodes. IS is used to explore the dynamics of bound or free charge carriers in the bulk or interfacial regions of any kind of solid or liquid material such as ionic, semiconducting, mixed electronic-ionic, and insulators/dielectrics [64]. In polycrystalline solids, electrical properties are strongly affected by microstructure and impedance spectra usually contain features that can be directly related to microstructure, such as grains and grain boundaries resistance and their associated capacitance on the basis of modelled equivalent circuit.

The concept of complex impedance (Z*) was first introduced by Heaviside in 1880 and further developed by *Kennelly* and *Steinmertz* [64]. Impedance is a more general concept than resistance because it takes phase differences into account. Complex electric impedance is the resistance offered to the alternating current (AC) current in a system and defined in terms of Ohm's law:

$$Z^*(\omega) = Z' - jZ'' = \frac{V^*(\omega)}{I^*(\omega)} \tag{1.13}$$

where Z' and Z'' represent real and imaginary components of complex impedance, V*(ω) is voltage across the dielectric material and I*(ω) is the current through the dielectric. For an ideal dielectric, Z' = 0. Hence, the net impedance is capacitive and is given by Z*(ω) = - j/ωC, where ω is angular frequency and C is the capacitance.

The frequency variation of Z' shows a dispersion behaviour and corresponding to this dispersion, a maxima is observed in Z'' versus frequency (*f*) plot. The frequency corresponding to such maximum value of Z'' is knows as relaxation frequency of charge carriers as shown in Figure 1.12. Such relaxation frequency can be written in terms of relaxation time τ (=1/2π*f*). At low frequency, space charge polarization is active and orientational polarization becomes active at higher frequency.

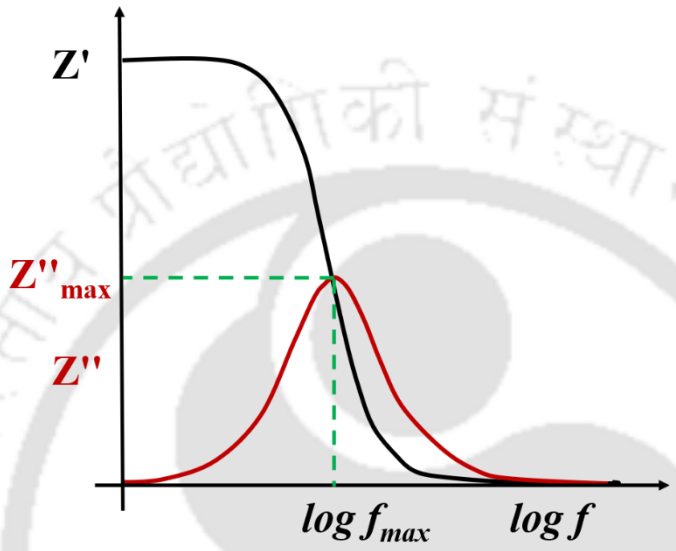

Figure 1.12: The frequency variation of Z' and Z'' showing dispersion and relaxation behaviour.

A special representation of Z* in complex plane is known as Nyquist plots, i.e., plot of Z'' vs. Z' and it provides several information about the electrochemical process inside a dielectric [64]. The impedance spectra are analyzed based on the modelled equivalent circuit. In an ideal case, such plot is always a semicircle with its centre on the Z' axis, as shown in Figure 1.13(a). Here, single semicircle appears and the diameter of this semicircle is equal to the resistance of the material. But in non-ideal case, the centre of the semicircle lies below the Z' axis, and the semicircle is depressed and asymmetric in nature as shown in Figure 1.13(b). In such case, the departure of certain elements from its ideal nature is represented by Constant Phase Element (CPE, denoted by Q), whose impedance is defined as [64],

$$Z_{CPE} = \frac{1}{A}(j\omega)^{-m} \tag{1.14}$$

Here A is a constant and *m* represents the distribution of relaxation time and it lies in the range of $0 \leq m \leq 1$. If $m = 0$, the CPE behaves like a resistance and if $m = 1$ it will behave like a capacitor.

The situation is slightly different in polycrystalline samples where both grains (G) and grains boundaries (GB) come into the picture. Grains are often more conductive, less capacitive as compared to grain boundaries. Single semicircle is generally represented by an equivalent circuit having R and C elements in parallel. If two semicircular arcs are observed, it may have contributions from both G and GB and having two sets of parallel R and C elements arranged in series (Figure 1.13(c)). The semicircle in the low frequency region (higher Z') corresponds to the GB due to larger time scale for long-range distance, while the semicircle in the high frequency region (low Z') is due to G due to the short time scale for short-range motion of charge carriers. The G and GB resistances are estimated from the diameters of corresponding semicircles [64].

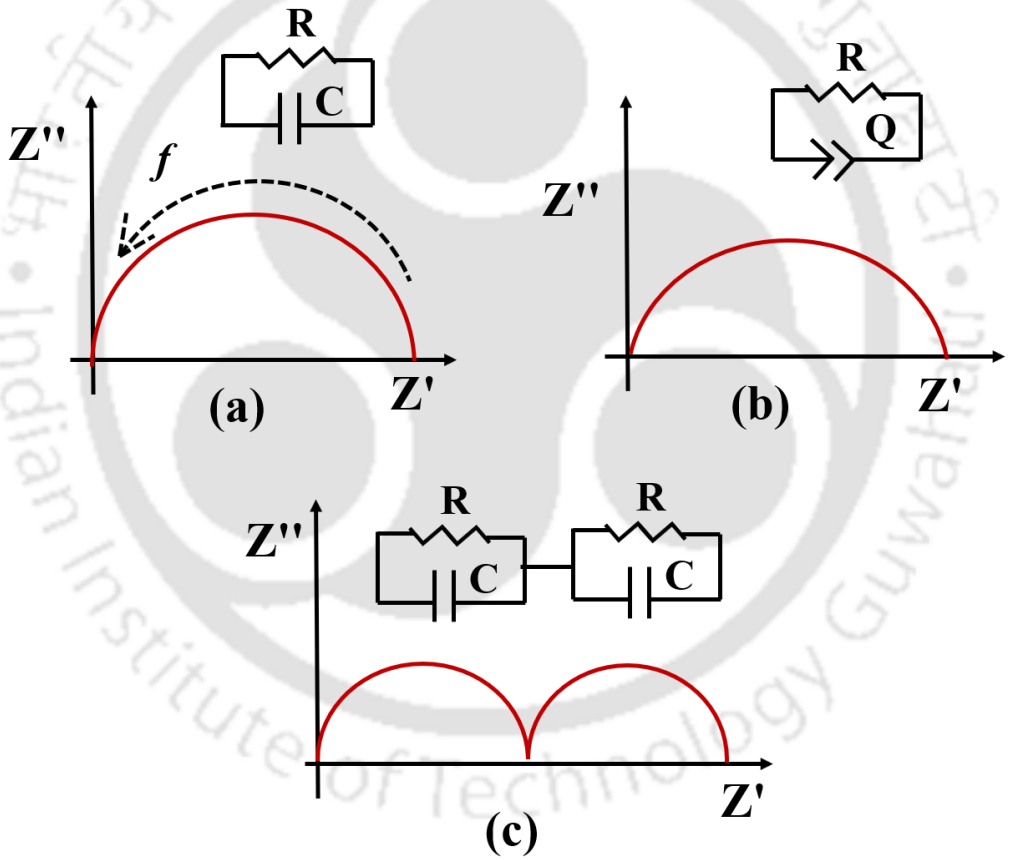

Figure 1.13: Schematic representation of Nyquist plots in different conditions.

1.7.2 Complex Dielectric Spectroscopy

A perfect dielectric is a material having zero electrical conductivity, therefore it stores and returns electrical energy as if it were an ideal capacitor [65,66]. The dielectric spectra unravel more information regarding polarization and dielectric properties as a function of frequency.

The dielectric constant (ε_r) or relative permittivity is defined as:

$$\varepsilon_r = \frac{C}{C_0} \tag{1.15}$$

where C and C_0 are the capacitance of a given assembly in the presence and absence (air) of dielectric medium, respectively. For parallel plate assembly $C_0 = \varepsilon_0 A/t$, where ε_0 is the permittivity of free space, A is the surface area of plate and t is the separation between them. Dielectric constant is a complex quantity,

$$\varepsilon^* = \varepsilon' - j\varepsilon'' \tag{1.16}$$

where ε' and ε" represent the real and imaginary components of dielectric constant. Subscript r is dropped for simplicity. Loss tangent is

$$tan\delta = \frac{\varepsilon''}{\varepsilon'} \tag{1.17}$$

Dielectric constant can also be defined in terms of Z* [64]

$$\varepsilon^* = \frac{1}{j\omega Z^*} = \varepsilon' - j\varepsilon'' \tag{1.18}$$

$$\varepsilon' = \frac{-Z''}{\omega C_0 (Z'^2 + Z''^2)} \tag{1.19}$$

$$\varepsilon'' = \frac{Z'}{\omega C_0 (Z'^2 + Z''^2)} \tag{1.20}$$

where Z' and Z" are respectively the real and imaginary components of impedance for the angular frequency of ω.

The ε' as a function of frequency generally exhibits a dispersion behaviour as shown in Figure 1.14(a) due to the lag between the applied electric field and polarization. It is observed as a relaxation peak in the plot of ε" versus frequency (Figure 1.14(a)). Debye explained the dielectric relaxation for an ideal case of non-interacting dipoles having single relaxation time τ as given below:

$$\varepsilon^* = \varepsilon' - j\varepsilon'' = \varepsilon_\infty + \frac{\varepsilon_s - \varepsilon_\infty}{1 + j\omega\tau} \tag{1.21}$$

Here ε_s and ε_∞ correspond to the dielectric constant in static (low frequency) and high frequency region respectively. τ is the relaxation time and ω is the measured angular frequency. As no dielectric material is ideal (σ→0), and there is a possibility of some free charges in addition to bound charges. So, generally more than one relaxation process is observed. Therefore, Havriliak–Negami (HN) [66,67] modified the relaxation behaviour of

dielectric constant, where the electrical conductivity contribution is also added (Figure 1.14(b)). According to HN model,

$$\varepsilon^* = \varepsilon_\infty + \frac{\varepsilon_s - \varepsilon_\infty}{(1 + (j\omega\tau)^{1-\alpha})^\beta} - j\frac{\sigma^*}{\varepsilon_0\,\omega^s} \tag{1.22}$$

The exponents α and β signify the broadness and asymmetry of dielectric spectra and as per the ideal Debye law, α = 0 and β = 1. $\sigma^*(= \sigma_1 + j\sigma_2)$ is the complex conductivity having the contributions from free charge carriers (σ_1) and space charges (σ_2). The dimensionless exponent s ($0 < s < 1$) signifies the degree of distribution of polarization. The complex dielectric constant shown in equation (1.22) can be resolved into ε' and ε'' as follows [66]:

$$\varepsilon' = \varepsilon_\infty + \frac{\Delta\varepsilon\cos(\beta\phi)}{\{1 + 2(\omega\tau)^{1-\alpha}\,sin(\alpha\pi/2) + (\omega\tau)^{2-2\alpha}\}^{\beta/2}} + \frac{\sigma_2}{\varepsilon_0\omega^s} \tag{1.23}$$

$$\varepsilon'' = \frac{\Delta\varepsilon\sin(\beta\phi)}{\{1 + 2(\omega\tau)^{1-\alpha}\,sin(\alpha\pi/2) + (\omega\tau)^{2-2\alpha}\}^{\beta/2}} + \frac{\sigma_1}{\varepsilon_0\omega^s} \tag{1.24}$$

$$\text{where } \phi = tan\left(\frac{(\omega\tau)^{1-\alpha}\,cos(\alpha\pi/2)}{1+(\omega\tau)^{1-\alpha}\sin(\alpha\pi/2)}\right) \text{ and } \Delta\varepsilon = \varepsilon_S - \varepsilon_\infty \tag{1.25}$$

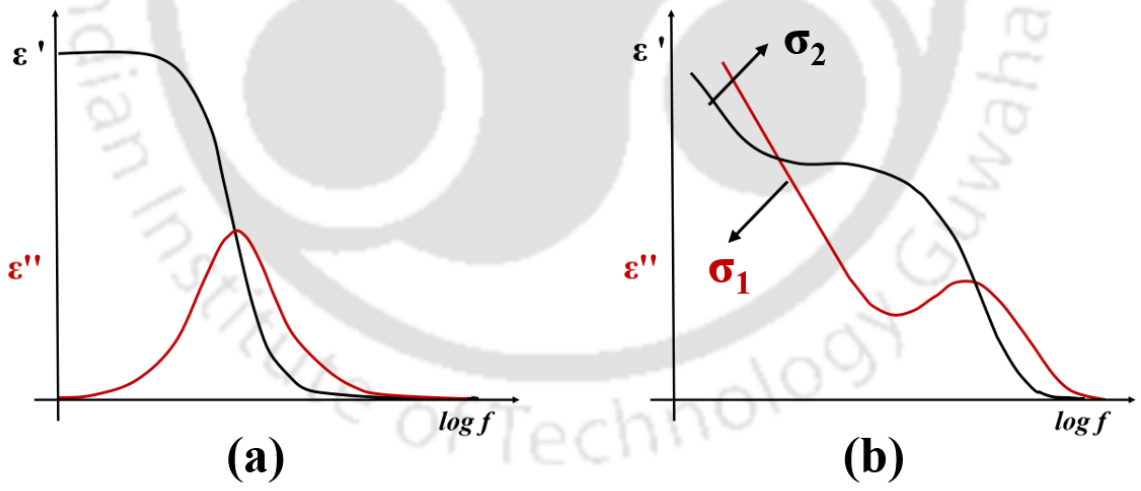

Figure 1.14: The schematic representation of ε' and ε'' as a function of log *f* for (a) an ideal case and (b) non-ideal case having conductivity contribution.

1.7.3 Complex Modulus Spectroscopy

Modulus spectroscopy adds another dimension to the interpretation of electrical response of polycrystalline materials. The reciprocal of complex dielectric permittivity is thought to be the analogue of mechanical shear modulus and this approach is known as

modulus spectroscopy [68]. It is particularly important for dielectrics having mobile charges. It can distinguish between G and GB contributions while suppressing the electrode effect. The grains effect is dominant in modulus spectrum due to its smaller capacitance as compared to that of grain boundaries. As the modulus is inverse of permittivity so, the dominant conductivity effect of ε" is suppressed in M" spectrum. Modulus can be represented in terms of both Z* and ε* such as follows [64]:

$$M^* = M' + iM'' = -i\omega Z^* = \frac{1}{\varepsilon^*} \tag{1.26}$$

$$M' = \frac{\varepsilon'}{\varepsilon'^2 + \varepsilon''^2} \tag{1.27}$$

$$M'' = \frac{\varepsilon''}{\varepsilon'^2 + \varepsilon''^2} \tag{1.28}$$

From the physical point of view, electric modulus assists the dielectric relaxation in the material having constant electric displacement [69]. These modulus spectra were analyzed on the basis of Bergman function explained by Kohlrausch-Williams-Watts (KWW) formula [70,71], written as:

$$M'' = \frac{M''_{max}}{1 - \beta + \left(\frac{\beta}{1+\beta}\right)\left[\beta\left(\frac{f_{max}}{f}\right) + \left(\frac{f}{f_{max}}\right)^{\beta}\right]} \tag{1.29}$$

where M''_{max} represents the peak value of M" and f_{max} is the corresponding frequency. β ($0 \leq \beta \leq 1$) is an exponent which is a measure of broadness of the spectra. Temperature dependent relaxation frequency or time can be analyzed based on Arrhenius law.

$$\tau = \tau_0 exp\left(\frac{E_a}{k_B T}\right) \tag{1.30}$$

Here τ is the relaxation time corresponding to the relaxation peak. τ_0 is a constant, which is a measure of τ at $T \rightarrow \infty$, E_a is the activation energy of relaxation and k_B is the Boltzmann constant.

1.7.4 AC Conductivity

The frequency dependent ac conductivity can be extracted using the relation [66]:

$$\sigma_{ac}(\omega) = \omega\varepsilon''\varepsilon_0 \tag{1.31}$$

where ε_0 is permittivity in free space (8.854×10^{-12} F/m). AC conductivity spectrum contains two regions as shown in Figure 1.15(a). (i) The dc plateau (dc conductivity) at lower frequency, which is independent of frequency due to long- range translational motion of charge carriers assisted by successful hopping of charge carriers to neighborhood vacant sites as shown in Figure 1.15(b). (ii) The other region is the frequency dependent region, where σ_{ac} increases with increase in frequency due to increase in the ratio of successful to unsuccessful hopping as shown in Figure 1.15(c) [72].

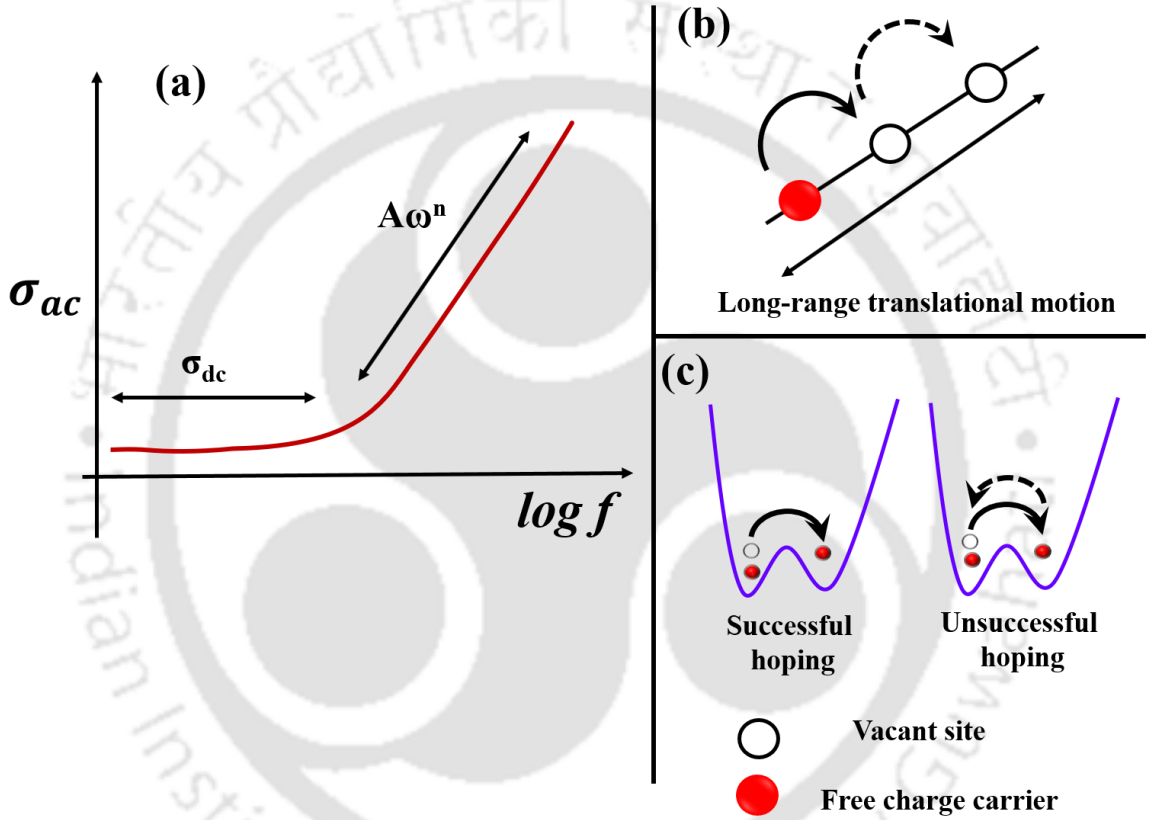

Figure 1.15: Pictorial view of (a) Ac conductivity spectra, (b) long-range transitional motion and (c) successful and unsuccessful hoping of charge carriers.

A convenient law which is used to investigate the $\sigma_{ac}(\omega)$ behaviour at constant temperature was proposed by *Jonscher* [73].

$$\sigma_{ac}(\omega) = \sigma_{dc} + A\omega^n \tag{1.32}$$

where σ_{dc} is dc conductivity, which is related to the plateau region or frequency independent region and $A\omega^n$ is frequency dependent term which characterizes dispersion phenomenon. A is constant and n is frequency exponent, which reflects the degree of

interaction between mobile ions and lattice around them. Generally, *n* lies between 0 and 1 but in some compounds, it can be more than 1. For $n < 1$, the conductivity corresponds to translation motion of charge carriers, and for $n > 1$ it is attributed to localized or reorientational hopping motion due to the back and forth movement of electrons between two charge defects [63].

1.8 Prior Work on Rare earth Iron Garnet

The interest in RIGs can be traced to way back its discovery in 1956 by *Bertaut* and *Forrat* [24]. In the vast ferrite family, RIGs form a huge part of it with R = Y, Nd, Sm, Gd, Tb, Dy, Ho, Er, Tm, Yb, Lu and Bi. In 1957, *Bertaut* and *Pauthenet* [74] have studied the structural and magnetic properties of several RIGs with R = Y, Gd, Tb, Dy, Ho, Er, Tm, Lu, etc. In general, RIGs are easily synthesized using solid-state reaction method [74–78]. RIGs exhibit many interesting properties such as, controllable saturation magnetization [79,80] dielectric [12,81], ferroelectric and multiferroic [18,82] magneto-electric and magneto-dielectric [83–87] and magneto-caloric [17,88,89] properties. Some of them are also known to exhibit magnetic compensation [19,51,74,90], negative magnetization [16,52,53] and spin-seeback effect [21,91–94], etc. Due to these phenomenal properties they are the key materials for oscillators, optical isolators, sensors, microwaves devices, spintronic devices, phase shifters and electrochemical devices etc. [19,20,91,95,96].

Among the RIG family, YIG is popularly known as interesting ferrimagnetic materials having applications in microwave devices, phase shifters, optical oscillators, circulators, magneto-optic devices. Their interesting physical properties such as controllable saturation magnetization, high electrical resistivity (10^{12} Ω), less dielectric loss, narrow linewidth of ferromagnetic resonance, etc. make them as natural choice for microwave applications. So, we shall first discuss about the YIG.

1.8.1 Yttrium Iron Garnet (YIG)

YIG can be chemically represented as $\{Y_3\}[Fe_2](Fe_3)O_{12}$. The crystal structure of YIG is similar to other RIGs as explained in section 1.1 [25]. The lattice constant and the density of YIG is 12.372 ± 0.004 Å and 5.17 g/cm^3, respectively [25]. In YIG, the bond lengths Fe(*a*)-Fe(*d*), Fe(*a*)-Y(*c*) and Fe(*d*)-Y(*c*) is 3.46 Å, 3.46 Å and 3.79 Å, respectively. The value of bond angles Y(*c*)-O-Fe(*d*), Y(*c*)-O-Fe(*a*) and Fe(*a*)-O-Fe(*d*) is 123.6°, 103.1° and 126.6°, respectively. Each oxygen ion is shared by $3Y^{3+}$(*c*), $2Fe^{3+}$(*a*) and $3Fe^{3+}$(*d*) nearest neighbour cations.

The origin of FIM in YIG is due to the exchange interaction between magnetic Fe^{3+} ions occupied in tetrahedral (*d*) and octahedral (*a*) sublattices through an oxygen ion. Such interaction leads to FIM due to antiparallel coupling of $3Fe^{3+}$ ions in '*d*' site with $2Fe^{3+}$ ions in '*a*' site as depicted in Figure 1.16. The ferrimagnetic transition temperature in YIG is 550 K [25]. The net magnetic moment per formula unit in YIG can be empirically written as:

$$M_{net} = (3M_d - 2M_a) \tag{1.33}$$

where M_d and M_a represent the magnetic moment of Fe^{3+} ions at tetrahedral and octahedral site, respectively. Here Y^{3+} does not contribute any magnetic moment due to its $4f^0$electronic configuration. In equation 1.33, the factor 3 and 2 represent number of Fe^{3+} ions at tetrahedral and octahedral site, respectively. As per equation 1.33, the net magnetic moment per formula unit is 5 μ_B since, each Fe^{3+} ion contribute 5 μ_B.

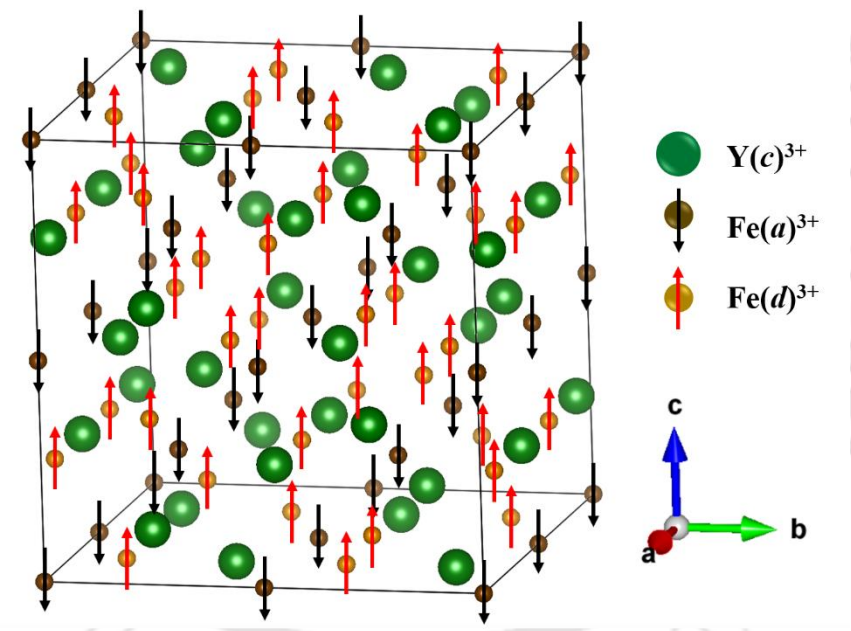

Figure 1.16: Pictorial representation of spin structure in YIG showing spin up and spin down for Fe^{3+} (*d*) and Fe^{3+} (*a*), ions respectively.

Since, YIG exhibits many interesting properties, so in order to improve the physical properties many researchers are performing the cationic substitution at Y and Fe site. Anderson [97,98] reported the magnetic and electric properties of parent and Dy, Er and Ho substituted YIG. The magnetic and dielectric properties of YIG by substituting La, Ce, Nd, Sm, Gd, Dy, Bi, etc., at Y site have been studied by several authors [99–103]. The substitution of Ce, Sm, Gd, Dy, and Bi results in decrease in the saturation magnetization. However, La and Nd substitution increases the saturation magnetization upto certain

concentration ($x < 1.0$) and beyond that it starts decreasing due to the lattice distortion. La and Bi-substitutions regulate the magneto-dielectric and magneto-capacitance behaviours in YIG [102,104]. Bi-substitution reduces the magneto-dielectric effect while La substitution enhances the same effect up to certain concentration. The dielectric constant (from 300 to 60 at 10 kHz) and dielectric loss values (0.75 to 0.25 at 10 kHz) are found to reduce upon Bi-substitution. Ce and Bi-substitutions also reduce the sample sintering temperature from 1673 K to 1373 K [22,99,100].

Several authors have studied the magnetic and dielectric properties with the substitution of transition elements such as Al, Mn, Cr, Ti, Sn and Mo at Fe site of YIG [87,105–112]. The substitution of Mn, Mo, and Cr increases the magnetic moment due to their preferential occupation at octahedral site. While, nonmagnetic Al substituted polycrystalline YIG leads to decrease in saturation magnetization due to their partial substitution at tetrahedral and octahedral site. Moreover the activation energy for hopping process increases with the increase in Al concentration [107,109]. The substitution of non-magnetic elements such as Sn and Ti at Fe site, shows magneto-dielectric behaviour due to higher Fe^{2+} concentration and Fe^{2+}-Fe^{3+} networks [87,112]. A few authors have studied the co-substitution of various cations such as Al-Cr, Ca-Zr, Ca-V, etc. [113–116]. The value of saturation magnetization and Curie temperature decrease with Al-Cr substitution due to the potential replacement of tetrahedral Fe ions. The co-substitution Ca-Zr enhances the saturation magnetization and coercivity values due to mismatch in Fe-O-Fe bond angle and generation of impurity phase [116]. The Ca-V substitution reduces the saturation magnetization from 25 emu/g to 5 emu/g, while increases the transition temperature due to the occupation of mixed valent ions at tetrahedral site which increases the exchange interaction between Fe and V.

1.8.2 Gadolinium Iron Garnet (GIG)

In addition to YIG, Gadolinium iron garnet (GIG) is another important compound in RIGs series, having excellent magnetic and dielectric properties [17,90,117,118] . GIG is also a potential candidate for microwave devices, circulators, high-density magnetic and magneto-optical storage application.

The detailed refined crystal structure of GIG was first determined by *Weidenborner* in 1961 [119]. The crystal structure of GIG is also similar to RIG (Figure 1.3). Since Gd^{3+} ion has larger ionic radius so, the lattice constant is larger (a = 12.470±0.005Å) and the density is 6.452 g/cm^3. The Fe^{3+}(a)-O^{2-}-Fe^{3+}(d) bond angle and Fe(a)-Fe(d) bond length

are relatively higher for GIG, i.e., 127.4° and 3.48 Å, respectively. The ferrimagnetic T_C is comparable with that of YIG i.e., (~560K) [118].

Unlike YIG, the GIG exhibits magnetic compensation around 286 K. The origin of magnetic compensation in GIG can be understood in terms of competition between magnetic moments of three Fe^{3+} ions in the tetrahedral site ($3M_{Fe}(d)$) and the total magnetic moment of two Fe^{3+} ions in the octahedral site ($2M_{Fe}(a)$) and the exchange enhanced PM moment of three Gd^{3+} ions at dodecahedral site ($3M_{Gd}(c)$). So, the net magnetic moment per formula unit (M_{net}) can be empirically written as [43,118]:

$$M_{net} = 3M_{Fe}(d) - [2M_{Fe}(a) + 3M_{Gd}(c)] \quad (1.34)$$

At T = T_{Comp}, it is expected that, $|3M_{Fe}(d)| = |2M_{Fe}(a) + 3M_{Gd}(c)|$. Here, the exchange enhanced PM moment of Gd^{3+} refers to weak exchange coupled magnetic moment of Gd^{3+} ions at '*c*' site with Fe^{3+} ions at the '*a*' site.

GIG also exhibits interesting magnetic and dielectric properties due to the presence of magnetic rare earth element (Gd) and its weak interaction with the net ferrimagnetic moment of Fe ions [21,118,120,121]. Several researchers have studied the Gd substitution in YIG and it was found that Gd substitution reduces the room temperature saturation magnetization however slightly increases the FIM T_C from 550 K to 560 K [14,15,122]. The magnetic properties of RIGs (R = Gd, Y, Tb) showed that GIG exhibit a reasonable value of coercivity (170 Oe) and low value of magnetization (0.30 emu/g) as compared to YIG and TbIG, at room temperature [43]. With increase in ionic radius (Gd<Tb<Dy<Ho<Er) the compensation temperature reduces from 288 K to 80 K [51]. The magnetic anisotropy for nanocrystalline GIG (10^5 J/m^3) is much higher that bulk GIG (10^4 J/m^3), which is due to presence of dipolar interaction and single-ion anisotropy. The fundamental properties of GIG can be improved with the cation substitution at Gd and Fe site in GIG compound. So, a very few authors have reported the electric properties in GIG [123]. The conduction mechanism is nearly similar in both the compound but the dc resistivity of GIG is smaller as compared to YIG.

During the course of my Ph.D. work, I have come across a few important works on RIGs. Multiferroic behaviour is observed by Bi-substitution in YIG [124]. Substitution of Zn^{2+} and Cu^{2+} at Fe site of YIG is reported to increase the magnetic moment. Er and Bi-substitutions at Gd site increase the magnetization and reduce the dielectric loss in GIG [125,126].

Thus, rare earth iron garnets are versatile materials having both interesting magnetic and dielectric properties. Further work is needed to tune their magnetic, dielectric and magneto-electric properties.

1.9 Motivation

In accordance with the above literature survey, it is well-established that YIG and GIG demonstrate remarkable magnetic and dielectric properties. Among ferrites family, YIG is a primary candidate for microwave application, while GIG is a potential candidate for magneto-caloric and thermally assisted random access memory applications. In addition, both are centrosymmetric, lacking the presence of ferroelectric and multiferroic properties. Yet, there is a lack of detailed magnetization and dielectric studies by tuning their magnetic interaction by substituting appropriate magnetic or non-magnetic impurity materials. A few reports are available on Bi and Sm-substitution in YIG, influencing the magnetic and dielectric properties, however, detailed investigation is required. The substitution of magnetic cations at Fe site is found to have large influence on its magnetic and dielectric properties. As appraised in the previous sections, a very few authors have reported the magnetic and dielectric properties of GIG by tuning their crystal structural parameters. The rare earth substitution at Gd site can provide us with interesting magnetic properties due to the presence of magnetic compensation near room temperature in GIG. Moreover, Sm exhibits high magnetic anisotropy compared to Gd that can lead to negative magnetization and exchange bias behaviour. Further, systematic analysis of the effect of Cr-substitution at Fe site in GIG is also very limited. The substitution of these cations is expected to regulate the magnetic and electrical properties such as the saturation magnetization, magnetocrystalline anisotropy, magnetic ordering temperature, permittivity of the materials for specific applications. Therefore, in the present thesis work, we have carried out extensive investigation of magnetic and dielectric relaxation of YIG and GIG based compounds. The samples chosen for the above study are as follows:

1) $Y_{3-x}Sm_xFe_5O_{12}$ (x = 0, 0.5, 1.0, 2.0 and 3.0)
2) $Y_3Fe_{5-x}Cr_xO_{12}$ (x = 0, 0.1, 0.2, 0.3, 0.4 and 0.5)
3) $Y_3Fe_{5-x}Mn_xO_{12}$ (x = 0, 0.1 and 0.2)
4) $Gd_{3-x}Sm_xFe_5O_{12}$ (x = 0, 0.5, 1.0, 2.0 and 3.0)
5) $Gd_{3-x}Bi_xFe_5O_{12}$ (x = 0, 0.5 and 1.0)
6) $Gd_3Fe_{5-x}Cr_xO_{12}$ (x = 0, 0.1, 0.2 and 0.3)

The above mentioned samples were characterized by using sophisticated instruments such as X-ray diffractometer (XRD), Raman spectrometer, Field emission scanning electron microscope (FESEM), Energy dispersive X-ray (EDX) spectrometer, Vibrating sample magnetometer (VSM), and LCR meter. The crystal structure, morphological and compositional analysis were carried out by recording micrographs using XRD, FESEM equipped with EDX. The magnetic properties of these samples were characterized by taking the temperature and field variations of dc magnetization using Lakeshore make VSM (model no. 7410). The dielectric data of these samples were obtained by using LCR meter. The preparation technique of the above proposed samples and the working principles of these sophisticated instruments are briefly discussed in Chapter 2.

Chapter 2

Experimental Techniques

This chapter discusses about different experimental methods and equipment used for material synthesis, characterization and various physical measurements. During my research work, we have used solid-state and sol-gel routes to synthesize the samples. The precursor obtained from either manually grinded powders or sol-gel route were subjected to various stages of presintering and sintering using commercial high temperature furnaces. The prepared samples were characterized using several sophisticated equipment, viz. X-ray Diffractometer (XRD) to record powder diffraction patterns for studying phase purity and crystal structure; Field Emission Scanning Electron Microscope (FESEM) to study the microstructural morphology and Energy Dispersive X-ray (EDX) Spectroscopy to carry out compositional analysis. Micro-Raman spectrometer was used to study Raman spectra in order to analyze vibration modes. Temperature and field variations of magnetization were measured by using Vibrating Sample Magnetometer (VSM) and Physical Properties Measurement System (PPMS) to study the magnetic properties. LCR meter was used to record the frequency and temperature variations of complex impedance spectra. The above said experimental techniques are elaborated as follows.

2.1 Sample Preparation

In general, materials do not form in single-phase at ambient temperature in laboratory due to the lack of diffusion among the constituent elements. Therefore, the materials require heat treatment to overcome the kinetic barriers and it is done by two processes, namely presintering and sintering. During presintering, the precursor decomposes to form the oxides and at this stage, the reaction among the preparatory materials begins. During sintering process, the densification and the reduction of total surface (interface) area due to the expansion of the grain size occurs. The material parameters such as grain size, grain growth, densification, etc. are controlled by the sintering process such as, the sintering temperature, duration, rate of heating and cooling, etc. [127]. Before the sintering process, the presintered powder was pressed into pellets

form, which increases the contact between the particles. Based on reaction time, it may take several days to make the best compound and to ensure the homogeneous samples.

In the present thesis, we have synthesized the samples using solid-state route and sol-gel chemical reaction method. Primarily, the solid-state reaction method was used for the ceramic samples, because it does not require any solvent. In solid-state reaction method, the oxides react chemically without any intermixing solvent at higher temperature and the yield product is dense and stable due to requirement of higher temperature. While in sol-gel method, the mixing of starting material occurs at molecular level and it does not require high sintering temperature as compared to the solid-state reaction method and gives the nanometer range of particles. The particle size, density, etc. can be further tuned by annealing at higher temperature.

2.1.1 Solid-State Reaction Method

The starting compounds were taken in the oxides form, viz. Yttrium Oxide (Y_2O_3), Gadolinium oxide (Gd_2O_3), Samarium Oxide (Sm_2O_3), Bismuth Oxide (Bi_2O_3), Ferric oxide (Fe_2O_3), Chromium oxide (Cr_2O_3) with purity > 99%. The compounds were weighed in stoichiometric ratio using a Mettler Toledo (model no AG135) make electronic weighing balance, with an accuracy of ± 0.01 mg. They were mixed and grinded in acetone medium for a few hours using an agate mortar and pestle. The mixed powder was transferred into an alumina crucible and were kept in a furnace to pre-sinter in the temperature range of 873 K to 1073 K for 12 hours. The pre-sintered powder was reground to make homogenous mixture. The ground powder samples were pressed into cylindrical shape pellets of 10 mm diameter and thickness within 2 mm under the pressure of 2.98×10^8 N/cm^2 by using a stainless-steel die and hand operated hydraulic KBr press supplied by Techno-Search instruments, India. The above presintering was repeated a few times with a few intermediate grinding and re-pelletisation. The final sintering was carried out in pellet form in the temperature range of 1373 K to 1673 K, and it may vary for different samples series. The different sintering temperature for the respective series are given in the respective chapters of series (chapters 3 to 6).

2.1.2 Sol-Gel Reaction Method

In the sol-gel reaction method, the starting materials were Yttrium oxide (Y_2O_3), Manganese nitrate ($Mn(NO_3)_2.4H_2O$), and Ferric nitrate ($Fe(NO_3)_3.6H_2O$) as per the

stoichiometric ratio with purity better than 99%. Y_2O_3 was dissolved in nitric acid to convert it into nitrate. The uniform mixture of starting compounds of nitrates was dissolved in distilled water. Excess amount of citric acid and ethylene glycol were added to the above mixture to convert them into citrate. The uniform and homogeneous mixture of the above solution was evaporated slowly using a hot plate at 348 K until a gel was formed. The polymeric gel was kept at 363 K for around 12 hours to completely evaporate the solvent. The obtained precursor powder was presintered at 873 K for 12 hours to decompose the remaining organic reagents. Before the final sintering, several intermediate grinding and re-pelletisation were imposed and the final sintering in pellet form was carried out at 1573 K.

2.2 High Temperature Furnace

In the present thesis work, the heat treatment of the precursors was carried out using commercial table-top high temperature furnaces with a maximum operating temperature of 1773 K (model HTCT 03/15). The furnace was supplied by K.G. Projects and Equipment manufactured by Nabertherm, Germany. The high temperature furnace diagram with accessories are shown systematically in Figure 2.1.

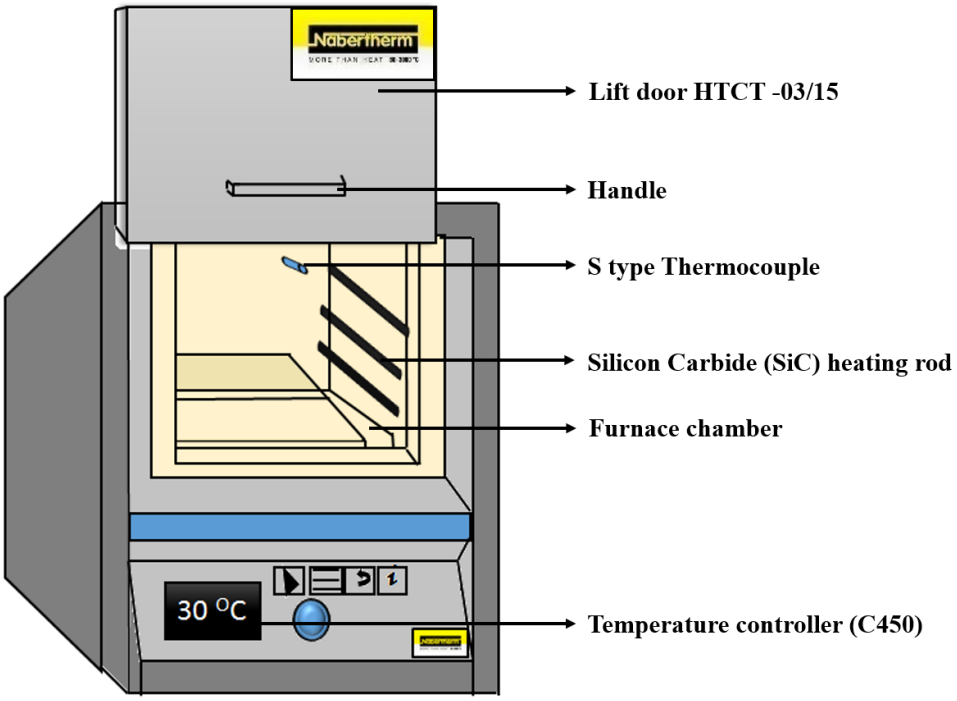

Figure 2.1: Overview of table-top high temperature furnace (model: HTCT 03/15).

The furnace housing body was made up of stainless steel with dual shell housing to avoid the heating of outer body and surroundings. The temperature was controlled using PID programmable temperature controller (model no. C450) with 10 program and 20 segments facility. The S type thermocouple (Platinum Rhodium - 10% / Platinum) was used as temperature sensor. The high-quality Silicon-Carbide (Si-C) rods were used as heating element. Solid-state relay was used as switching system to turn on the power to the Si-C rod. The accuracy of temperature controller is ± 1 K. The operating voltage of the furnace is 380 V - 400 V (50 Hz - 3 Phase) with a current rating of 20 A.

2.3 X-ray Diffraction

Powder diffraction technique is an essential and crucial tool in the characterization of materials and the data analysis makes it more powerful and quantitative. The powder diffraction pattern gives several important information, such as crystallographic lattice parameters, crystallite size, etc. The X-ray diffraction is the outcome of Bragg's law. When an X-ray beam is incident on the powder sample having several lattice planes with interplanar distance of few Angstroms (Å) units, which is comparable to the wavelength of incident monochromatic X-ray. The diffracted X-ray from the surface of lattice planes undergoes constructive and destructive interference depending upon the interplanar distance and inclination angle (θ). The constructive interference obeys Bragg's law, i.e.,

$$n\lambda = 2dsin\theta \qquad (2.1)$$

where n and λ represent the order of the spectrum and wavelength of the incident X-ray beam, d represents for distance between two consecutive planes corresponding to the particular miller indices, (hkl) as shown in Figure 2.2(a)**.**

In the current thesis work, the XRD patterns were recorded at room tempeartrue with the help of X-ray diffractometer, (θ-2θ Rotating Anode X-ray) of Rigaku make TTRAX III with CuK_α radiation (λ = 1.5406 Å). Here, X-rays were produced by maintaining the X-ray generator voltage and current around 50 kV and 220 mA, respectively. The basic principle of powder XRD based on Bragg-Brentano geometry is illustrated in Figure 2.2(b). In this geometry, both X-ray generator and detector are placed at equidistance from the sample holder. The X-ray source (F1), sample and the slit in the detector (F2) lie always in a circle, so that X-rays produced from source and diffracted by an angle 2θ, will arrive exactly at the same point F2. In other words, when the X-ray tube and detector lie on the circle with its centre positioned on the sample gives the perfect

focusing [128]. The data were collected in a usual θ-θ scanning from 15° to 80° (2θ angle) with the step size ($\Delta\theta$) of around 0.03° and scan speed of 3°/min.

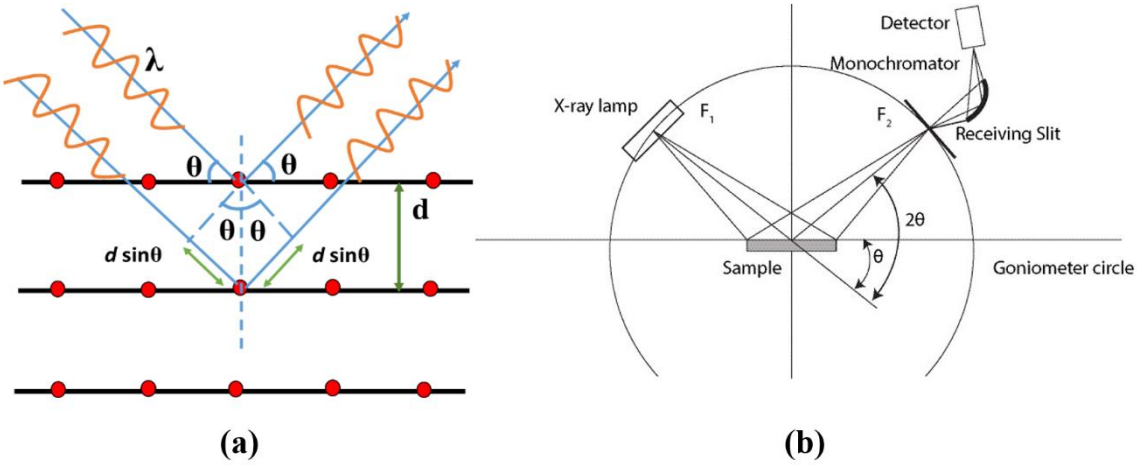

Figure 2.2: (a) Schematic representation of Bragg's Law and (b) Bragg-Brentano geometry or ray diagram of XRD.

The major breakthrough in the XRD analysis was the Rietveld refinement method developed in 1969. The XRD patterns were analyzed using Fullprof software based on the Rietveld technique. It examines the phase purity using crystal structure refinement, along with the structural parameters such as atomic positions, lattice parameters, and experimental factors. A Pseudo-Voigt and polynomial functions were used to refine peak shape and background, respectively. It minimizes the difference between the calculated and measured diffraction profiles using a least-squares approach. During the refinement, mainly the global parameters, such as background polynomial, scaling factor, half-width parameters (u, v, w) and lattice parameters (a, b, c) were varied. Besides, isotropic displacement (temperature) parameters (B_{iso}), nuclear structure variables such as fractional atomic coordinates (x, y, z), and occupancy values (Occ) were varied. Here, occupancy is the chemical occupancy normalized to the multiplicity of the general position of the group, where the oxygen occupancy was taken as 1.0 for all the refinements, and it was constant during the refinement. The quality of the refinements are based on the values of reliability factors such as, R_p, R_{wp}, R_{exp}, R_{Bragg}, R_F and χ^2 and they are defined as follows [129].

Profile factor, $$R_F = 100 \times \frac{\sum_{i=1,n}|y_i - y_{c,i}|}{\sum_{i=1,n} y_i} \quad (2.2)$$

Here, y_i is the observed data and $y_{c,i}$ is the calculated data and n represents the number of data points.

Weighed profile factor, $$R_{wp} = 100\times\left[\frac{\sum_{i=1,n}\omega_i|y_i-y_{c,i}|^2}{\sum_{i=1,n}\omega_i y_i^2}\right]^{1/2} \quad (2.3)$$

Here, $\omega_i = \frac{1}{\sigma_i^2}$, σ_i^2 is the variance of y_i.

Expected weight factor, $$R_{exp} = 100\times\left[\frac{|n-p|}{\sum_{i=1,n}\omega_i y_i^2}\right]^{1/2} \quad (2.4)$$

Here, (n - p) gives the number of degrees of freedom, where n is the total number of experimental data points and p is the number of refined parameters.

Reduced chi-square, $$\chi^2 = \left[\frac{R_{wp}}{R_{exp}}\right]^2 \quad (2.5)$$

Bragg factor, $$R_{Bragg} = 100\times\frac{\sum_h|I_{obs,h}-I_{calc,h}|}{\sum_h I_{obs,h}} \quad (2.6)$$

Here, h represents the particular hkl Bragg peak. The $I_{obs,h}$ and $I_{calc,h}$ are the observed and calculated intregated intensities, respectively.

Crystallographic R_F factor, $$R_F = 100\times\frac{\sum_h|F_{obs,h}-F_{calc,h}|}{\sum_h F_{obs,h}} \quad (2.7)$$

$F_{obs,h}$ and $F_{calc,h}$ are the observed and calculated structural factor, respectivley. Visualiation of electronic and structural analysis (VESTA, version 4.3.0) software was used to generate the crytsal strutre of RIGs.

2.4 Raman Spectroscopy

In addition to XRD, Raman spectroscopy is a versatile and adaptable tool for studying the crystal structure and their bonding information. Raman scattering was experimentally first found by *C. V. Raman* in 1928 and he won Nobel prize in 1930 for this significant discovery. It is a kind of vibrational spectroscopy, generally used to study properties such as crystalline phases, defects, strain, etc., within a system.

Raman scattering is easily understood as per quantum theory of radiation. When a monochromatic radiation of energy $h\nu_0$, incident on the sample and it interacts with the molecular vibration. In elastic scattering, the energy of incident light and scattered wave light remain same and it is known as Rayleigh scattering. However, a fraction of scattered light exhibit different energy (low or high) than that of incident light, due to the change in

vibrational or rotational modes within a sample and it is known as inelastic or Raman scattering [130].

The Raman spectra contain three different segments, Rayleigh, Stokes, and anti-Stokes scattering. If ν_0 and ν_s are the incident light and scattered light frequency, then Raman spectra or Raman shift present, $\Delta\nu = \nu_0 - \nu_s$. For $\nu_s < \nu_0$, Stokes lines are observed and it is basically the red shifting the spectrum. While, if the molecule is already in the excited energy state, the scattering process may lead to $\nu_s > \nu_0$ and it is known as anti-Stokes line, where blue shift is observed. Stokes radiations are more intense than anti-Stokes radiation, since the population in the vibrational ground state is larger and have more intensity. So, mostly the Stokes radiation were collected for the analysis. The shift in wavelength of the scattered light depends upon the chemical composition of the molecules, which are responsible for scattering. The intensity of Raman scattering is proportional to the magnitude of the change in the molecular polarization. According to Raman selection rule, the displacement of the constituent atoms from the equilibrium positions leads to molecular vibration and hence change in molecular polarizability [131].

Raman spectrometer is classified as dispersive and non-dispersive. Dispersive spectrometer based on the light scattered from a sample using a diffraction grating, while non-dispersive spectrometer works based on Michelson interferometer. Figure 2.3 depicts the block diagram of micro-Raman spectrometer, which is of dispersive type. In the present thesis, the Raman spectra was recorded at room temperature by using micro-Raman spectrometer (LabRam HR800, Horiba Jobin Yvon) in the wavenumber range of 100-800 cm^{-1} with an excitation wavelength of 514 nm. Here, the intense monochromatic laser beam is incident on a sample through a microscope with spot size of a few microns. The spectrometer of 800 mm focal length is confocally coupled with the microscope having two switchable gratings. Two laser sources are mainly used as a photon source, He-Ne laser (λ = 632.8 nm) and Argon laser (λ = 488 nm and 514 nm). The laser beam from the source is fully reflected by the beam splitter and splits the beam into two parts with equal wavelengths. The beam was allowed to fall on the sample, which generates both Rayleigh and Raman scattering. Here the notch filter blocks the Rayleigh scattered wavelength and allows the inelastic scattered wavelength. The scattered light was allowed to pass through the grating and etalon, which in turn resolve the weak inelastic scattered wavelength coming from the sample more efficiently. Further, the beam was allowed to enter into a charge couple device (CCD), where it detects the change in polarizability of the sample

from the change in wavelength and converts into the intensity. The intensity variation as a function of the wavenumber is displayed on the computer screen for the user.

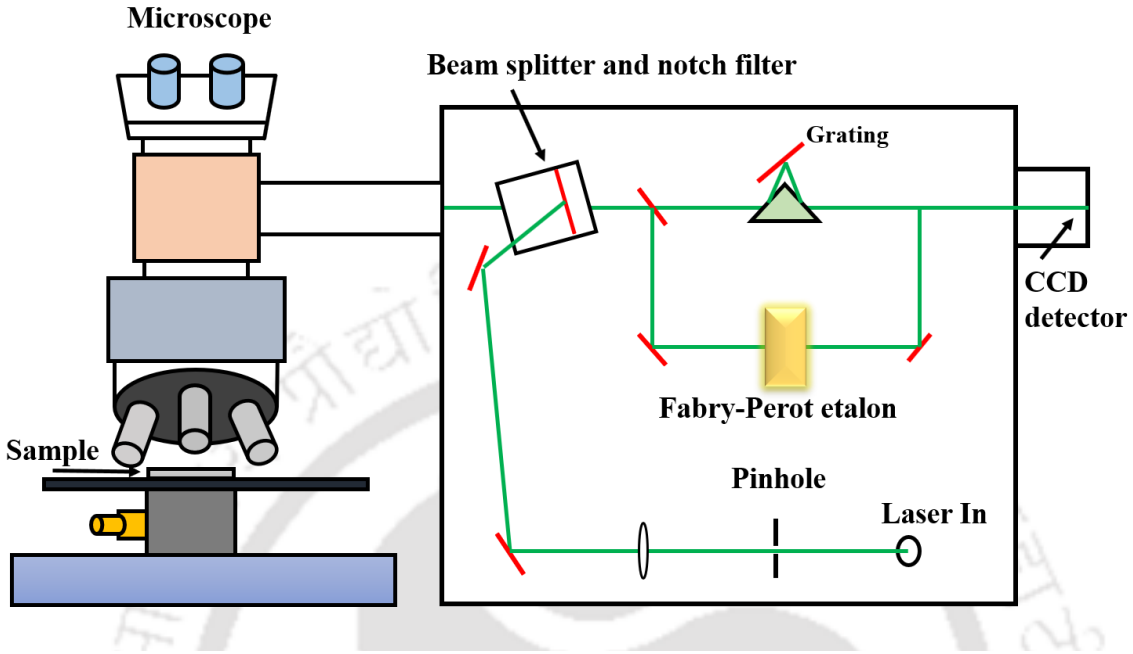

Figure 2.3: Block diagram of Raman spectrometer.

2.5 Field Emission Scanning Electron Microscope

Field emission scanning electron microscopy (FESEM) provides surface morphology and the elemental information of a wide variety of samples (material, biological, chemical, etc.) at different magnifications (10X to 3,00,000X). The FESEM produces clear, electrostatically less distorted images with high spatial resolution down to 1 nm compared to that of the conventional scanning electron microscope (SEM). The in-lens FESEM can be used for ultra-high magnification imaging.

FESEM works with a field emission source called as cold cathode field emitter. The field emission source is basically a zirconium oxide coated tungsten (ZrO_2/W) emitter, which operates in a thermally assisted Schottky emission anode. This type of gun provides narrower probing beams as well as high electron energy, resulting in both improved spatial resolution and minimized sample damage due to charging. The electrons liberated from the field emission source are accelerated in a high electrical field gradient under extreme vacuum. The accelerating voltage between cathode (electron gun) and first condenser lens (anode) is commonly in the order of 0.5 to 30 kV. The high vacuum helps to prevent

discharges inside the instrument, and allows the electrons to move along a column without scattering. Under the high vacuum column, the primary electrons are focused and deflected by the second condenser lens (magnetic lens) to produce a narrow scan beam, which scan point-to-point across the sample using scanning coil and interact with the sample (Figure 2.4). Thus, this bombardment gives different types of emitted electrons from each spot of the specimen as displayed in Figure 2.5. Upon electron impingement on the surface, the interaction volume assumes a drop shape. The dislodged electrons scattered from the surface are known as secondary electrons. A highly efficient annular in-lens detector (working distance < 10 mm) receives the secondary electrons and produces an electronic signal. This signal is amplified and transformed into a digital image of the sample, which is displayed on a monitor.

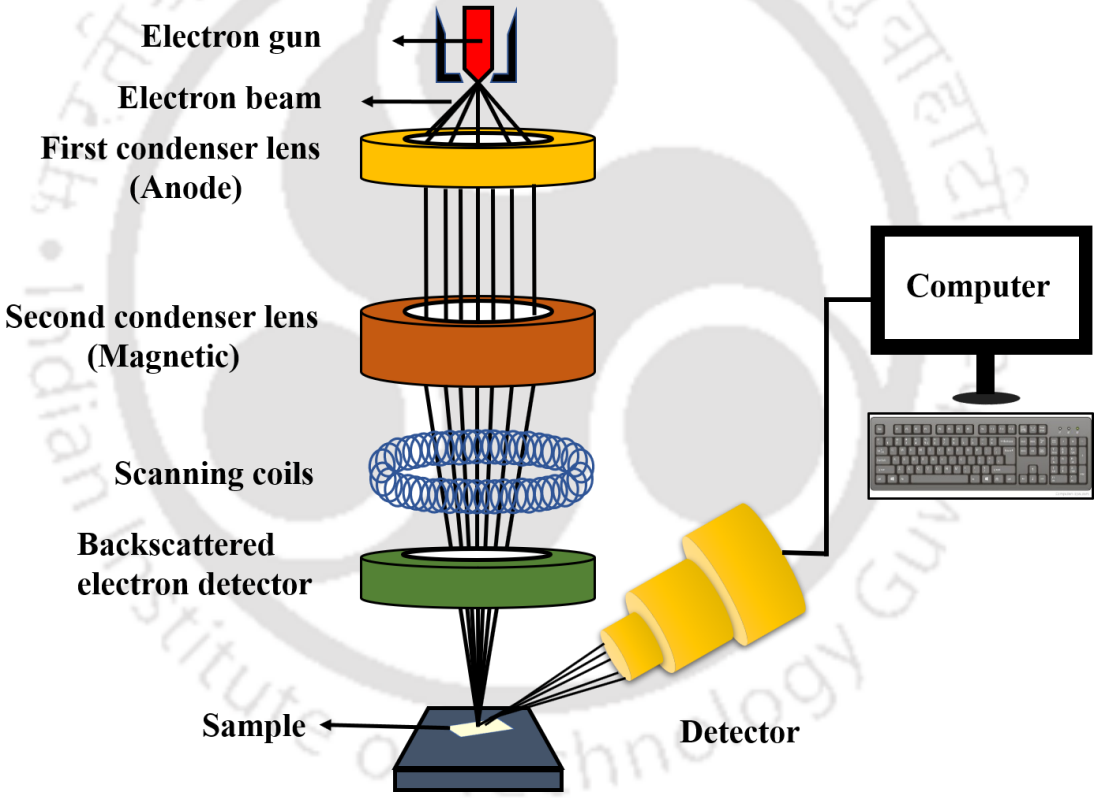

Figure 2.4: Schematic overview of FESEM.

Apart from secondary electrons (SE), the back scattered electrons (BSE), characteristic X-rays, light (cathode-luminescence), specimen current and transmitted electrons are also emitted from the specimen surface. Specialized detectors are needed to record them and all such detectors are not present in a single machine. The incident electron beam results in the emission of BSE from the specimen by elastic scattering and such beam

gives deeper information about the interaction volume. BSE have more energy than SE and have a definite direction and all emissions above 50 eV are considered to be BSE. As such, they cannot be collected by a SE detector, unless the detector is directly in their travel path. This imaging is useful in distinguishing one material from another, since the yield of the collected BSE increases monotonically with the specimen's atomic number Z (~ 0.05 $Z^{1/2}$). Backscattered imaging can distinguish elements with atomic number difference of at least 3.

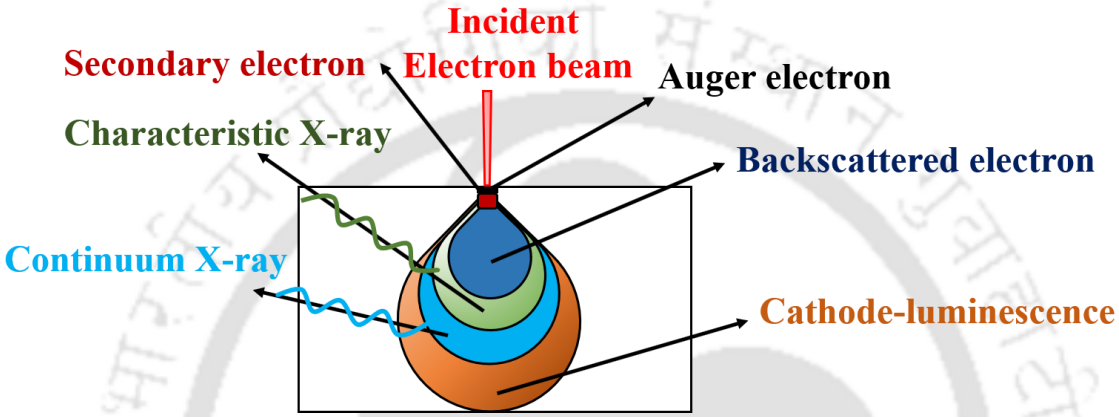

Figure 2.5: The scattering of electron and photon from the drop-shaped interacting volume.

Samples used in the present thesis work are semiconducting in nature thus, before taking the FESEM images a small piece of the sample was placed on the FESEM holder using carbon tape and then coated with gold to make them electrically conducting during the measurement. The surface morphology of the samples was studied using ZEISS make FESEM (model: SIGMA 300) with 2μm range.

2.6 Energy Dispersive X-ray Spectroscopy

Energy dispersive X-ray (EDX) spectrometer is an equipment attached to FESEM, which collects the elemental or compositional information about the specimen under investigation. Each element has a unique atomic structure, which emits its unique characteristic X-ray. To excite the emission of characteristic X-rays from a sample, a high energy beam of charged particles such as electrons or protons, or a beam of X-rays, is focused on to the sample being studied. Such excitation leads to dislodging of some inner core electrons and it is further filled by some outer core electrons by releasing the characteristic X-rays. Thus, by measuring the amount of energy released by X-rays emitted from the sample, one can identify the elements. Hence, we get an EDX spectrum as an

output, which normally displays peaks corresponding to the energy levels. The peak position and its intensity give the information about the elements and their concentration. The EDX spectra of the samples in the present thesis work were recorded using ZEISS make FESEM (SIGMA) equipped with oxford EDX facility.

2.7 Vibrating Sample Magnetometer

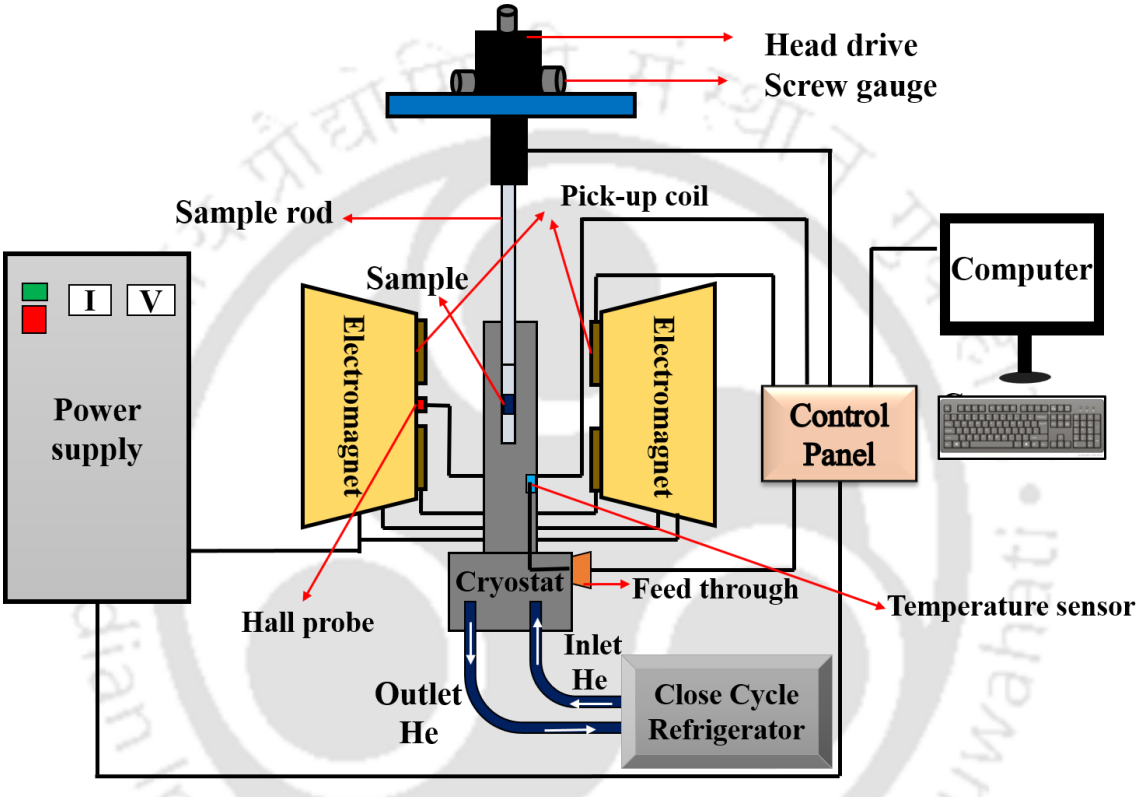

Figure 2.6: Block diagram of VSM along with accessories.

The vibrating sample magnetometer (VSM) has become a widely used instrument for measuring the magnetic properties of a large variety of magnetic materials. The VSM was developed originally by *Foner* [132]. It has been the most successful technique to measure magnetic moment at low/high temperature and for low/high applied magnetic field. VSM can measure magnetic moment with an accuracy of 5×10^{-6} emu.

The VSM is based upon Faraday's law, according to which an electromotive force (*emf*) is induced in a conductor/coil when there is a change in the magnetic flux through the coil. If a small piece of magnetic sample is placed in a uniform magnetic field generated by electromagnet, a dipole moment will be induced. If the sample or the pickup coil is allowed to vibrate under the magnetic field, they would experience a change in magnetic

flux. This induces a voltage in the pickup coils mounted on the pole pieces of the electromagnet and this induced voltage is proportional to the magnetic moment of the sample. Voltage, $V(t)$ can be detected by means of suitable VSM signal detector (Lock in Amplifier). The magnetic field is measured by a Gauss-meter with analog output capabilities. Hall probe is mounted between the magnetic pole pieces close to the sample position. The block diagram of VSM and its accessories are shown in Figure 2.6.

For low temperature measurement, the temperature variation down to 20 K was achieved using an oxford make close cycle refrigerator (CCR) cryostat (model M125) equipped with a temperature controller. Dry Helium gas is allowed to continuously flow into the sample chamber for a good thermal contact and temperature uniformity over the sample. The temperature is measured using a cernex sensor.

Figure 2.7: High temperature oven attached with VSM.

For high temperature measurements, the cryostat is replaced by a high temperature oven as shown in Figure 2.7, (Lakeshore, Model 74034), with suitable temperature controller to vary the temperature from 300 K to 1273 K. During the experiment in the high temperature, Argon/Nitrogen gas was allowed to flow into the oven throughout the experiment. Here, temperature is recorded using a K type thermocouple attached to the oven.

In the current thesis work, the field and temperature variations of magnetization were measured out by using the Lakeshore make VSM (model no. 7410). Here, the sample vibrates at a frequency of 70-80 Hz using the mechanical vibrator attached to the head drive. The calibration of the VSM was done by measuring the magnetic moment of a standard pure spherical Ni sample having 6.92 emu/g moment at 5000 Oe. The IDEASVSM software was used to run the sequence provided with the instrument. The magnetic field was generated by using a 10″ electromagnet capable of producing 2 T field at 2" air gap.

2.8 Physical Properties Measurement System

The physical properties measurement system (PPMS) is a non-destructive tool to measure many physical properties such as, magnetic moment, ac susceptibility, magneto-resistance, specific heat capacity etc. The system uses a single, two-stage pulse tube cryo-cooler.

In the present thesis work, we have used Quantum Design make Dynacool model of PPMS equipped with VSM. The superconducting magnet provides magnetic field from 9T to -9T. The accuracy of measured magnetic moment is 7×10^{-7} emu. The measured temperature range is 2 K to 300 K with a linear motor transport. The MultiVu software is used for automation and control the program.

2.9 Dielectric Measurements

Impedance data were measured by using a Wayne Kerr make LCR meter (Model 1J4300R/43100R) in the frequency range of 10^2 Hz - 10^6 Hz with an ac voltage of 1.0 V_{rms}. The data were collected by using a software provided by Wayne Kerr, which connects the LCR meter to computer through RS232 interface. The temperature variation of impedance data was collected using a high temperature oven supplied by Wayne Kerr. The Chromal-Alumel (Cr-Al) thermocouple and a Eurotherm make temperature controller (Model no. 3216) was used for temperature controlling. For dielectric measurements, samples were taken in cylindrical pellet form with typical thickness of 1 - 1.5 mm and diameter 8 - 10 mm. The thickness and diameter were calculated using a screw gauge and a digital Vernier calliper, respectively. Before performing the measurement, the calibration was carried out using Kelvin clip with open and close circuit model to avoid stray impedance data. Silver paste (Sigma Aldrich) was applied to both the surface of the pellets to make electrodes. The

samples were fired at 473 K in air for 2 hours and furnace cooled to room temperature before carrying out the electrical measurement.

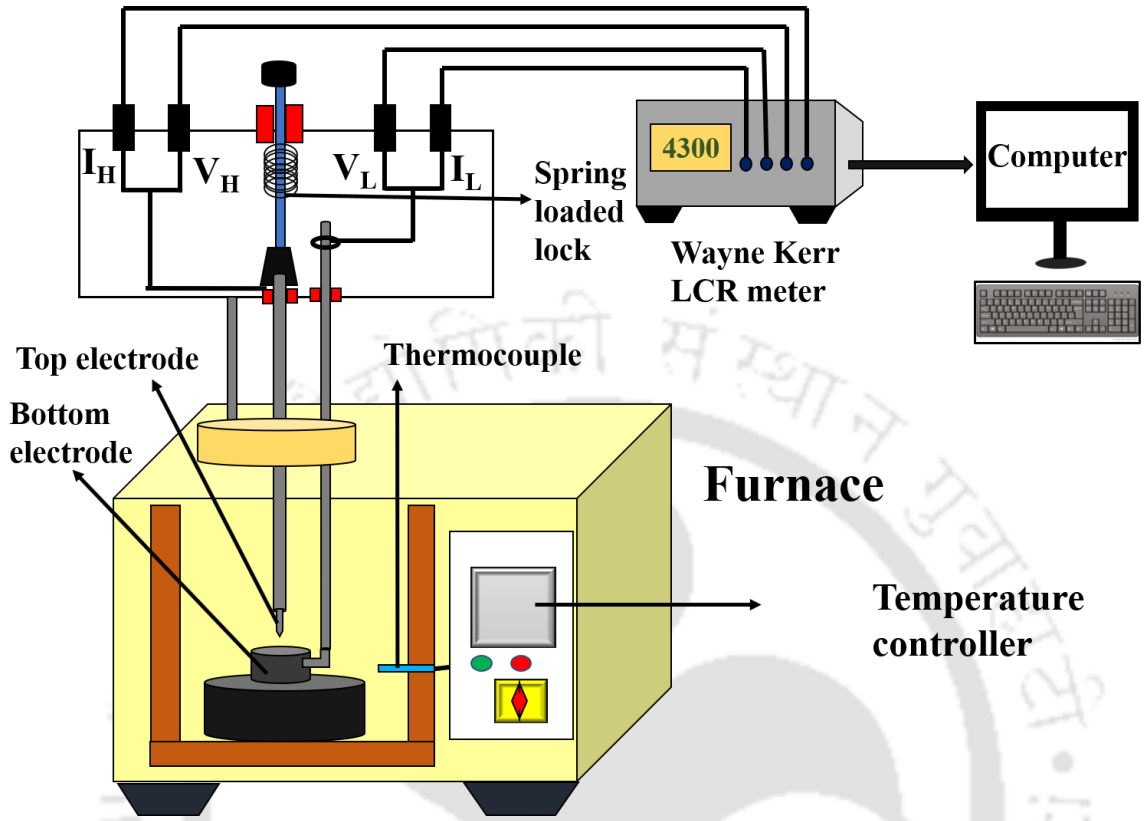

Figure 2.8: Schematic diagram of dielectric measurement system.

The basic diagram of impedance measurement set up is depicted in Figure 2.8. The set up consist of an LCR meter, which is connected to a sample holder through four BNC connectors. The sample holder is made up of stainless steel. The measurement is carried out in a parallel plate capacitor arrangement by employing the four terminals method. The top electrode is spring loaded, thus making it possible to have good electrical contact for samples of different dimension. The LCR meter is connected with the four leads and these leads are connected with the sample holder in such a way that, the top electrode is connected as I_H, V_H, while the bottom electrodes are connected to the I_L and V_L terminals. The bottom electrode is connected with an insulating base. The I_H/I_L pair is attached to the signal generator to pass the current through the sample, while V_H/V_L pair is coupled to the voltage measurement. The LCR meter measures the voltage across the device by sending current of certain frequency (*f*) and by calculating the impedance of the sample using the relation:

$$Z^*(f) = \frac{V^*(f)}{I^*(f)} \tag{2.8}$$

where Z*, V*and I* represent the complex impedance, voltage and current, respectively. The LCR meter used in the current work, displays the real Z' and imaginary Z" parts of the Z*. So, we obtained the values of Z' and Z" in the frequency range of 10^2 Hz to 10^6 Hz and calculated the related parameter such as real and imaginary part of dielectric constant (ε' and ε"), loss tangent (tanδ), electric modulus (M' and M"), conductivity (σ') using the following relations [64]:

$$\varepsilon' = \frac{-Z''}{2\pi f C_0 (Z'^2 + Z''^2)} \tag{2.8}$$

$$\varepsilon'' = \frac{Z'}{2\pi f C_0 (Z'^2 + Z''^2)} \tag{2.9}$$

$$M' = j2\pi f C_0 Z'' \; or \; \frac{\varepsilon'}{(\varepsilon'^2 + \varepsilon''^2)} \tag{2.10}$$

$$M'' = -j2\pi f C_0 Z'' \; or \frac{\varepsilon''}{(\varepsilon'^2 + \varepsilon''^2)} \tag{2.11}$$

$$tan\delta = \frac{\varepsilon''}{\varepsilon'} \tag{2.12}$$

$$\sigma_{ac}(\omega) = 2\pi f \varepsilon'' \varepsilon_0 \tag{2.13}$$

where C_0 is the geometrical capacitance of the sample having thickness *t* and area *A* which is given by

$$C_0 = \frac{\varepsilon_0 A}{t} \tag{2.14}$$

The above dielectric data was analyzed using standard theoretical models as presented in chapter 3-6.

Chapter 3

Sm-Substituted Yttrium Iron Garnet

YIG is a natural choice for microwave, optical, and spintronic devices, etc. due to their interesting magnetic and dielectric properties [19,20,91,95,96]. *Saha* et al. [133] reported relaxor and magneto-electric behaviour in YIG at high temperature, and it suggests the potential application of YIG in memory storage devices. YIG undergoes ferrimagnetic transition at 550 K [105]. Magnetic rare earth (RE) elements substituted YIG show decrease in the saturation magnetization due to the antiferromagnetic coupling of RE moment with the net magnetic moment of Fe sublattice. However, the substitution of non-magnetic La increases the saturation magnetization up to a certain concertation, however, Sm-substitution reduces the magnetic moment [101,134]. Debye and Maxwell-Wagner type dielectric relaxation behaviour have been reported at low and high temperature, respectively in pure as well as impurity doped YIG [81,135]. In addition to that, the oxygen vacancies also take part in relaxation dynamics [81,135,136]. *Haung* et al. [103] found high dielectric constant and low dielectric loss in $Sm_3Fe_5O_{12}$. The detailed study of Sm-substituted YIG is required to understand the variation in magnetic and dielectric properties in the vicinity of FIM T_C. Therefore, in this chapter we have described the structural, magnetic and dielectric properties of YIG by Sm-substitution. It gives the signature of magneto-electric behaviour in the vicinity of FIM T_C.

We have prepared $Y_{3-x}Sm_xFe_5O_{12}$ ((Y, Sm)-Fe-O) compounds with x = 0, 0.5, 1.0, 2.0 and 3.0 using the solid-state reaction method as discussed in chapter 2 (section 2.2.1). The weighed amount of Y_2O_3, Sm_2O_3 and Fe_2O_3 (purity > 99%) were mixed together and the powder was presintered at 873 K for 12 hours. The final sintering was carried out at 1673 K for 6 hours.

3.1 Structural Studies

The powder XRD patterns of parent and Sm-substituted YIG recorded at room temperature are displayed in Figure 3.1. These patterns were refined with the help of Fullprof software using the space group $Ia\bar{3}d$ (O_h^{10}) in cubic unit cell and the samples are found to be in pure-phase form. The typical Rietveld refined XRD patterns (black solid

line) for x = 0.0, 1.0, 2.0 and 3.0 samples of (Y, Sm)-Fe-O along with recorded patterns (red open circles) are shown in Figure 3.2. The recorded and refined patterns are close to each other with a small difference between them. The lattice parameter (a), volume (V) of the unit cell and various reliability factors such as χ^2, R_P R_{exp}, R_F and R_{Bragg} obtained from the refinement are given in Table 3.1. The Sm-substitution at Y site gives rise to increase in a and V values and it is attributed to the larger ionic radius of Sm^{3+} (1.02 Å) ion as compared to Y^{3+} (0.94 Å) ion. The obtained values of a and V for parent compound are comparable with the literature [25]. Figure 3.3 shows the pictorial view of arrangement of three ions (Y(c), Fe(a), Fe(d)) for x = 0 and x = 2.0 with details of bond lengths and bond angles.

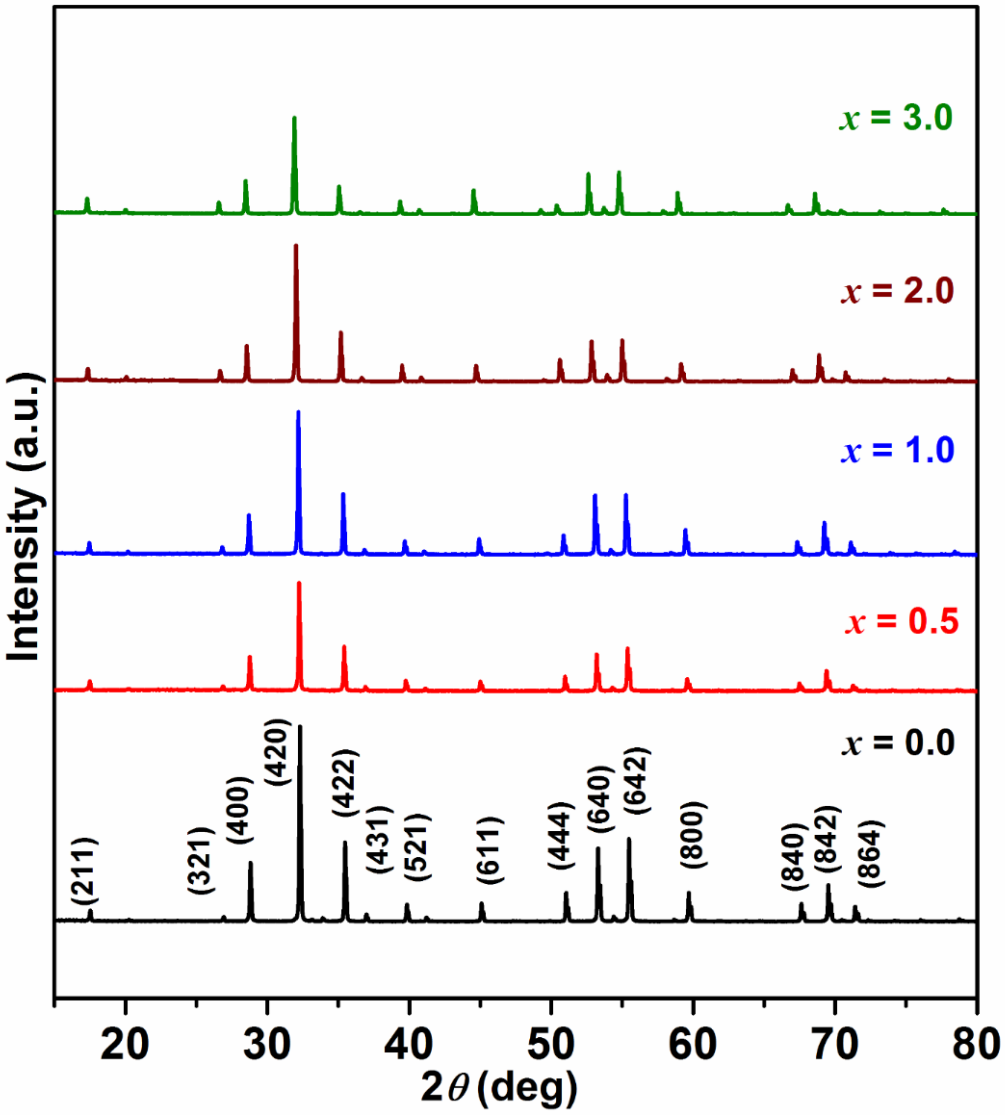

Figure 3.1: XRD patterns of (Y, Sm)-Fe-O samples with x = 0 to 3.0

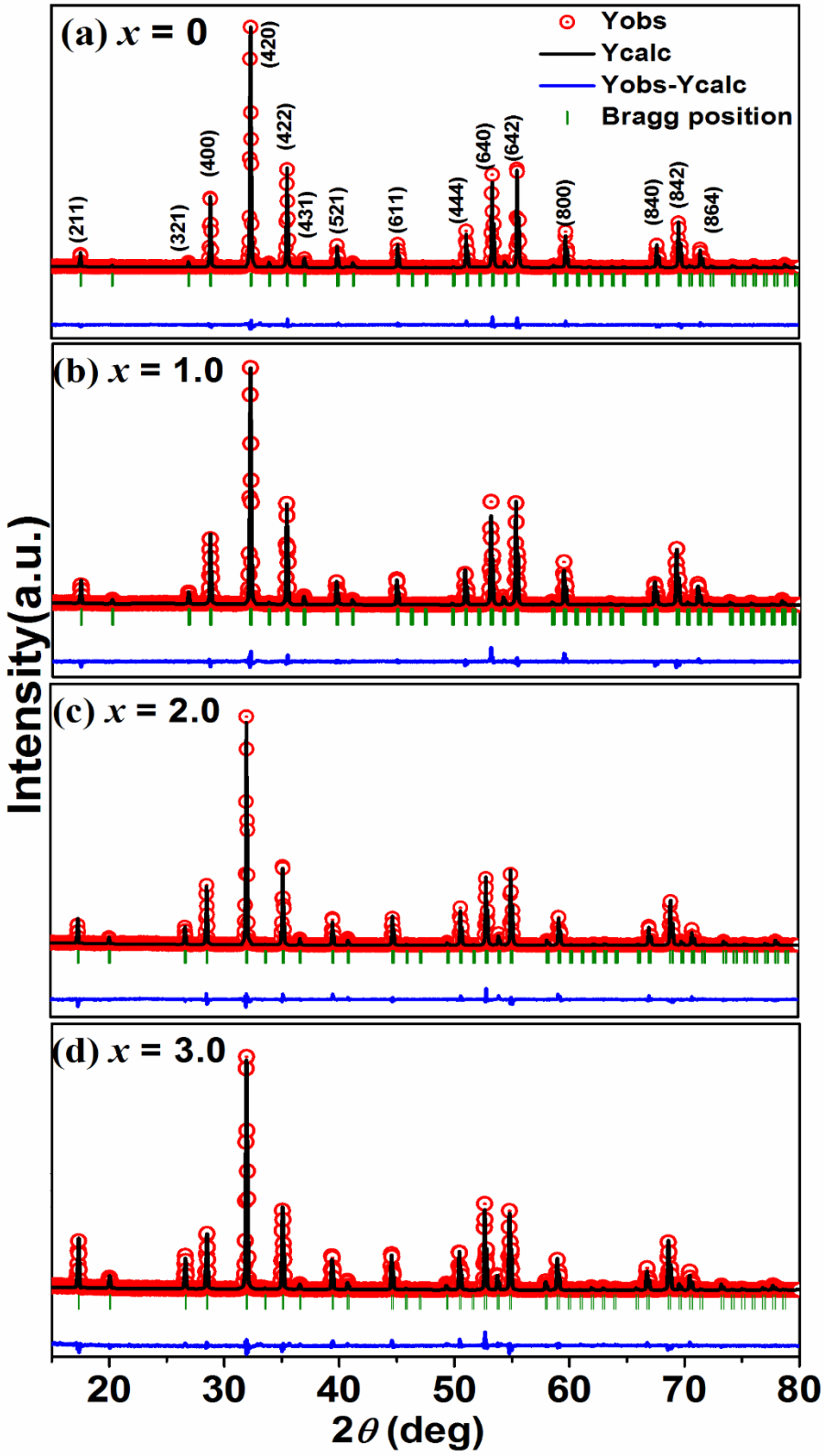

Figure 3.2: XRD patterns of (Y, Sm)-Fe-O samples along with the Rietveld refined patterns.

Table 3.1: Structural and reliability parameters obtained from the Rietveld refinement of XRD patterns of (Y, Sm)-Fe-O samples with x = 0 to 3.0.

x		0	0.5	1.0	2.0	3.0
Space group		$Ia\bar{3}d$	$Ia\bar{3}d$	$Ia\bar{3}d$	$Ia\bar{3}d$	$Ia\bar{3}d$
$a = b = c$ (Å)		12.3726 (4)	12.3950 (6)	12.4208(6)	12.4751(7)	12.5245(4)
V (Å^3)		1895.8	1904.3	1916.2	1941.4	1964.3
R_p (%)		8.99	9.02	9.32	11.40	12.40
R_{exp} (%)		7.29	7.50	7.11	7.79	9.23
R_f (%)		5.89	6.84	7.40	10.2	8.70
R_{Bragg} (%)		3.65	4.18	5.77	7.92	6.92
χ^2		3.21	2.72	3.37	4.64	4.40
Occupancy	Y	2.98	2.49	1.97	0.98	0.00
	Sm	0.00	0.50	0.98	2.01	2.97
	Fe	4.99	4.98	4.99	4.98	4.97

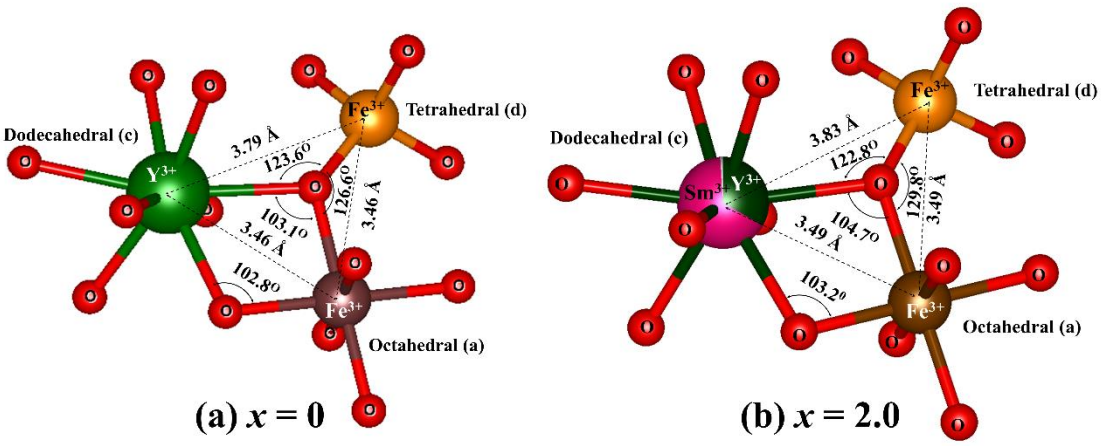

Figure 3.3: Schematic representation of bonding of Fe ions with Y ions for (a) x = 0 and (b) x = 2.0 sample.

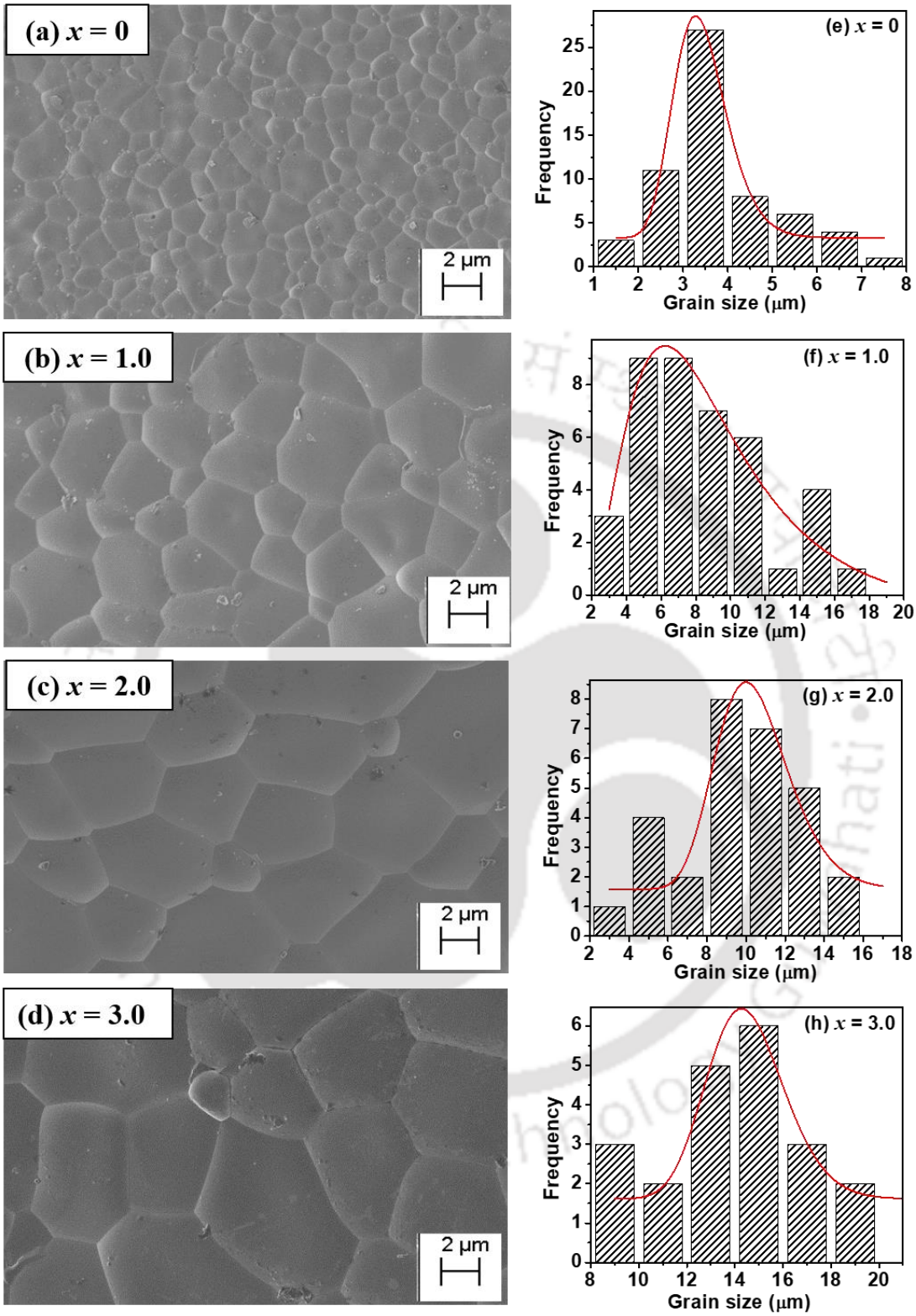

Figure 3.4: (a-d) FESEM micrographs along with (e-h) grain size distribution for x = 0, 1.0, 2.0 and 3.0 samples.

Figure 3.4(a-d) shows the typical FESEM microstructural images of x = 0, 1.0, 2.0 and 3.0 samples. The average grain size of each sample is obtained by fitting the size distribution histogram (Figure 3.4(e-h)) to log-normal distribution function as reported by *Odo* [137].

$$f(l,\mu,\sigma_s) = \frac{1}{l\sigma_s\sqrt{2\pi}} exp\left(-\frac{(lnl-\mu)^2}{2\sigma_s^2}\right) \quad (3.1)$$

where μ is the logarithmic mean, l is the cross-sectional length of the particle, and σ_s represents the standard deviation. The average grain size values are 3.4 µm, 5.7 µm, 8.2 µm, 10.3 µm and 14.4 µm for x = 0, 0.5, 1.0, 2.0 and 3.0, respectively. Grains and grain boundaries are clearly visible in the shown micrographs and they are highly dense. The grain growth with Sm-substitution is possibly due to the reduction in melting point and hence, better mobility of grain boundaries leading to a larger grain size [138]. The presence of Y/Sm and Fe elements has been witnessed as per the EDX spectra shown in Figure 3.5 for x = 0 and 2.0 samples**.** The chemical composition determined from EDX result is consistent with the nominal starting composition. For example, cationic ratio Y:Sm:Fe = 2.48:0:4.97 and 0.98:1.98:4.98 for x = 0 and 2.0, respectively. The density values of the prepared pellets, determined from the Archimedes' principle, show that they lie in the range of 90 to 95% of the theoretical density.

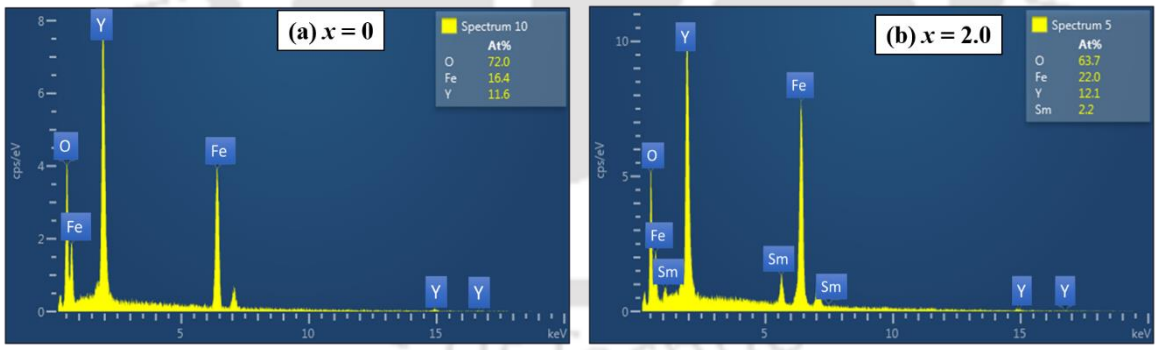

Figure 3.5: EDX spectra of (Y, Sm)-Fe-O samples for (a) x = 0, and (b) x = 2.0 samples.

The Raman spectra recorded for x = 0.0 to 3.0 samples are illustrated in Figure 3.6. The peaks observed in the range of 100 cm^{-1} to 300 cm^{-1} are primarily due to the translational motion of cations Y^{3+} and Sm^{3+} at dodecahedron sites. The peaks observed in the range of 300 cm^{-1} to 800 cm^{-1} correspond to Fe-O stretching in '*a*' and '*d*' sublattices [102]. Sharp F_{2g} modes are shifting towards the lower wavenumber side (274.5 cm^{-1} to 262.5 cm^{-1}) with increase in Sm-substitution. Increase in lattice constant will lead to

decrease in the force constants and this will lead to decrease in frequency of vibrational modes, and it is referred as red shift. Besides, the substitution of heavier element at lighter element site increases the effective atomic mass and hence, F_{2g} mode shifts towards lower wavenumber.

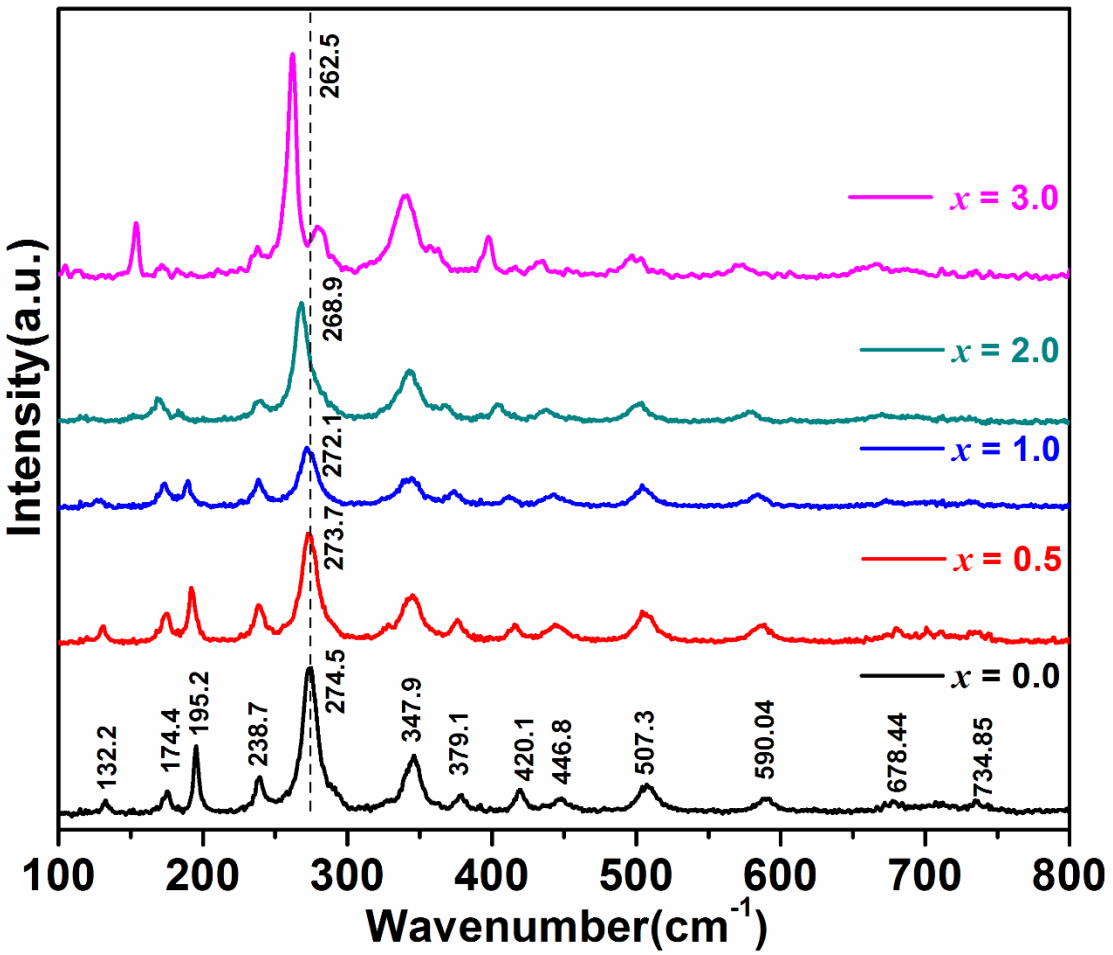

Figure 3.6: The room temperature Raman spectra for (Y, Sm)-Fe-O samples.

3.2 Magnetic Studies

Figure 3.7(a) shows the normalized plots of temperature dependence of magnetization data for an applied field of 100 Oe for pure and Sm-substituted YIG samples. The FIM T_C was determined from *dM/dT* versus T plots (Figure 3.7(b)). FIM T_C is found to be 550 K for x = 0.0 and increases up to 573 K for x = 3.0 (Figure 3.8). The value of T_C for x = 0.0 is comparable with the literature [25]. The increase in T_C is due to the strengthening of superexchange interaction among Fe^{3+} ions at octahedral and tetrahedral

site, which is in accordance with the increase in bond length (Fe(a)-Fe(d)) and bond angle (Fe(a)-O-Fe(d)) as per XRD analysis [34].

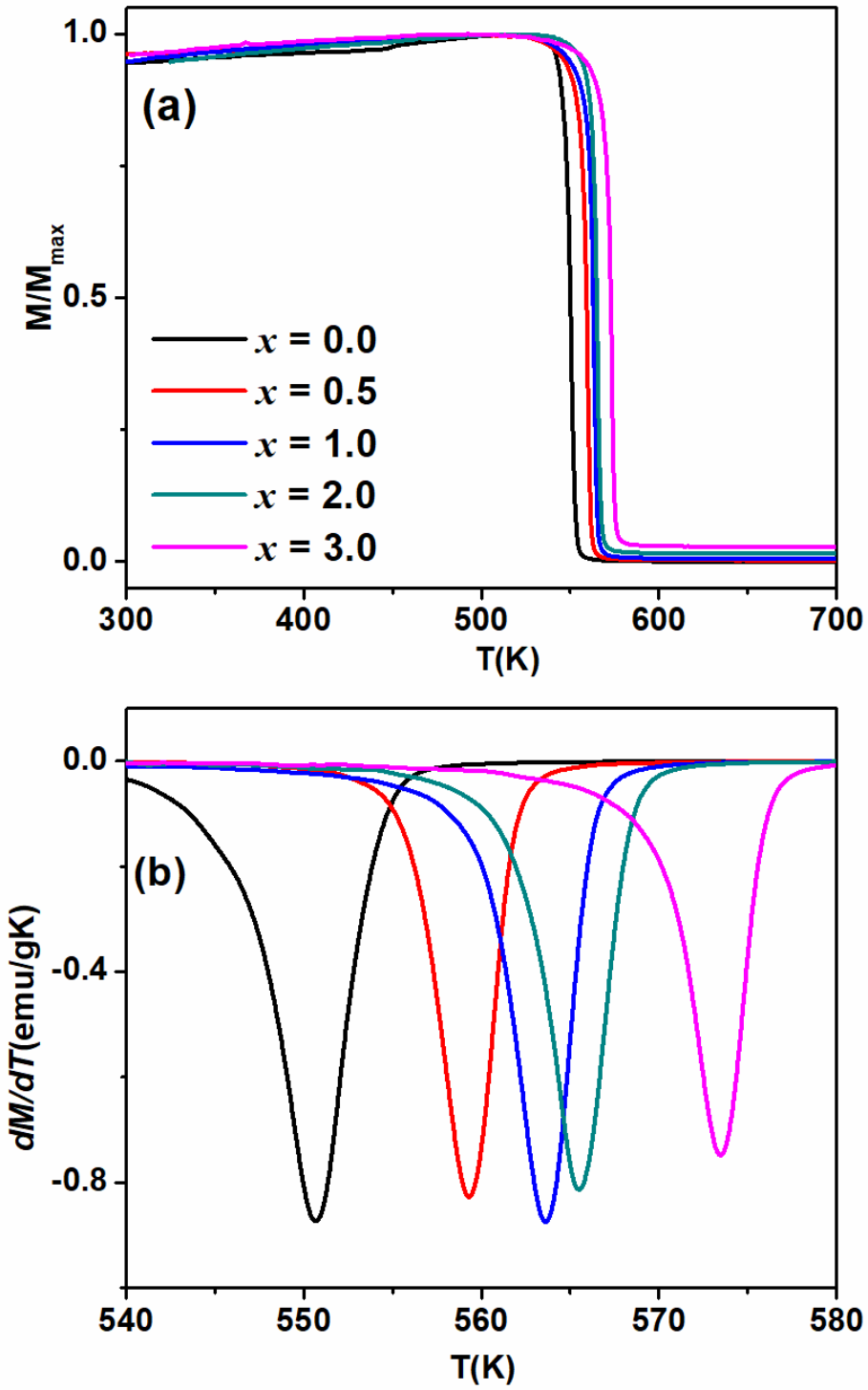

Figure 3.7: (a) The normalized magnetization (M/M_{max}) as a function of temperature (*M-T*) plots were recorded at H = 100 Oe under the zero field condition (ZFC) and (b) *dM/dT* versus T plots for (Y, Sm)-Fe-O samples.

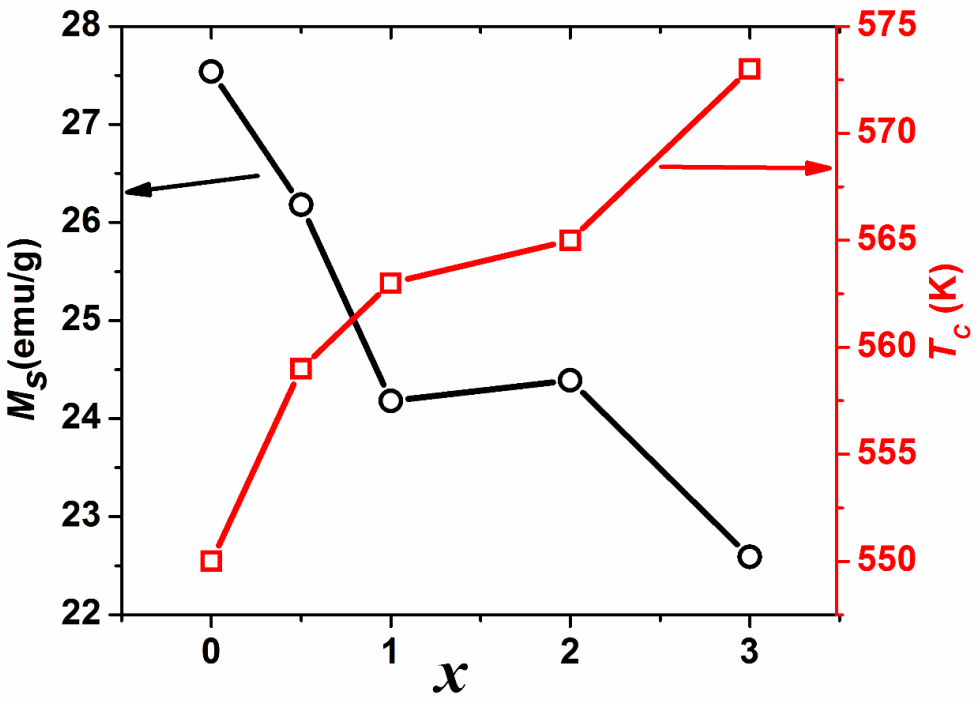

Figure 3.8: The variation of M_S and T_C with Sm-concentration.

Figure 3.9(a) shows the magnetic hysteresis loops (*M-H*) recorded at room temperature (300 K) for parent and Sm-substituted samples. They all are found to saturate. The magnetization data are generally analyzed based on Law of approach to saturation (LAS) model as given below [111,139]. They are mostly used at higher applied field where, the rotation process of magnetic domains against anisotropy occurs.

$$M = M_s\left(1 - \frac{8K_1^2}{105\mu_0^2 M_S^2 H^2}\right) + cH \tag{3.2}$$

where, M_S is the saturation magnetization, H is the applied magnetic field, μ_0 is magnetic permeability in free space, K_1 is effective magnetic anisotropy constant. The numerical coefficient 8/105 corresponds to polycrystalline material with cubic symmetry. The last term *cH* represents forced magnetization due to the increase of saturation magnetization in high fields. The M_S value is estimated by analyzing the initial magnetization curve to LAS model. Figure 3.9(b) shows the field variation of initial magnetization (open symbol) data along with the fitted data (solid line) using LAS model for x = 0.0 to 3.0. The room temperature M_S value is found to decrease with increase in Sm-concentration, i.e., from 27.5 emu/g for x = 0.0 to 22.6 emu/g at x = 3.0, and it is shown in Figure 3.8.

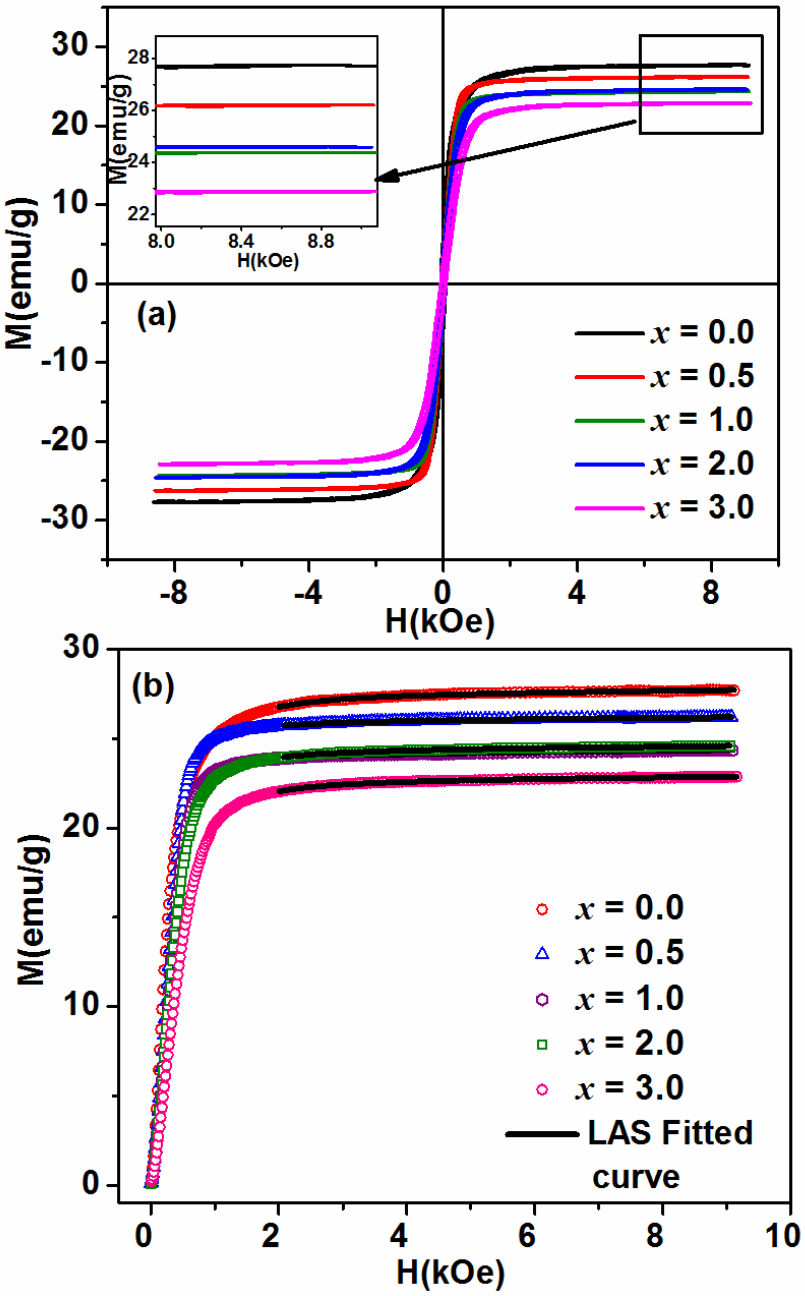

Figure 3.9: (a) *M-H* loops of (Y, Sm)-Fe-O for x = 0.0 to 3.0 at room temperature. (b) Experimental initial magnetization data (symbol) along with fit to LAS (solid line) model.

The cation distribution of (Y, Sm)-Fe-O can be expressed as $\{Y_{3-x}Sm_x\}^c[Fe_2]^a(Fe_3)^dO_{12}$. Magnetic moment in YIG generally originates from Fe^{3+} ions located at '*a*' and '*d*' sites. The ferrimagnetic alignment between two Fe^{3+} ions at octahedral site and three Fe^{3+} ions at tetrahedral sites gives rise to a net magnetic moment corresponding to a single Fe^{3+} ion. According to theoretical explanation, for lighter rare earth garnet the '*c*' sublattice (dodecahedral) formed by magnetic ions such as Sm^{3+}, Er^{3+}, and Pr^{3+} are coupled ferromagnetically to the net magnetic moment of Fe^{3+} ions, which

results in increase of saturation magnetization [79]. As we know, the magnetic moment of Sm^{3+} is 0.7 μ_B at room temperature and it is quite small to considerably influence the magnetic moment of samples. However, in our case M_S value is found to decrease with increase with Sm-concentration and this can be explained in terms of the antiferromagnetic alignment of Sm^{3+} ions to the magnetic moment of three Fe^{3+} ions situated at tetrahedral site while the ferromagnetic alignment with two Fe^{3+} ions situated at octahedral site. This results in antiferromagnetic alignment of Sm^{3+} ions to the net magnetic moment of Fe^{3+} ions. Such kind of behaviour is also reported in *Sadhana* et al [134]. However, one cannot rule of the possibility of ferromagnetic alignment but with a weak magnetic moment of Sm^{3+} ions. The estimated value of K_1 determined from the fitted initial magnetization curve to LAS model is found to be 1.61×10^5 erg/cm^3 for x = 0.0 and it is found to be independent of Sm-concentration, i.e., K_1 remains to be 1.63×10^5 erg/cm^3 for x = 3.0 also. Such type of behaviour is reported by *Nekvasil* [140].

3.3 Complex Impedance Spectroscopy Studies

Dielectric characterization plays an important role to understand the electrical property of a material. The frequency (*f*) variation of real (Z') and imaginary (-Z") parts of impedance at room temperature are shown in Figure 3.10 (a) and (b), respectively. The impedance arises due to resistance, reactance, etc., experienced by charge carriers during their movements across inter-grains, intra-grains and sample-electrode interface. The monotonic decrease in Z' and -Z" with rise in frequency is mainly due to the absence of relaxation at room temperature. It means relaxation species at room temperature may be immobile charge carriers or defects. It also indicates a possibility of increase in ac conductivity with increase in frequency [141]. Moreover, the merger of both Z' and -Z" at high frequency for all the compositions suggests possible release of space charges accumulated at grain boundaries (GB). The value of Z' reduces sharply from 5 MΩ for x = 0 to 0.10 MΩ for x = 3.0 at 100 Hz. The decrease in Z' and -Z" with increase in Sm-concentration may be attributed to the increase in oxygen vacancies, which results in increase in charge carriers. In order to compensate the oxygen vacancies, some of Fe^{3+} ions reduce to Fe^{2+} ions. The presence of Fe^{2+} and Fe^{3+} ions in YIG on the basis of XPS studies is reported in literature [102].

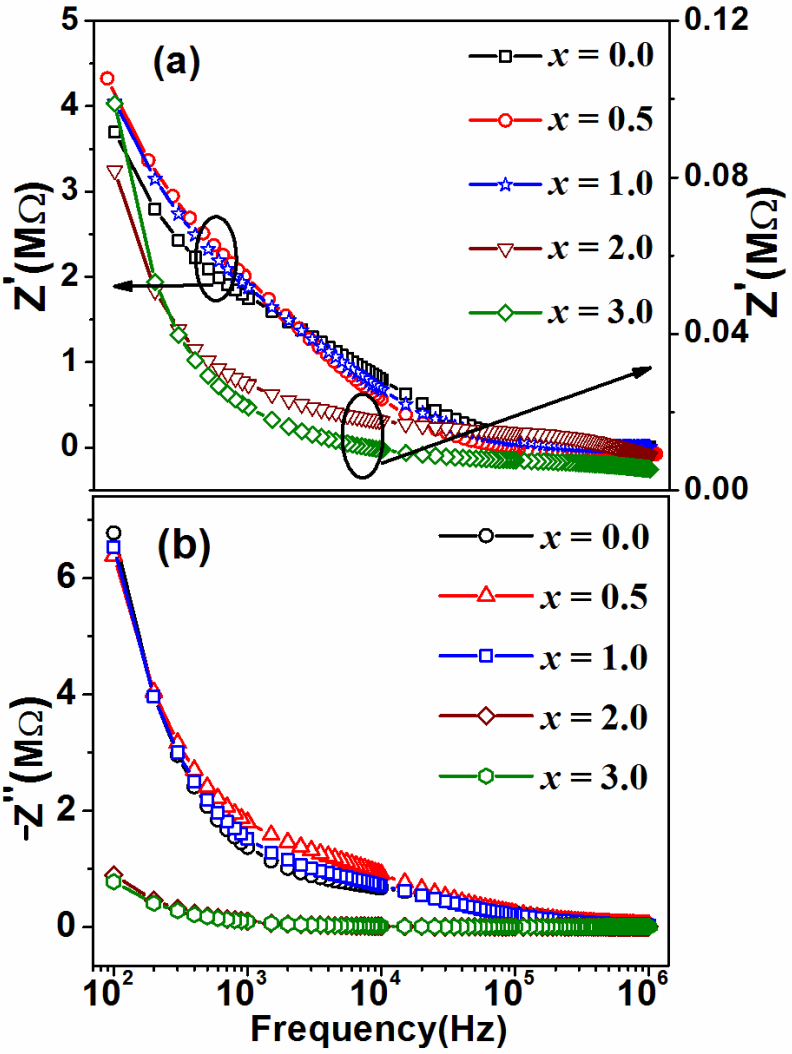

Figure 3.10: (a) Real part (Z') and (b) imaginary part (-Z'') of impedance as a function of frequency at room temperature for (Y, Sm)-Fe-O samples.

Figure 3.11 shows the frequency variation of Z' at different temperatures (548 K to 623 K) for various Sm-concentration. The magnitude of Z' decreases with increase in frequency. Z' values undergo a step like decrease in magnitude as the frequency is increased through certain characteristic frequency and it indicates the presence of dielectric relaxation process in these samples. The merger of Z' at higher frequency for all samples is due to the release of space charges [142]. The characteristic frequency shifts towards the higher frequency regime as the temperature is increased. The reduction in the magnitude of Z' with increase in temperature suggests that the temperature coefficient of resistance is basically negative. For a given temperature and frequency, Z' value is found to decrease with increase in Sm-concentration and it suggests the increase in electrical conductivity. It can be explained in terms of increase in grain size for Sm-substituted samples, which in turn

reduces the number of grain boundaries (GB) or resistance across GB. One cannot rule out the generation of additional charge carriers upon Sm-substitution.

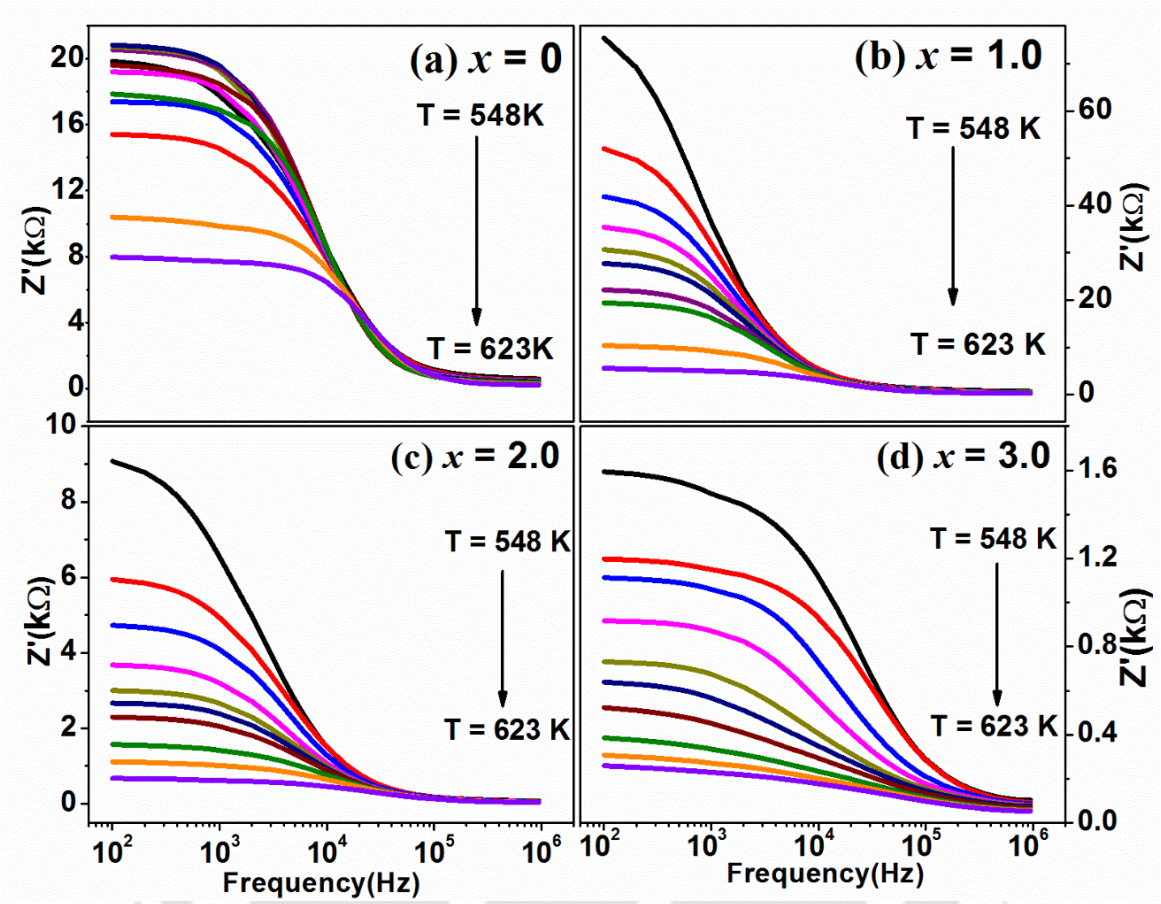

Figure 3.11: Z' versus frequency plots of polycrystalline samples of $Y_{3-x}Sm_xFe_5O_{12}$ in the temperature range of T = 548 K to 623 K.

Figure 3.12 shows frequency variation of -Z" over a wide range of temperature for x = 0, 0.5, 2.0 and 3.0 samples. The -Z" versus f plots show relaxation peak, which depict the relaxation of the charge carriers. The peak shape is not symmetric with respect to the characteristic frequency and it broadens as the temperature rises. For x = 0, the relaxation peak is at $f = 10^4$ Hz which is attributed to the GB. Since, at higher temperature, the thermally activated hopping of charge carriers takes place in long-range scale, i.e., having large relaxation times (less frequency). So, relaxation process is associated to the charge carriers across GB. The asymmetric nature of -Z" peaks suggest the deviation of relaxation dynamics from the ideal Debye type. With increase in temperature, the relaxation peak gets depressed and shifts towards higher frequency, which reveals that, relaxation is due to thermally activated charge carriers [142]. However, for x = 3.0 sample, we have observed that peaks are shifting towards lower frequency side from T = 573 K to 598 K, which is in the vicinity of FIM T_C. Such behaviour may be attributed to the coupling between electric

and magnetic polarization. This coupling effect is clearly visible in Arrhenius plots explained later.

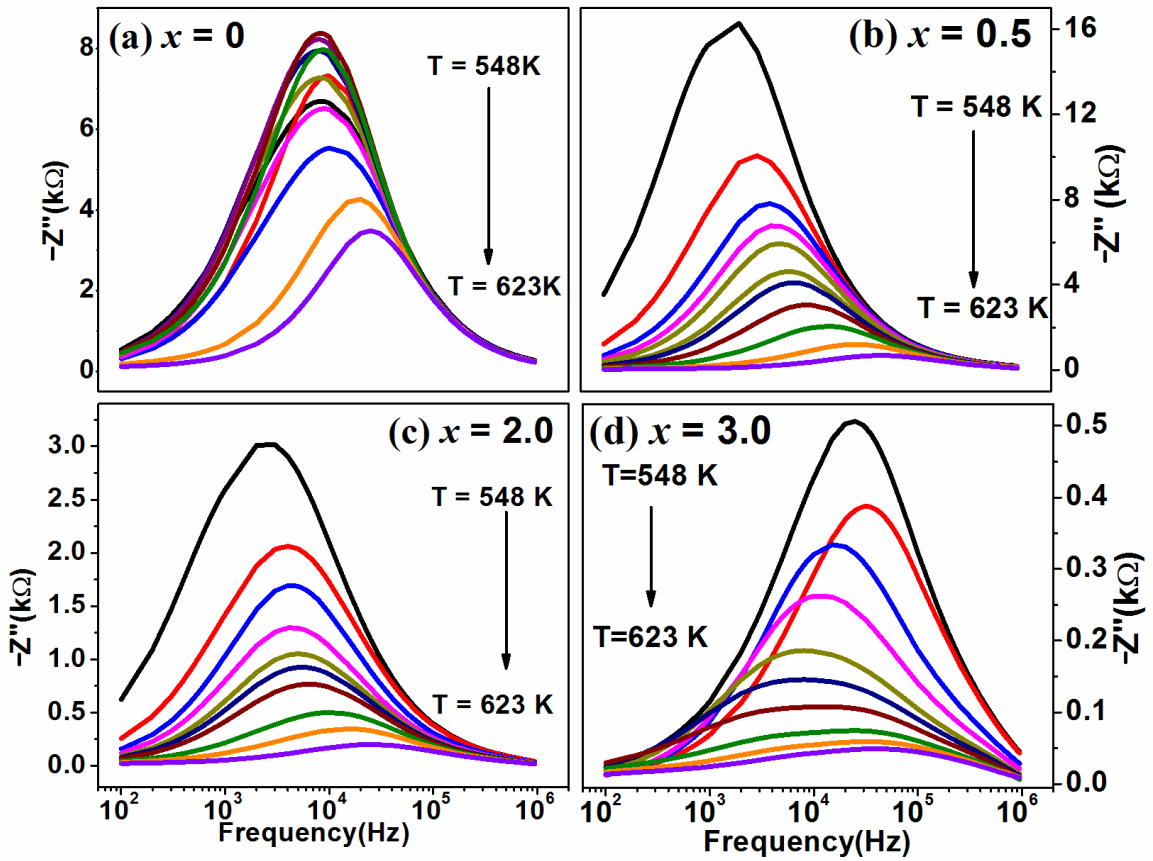

Figure 3.12: Z" versus frequency plots of polycrystalline samples of (Y, Sm)-Fe-O for (a) x = 0.0 (b) x = 0.5 (c) x = 2.0 and (d) x = 3.0 at different temperatures in the range of 548 K to 623 K.

Figure 3.13 shows the complex impedance (Z*: -Z" versus Z') plots for (Y, Sm)-Fe-O with x = 0.0, 1.0, 2.0 and 3.0. A clear semicircle can be observed at 548 K, which persists up to 623 K. Generally, for polycrystalline materials two semicircles are expected: one due to grains (G) and the other due to grain boundaries (GB) provided their relaxation time constant values are quite different. For an ideal Debye type behaviour, the semicircle is expected to be symmetric with its centre lying on Z' axis. In such case, the semicircles can be modelled to an equivalent circuit comprising two parallel RC elements connected in series [142]. As can be seen from the Figure 3.13, the semicircles are asymmetric and their centres lie below the Z' axis revealing the departure of relaxation from the ideal Debye type behaviour. In impedance spectroscopy, such departure can be explained using constant phase element (CPE, denoted by Q) such that,

$$Z_{CPE} = \frac{1}{A}(j\omega)^{-m} \tag{3.3}$$

where A is a constant and m represents the distribution of relaxation time ($0 \leq m \leq 1$). For an ideal capacitor $m = 1$, while for an ideal resistor $m = 0$ and the deviation of m from ideal values marks the departure of relaxation dynamics from the ideal Debye type behaviour.

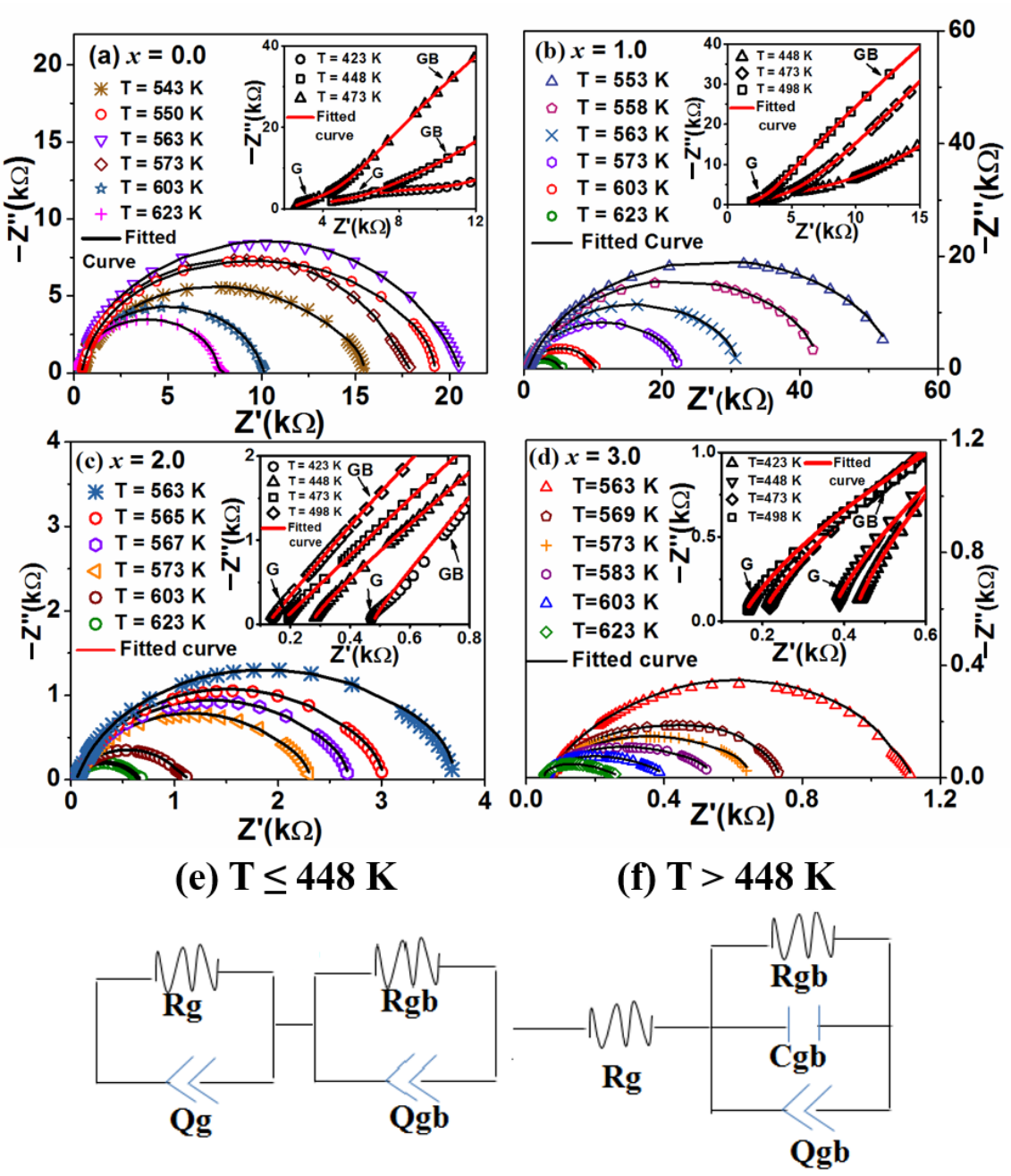

Figure 3.13: Nyquist plots of polycrystalline samples of (Y, Sm)-Fe-O for (a) x = 0.0 (b) x = 1.0 (c) x = 2.0 and (d) x = 3.0 at high temperature. Insets shows the similar plots for T < 543 K along with their respective equivalent circuits for (e) T ≤ 448 K and (f) T > 448 K.

The insets of Figure 3.13 show the Z* plots in expanded scale for T < 523 K. Here the G and GB contribution can be seen clearly. The small semicircular arc at higher frequency regime (marked as G) is attributed to grains, while the bigger semicircular arc is marked as GB. As the temperature rises to 543 K, the grains contribution goes out of the measured frequency region, and the Z* plot mainly shows the grain boundaries contributions. The semicircles can be modelled to an equivalent circuit as shown in Figure 3.13(e, f), where R_g and R_{gb} represent the G and GB resistances, respectively. Q_g and Q_{gb} represent constant phase element associated with G and GB respectively. C_{gb} represents the capacitance of GB. The circuit shown in Figure 3.13(e) is used to fit the Z* spectra for T< 448 K and similarly for T > 448 K the equivalent circuit is shown in Figure 3.13(f).

3.4 Complex Dielectric Permittivity Studies

The real (ε') and imaginary (ε'') parts of complex dielectric constant (ε^*) can be calculated by using the relation:

$$\varepsilon' = \frac{-Z''}{2\pi f C_0 (Z'^2 + Z''^2)} \quad (3.4)$$

$$\varepsilon'' = \frac{Z'}{2\pi f C_0 (Z'^2 + Z''^2)} \quad (3.5)$$

Here, C_0 is the geometrical capacitance and *f* is the applied frequency. Z' and Z'' represent the real and imaginary components of impedance, respectively. Figure 3.14 shows the frequency variation of real part (ε') of dielectric constant of (Y, Sm)-Fe-O at different temperatures. The value of ε' for *x* = 0 sample at 1 MHz is found to be 22 at 300 K which is nearly equal to the reported value by *Larsen* et al. [143]. The ε' value is found to increase with increase in temperature, i.e., from 22 at T = 300 K to 700 at 573 K for a frequency of 1 MHz in *x* = 0 sample. It is also found to increase with increase in Sm concentration. Sm-substitution at Y site increases the oxygen vacancies (i.e., increase in Fe^{2+} ions) especially at higher Sm-concentration, and it leads to sufficient number of electrons for polarization, which results in increase in dielectric constant. For example, the value of ε' = 29 at 300 K for *x* = 3.0. At high temperature, the observed linear behaviour in the ε' value at lower frequency could be attributed to the contribution of accumulated space charges at GB. Moreover, the high magnitude (~10^5) of ε' at lower frequency is attributed to Maxwell-Wagner type relaxation. Such type of relaxation is generally observed in heterogeneous system where grains, grain boundaries and electrode effect contribute to different

conductivity [144]. With the increase in temperature ε' value increases and is attributed to increase in the conductivity.

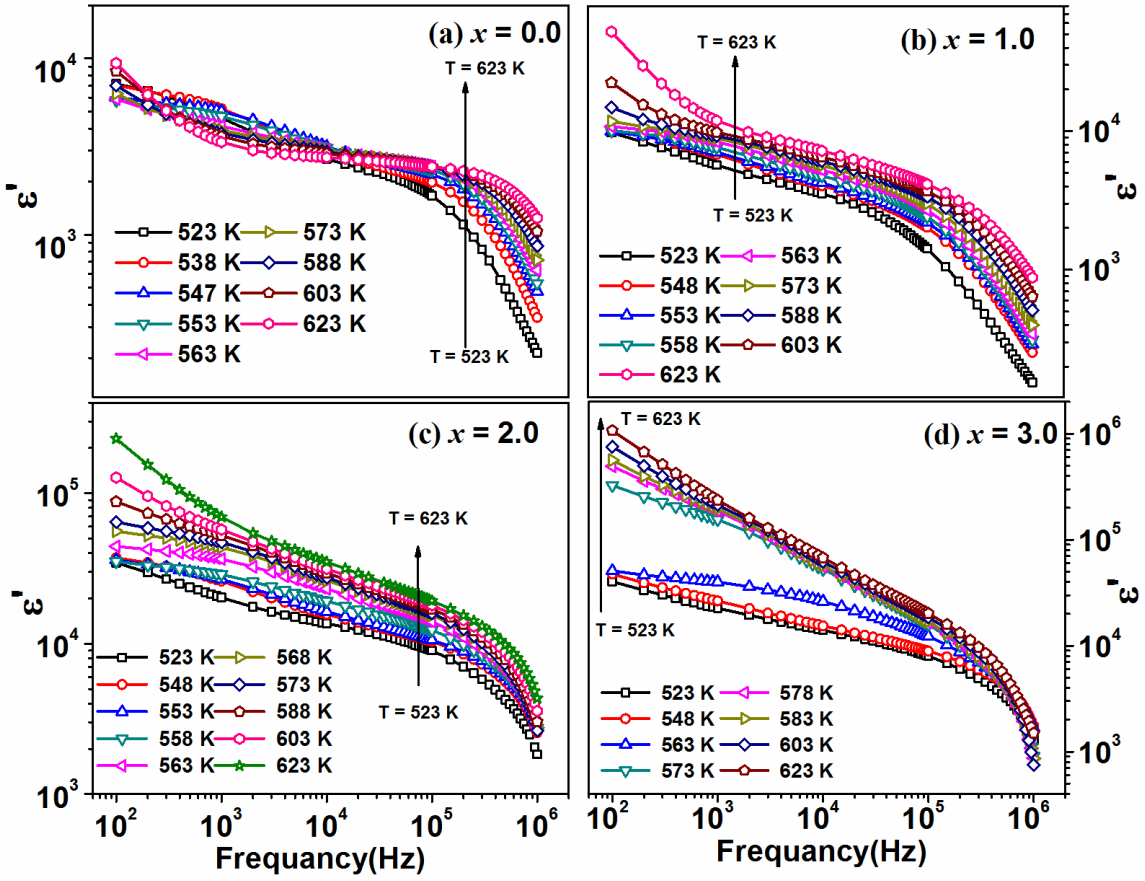

Figure 3.14: Real part (ε') of complex dielectric constant as a function of frequency in logarithmic scale at different temperatures for (Y, Sm)-Fe-O with *x* = 0.0, 1.0, 2.0 and 3.0.

Figure 3.15 shows the logarithmic plots of imaginary part (ε") of dielectric constant as a function of frequency at different temperatures. The slope of linear region at lower frequency of logarithmic plot of ε" with frequency is found to be nearly equal to -1, which suggests that the conductivity follows the typical power-law response known as Universal Dielectric Response (UDR), i.e., $\varepsilon' \alpha\, \omega^{s-1}$ and $\varepsilon'' \alpha\, \omega^{s-1}$, where $s < 1$ [73]. The large value of ε" signifies the large conductivity at higher temperatures. The value of ε" increases with increase in temperature due to increase in the thermally induced charge carriers and hence the conductivity. Such enhancement in ε" due to increase in conductivity has been reported by *Wu* et al. and *Patri* et al. [81,145] in YIG. The conduction loss may occur due to leakage current that depends upon vacancies and space charge accumulation across grain boundaries. The slight increase in ε" at higher frequency (>10^5 Hz) is attributed to LC resonance like effect between electrode and samples [146].

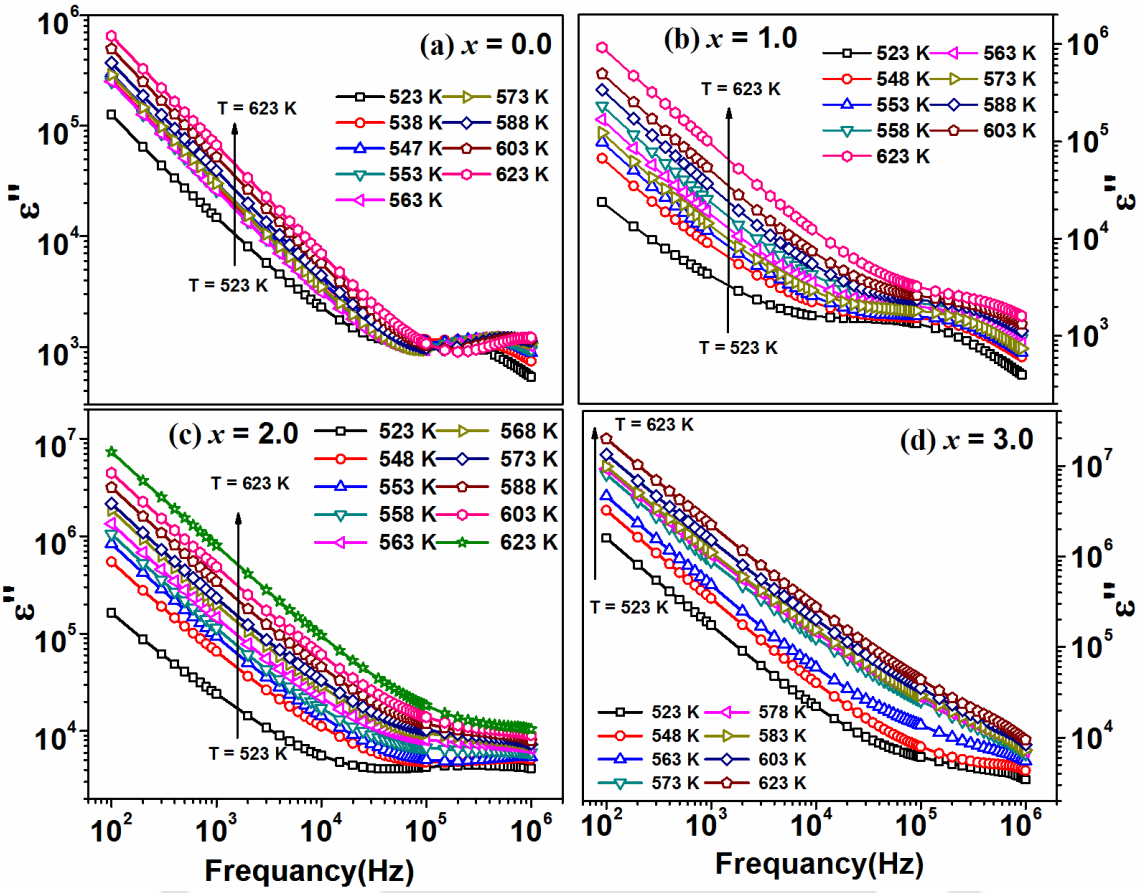

Figure 3.15: Imaginary part (ε") of complex dielectric constant as a function of frequency in logarithmic scale at different temperatures for x = 0.0, 1.0, 2.0 and 3.0 samples.

3.5 AC Conductivity Studies

In order to elucidate the electrical transport of $Y_{3-x}Sm_xFe_5O_{12}$ compounds we calculated the real part of ac conductivity using relation:

$$\sigma_{ac}(\omega) = 2\pi f \varepsilon'' \varepsilon_0 \qquad (3.6)$$

Here, ε" represents the imaginary part of dielectric permittivity. Figure 3.16 shows the frequency variation of σ_{ac} over a wide temperature range (T > 523 K) for all Sm-concentrations. The observed increase in electrical conductivity with the increase in temperature demonstrates the thermally assisted hopping of charge carriers. The increase in ac conductivity with increase in Sm-concentration could be attributed to the increase in the oxygen vacancies and hence, increase in concentration of hopping charge carriers (Fe^{2+} and Fe^{3+} ions). Moreover, at higher temperature the collective motion of oxygen vacancies increases the conductivity. For T ≥ 523 K, the ac conductivity data were fitted to Jonscher power law (JPL) by varying parameter σ_0, A and n.

$$\sigma_{ac} = \sigma_0 + A\omega^n \tag{3.7}$$

where, σ_0 represents the dc conductivity. A is a constant and n represents the frequency exponent. The fitted data are shown as solid line in Figure 3.16. The mechanism associated with conduction process can be understood from the nature of n values. Temperature variations of n for all Sm doped YIG samples are shown in Figure 3.17(a). For x = 0.0 and 0.5, the value of n lies in the range of $1 < n < 1.5$ and it is found to increase with increase in temperature and it indicates that the conduction process is governed by localized small polaron hopping model (back and forth motion of charge carriers between defects) [147,148]. A small polaron is created when an electron gets trapped at a given site as a consequence of the displacement of adjacent atoms or ions. Thermally activated hopping is an important characteristic of small polaron model. For x = 1.0 the conduction process is controlled by small polaron tunnelling up to a temperature of 560 K and beyond that it is governed by overlapping large polaron tunnelling model [144]. Further increase in Sm-concentration gives rise to the domination of conduction mechanism by overlapping large polaron tunnelling model. It is due to the coulomb interaction associated with the large Sm^{3+} ions (lager ionic radii) whose broader potential well overlap with the well of the other ions.

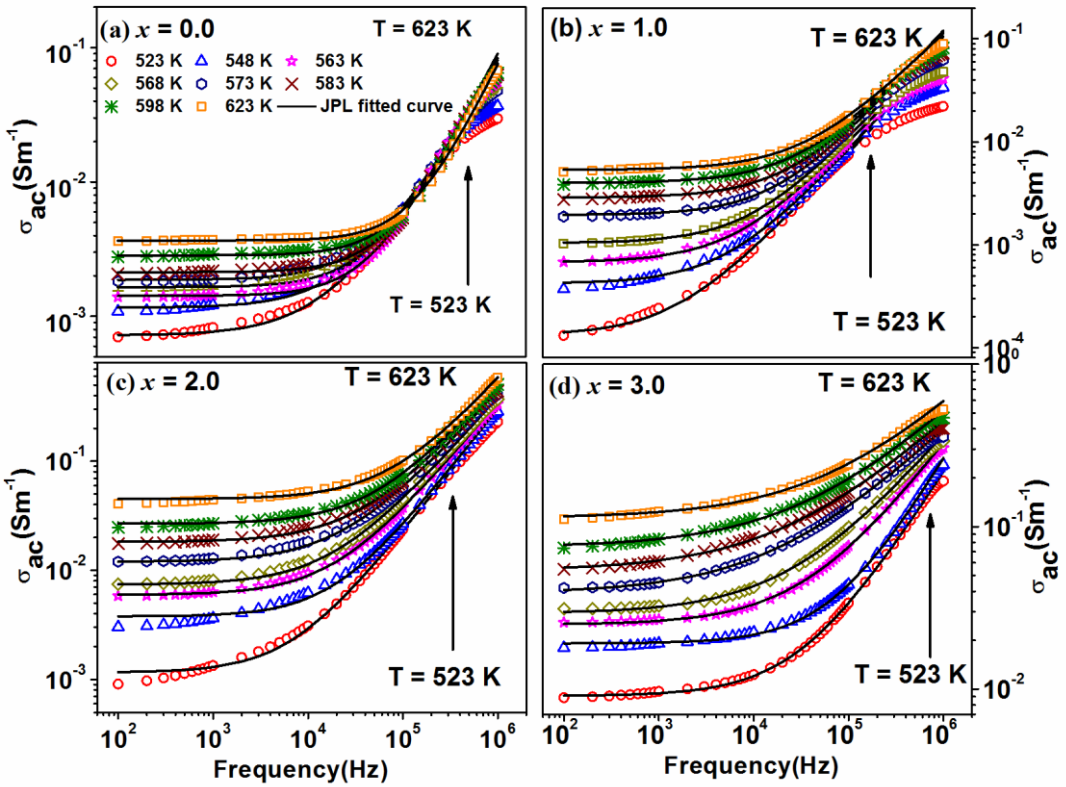

Figure 3.16: Frequency variation of ac conductivity in logarithmic scale along with fitted data (solid lines) using JPL model for (a) x = 0, (b) x = 1.0, (c) x = 2.0 and (d) x = 3.0 at different temperature ranging from 523 K to 623 K.

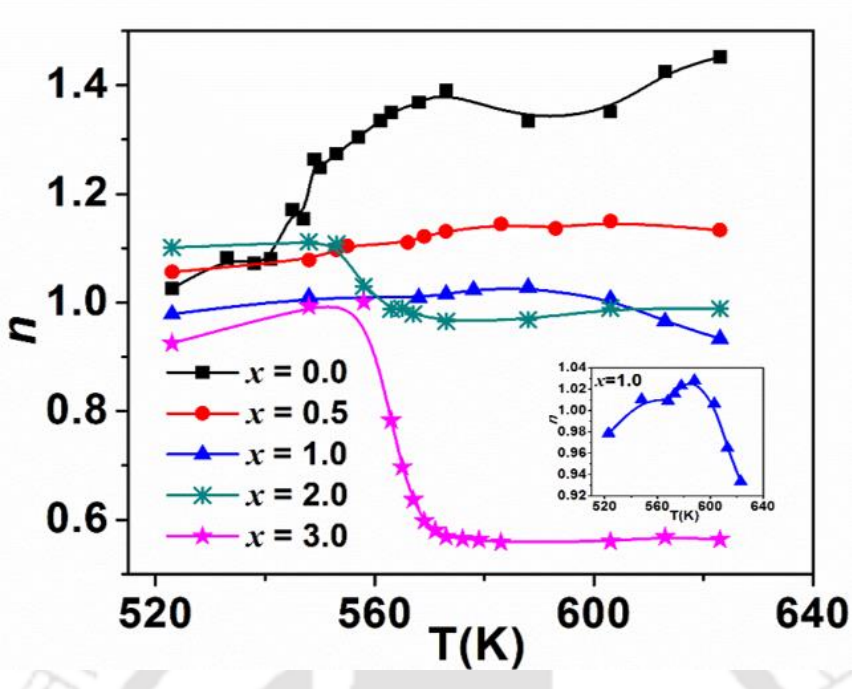

Figure 3.17: (a) Temperature variation of frequency exponent of polycrystalline samples of (Y, Sm)-Fe-O.

3.6 Arrhenius Plots and Activation Energy

The thermal activation process of relaxation time is analyzed by using the Arrhenius law [66]:

$$\tau(T) = \tau_0 \exp\left(\frac{E_a}{k_B T}\right) \tag{3.8}$$

Here τ is the relaxation time corresponding to the relaxation peak in the plots of -Z" versus f, τ_0 is a constant which is a measure of τ at T $\rightarrow \infty$, E_a is the activation energy of relaxation and k_B is the Boltzmann constant.

In order to unravel the nature of the charge carriers taking part in the relaxation dynamics, it is very important to estimate the relaxation energy. The value of E_a can be estimated by plotting lnτ versus 1/T and carrying out the linear fit as shown in Figure 3.18. It is very interesting to note that the temperature dependence of τ could not be fitted to a single Arrhenius equation throughout the whole range of temperature under investigation. The discontinuity in the plot is in the vicinity of FIM T_C as per the magnetic analysis. For instance, the lnτ vs 10^3/T data for x = 0 were fitted to two different linear relations with different set of τ_0 and E_a values. They are found to be $\tau_0 = 4.0\times10^{-7}$ Hz and E_a = 0.40 eV for T < 550 K (FIM) and $\tau_0 = 1.4\times10^{-5}$ Hz and E_a = 0.25 eV for T > 550 K (PM). Similar

change in the value of activation energy is observed across the T_C for other samples as shown in Table 3.2.

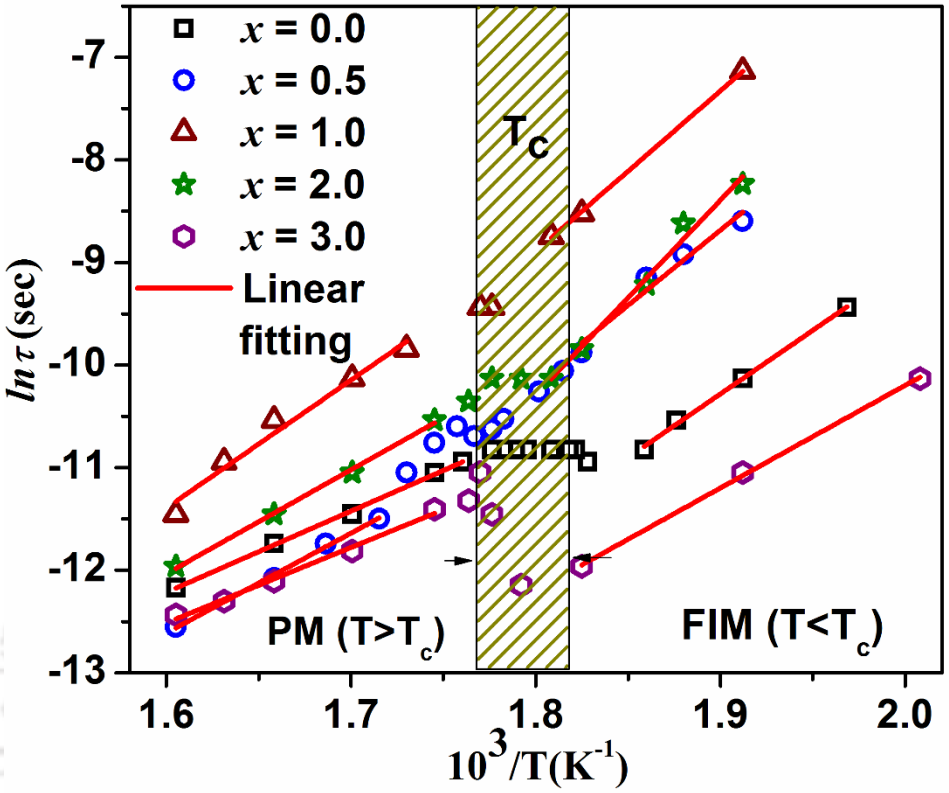

Figure 3.18: Relaxation time as a function of inverse temperature (10^3/T) for the (Y, Sm)-Fe-O samples along with fit to Arrhenius model.

The grains and grain boundaries contribution to conductivity (σ_g and σ_{gb}) were estimated from their respective resistance values (R_g, R_{gb}) using the relation $\sigma_g = \frac{t}{SR_g}$ and $\sigma_{gb} = \frac{t}{SR_{gb}}$, where t is the thickness of sample and S is the surface area of the sample. Both contributions of conductivity follow the Arrhenius law:

$$\sigma = \sigma_0 \exp\left(\frac{-E_c}{k_B T}\right) \tag{3.9}$$

where E_c is the activation energy for conduction and σ_0 is prefactor. k_B represents the Boltzmann constant. Figure 3.19 presents the plots of $\ln\sigma_g$ and $\ln\sigma_{gb}$ versus 10^3/T for all the Sm-substituted samples. The conduction activation energy values corresponding to grain (E_{cg}) and grain boundaries (E_{cgb}) were estimated by fitting the σ_g and σ_{gb} data to Arrhenius law and they are presented in Table 3.2. The value of E_{cg} is comparable to the activation energy involved in the hopping of charge carriers between Fe^{2+} and Fe^{3+} ions [81,149]. It

is very reasonable to believe the presence of oxygen vacancies (OVs) in our samples as they were sintered at high temperature in air for a long duration of time [143]. Moreover, the presence of Fe^{2+} and Fe^{3+} ions in YIG have been reported in literature on the basis of XPS analysis [102]. Due to the ionization of oxygen vacancies, some of Fe^{3+} ions are expected to reduce to Fe^{2+} ions, giving rise to mixed valance state. The electrons produced as a result of ionization of OVs hop between the available Fe^{2+} and Fe^{3+} sites. Hence, the electrical conduction in the grains are mainly contributed from the hopping of charge carriers between Fe^{2+} and Fe^{3+}. On the other hand, the nearly similar values of E_{cgb} and E_a suggest that the frequency relaxation in -Z" is basically attributed to the GB conduction relaxation. Moreover, the value of E_{cgb} and E_a are close to the activation energy for singly ionized OVs as reported in literature [149,150]. The electrons released from the ionized OVs move into the G and enhance the conductivity.

The change in the value of activation energy in FIM and PM regions suggests the change in the relaxation dynamics, which happens when the electric dipoles transit from one ordered state to another. As YIG is non-ferroelectric in nature, it is unlikely that samples undergo any electrical transition. The temperature variation of magnetization data of the samples reveal that the $x = 0$ sample undergoes a ferrimagnetic transition at $T_C = 550$ K. Similar, magnetic transition is expected for other samples. Thus, the change in E_a values across the ferrimagnetic T_C suggests the impending coupling between the magnetic order parameter (magnetization, M) and the electric order parameter (polarization, P) and their decoupled state above T_C (PM). Such a change in the value of E_a across the magnetic transition has been reported in Mn doped $YFeO_3$ [146]. Moreover, the observed higher E_a values below T_C suggest that the ordered magnetic ions hinder the relaxation process. Similar to the case of dielectric relaxation, we observed different set of E_{cg} and E_{cgb} values in the FIM and in the PM regions and it depicts the influence of magnetic ordering on the electrical conductions.

We have also plotted the σ_{dc} versus T and estimated the values of conduction activation energy. The dielectric anomalies in the vicinity of magnetic transition temperature are reported in literature [145,151,152]. The values of E_{cdc} for $T > T_C$ (PM) lie in range of 0.34 eV to 0.71 eV. On the other hand, for $T < T_C$ (FIM), it is found to lie in the range of 0.20 eV to 0.40 eV which can be attributed to singly ionized OVs.

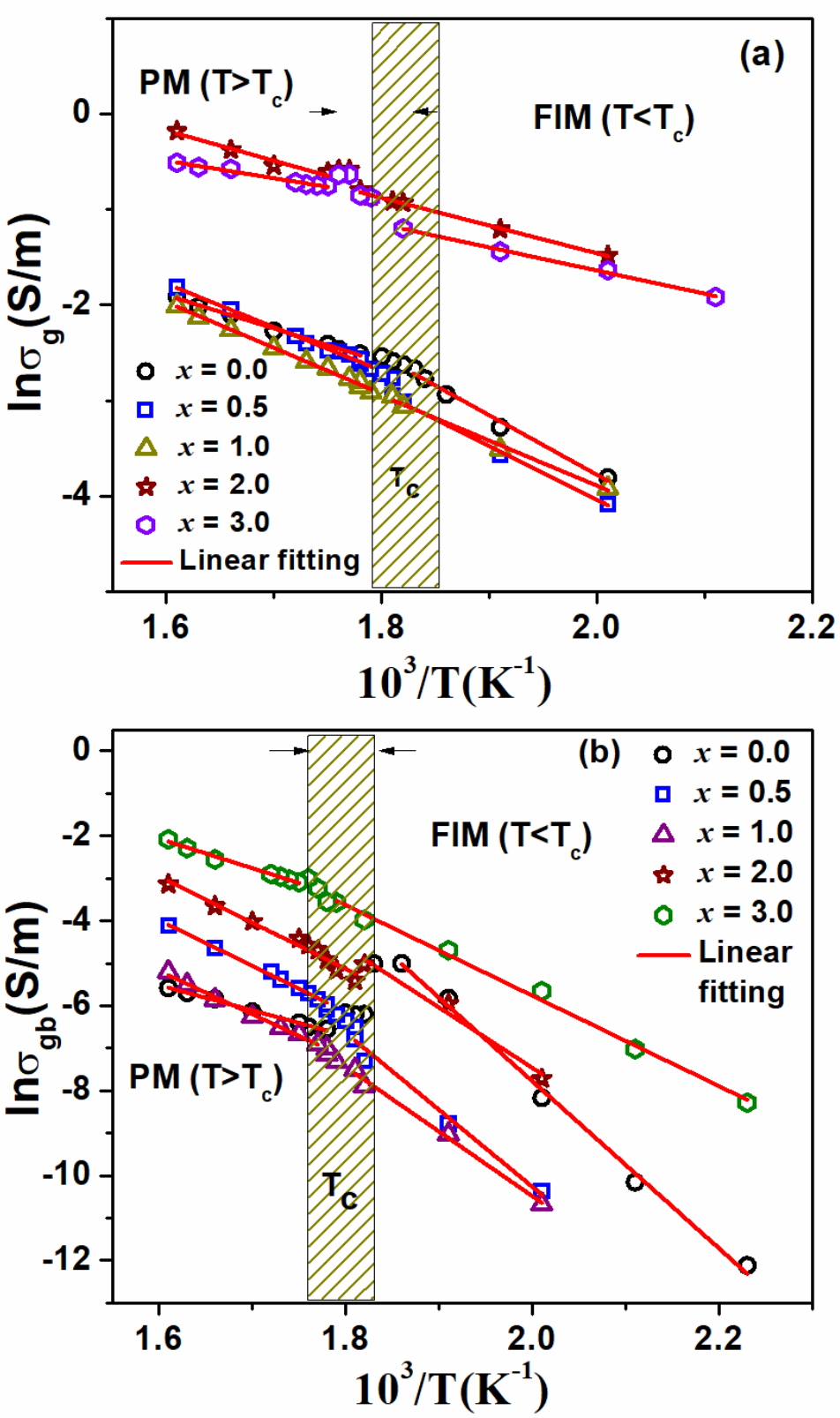

Figure 3.19: (a) Grain boundaries conductivity and (b) grains conductivity as a function of inverse of temperature (1/T). Solid lines are the fitted data as per Arrhenius law.

Table 3.2: Activation and conduction energy of (Y, Sm)-Fe-O for all composition.

x	Activation energy E_a (eV)		Grain boundary conduction activation energy *Ecgb* (eV)		Grain conduction activation energy E_{cg} (eV)	
	FIM	**PM**	**FIM**	**PM**	**FIM**	**PM**
0.0	0.41	0.25	0.73	0.22	0.24	0.13
0.5	0.81	0.43	0.76	0.41	0.27	0.18
1.0	0.62	0.44	0.57	0.38	0.17	0.17
2.0	0.68	0.39	0.55	0.34	0.11	0.11
3.0	0.35	0.33	0.39	0.26	0.09	0.07

3.7 Conclusion

The polycrystalline samples of $Y_{3-x}Sm_xFe_5O_{12}$ for x = 0 to 3.0 were synthesized using solid-state reaction method in single-phase form. All the XRD patterns were refined using cubic unit cell with $Ia\bar{3}d$ space group. The lattice parameter increases with Sm-concentration from 12.3726 Å for x = 0 to 12.5245 Å for x = 3.0, such increase is well explained in terms of substitution of Sm^{3+} ions having larger ionic size as compared to Y^{3+} ions. The saturation magnetization of (Y, Sm)-Fe-O samples are found to decrease while the FIM T_C increases with increase in Sm-concentration. The moment of Sm^{3+} ions are antiferromagnetically coupled with the net magnetic moment of Fe^{3+} ions and thus results in decrease in saturation magnetization. The increase in FIM T_C is described in terms of strengthening of superexchange interaction between $Fe^{3+}(a)$-O^{2-}-$Fe^{3+}(d)$ networks. In addition to structural and magnetic properties, we have also studied the electrical properties. The relaxation dynamics was examined based on -Z" versus frequency plots. The plots are asymmetric and broad in nature. The relaxation time is temperature dependent suggesting the thermal activation of charge carriers. The complex impedance spectroscopy plots show the contributions from both grains and grain boundaries at lower temperature and however, at higher temperature grain boundaries contribution dominate. The depressed and asymmetric nature of semicircular arc suggest non-Debye like relaxation and it is controlled by thermally activated charge carriers. The temperature dependence of relaxation frequency exhibits a change in slope in the vicinity of ferrimagnetic transition

temperature. Sm-substitution reduces the electrical resistance at room temperature from 5 MΩ to 0.10 MΩ at 100 Hz. The dielectric constant increases with Sm-concentration from 22 to 29 for f = 1 MHz. The ac conductivity data estimated from dielectric constant measurement show increasing trend with increase in Sm-concentration and it suggests that the conduction process is governed by the localized small polaron and overlapping of large polaron tunnelling models. The observed anomaly in relaxation frequency data in the vicinity of ferrimagnetic transition temperature suggests the presence of magneto-electric coupling.

Chapter 4

Magnetic and Dielectric Properties of Y-(Fe, M)-O Compounds (M = Cr, Mn)

The yttrium iron garnet (YIG) is known to undergo ferrimagnetic (FIM) transition around T_C = 550 K and the substitution of other rare earth elements at Y site mostly does not affect the FIM T_C [20,153]. However, the substitution of Al, Cr, Mn, Ti, etc. at the Fe site affects the magnetic as well as dielectric properties [87,105,107,108,110]. In RIGs, the substitution of smaller ions (Al^{3+}, Ga^{3+} etc.) mostly occupy the tetrahedral site, while those of larger ions (In^{3+}, Sc^{3+} etc.) occupy the octahedral site and they lead to decrease and increase in saturation magnetization, respectively. However, the 3*d* transition elements such as Cr^{3+} and Mn^{3+} ions are known to mostly occupy the octahedral site of Fe^{3+} ions and thus affecting its saturation magnetization [105,108]. In order to understand the dielectric and magnetic properties of YIG, we have taken up Cr and Mn-substitution at Fe site and studied their structural, magnetic and dielectric properties.

4.1 Cr-Substituted $Y_3Fe_5O_{12}$

This section deals about the preparation of Cr-substituted YIG ($Y_3Fe_{5-x}Cr_xO_{12}$: Y-(Fe, Cr)-O) with x = 0, 0.1, 0.2, 0.3, 0.4, and 0.5 and study of structural, magnetic and dielectric properties.

Polycrystalline samples of Y-(Fe, Cr)-O series for x = 0 to 0.5 were prepared by solid-state reaction method as mentioned in section 2.2.1. The chosen starting compounds are Y_2O_3, Fe_2O_3 and Cr_2O_3 with 99.9 % purity. The pre-sintering of the mixed powders was done at 873 K for 12 hours and the pellets were finally sintered at 1673 K for 8 hours.

4.1.1 Structural Studies

The powder XRD patterns of Y-(Fe, Cr)-O samples are displayed in Figure 4.1. These XRD patterns were refined by choosing $Ia\bar{3}d$ space group (cubic) and the samples are found to be in single-phase form. The typical XRD patterns (red open circle) along with Rietveld refined data (black solid line) for Y-(Fe, Cr)-O samples with x = 0, 0.1, 0.3 and 0.5 are shown in Figure 4.2. The lattice parameter of x = 0 sample is found to be a = 12.3778

(4) Å and is comparable with that of reported value [25]. The structural parameters (a, V) and reliability factors (R_p, R_{exp}, R_{Bragg}, R_F, χ^2, etc.) along with the cation occupancy obtained from the Rietveld refinement are given in Table 4.1. The values of lattice constant (a) and the unit cell volume (V) are found to decrease systematically with increase in Cr-concentration. Such decrease in lattice parameter is attributed to the substitution of smaller Cr^{3+} (0.615 Å) ions at the octahedral site of Fe^{3+} (0.645 Å) ions and such substitution is further emphasized from magnetization measurement discussed later. The interatomic distance (Fe(a)-Fe(d)) and bond angle (Fe(a)-O-Fe(d)) obtained from the Rietveld analysis are shown in Figure 4.3. The observed interatomic distance (Fe(a)-Fe(d)) and bond angle (Fe(a)-O-Fe(d)) is 3.459 Å and 126.37^0 for x = 0 sample, which are comparable with those of reported values [25]. These values are found to decrease with increase in Cr concentration. The schematic of bond distance and bond angle among Y(c), Fe/Cr(a), and Fe(d) atoms are shown in Figure 4.4, typically for x = 0 and 0.4 sample. The picture shows the presence of Cr (blue in color) at Fe(a) site for x = 0.4.

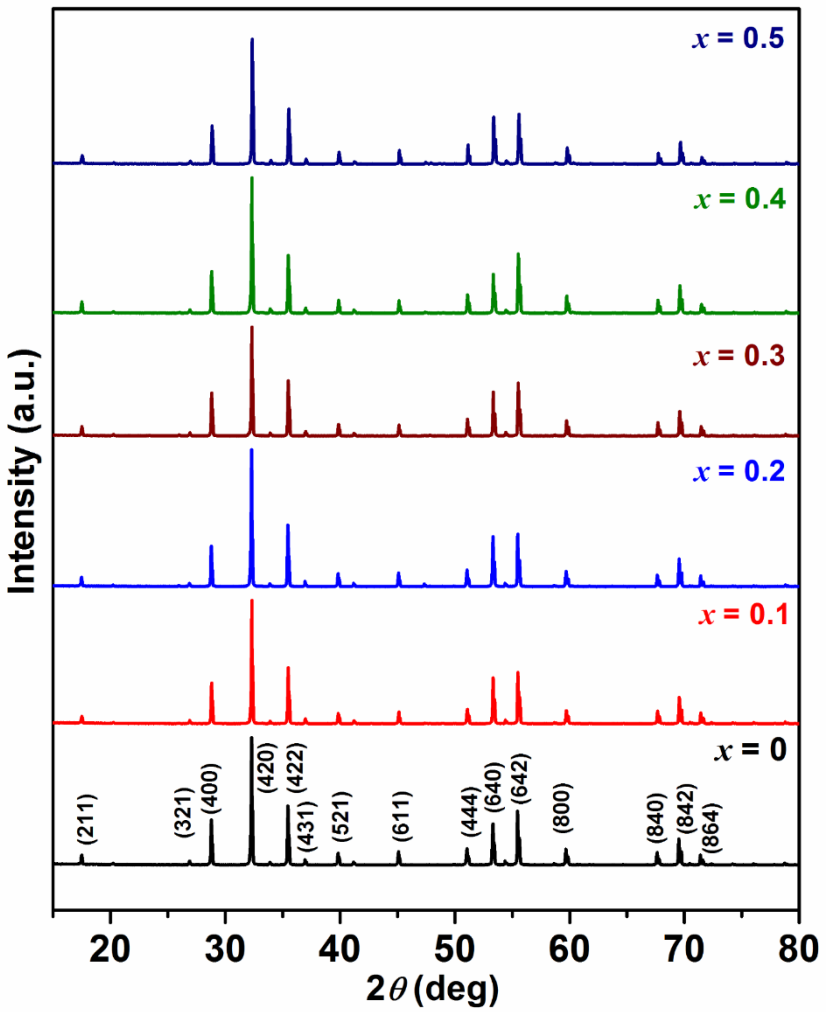

Figure 4.1: Powder XRD patterns of polycrystalline Y-(Fe, Cr)-O compound.

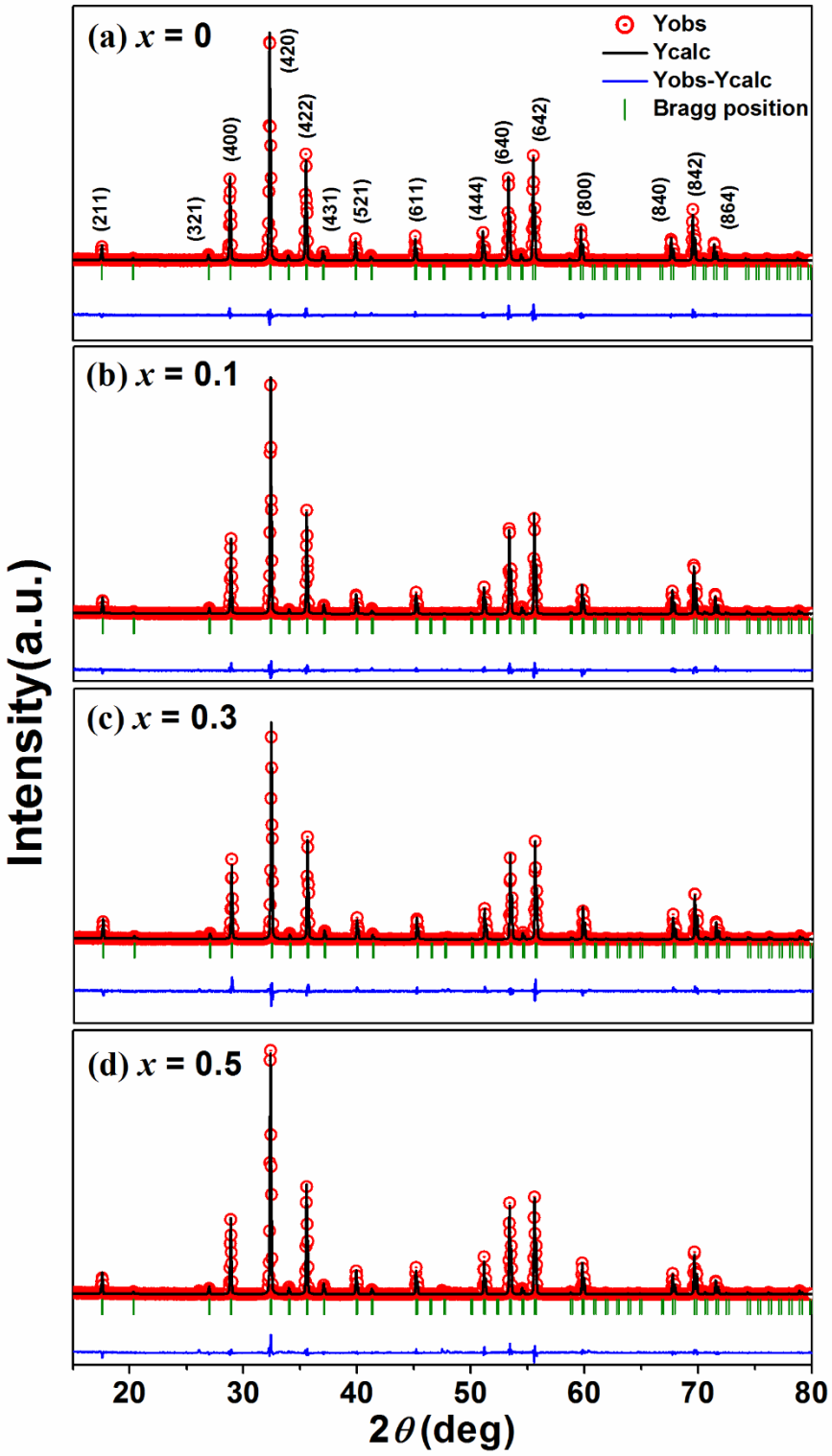

Figure 4.2: Typical XRD patterns (open red circle) along with Rietveld refined data (black solid line) for a few selected Y-(Fe, Cr)-O samples.

Table 4.1: Structural and reliability parameters along with cationic occupancy obtained from the Rietveld refinement of XRD patterns of Y-(Fe, Cr)-O samples with x = 0 to 0.5.

x		0	0.1	0.2	0.3	0.4	0.5
Space group		$Ia\bar{3}d$	$Ia\bar{3}d$	$Ia\bar{3}d$	$Ia\bar{3}d$	$Ia\bar{3}d$	$Ia\bar{3}d$
$a = b = c$ (Å)		12.3778(4)	12.3687(3)	12.3641(4)	12.3621(4)	12.3579(4)	12.3560(4)
V (Å^3)		1896.4	1892.2	1890.1	1889.2	1887.3	1886.4
R_p (%)		8.41	9.17	9.05	9.41	10.5	11.2
R_{exp} (%)		7.00	8.13	7.83	8.20	7.77	8.04
R_f (%)		5.50	5.84	7.80	7.94	6.71	7.44
R_{Bragg} (%)		4.25	5.18	4.86	5.92	5.89	5.10
χ^2		3.28	3.94	3.51	3.64	4.05	4.16
Occupancy	Y	2.98	2.98	2.99	2.98	2.99	2.99
	Fe	4.99	4.88	4.79	4.68	4.57	4.49
	Cr	0	0.09	0.19	0.27	0.38	0.49

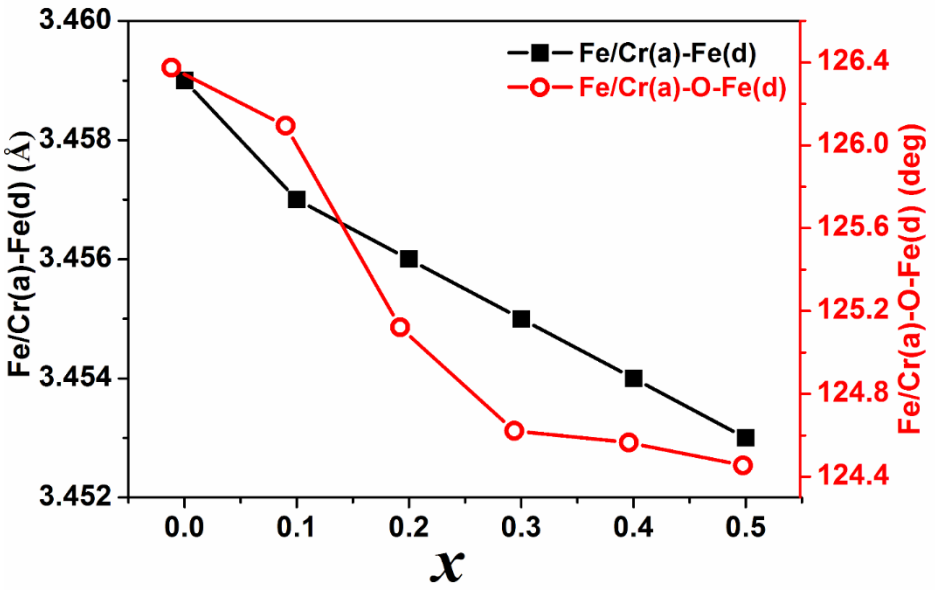

Figure 4.3: The average Fe/Cr(a)-Fe(d) bond length and Fe/Cr(a)-O-Fe(d) bond angle as a function of Cr-concentration.

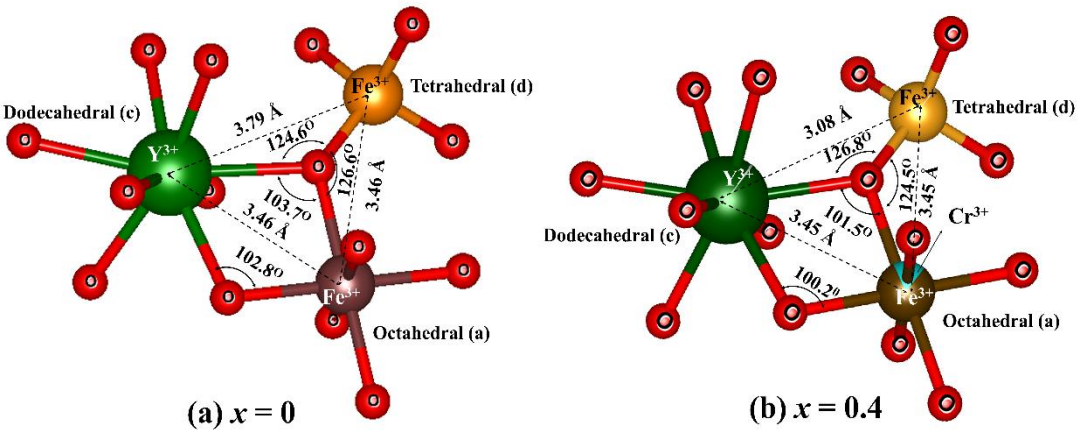

Figure 4.4: Schematic bonding diagram of Y and Fe atoms through O in Y-(Fe, Cr)-O for x = 0 and 0.4 samples using VESTA software.

Figure 4.5(a-d) shows the FESEM micrographs of Y-(Fe, Cr)-O for x = 0 to 0.5. The grain size values were estimated by using ImageJ software [154]. The average grain size of each sample is obtained by fitting the size distribution histogram (Figure 4.5(e-h)) to log-normal distribution function (equation 3.1). The average grain size values of x = 0, 0.1, 0.2, 0.3, 0.4 and 0.5 samples are found to be 3.39 μm, 4.23 μm, 4.45 μm, 4.66 μm, 5.81 μm and 7.17 μm, respectively with a maximum standard deviation of 0.22 μm. The densities of the sintered pellets were measured using Archimedes' principle and they are found to be 5.168, 5.177, 5.180, 5.181, 5.182, 5.183 g/cm^3 for x = 0, 0.1, 0.2, 0.3, 0.4 and 0.5 samples respectively. They are found to be in the range of 75 % to 88 % of the theoretical density. The increase in average grain size with Cr-concentration can be attributed to enhanced grain boundary mobility due to the small ionic size of substituted Cr^{3+} ions as reported by *Chen* et al. [138]. One cannot rule out the possibility of increase in grain size due to the reduction in melting point of Y-(Fe, Cr)-O. The chemical composition is found to be consistent with the nominal starting composition as per EDX spectra (Figure 4.6). For example, cationic ratio Y:Fe:Cr = 2.98:4.78:0.18 and 2.97:4.57:0.37 for x = 0.2 and 0.4, respectively.

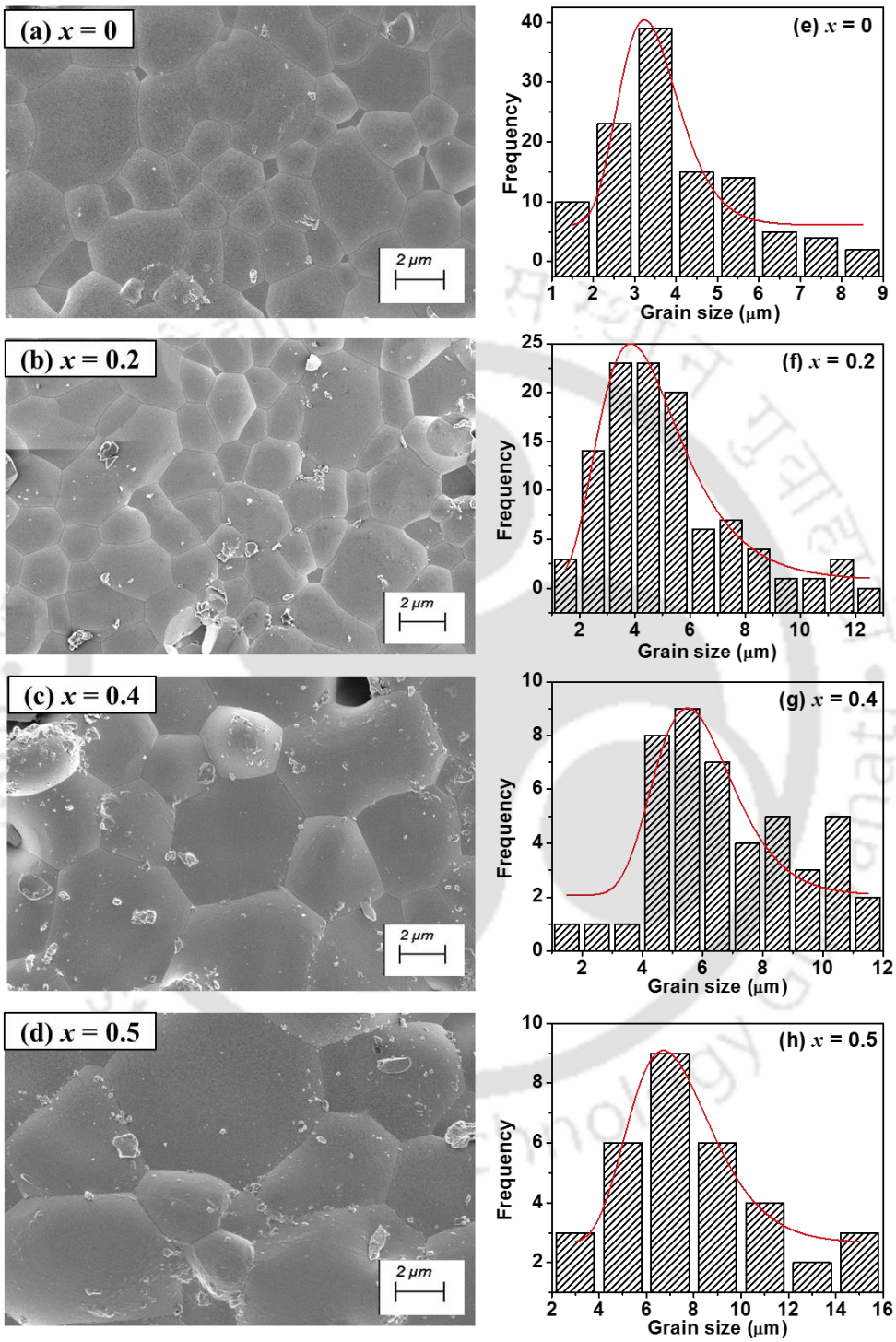

Figure 4.5: (a-d) Typical FESEM images and (e-h) grain size distribution of x = 0, 0.2, 0.4 and 0.5 samples.

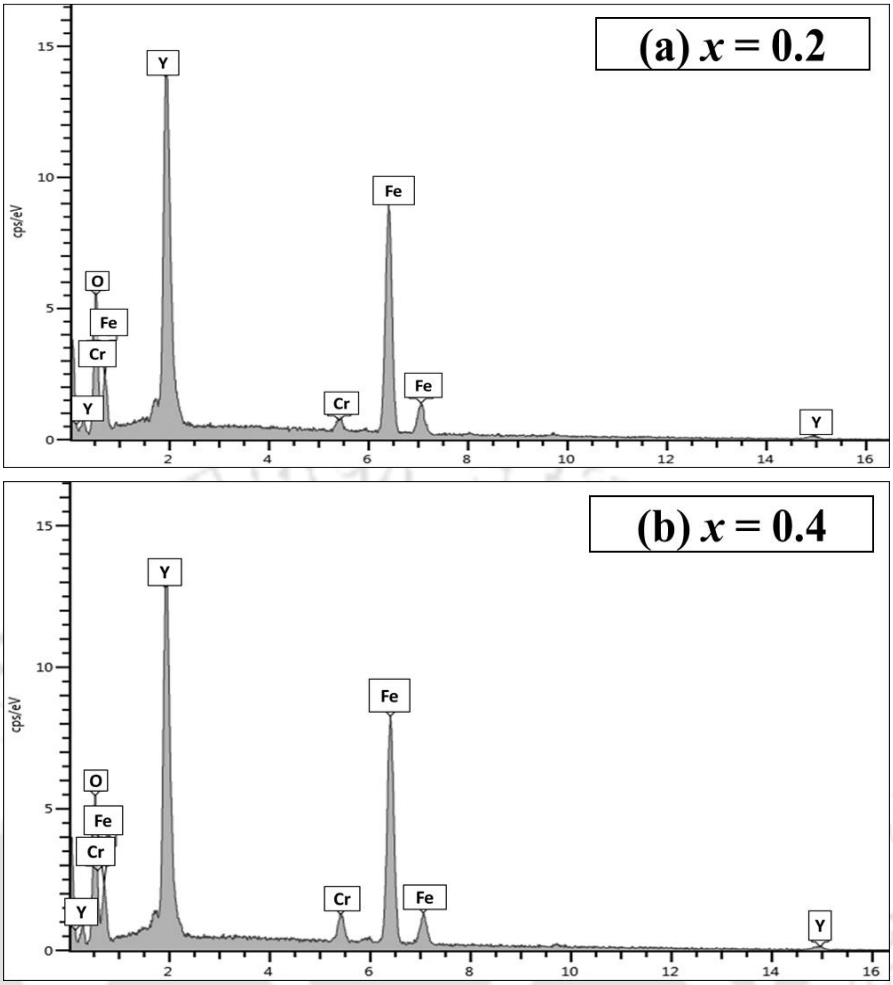

Figure 4.6: EDX spectra of Y-(Fe, Cr)-O samples for (a) x = 0.2 and (b) x = 0.4 samples.

Raman spectra were recorded from wavenumber ranging from 100 cm^{-1} to 800 cm^{-1}. According to group theory analysis, there are 25 ($3A_{1g}$ + $8E_g$ + $14F_{2g}$) allowed Raman active modes in YIG [155]. The room temperature (RT = 300 K) Raman spectra for x = 0 to 0.5 samples are shown in Figure 4.7. The peaks observed in the wave number range of 100 cm^{-1} to 300 cm^{-1} are primarily due to the translational motion of Y^{3+} ions at the dodecahedral site. The peaks observed in the range of 300 cm^{-1} to 800 cm^{-1} correspond to the stretching and bending modes of Fe-O bonds in tetrahedral and octahedral sites [102]. It is observed that the peak corresponding to the F_{2g} vibrational mode is shifting towards higher wavenumber (271.4 cm^{-1} to 277.4 cm^{-1}) as the Cr-concentration is increased and it can be attributed to the decrease in the lattice constant and the bond length (Figure 4.3) as discussed in the XRD analysis.

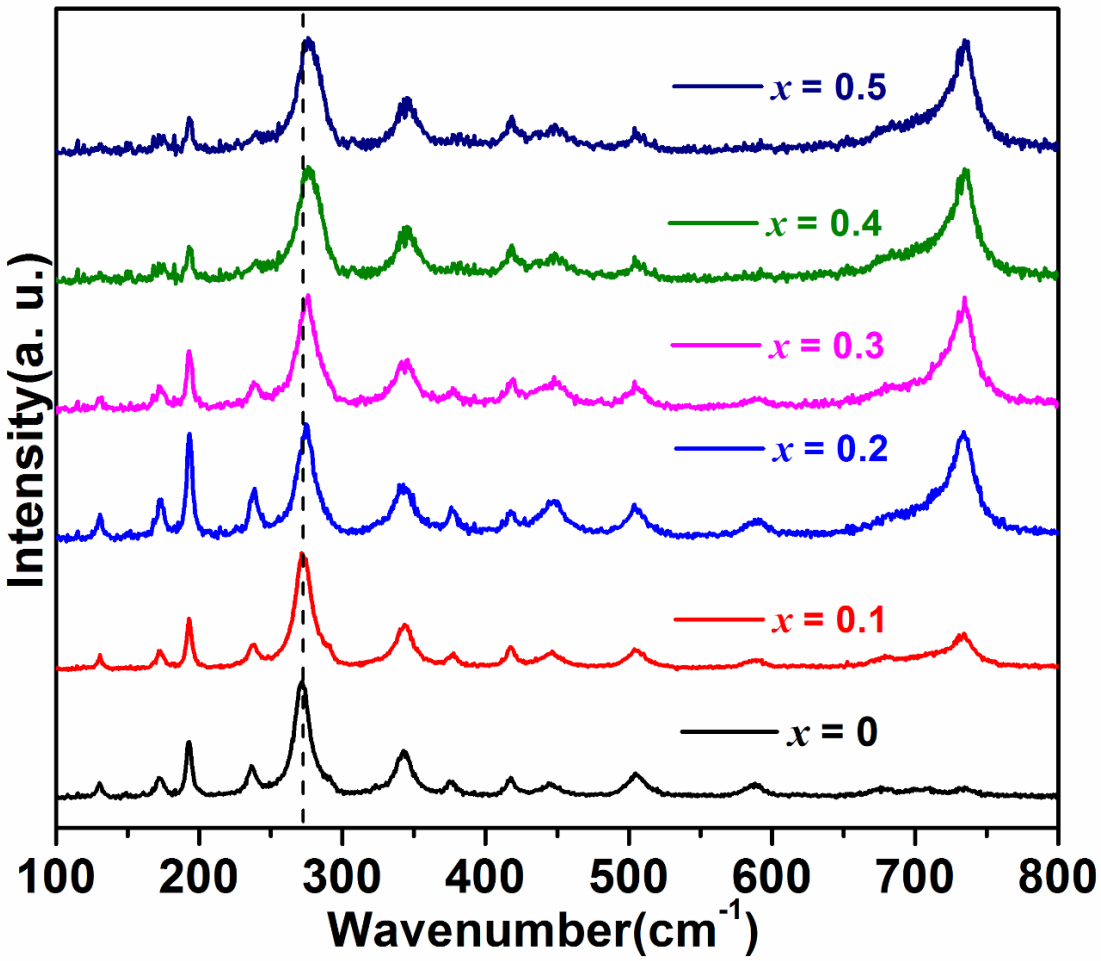

Figure 4.7: Room temperature Raman spectra for Y-(Fe, Cr)-O samples with x = 0 to 0.5. The vertical dashed line is shown to clearly see the shift in F_{2g} (271.4 cm^{-1} to 277.4 cm^{-1}) vibrational mode.

4.1.2 Magnetic Studies

Temperature variation of magnetization (*M-T*) data were recorded for Y-(Fe, Cr)-O samples by heating them from 300 K to 700 K in the presence of an applied magnetic field of 200 Oe. The *M-T* plots in the normalized form of magnetization are shown in Figure 4.8(a), where they all exhibit clear ferrimagnetic (FIM) transition. The FIM T_C was determined from the plots of *dM/dT* versus T (Figure 4.8(b)), and it is found to decrease from 547 K for x = 0 to 494 K for x = 0.5 as given in Table 4.2. The decrease in FIM T_C with increase in Cr-concentration can be understood as per the analysis of XRD patterns where the bond angle between Fe ions reduces thus result in the weakening of superexchange interaction in $Fe^{3+}(a)$-O^{2-}-$Fe^{3+}(d)$ networks due to Cr-substitution.

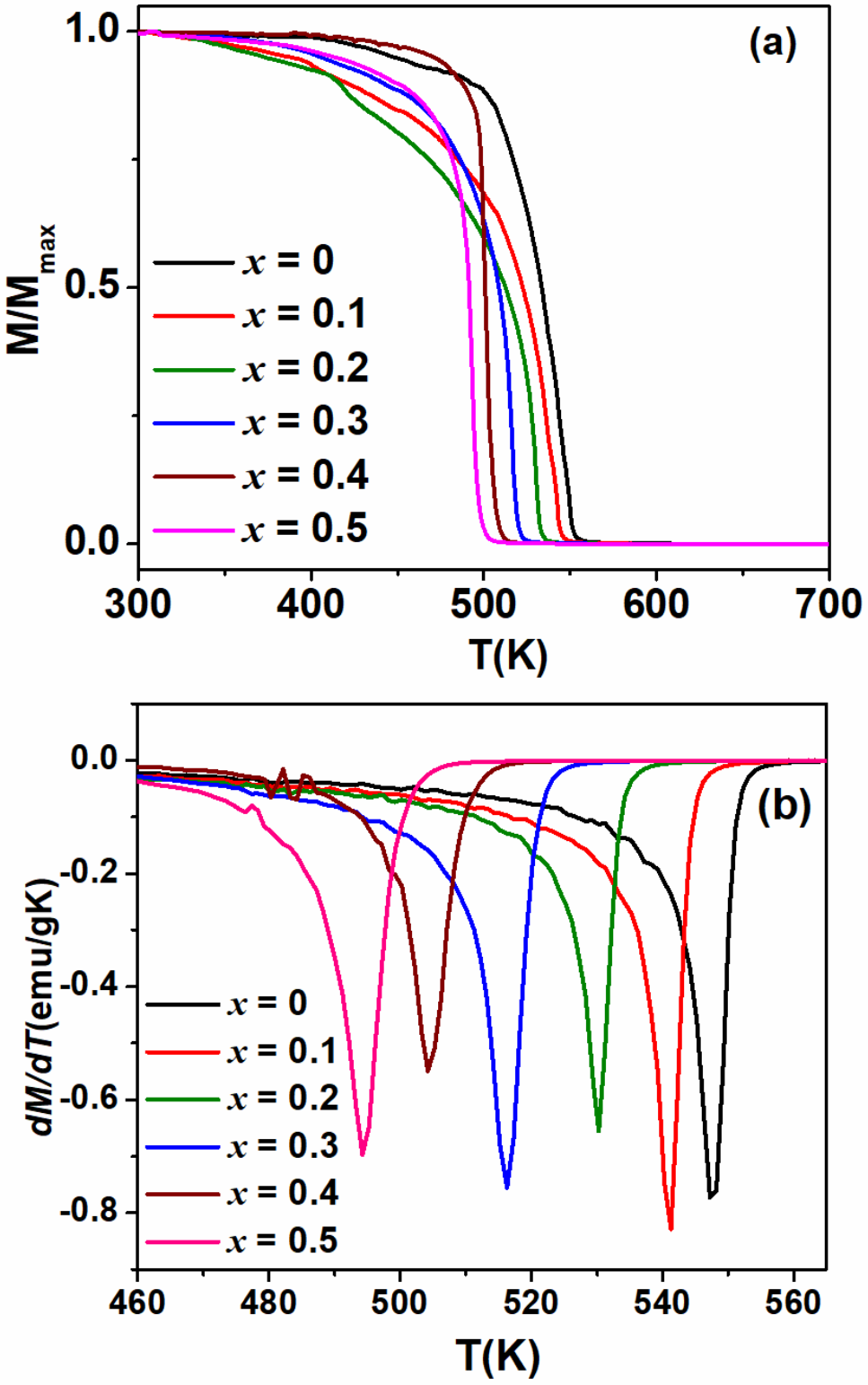

Figure 4.8: (a) Normalized *M-T* plots (b) *dM/dT* versus T plots of Y-(Fe, Cr)-O samples for an applied field of 200 Oe.

The field variation of magnetization (*M-H*) loops recorded at room temperature in the field range of -5 kOe to +5 kOe are shown in Figure 4.9(a) and they all almost saturate for H ≥ 2 kOe. In order to determine the saturation magnetization (M_S) and the effective anisotropy constant (K_1), the initial magnetization curves were analyzed in terms of the law of approach to saturation (LAS) [139]:

$$M = M_S\left(1 - \frac{8K_1^2}{105\mu_0^2 M_S^2 H^2}\right) + cH \tag{4.1}$$

where M_S represents the saturation magnetization, K_1 is effective magnetic anisotropy constant. The last term *cH* represents forced magnetization due to the increase of saturation magnetization in high fields. The initial magnetization curves along with fitted data to LAS model are displayed in Figure 4.9(b). The M_S value at RT is found to increase with increase in Cr-concentration, i.e., from 24.8 emu/g for x = 0 to 26.6 emu/g for x = 0.5 (Table 4.2). The increase in magnetization value can be understood in terms of Cr^{3+} (3 μ_B) ions having smaller magnetic moment substituting the Fe^{3+} (5 μ_B) ions at the octahedral (*a*) site as per the following empirical equation:

$$M_{net} = 3M_{Fe}(d) - (2 - x)M_{Fe}(a) - xM_{Cr}(a) \tag{4.2}$$

Here $M_{Fe}(d)$, $M_{Fe}(a)$ and $M_{Cr}(a)$ correspond to magnetic moments of Fe^{3+} ions at tetrahedral (*d*) site and, Fe^{3+} and Cr^{3+} ions at octahedral (*a*) site respectively. The estimated value of K_1 is found to increase marginally from (7.94±0.03)×10^4 erg/cm^3 for x = 0 to (8.23± 0.02)×10^4 erg/cm^3 for x = 0.5. The K_1 value is found to be one order of magnitude smaller than that reported in ferromagnetic Fe (4.2×10^5 erg/cm^3) and ferrimagnetic hexaferrites [29]. Based on these values they are categorized as magnetically soft materials. The value of anisotropy constant of x = 0 at RT is comparable with those reported in the literature [111]. The anisotropy constant K_1 plays a major role in controlling the saturation magnetization and coercive field. It is mainly due to magnetocrystalline anisotropy and it depends on the interaction of Fe^{3+} ions with the crystalline field at '*a*' and '*d*' sites.

Table 4.2: The obtained values of T_C and M_S for Y-(Fe, Cr)-O samples as per the above analysis.

x	**0**	**0.1**	**0.2**	**0.3**	**0.4**	**0.5**
T_C **(K)**	547	541	530	516	504	494
M_S **(emu/g)**	25.5	27.7	27.7	28.2	28.6	28.7

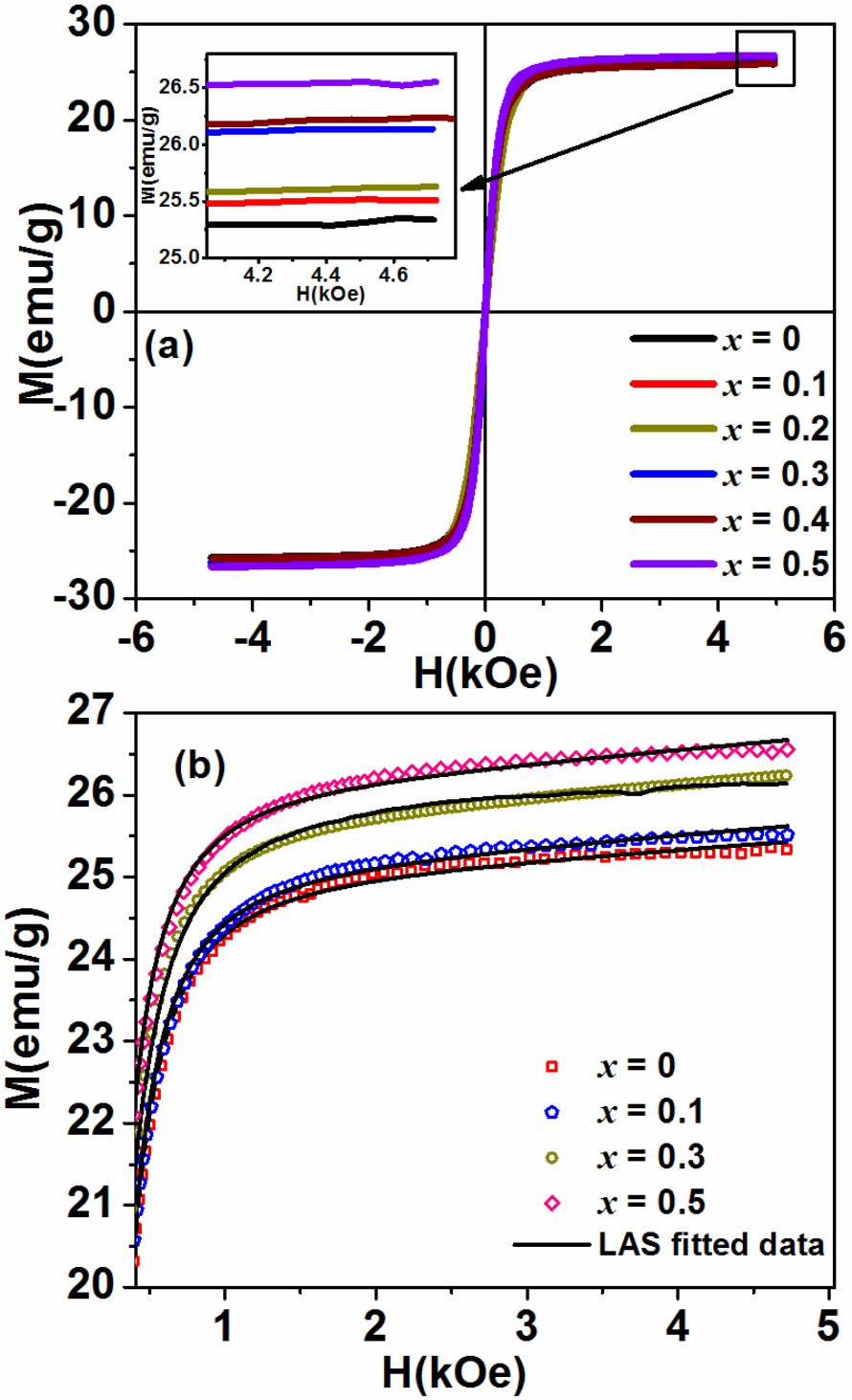

Figure 4.9: (a) *M-H* loops of Y-(Fe, Cr)-O for x = 0 to 0.5 at room temperature. (b) Experimental initial magnetization data (symbol) along with the fit to the law of approach to saturation (solid line).

4.1.3 Complex Impedance Spectroscopy Studies

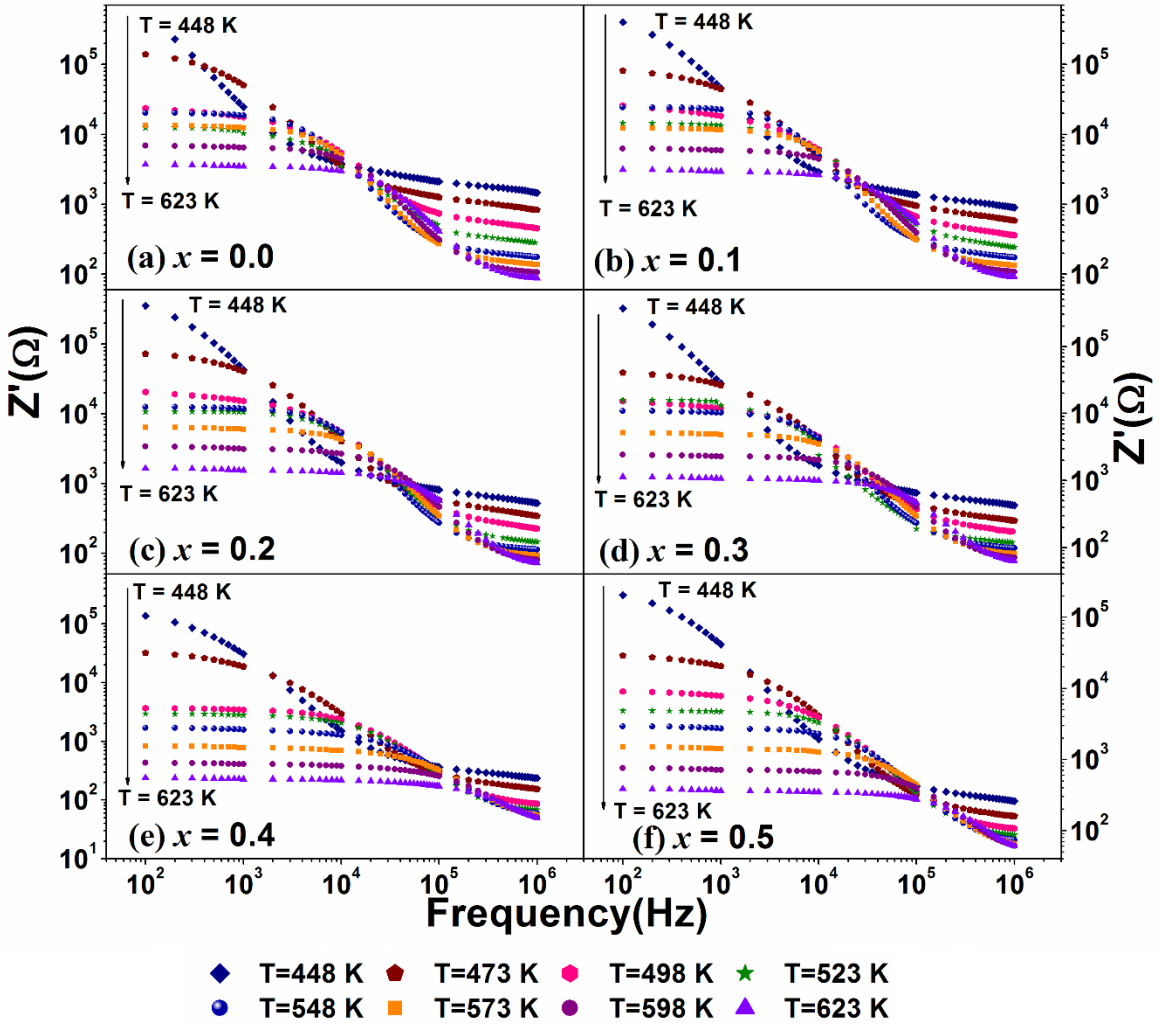

Figure 4.10: Z' versus frequency plots of polycrystalline samples of Y-(Fe, Cr)-O in the temperature range of T = 448 K to 623 K.

The frequency variation of Z' at different temperature (448 K to 623 K) for Y-(Fe, Cr)-O samples are shown in Figure 4.10. The Z' value is found to gradually decrease with increase in frequency upto around 10^4 Hz and it falls quite sharply in the frequency range of 10^4 to 10^5 Hz (for x = 0). Thus, the conduction process increases with increase in frequency and the sharp fall in Z' around 10^4 to 10^5 Hz is attributed to the matching relaxation time of charge carriers (e.g., electrons and holes) across hopping centres (Fe^{2+} and Fe^{3+} ions). The presence of high magnitude of Z' value at low frequency is associated to the space charge carries [142]. The characteristic frequency (frequency at sharp fall) shifts towards the higher frequency regime as the sample temperature is raised. The reduction in the magnitude of Z' with increase in temperature suggests the negative

temperature coefficient of resistance (NTCR). The magnitude of Z' is found to decrease systematically from 10 kΩ for $x = 0$ to 1 kΩ for $x = 0.5$ (at T = 573 K, $f = 100$ Hz) with increase in Cr-concentration highlighting the increase in electrical conductivity.

In order to understand the relaxation process, we have measured -Z" as a function of frequency at different temperatures, i.e., 448 K to 623 K. Typical plots of -Z" versus *f* at different temperatures for Y-(Fe, Cr)-O samples are shown in Figure 4.11. We can see relaxation peaks in the low frequency region ($f < 10^4$ Hz) for the measurements carried out at higher temperature (448 K to 623 K). Generally, at higher temperature, the thermally activated hopping of charge carriers takes place in long-range length and hence the relaxation peaks at lower frequency ($f < 10^4$ Hz) can be attributed to the contribution from grain boundaries (GB). The observed behaviour of -Z" is comparable with that reported by *Siao* et al. in RIGs [136]. The relaxation peaks due to GB are found to shift towards higher frequency with increase in temperature for all the samples and it indicates that the conduction process is thermally activated. With increase in Cr-concentration, the peak value of -Z" is found to be suppressed and such trend is in agreement with decrease in Z' value. In addition to that, the relaxation peak corresponding to a particular temperature systematically shifts towards higher frequency with increase in Cr-concentration except for $x = 0.5$ sample. Thus, even though the grain size is increased with increase in Cr-concentration, the relaxation peak is found to shift towards higher frequency side, i.e., towards lower relaxation time. The decrease in relaxation time in Cr substituted samples could be attributed to the effective reduction in interatomic distance between Fe ions situated at '*a*' and '*d*' sites**.** This argument can be validated with the observed decrease in lattice constant and interatomic distance of Fe ions with the increase in Cr-concentration. However, the anomaly observed for $x = 0.5$ sample can be attributed to the considerable concentration of Fe^{3+}-O^{2-}-Cr^{3+} and Cr^{3+}-O^{2-}-Cr^{3+} networks, affecting the charge carriers hopping. For a given temperature and frequency, the GB contribution of -Z" value is found to drastically decrease with increase in Cr concentration. For example, -Z" (623 K, 10^3 Hz) value decreases from ~10^2 Ω for $x = 0$ to ~10^0 Ω for $x = 0.4$. This can be understood in terms of increase in grain size and hence the decrease in the concentration of GB.

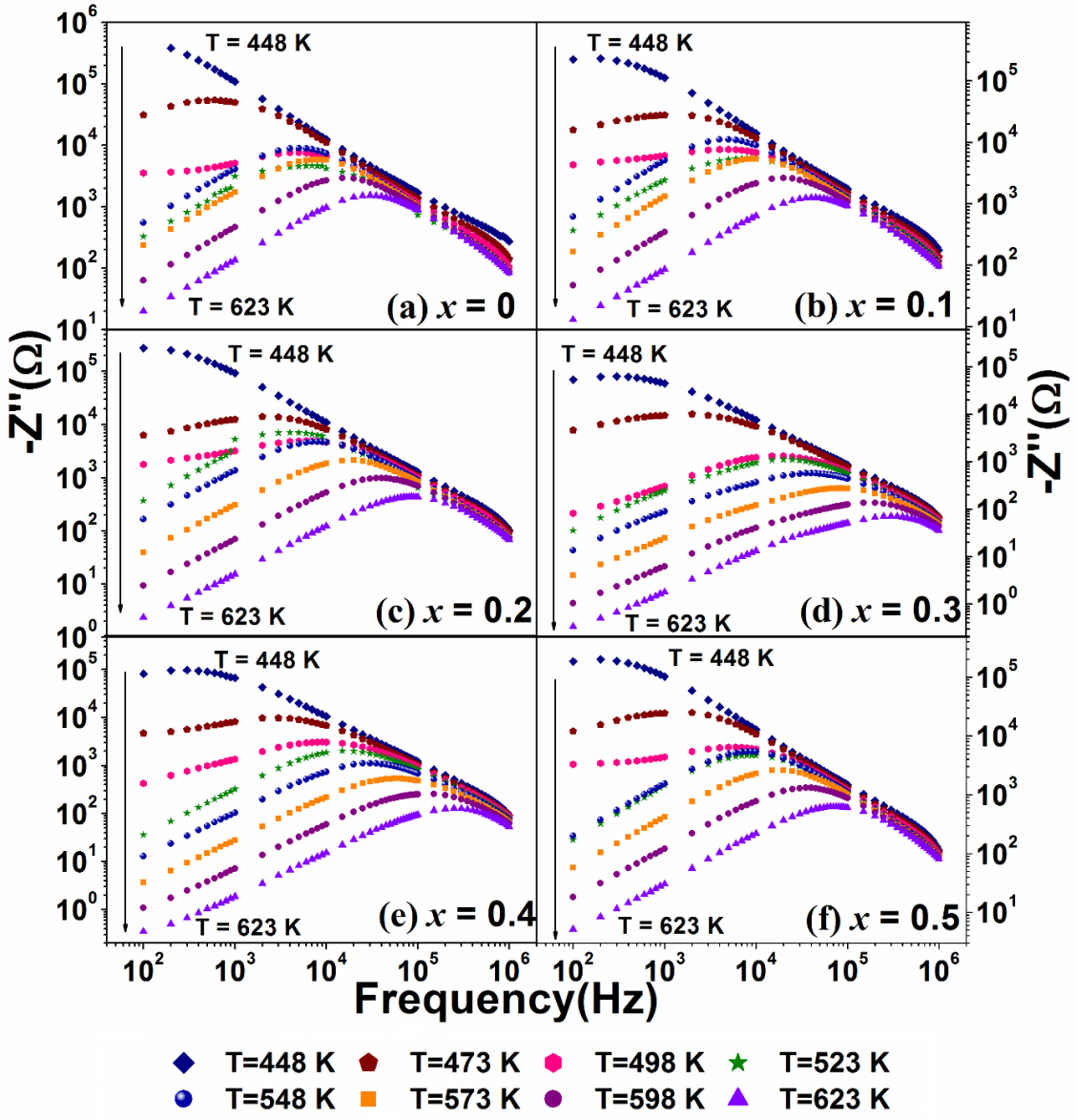

Figure 4.11: -Z" versus frequency plots of polycrystalline samples of Y-(Fe, Cr)-O in the temperature range of T = 448 K to 623 K.

Figure 4.12 shows the typical complex impedance plane plots (-Z" vs Z': Nyquist plots) of Y-(Fe, Cr)-O samples for x = 0, 0.2 and 0.5. We see a semicircular arc followed by a secondary rise in -Z" values in the low temperature region (300 K to 448 K) for x = 0 sample, as shown in Figure 4.12(a). The arc at lower -Z" value is assigned to the relaxation of charge carriers within the grains (G) and the secondary rise in -Z" is due to the contribution from grain boundaries (GB). The lack of complete semicircular arc due to the GB contribution in the low temperature region is mainly due to their relaxation frequency values falling below the measured frequency range. The arc due to G is shifting towards

higher frequency side (lower Z') with increase in the temperature. The G contribution could not be clearly seen for T > 348 K due to the shifting of the arc above the measured frequency range. In the high temperature region (523 K to 623 K) for $x = 0$ sample, the Nyquist plots (Figure 4.12(b)) exhibit clear semicircular arcs due to the contribution from GB. The magnitude of arc is found to increase with increase in temperature in the temperature range of 523 K to 548 K and beyond that, it decreases systematically. Therefore, a positive temperature coefficient of impedance is observed in the narrow temperature range (523 K to 548 K) and with a negative temperature coefficient of impedance outside this region. The observed electrical conduction anomaly in the vicinity of 547 K highlights the possible correlation between the magnetic ordering and electrical charge. Such observation is in accordance with the magnetization measurements, where FIM T_C of $x = 0$ sample is 547 K. Similar trends of shifting of arcs due to G contribution towards higher frequency (lower Z') region and anomaly in the magnitude of semicircular arcs due to GB in the vicinity of FIM T_C are seen for Y-(Fe, Cr)-O samples as shown in Figure 4.12(c-f). The semicircular arcs due to G and GB are found to be asymmetric and depressed, such that their centre lying below the Z' axis. The above trend suggests that the relaxation dynamics deviate from the ideal Debye type. In impedance spectroscopy, the deviation from Debye behaviour can be explained by using a Constant phase element (CPE) denoted by Q with impedance:

$$Z_{CPE} = \frac{1}{A}(j\omega)^{-m} \tag{4.3}$$

where A is a constant and m represents the distribution of relaxation time ($0 \leq m \leq 1$). For an ideal capacitor (resistor) $m = 1$ (0).

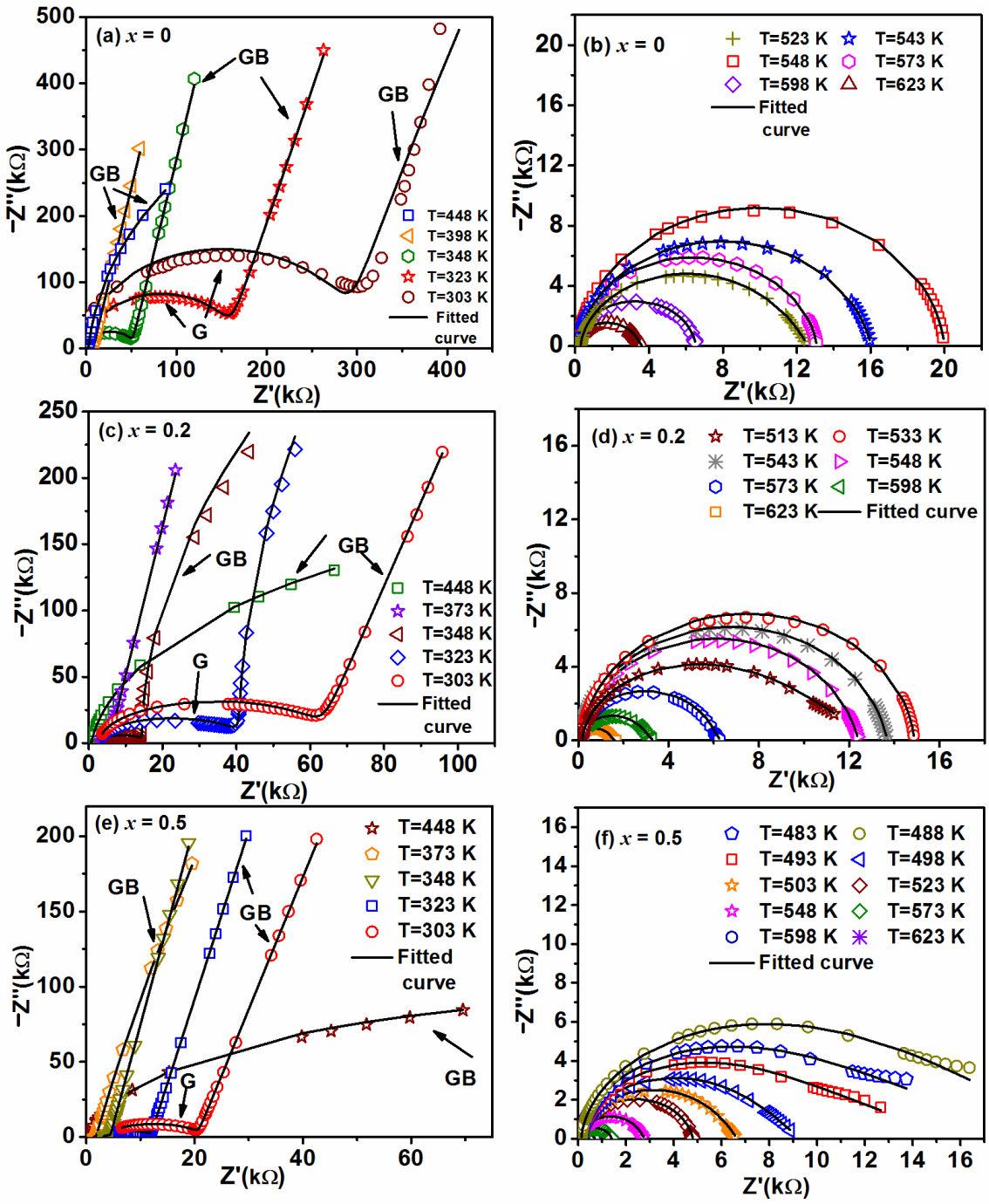

Figure 4.12: Nyquist Plots in the low temperature T ≤ 448 K (a, c and e) and the high temperature T > 448 K (b, d and f) regions of Y-(Fe, Cr)-O samples with x = 0, 0.2 and 0.5.

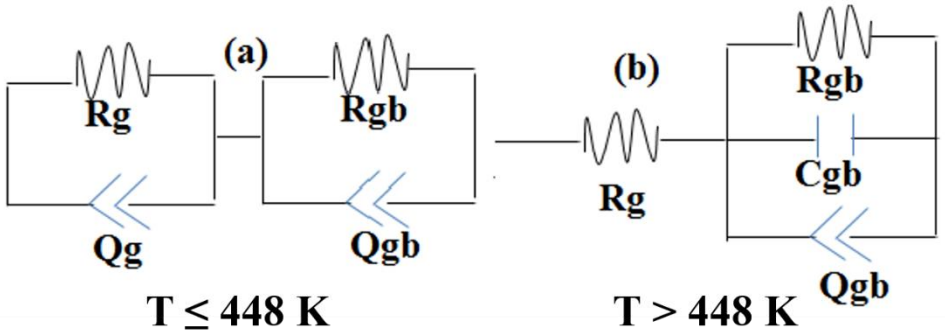

Figure 4.13: The modelled equivalent circuits for (a) T ≤ 448 K and (b) T > 448 K.

The Nyquist plots in the low temperature region (≤ 448 K) were fitted to the equivalent circuit shown in Figure 4.13(a) and the fitted data are shown as solid lines in Figure 4.12 (a, c and e). The fitted data follow the experimental data nicely. Here R_g and R_{gb} represent the grains and grain boundaries resistance respectively. The values of fitted parameter *m* corresponding to contributions of CPE for G (m_g) and GB (m_{gb}) are given in Table 4.3. The Nyquist plots in the high temperature region (T > 448 K) were fitted by choosing the equivalent circuit shown in Figure 4.13(b). Here a pure R_g without a capacitive component is observed as a result of the absence of semicircular arcs due to G. Here C_{gb} corresponds to the capacitance across GB. The fitted values of *m* in the high temperature region are also given in Table 4.3. The m_g and m_{gb} values in the low temperature region lie in the range of 0.75 to 0.98. These values suggest that CPE is mostly of capacitive nature. On the other hand, m_{gb} values in the high temperature region are found to decrease with increase in temperature and falling close to 0.3 at 623 K. It suggests that, at higher temperature the resistive contribution to CPE dominates.

Table 4.3: The estimated values of relaxation time distribution parameter (m_g and m_{gb}) for G and GB as a function of temperature for Y-(Fe, Cr)-O samples.

T(K)	$x = 0$		$x = 0.1$		$x = 0.2$		$x = 0.3$		$x = 0.4$		$x = 0.5$	
	m_g	m_{gb}	m_g	m_{gb}	m_g	m_{gb}	m_g	m_{gb}	m_g	m_{gb}	m_g	m_{gb}
300	0.99	0.85	0.86	0.99	0.90	0.99	0.91	0.96	0.93	0.98	0.92	0.98
373	0.88	0.98	0.91	0.92	0.94	0.92	0.94	0.87	0.95	0.87	0.98	0.95
423	0.79	0.89	0.92	0.94	0.95	0.86	0.95	0.75	0.96	0.88	0.76	0.85
448	0.74	0.95	0.95	0.95	0.95	0.76	0.96	0.64	0.93	0.89	0.87	0.89
498	—	0.89	—	0.98	—	0.58	—	0.59	—	0.79	—	0.76
523	—	0.61	—	0.98	—	0.93	—	0.67	—	0.52	—	0.83
573	—	0.82	—	0.86	—	0.48	—	0.55	—	0.38	—	0.90
623	—	0.41	—	0.34	—	0.27	—	0.32	—	0.40	—	0.41

4.1.4 Complex Dielectric Spectroscopy Studies

Beside impedance spectroscopic analysis, we have analyzed the dielectric properties as well in order to understand the polarization within the Y-(Fe, Cr)-O samples. Therefore, we have obtained the experimental real (ε') and the imaginary (ε") components of complex dielectric constant from the measured impedance data by using the relation [64]:

$$\varepsilon' = \frac{-Z''}{wC_0(Z'^2 + Z''^2)} \tag{4.4}$$

$$\varepsilon'' = \frac{Z'}{wC_0(Z'^2 + Z''^2)} \tag{4.5}$$

The plots of ε' and ε" as a function of frequency for Y-(Fe, Cr)-O samples measured at RT are shown in Figure 4.14(a) and (b). The ε' values of all the samples are found to fall quite sharply with increase in frequency due to the relaxation of electric dipoles but at higher frequency they are found to be flat coinciding with each other close to zero. This indicates that the relaxation process ceases at higher frequency due to the involvement of short-time scale. The corresponding ε" versus frequency plots show relaxation peaks with

f_{max} in the range of 10^3 to 10^4 Hz. The values of ε' and the relaxation peak in ε" are found to increase with increase in Cr-concentration. This trend is mainly due to the increase in the concentration of Fe^{2+}-Fe^{3+} networks and reduction in inter-atomic distance, which considerably reduces the relaxation time.

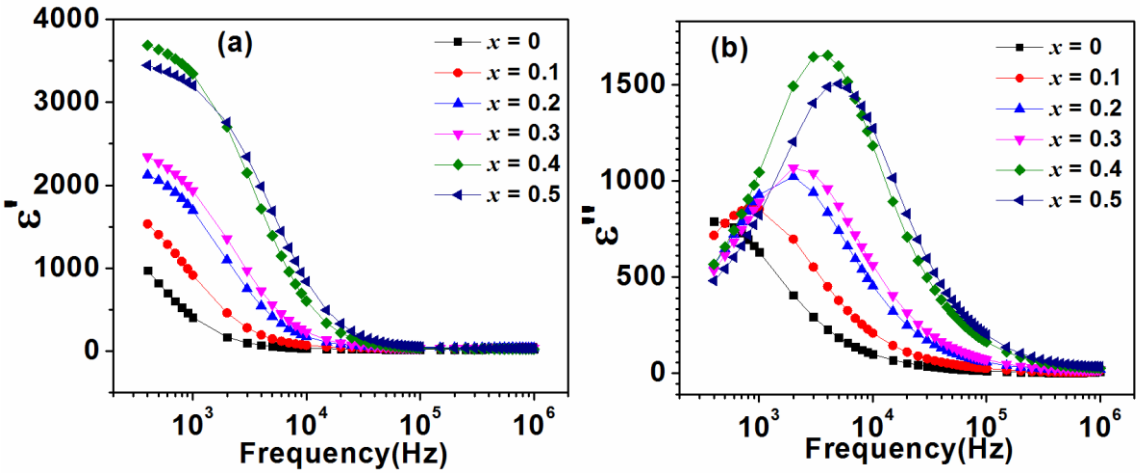

Figure 4.14: Frequency dependence of (a) the real component of dielectric constant (ε') and (b) its imaginary component (ε") at 300 K for different Y-(Fe, Cr)-O samples.

The frequency dependence of ε' and ε" measured at different temperatures (300 K to 498 K) are shown in Figure 4.15(a-f). It is clearly observed that ε' exhibits a plateau like behaviour in the low frequency region followed by sharp drop in ε' value as the frequency is increased and in the corresponding frequency region ε" exhibits a relaxation peak. The relaxation peak is found to shift towards higher frequency side with increase in temperature. At higher temperature, i.e., T ≥ 448 K the plateau is observed only in the intermediate frequency of range 10^3 to 10^5 Hz and on its either side ε' is found to decrease with increase in frequency. The sharp fall in ε' at higher frequency continues to be originated from dielectric relaxation. The observed gradual decrease in ε' in the low frequency region can be attributed to space charge polarization due to blocked charge carriers at physical barriers such as GB. In the corresponding frequency region ε" exhibits a linear behaviour with a slope close to -1 especially for T ≥ 448 K. This suggests that the contribution of conductivity at higher temperature follows the typical power law, known as Universal Dielectric Response (UDR) [73]. Generally, in the high frequency region, orientation or dipolar polarization is activated due to the lag of polarization with respect to the applied electric field.

The relaxation behaviour of dielectric constant can be studied by using modified Havriliak–Negami (HN) equation (4.6 and 4.7), where the electrical conductivity contribution is also added [67,68].

$$\varepsilon' = \varepsilon_\infty + \frac{\Delta\varepsilon \cos(\beta\phi)}{\{1 + 2(\omega\tau)^{1-\alpha} sin(\alpha\pi/2) + (\omega\tau)^{2-2\alpha}\}^{\beta/2}} + \frac{\sigma_2}{\varepsilon_0\omega^s} \quad (4.6)$$

$$\varepsilon'' = \frac{\Delta\varepsilon \sin(\beta\phi)}{\{1 + 2(\omega\tau)^{1-\alpha} sin(\alpha\pi/2) + (\omega\tau)^{2-2\alpha}\}^{\beta/2}} + \frac{\sigma_1}{\varepsilon_0\omega^s} \quad (4.7)$$

$$\text{where } \phi = tan\left(\frac{(\omega\tau)^{1-\alpha} cos(\alpha\pi/2)}{1+(\omega\tau)^{1-\alpha}\sin(\alpha\pi/2)}\right) \text{ and } \Delta\varepsilon = \varepsilon_s - \varepsilon_\infty \quad (4.8)$$

Here ε_s and ε_∞ represent the dielectric constant in static (low frequency) and high frequency region, respectively. τ and ω correspond to the relaxation time and the measured angular frequency, respectively. The exponents α and β signify the broadness and asymmetry of dielectric spectra. The fitted parameters such as ε_∞, $\Delta\varepsilon$ and α at 300 K and 473 K are given in Table 4.4. The experimental values of ε_∞ from the above analysis are found to increase from 20 for x = 0 to 52 for x = 0.5 due to the possible increase in Fe^{2+} concentration. The value of α at 300 K is found to increase from 0.03 to 0.25 with Cr-concentration. Thus for x = 0 sample at 300 K, the dielectric relaxation is close to ideal Debye like behaviour and such behaviour is similar to one reported in YIG [136]. The relatively large value of α in Cr-substituted samples can be ascribed to the structural distortion. At 473 K, the obtained value of α is found to increase from 0.16 to 0.34 for x = 0 to 0.5 sample. No conductivity contribution is seen at 300 K and the value of s at 473 K is found to be in the range of 0.87 to 0.91 for x = 0 to 0.5. The space-charge contribution of conductivity is found to decrease systematically from 0.51×10^{-6} S/m for x = 0 to 0.04×10^{-6} S/m for x = 0.5 at T = 473 K. This can be attributed to increase in average grain size and hence reduction in GB concentration with Cr-substitution.

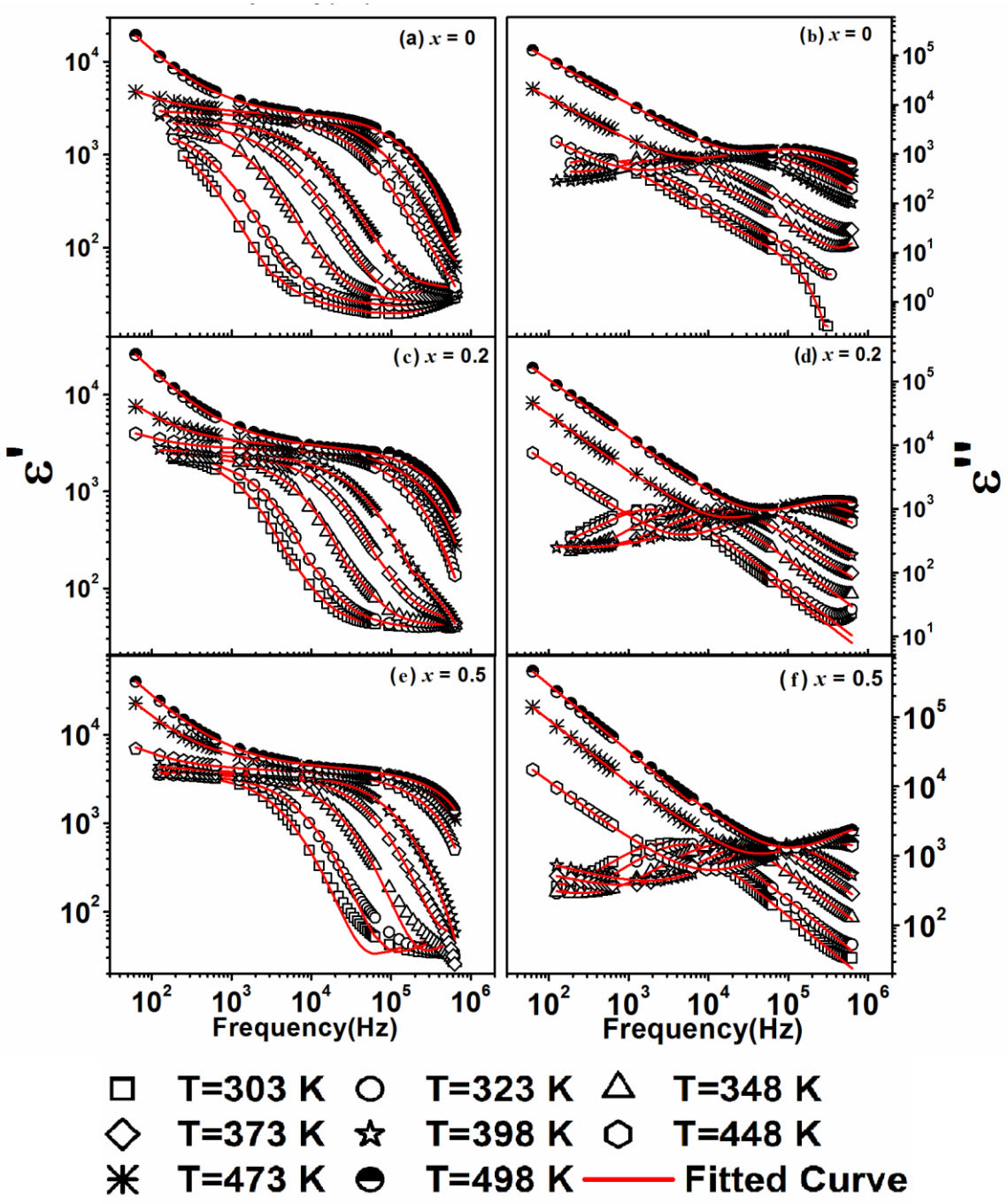

Figure 4.15: The frequency variations of ε' and ε'' in logarithmic scale for (a, b) x = 0, (c, d) x = 0.2 and (e, f) x = 0.5 samples of Y-(Fe, Cr)-O at different temperatures. The solid lines represent the fit of experimental data to the equations (4.6) and (4.7).

Table 4.4: Parameters obtained from the analysis of ε' and ε" data using modified HN equations (4.6) and (4.7) for Y-(Fe, Cr)-O samples with x = 0 to 0.5.

x	$\Delta\varepsilon$ (10^3)		α		s	
	300 K	**473 K**	**300 K**	**473 K**	**300 K**	**473 K**
0	2.34	2.79	0.03	0.16	—	0.87
0.1	3.07	3.81	0.05	0.10	—	0.88
0.2	3.15	4.18	0.17	0.19	—	0.89
0.3	3.47	4.63	0.18	0.20	—	0.89
0.4	5.34	6.41	0.23	0.33	—	0.88
0.5	5.69	7.01	0.25	0.34	—	0.91

4.1.5 AC Conductivity Studies

The ac conductivity data in the high temperature region are plotted as a function of frequency as shown in Figure 4.16(a-f) for Y-(Fe, Cr)-O samples. The values of ac conductivity were estimated using the relation:

$$\sigma_{ac}(\omega) = 2\pi f \varepsilon'' \varepsilon_0 \qquad (4.9)$$

The increase in σ_{ac} value with increase in Cr-concentration at a given temperature can be attributed to the possible increase in oxygen vacancies, which increases the number of Fe^{2+} ions at octahedral site. The observed increase in ac conductivity with rise in temperature can be attributed to the thermally active hopping of charge carriers across Fe ions. The characteristic behaviour of σ_{ac} with frequency at different temperature can be explained in terms of Jonscher power law (JPL) [73].

$$\sigma_{ac}(\omega) = \sigma_{dc} + A\omega^n \qquad (4.10)$$

where σ_{dc} is dc conductivity which is related to the plateau region or frequency independent region and $A\omega^n$ is frequency dependent term which characterizes dispersion phenomenon. The exponent n defines the nature of motion of charge carriers. The experimental σ_{ac} data were fitted to JPL equation by taking σ_{dc}, A and n as free parameters. They fitted data closely follow the experimental data. The temperature variation of exponent n for all Y-(Fe, Cr)-O samples are shown in Figure 4.17. The value of n is found to increase with

increase in temperature for all the Y-(Fe, Cr)-O samples and it lies in the range of $1 < n < 2$ which indicates that the conduction process is governed by localized small polaron hopping model [147,148].

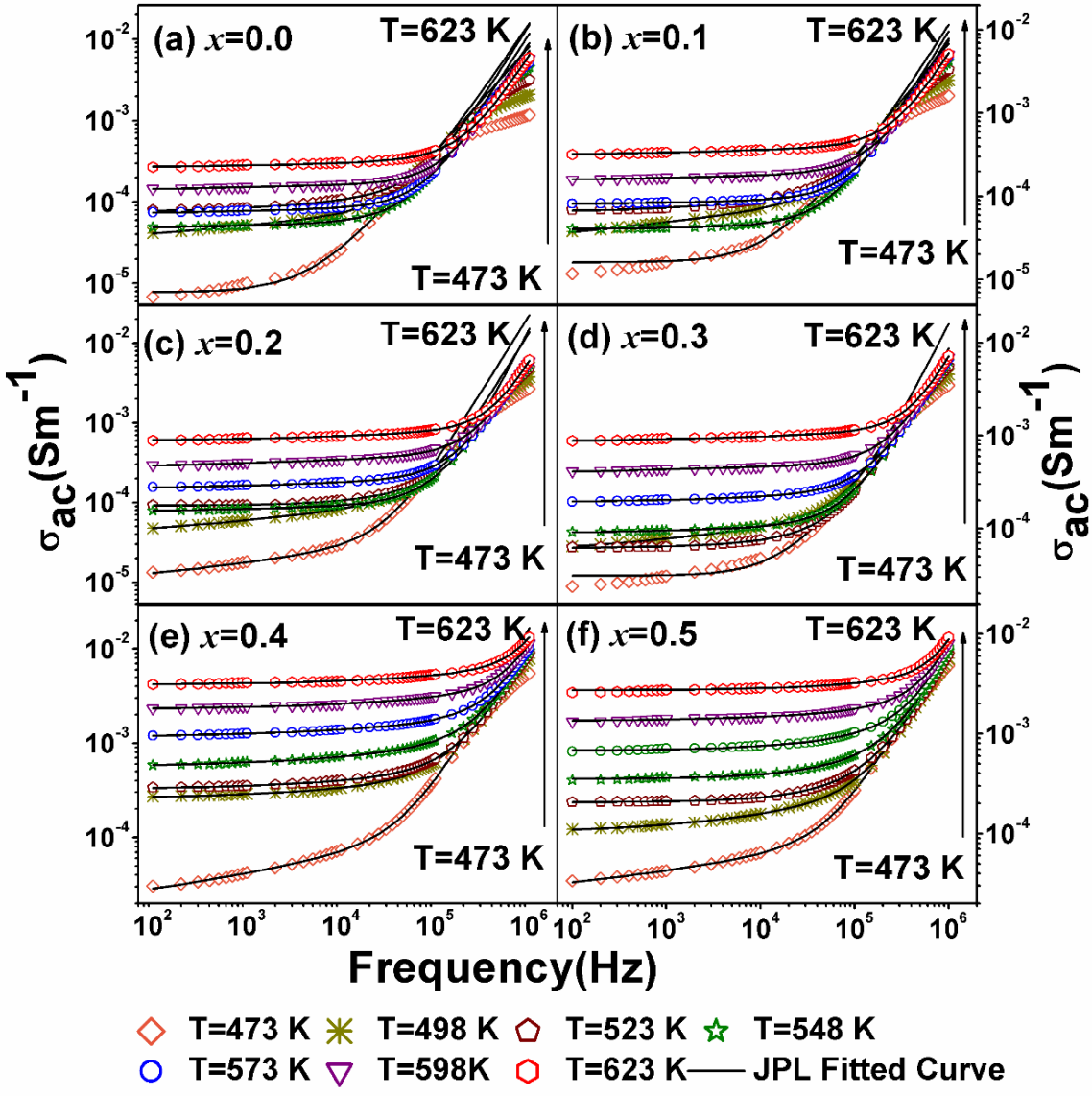

Figure 4.16: (a-f) Frequency variations of ac conductivity in logarithmic scale along with fitted data (solid line) using JPL model for x = 0 to 0.5 samples over a temperature range of 473 K-623 K.

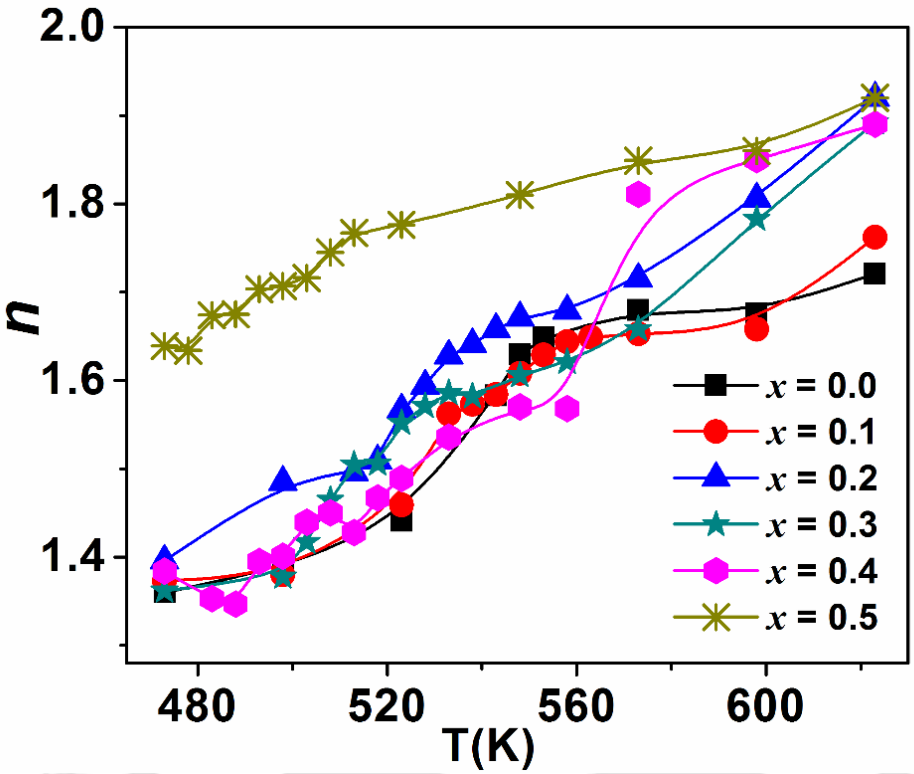

Figure 4.17: Temperature variations of frequency exponent (*n*) for Y-(Fe, Cr)-O samples.

4.1.6 Relaxation time, Grains and Grain Boundaries Conductivity

The relaxation time and conductivity contribution of grains and grain boundaries obtained from the impedance spectroscopy at different temperature are analyzed based on Arrhenius relation.

The thermal activation process of relaxation time (τ) as per the Arrhenius law is,

$$\tau(T) = \tau_0 \exp\left(\frac{E_a}{k_B T}\right) \tag{4.11}$$

Here τ_0 is a constant and E_a is the activation energy of relaxation. Figure 4.18(a) shows the plots of lnτ versus 10^3/T for the data collected in the temperature range of 423 K to 623 K for all the samples, i.e., by considering only the relaxation due to GB. They all exhibit a linear behaviour with an anomalous behaviour, i.e., change of slope in the vicinity of FIM T_C. The values of activation energy E_a estimated from the linear fit of lnτ versus 10^3/T plots are 0.75 eV and 1.05 eV for T > 550 K and T < 550 K respectively for x = 0. Similar trend of change in E_a value is observed in Cr-substituted samples across T_C. The change in the value of E_a across T_C suggests the coupling between electric polarization and the magnetic polarization for T < T_C. Such type of anomaly in the vicinity of T_C with the change in E_a values is reported in YIG, Mn doped $YFeO_3$, etc. [136,146]. Moreover, the observed higher

value of E_a for T < T_C (FIM) suggests that the ordered magnetic ions inhibit the relaxation process. The E_a values for T < T_C are found to be in the range of 1.05 ± 0.40 eV to 1.30 ± 0.38 eV and they can be attributed to the second ionization of oxygen vacancies ($V_0^{\bullet\bullet}$) [150]. On the other hand, the smaller values of E_a in the range of 0.75 ± 0.03 eV to 0.84 ± 0.04 eV for T > T_C (PM) can be attributed to the single ionization of oxygen vacancies ($V_0^{\bullet}$) across grain boundaries.

Here, neutral oxygen vacancy V_o in YIG is created due to sintering at high temperature. The neutral oxygen vacancy in Fe^{2+} – □ – Fe^{3+} networks can be converted to a singly ionized positive charge, $V_0^{\bullet}$ by releasing an electron as per the relation $V_0 = V_0^{\bullet} + e'$. Further releasing of an electron leads to second ionization of oxygen vacancy $V_0^{\bullet\bullet}$ as per the relation $V_0^{\bullet} = V_0^{\bullet\bullet} + e'$. The electrons may hop between Fe^{2+} and Fe^{3+} ions leading to their exchange of valency as per the relation $Fe^{2+} \rightarrow Fe^{3+} + e'$ [150].

In order to understand the contribution of grains and grain boundaries towards conduction mechanism, we have estimated their conductivity (σ_g and σ_{gb}) using their respective resistance values obtained from the analysis of Nyquist plots and using the relation $\sigma = \frac{t}{SR}$, where t is the thickness of the sample, S is area of the sample and R is the resistance. They are found to increase with increase in Cr-concentration due to the possible increase in oxygen vacancies and hence the increase in Fe^{2+} concentration. The above process enhances the hopping of electrons across Fe^{2+}–Fe^{3+} networks. The σ_g and σ_{gb} values can be studied using the Arrhenius relation. Here, E_c is the activation energy of conduction. The plots of lnσ_g and lnσ_{gb} versus 10^3/T for all the Y-(Fe, Cr)-O samples are shown in Figure 4.18(b) and (c) respectively for T > 448 K. They all follow a linear behaviour with an anomaly in the vicinity of FIM T_C. They were fitted to Arrhenius relation separately in the FIM (T < T_C) and PM (T > T_C) regions. The fitted data are shown as solid lines in Figure 4.18 (b) and (c). The estimated values of activation energy corresponding to G (E_{cg}) for FIM region are found in the range of 0.41 ± 0.02 eV for x = 0 to 0.45 ± 0.02 eV for x = 0.5, while in the PM region these values are found to be in the range of 0.27 ± 0.01 eV for x = 0 to 0.31 ± 0.02 eV for x = 0.5. These values are comparable to the activation energy attributed to the hopping of charge carriers between Fe^{2+} and Fe^{3+} ions [149]. Hence, the electrical conduction in grains is mainly attributed to the hopping of charge carriers (electrons) between Fe^{2+} and Fe^{3+} ions. On the other hand, the estimated values of the activation energy corresponding to GB (E_{cgb}) are found to be in the range of 1.07 ± 0.12 eV for x = 0 to 1.33 ± 0.11 eV for x = 0.5 for T < T_c and 0.73 ± 0.04 eV for x = 0 to 0.81 ± 0.03

eV for x = 0.5 in the PM region. The values of E_{cgb} are comparable to the E_a, i.e., activation energy estimated from the analysis of thermally activated relaxation process (Figure 4.18(a)) of -Z" peaks. They suggest that the electrical conduction in GB is mainly due to the singly and doubly ionized oxygen vacancies above and below the FIM T_C respectively.

The temperature dependence of estimated σ_{dc} values are shown in Figure 4.18(d) in the form of lnσ_{dc} versus 10^3/T plots. They exhibit linear behaviour with a change of slope in the vicinity of FIM T_C. Here E_{cdc} is the activation energy for the conduction process. The estimated values of E_{cdc} lie in range of 0.72 ± 0.04 eV to 0.86 ± 0.05 eV, which is nearly similar to the value of E_{cgb} for the PM region and it is attributed to the singly ionized oxygen vacancies. On the other hand, the values of E_{cdc} in the FIM region lies in range of 1.15 ± 0.12eV to 1.33 ± 0.11eV, which is similar to the value of E_{cgb} for the FIM region and it is attributed to the doubly ionized oxygen vacancies.

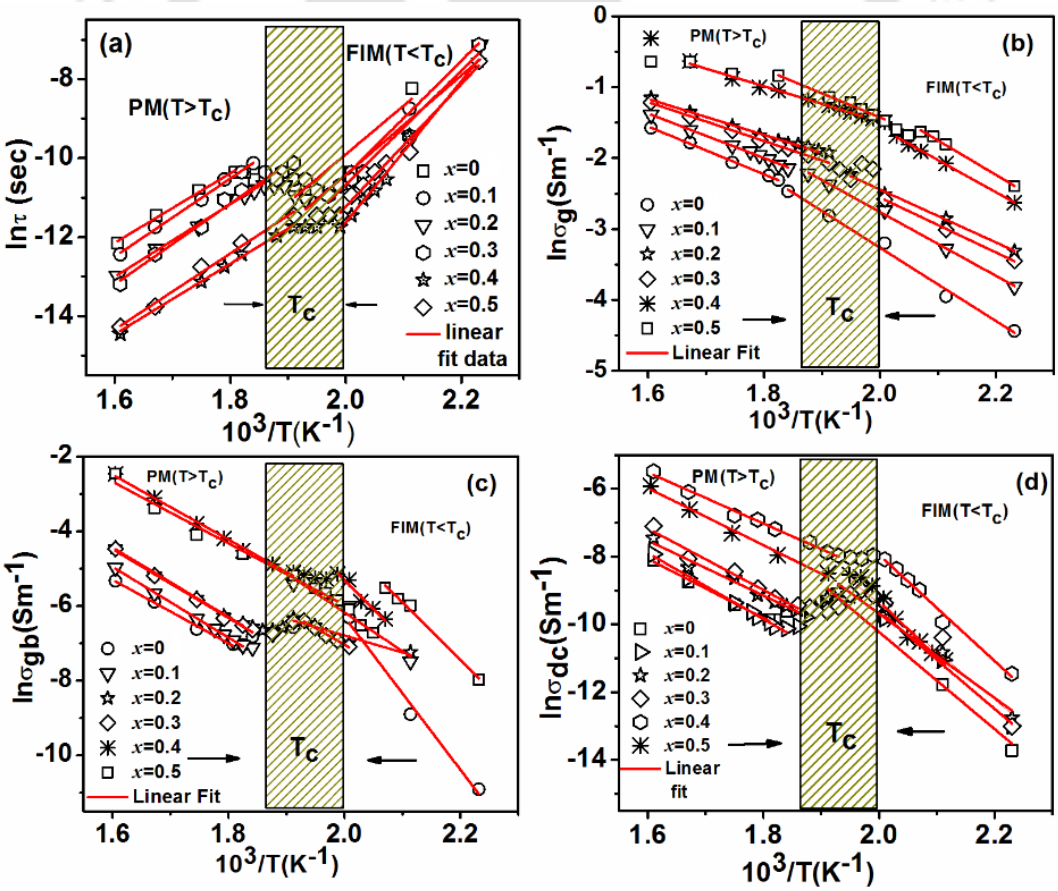

Figure 4.18: Arrhenius plots along with fitted data (solid lines) of (a) relaxation time, (b) grains conductivity, (c) grain boundaries conductivity and (d) dc conductivity of Y-(Fe, Cr)-O samples for T > 448 K.

4.2 Mn-Substituted $Y_3Fe_5O_{12}$

In this section, we have described the preparation of Mn-substituted YIG ($Y_3Fe_{5-x}Mn_xO_{12}$: Y-(Fe, Mn)-O) for x = 0, 0.1 and 0.2 and studied their structural, magnetic and dielectric properties. Mn-substitution reduces the FIM T_C and dielectric constant without varying the saturation magnetization.

Polycrystalline samples of $Y_3Fe_{5-x}Mn_xO_{12}$ (Y-(Fe, Mn)-O with x = 0, 0.1 and 0.2) were prepared by the standard sol-gel route method. The samples were prepared by using Y_2O_3, $Mn(NO_3)_2.4H_2O$ and $Fe(NO_3)_3.6H_2O$ as starting materials as per the stoichiometric ratio with purity better than 99%. Uniform mixture of Fe and Mn nitrates were dissolved in distilled water, and Y_2O_3 was dissolved in small amount of nitric acid. Citric acid and ethylene glycol were added to the above mixture and it was heated at 473 K to get a fine powder. The powder was presintered at 873 K for 12 hours. The presintered powder was finally sintered in the form of cylindrical pellets at 1573 K for 12 hours with an intermediate grinding.

4.2.1 Structural Studies

Figure 4.19 shows the observed XRD patterns (open circle) along with Rietveld refined data (black solid line) of Y-(Fe, Mn)-O samples. These samples are found to be in single-phase form and crystallize in cubic unit cell with space group $Ia\bar{3}d$. The obtained values of various parameter from Rietveld refinement analysis using Fullprof software are given in Table 4.5. The decrease in lattice constant (a) with increase in Mn-concentration can be attributed to some of the substituted Mn ions taking the Mn^{4+} (0.530 Å) state having the ionic radius smaller than that of host Fe^{3+} (0.645 Å) ions as reported in reference [156]. However, our result differs from that of *Jiaqian* et al. [108], who have observed no change in lattice constant.

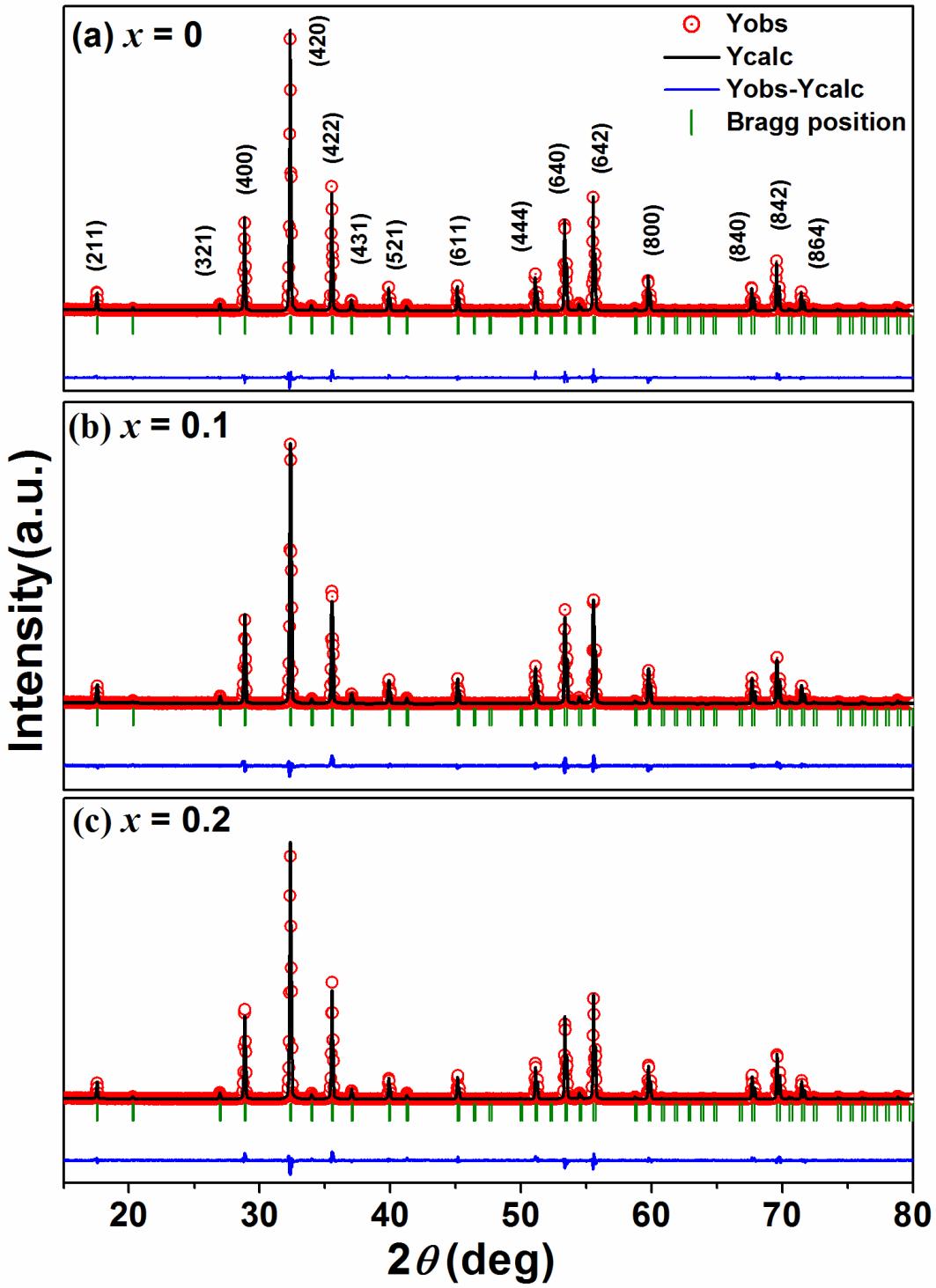

Figure 4.19: XRD patterns (open red circle) along with Rietveld refined data (black solid line) for Y-(Fe, Mn)-O samples with (a) $x = 0$ and (b) $x = 0.2$.

Table 4.5: Various structural and reliability parameters along with cationic occupancy obtained from the Rietveld refinement of XRD patterns of Y-(Fe, Mn)-O samples with x = 0 to 0.2.

x		**0**	**0.1**	**0.2**
Space group		$Ia\bar{3}d$	$Ia\bar{3}d$	$Ia\bar{3}d$
$a = b = c$ **(Å)**		12.3727(3)	12.3709(3)	12.3674(4)
V **(Å^3)**		1894.1	1893.3	1891.6
R_p **(%)**		9.31	9.82	9.86
R_{exp} **(%)**		6.67	7.75	7.77
R_f **(%)**		6.78	6.20	6.88
R_{Bragg} **(%)**		4.16	4.53	4.45
χ^2		3.21	3.54	3.31
Occupancy	Y	2.98	2.98	2.97
	Fe	4.98	4.87	4.78
	Mn	0	0.08	0.17

Figure 4.20 shows the FESEM micrographs for x = 0 and 0.2 samples. The average grain size value for x = 0 is found to be 7.77 μm, which is reduced to 6.52 μm, 3.54 μm for x = 0.1 and 0.2 samples, respectively with an error of ±0.20 μm. The grain size depends on the mobility of grain boundaries and the grain boundaries mobility is controlled by defects and oxygen vacancies [138]. There is a possibility of some of doped Mn ions oxidizing to Mn^{4+} state, which in turn reduces the oxygen vacancies. Such reduction in oxygen vacancies is expected to hinder the movement of host ions across the grain boundaries thereby affecting the grain growth. One cannot rule out the possibility of increase in melting temperature of the solid due to the Mn-substitution and such effect may cause decrease in

grain growth. The density of the samples is found to increase with Mn-substitution, i.e., 4.95 g/cm^3, 5.01 g/cm^3 and 5.08 g/cm^3 for x = 0, 0.1 and 0.2 respectively.

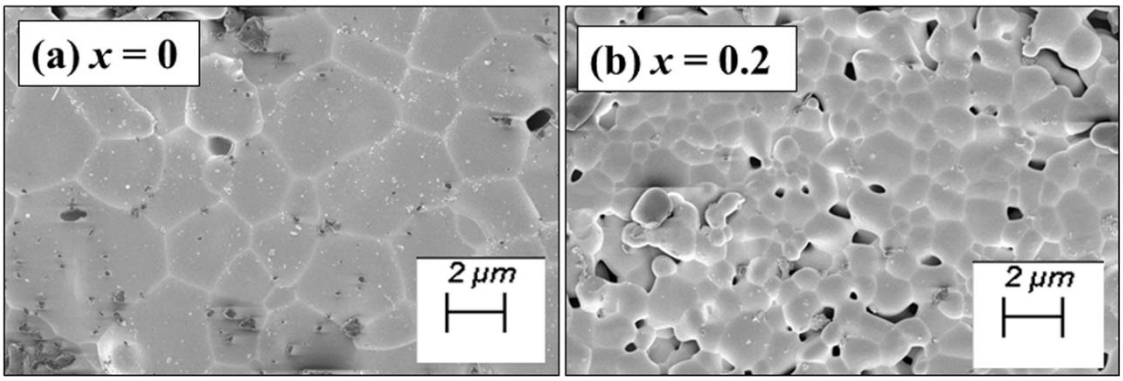

Figure 4.20: FESEM micrographs of Y-(Fe, Mn)-O samples for (a) x = 0 and (b) x = 0.2.

4.2.2 Magnetic Studies

Figure 4.21(a) shows the magnetic hysteresis loops (*M-H*) recorded at 300 K for Mn-substituted YIG samples and they are all found to saturate at 1 kOe. The saturation magnetization (M_S) value is found to be 25.5, 25.9 and 25.3 emu/g for x = 0, 0.1 and 0.2 sample respectively. No appreciable variation in M_S is observed with Mn-substitution. The net magnetic moment in YIG is due to the ferrimagnetic interaction between two Fe^{3+} ions in octahedral ($2Fe^{3+}$) site and three of them in tetrahedral ($3Fe^{3+}$) site per formula unit [25]. So, the observed magnetization in Y-(Fe, Mn)-O can be attributed to the partial substitution of Mn ions at both tetrahedral and octahedral site especially for low Mn-concentration.

Figure 4.21(b) shows the temperature variation of normalized magnetization (*M-T*) plots for Mn-substituted YIG samples for an applied magnetic field of 200 Oe. All samples exhibit FIM transition. The FIM T_C is determined from the first order derivative of magnetization with respect to temperature (*dM/dT* versus T) plot and it is found to decrease with increase in Mn-concentration, i.e., T_C = 550 K, 548 K and 539 K for x = 0, 0.1 and 0.2, respectively. Such reduction in T_C value can be understood in terms of weakening of superexchange interaction in $Fe^{3+}(a)$-O^{2-}-$Fe^{3+}(d)$ networks due to Mn-substitution.

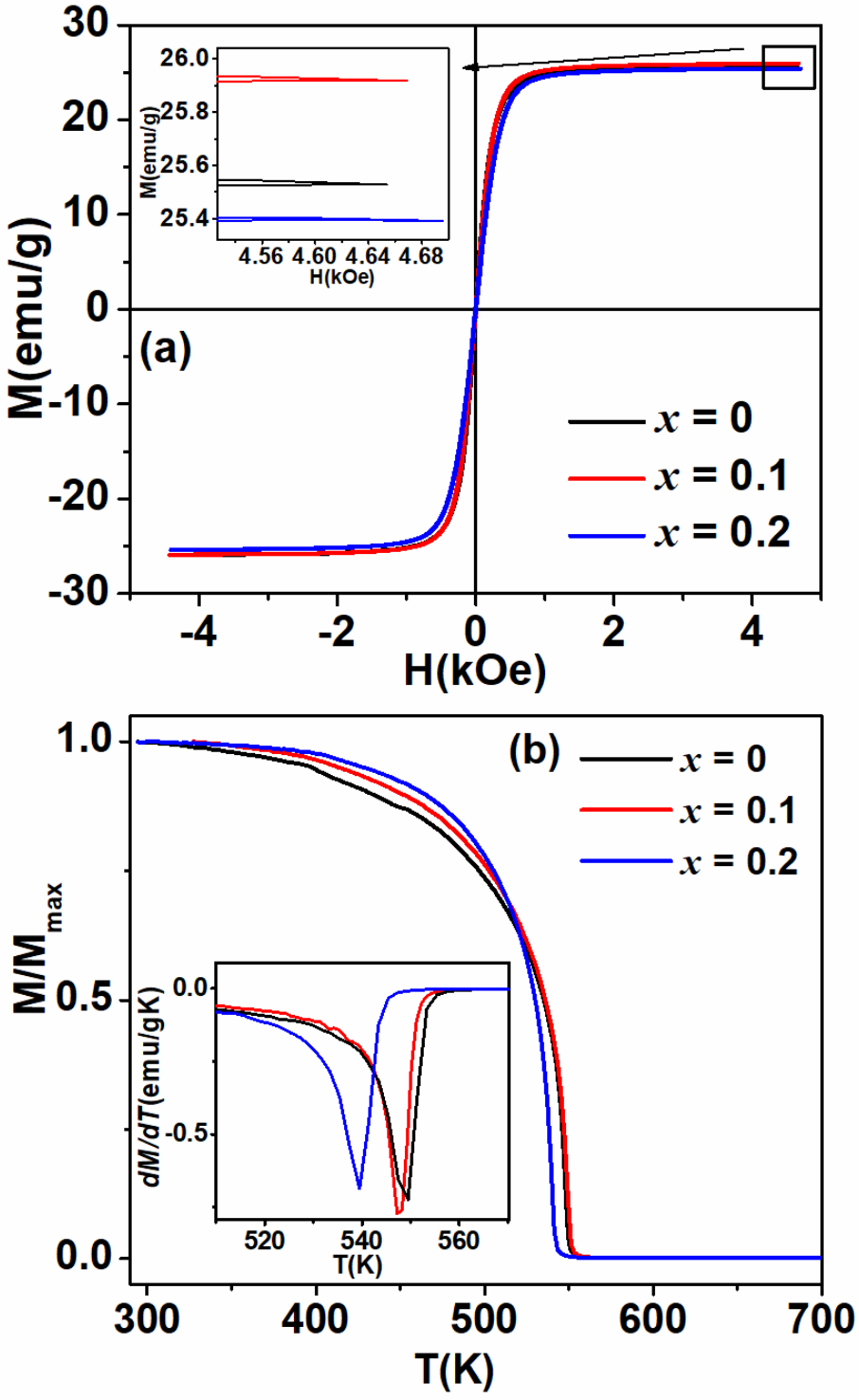

Figure 4.21: (a) Room temperature *M-H* loops and (b) Temperature variation of magnetization of Y-(Fe, Mn)-O samples for an applied field of 200 Oe. Insets show enlarged view of *M-H* plot close to saturation and temperature variation of magnetization derivative, respectively.

4.2.3 Complex Impedance Spectroscopy Studies

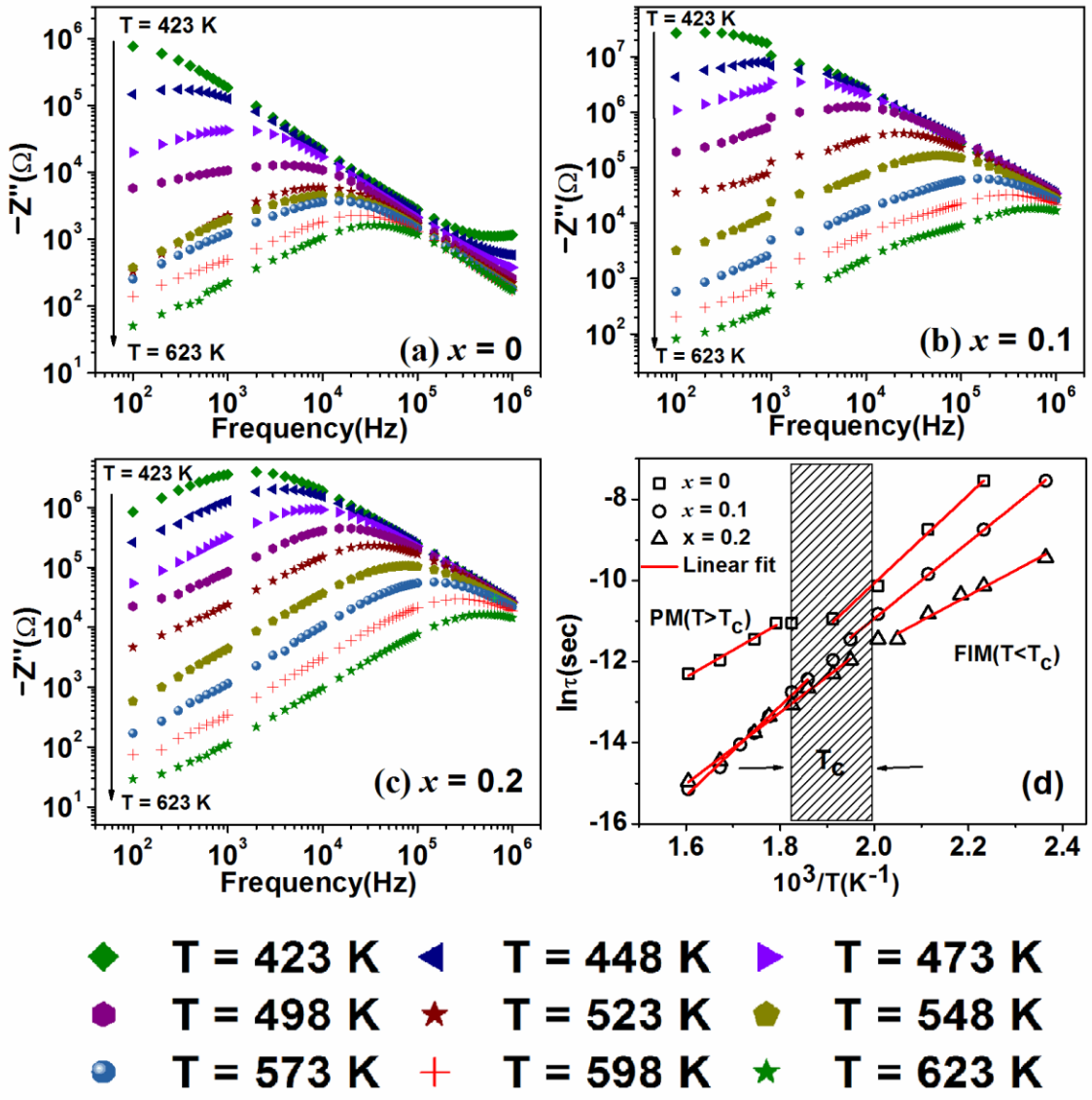

Figure 4.22: Frequency dependence of imaginary component (-Z") of impedance at different temperatures (423 K - 623 K) for (a) $x = 0$, (b) $x = 0.1$ and (c) $x = 0.2$ samples. (d) Relaxation time (τ) as a function of inverse of temperature (10^3/T) along with fit to Arrhenius law.

Figure 4.22 shows the frequency (f) variation of imaginary part (-Z") of impedance in logarithmic scale at different temperatures for Y-(Fe, Mn)-O samples. They all exhibit peak at a characteristic frequency (f_{max}) suggesting the relaxation of the charge carriers (electrons and holes) towards the applied ac electric field. Generally, at higher temperature, the thermally activated charge carriers undergo long-range hopping and it gives rise to large relaxation time and hence relaxation peak occurring at lower frequency ($f < 10^5$ Hz). Thus,

the relaxation peak observed in the low frequency region ($f < 10^5$ Hz) is attributed to the relaxation across grain boundaries (GB). These peaks are found to be quite broad and asymmetric suggesting the deviation of relaxation dynamics from the ideal Debye law. With increase in temperature, the relaxation peak is found to shift towards higher frequency values, which indicates that the relaxation is due to thermally activated charge carriers.

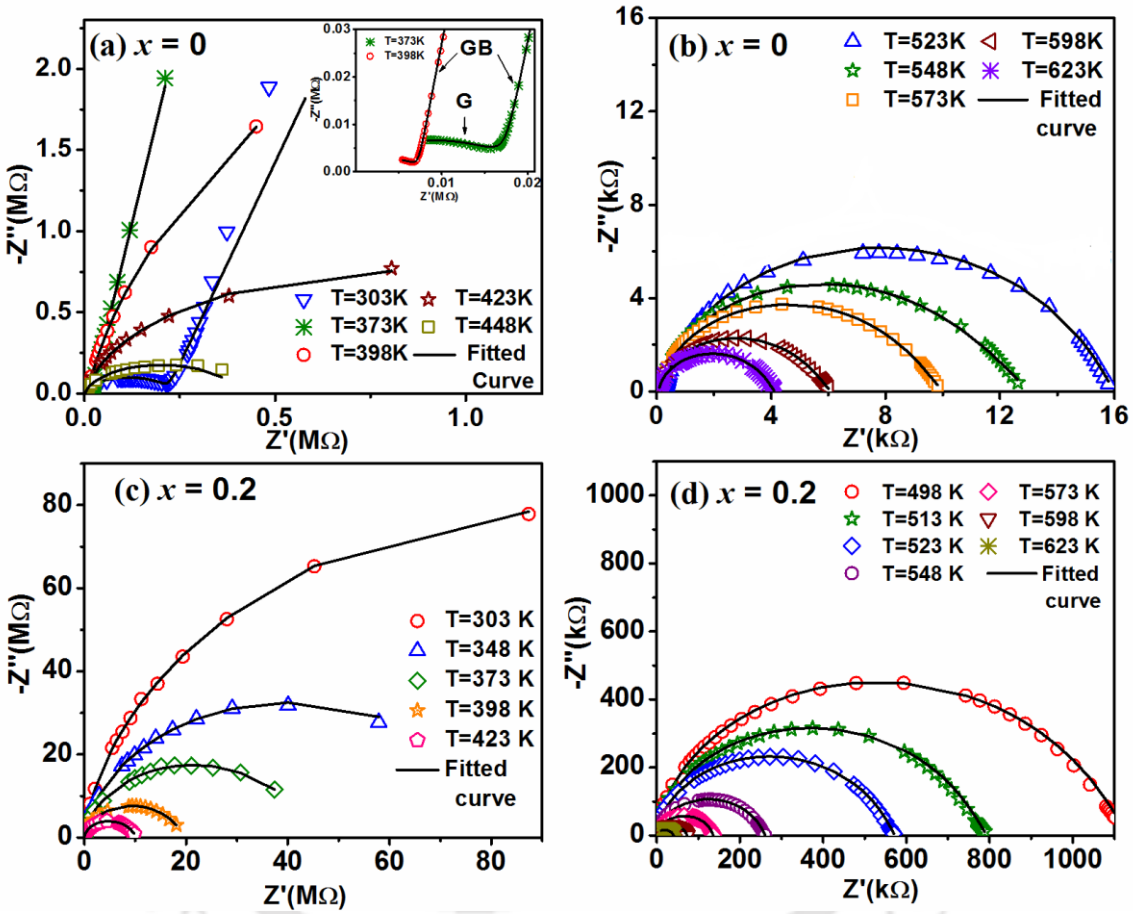

Figure 4.23: Nyquist Plots in the low temperature T ≤ 448 K (a and c) and the high temperature T > 448 K (b and d) regions for Y-(Fe, Mn)-O samples with x = 0 and 0.2.

Figure 4.23 shows the Nyquist (Z*) plots of complex impedance. Here -Z'' is plotted as a function of Z' at different temperature. For x = 0 sample, the plots are grouped into two different temperature regions namely, low temperature region (T1 = 300 K to 448 K) and high temperature region (T2 = 523 K to 623 K) and they are shown in Figure 4.23(a) and (b) respectively. In the T1 region, we see a small semicircular arc followed by a secondary rise in -Z'' as Z' increased especially for T = 300 K. As the temperature is raised, the semicircular arc seen at lower Z' is shifted towards lower Z' values, and the secondary rise to -Z'' data slowly bend towards Z' axis forming a semicircular arc at higher Z' value. The semicircular arc observed in the lower Z' corresponds to higher frequency (lower relaxation

time) and it is attributed to relaxation within grains (G). The secondary rise in -Z'' is attributed to GB contribution and its semicircular arc could not be seen due to the limitation of measured frequency range in the low temperature region [145]. The peak position is found to shift towards higher frequency (lower Z') as the temperature is increased. The G contribution could not be seen clearly for T > 398 K due to the shifting of arc above the measured frequency range, which is shown in inset of Figure 4.23(a). The Nyquist plots in the T2 region are shown in Figure 4.23(b) where clear semicircular arc due to the GB is observed, since long-range hopping across GB occurs due to thermally activated charge carriers at higher temperature. The magnitude of arc is found to decrease systematically with rise in temperature. However, for x = 0.1 and 0.2, the Nyquist plots are mainly associated to the GB over the entire measured temperature range due to low relaxation time of G which is out of the measured frequency range as well as temperature as shown in Figure 4.23(c) and (d). The radius of these semicircular arcs for Y-(Fe, Mn)-O samples are found to decrease with increase in temperature and it suggests that these samples exhibit negative temperature coefficient of impedance. Moreover, for a given measured frequency, the magnitudes of Z' and -Z'' are found to be quite large compared to the parent compound. The observed semicircles in the impedance plane plots are found to be asymmetric and depressed in nature with their center lying below the Z' axis and it suggests the departure of relaxation dynamics from the ideal Debye behaviour. It can be explained using a Constant Phase Element (CPE) denoted as Q. The Nyquist plots for x = 0 sample were fitted to equivalent circuits shown in Figure 4.24(a) and (b) for T ≤ 448 K and T > 448 K respectively. For T ≤ 448 K the resistances due to G and GB (R_g, R_{gb}) contribution and constant phase element due to G and GB (Q_g, Q_{gb}) contribute to the measured impedance. For T > 448 K, an additional component C_{gb}, i.e., capacitance across grain boundaries also contributes to the relaxation process. For x = 0.1 and 0.2 samples, Nyquist plots are explained by considering the parallel combination of resistance, capacitance and Q due to GB (R_{gb}, C_{gb}, Q_{gb}) (Figure 4.23(b, c))**.** The experimental data (symbols) were fitted to the equivalent circuits (Figure 4.24) and they are shown as solid line.

From the estimated resistance values due to G and GB contribution, their respective conductivity values (σ_g and σ_{gb}) were determined using the standard relation $\sigma = \frac{t}{RS}$ (S = surface area, t = thickness). The estimated values of σ_g and σ_{gb} are given in Table 4.6, and they are found to decrease with increase in Mn concentration due to the possible disruption of hopping of charge carriers across Fe^{2+}-Fe^{3+} networks due to the substitution of Mn at

random Fe site. Moreover, the conductivity value is found to increase with increase in temperature due to thermally activated charge carriers.

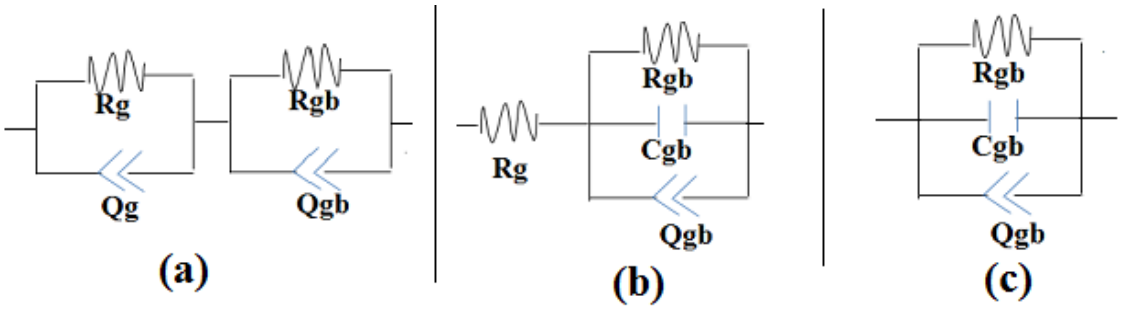

Figure 4.24: Equivalent circuits for x = 0 sample for (a) T ≤ 448 K and (b) T > 448 K. (c) Equivalent circuit for x = 0.1 and 0.2 samples.

Table 4.6: The estimated values of σ_g and σ_{gb} at different temperature for Y-(Fe, Mn)-O samples.

T(K)	x = 0		x = 0.1	x = 0.2
	σ_g (S/m)	σ_{gb} (S/m)	σ_{gb} (S/m)	σ_{gb} (S/m)
423	0.90×10^{-3}	1.12×10^{-5}	2.08×10^{-6}	2.89×10^{-7}
473	1.67×10^{-2}	2.58×10^{-4}	9.15×10^{-6}	2.25×10^{-6}
523	5.94×10^{-2}	1.22×10^{-3}	3.77×10^{-5}	5.59×10^{-6}
573	1.47×10^{-1}	1.93×10^{-3}	5.59×10^{-4}	1.21×10^{-4}
623	1.37×10^{-1}	1.53×10^{-3}	1.53×10^{-4}	4.01×10^{-4}

4.2.4 Relaxation Time

For thermally activated process, the temperature dependence of relaxation time (τ) can be explained based on Arrhenius law (equation 4.10). These τ values were obtained from the peak position of -Z" versus f plots. The plots of lnτ versus 10^3/T for x = 0, 0.1 and 0.2 samples are shown in Figure 4.22(d) for the data collected in the temperature range of 423 K < T < 623 K, i.e., by considering relaxation due to GB. They all exhibit a linear behaviour along with anomalous behaviour in the vicinity of FIM T_C, which indicates the presence of magneto-electric coupling. Similar behaviour is reported by *Patri* et al. in YIG [145]. For x = 0, there is an anomalous behaviour in the vicinity of FIM T_C of 550 K and as a result Arrhenius law fitting was carried out separately in two different temperature

regions (423 K < T ≤ T_C (FIM) and T_C < T ≤ 623 K (PM)) by taking E_{az} and τ_0 as free parameters of fit. E_{az} is the activation energy. In the FIM region, the estimated value of E_{az} is found to be 0.93 ± 0.07 eV and in the PM region it is found to be 0.86 ± 0.03 eV. The E_{az} values in the FIM region is found to decrease from 0.93 eV to 0.41 eV with increase in Mn-concentration. The E_{az} values in the PM region is found to decrease from 0.86 eV to 0.57 with increase in Mn-concentration. The relatively large E_{az} value observed in the FIM region is due to the ordering of Fe ions in Fe^{2+}-Fe^{3+} networks, which hinder the smooth hopping of charge carriers.

4.2.5 Complex Dielectric Spectroscopy Studies

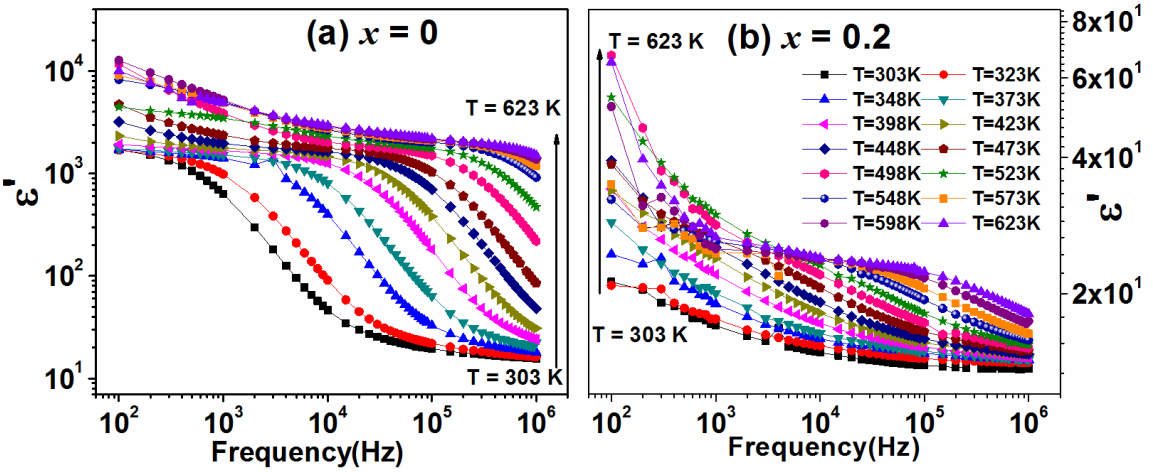

Figure 4.25: Real (ε') component of complex dielectric constant as a function of frequency in logarithmic scale at different temperatures (T = 300 K to 623 K) for (a) x = 0 and (b) x = 0.2 samples.

The real (ε') and imaginary (ε") components of complex dielectric constant (ε*) were obtained from the experimental Z' and -Z" values by using the relations (4.4) and (4.5). Figure 4.25(a) and (b) show the frequency variation of ε' of Y-(Fe, Mn)-O at different temperatures. For T < 423 K, it is clearly observed that ε' exhibits a plateau like behaviour in the low frequency region followed by a sharp decrease in ε' value as the frequency is increased. The upturn in ε' in the low frequency region especially for T > 423 K can be attributed to the contribution of space-charge polarization due to blocking of charge carriers across the GB. Higher magnitude of ε' with strong frequency dispersion at lower frequency is attributed to Maxwell-Wagner relaxation. Such relaxation behaviour is generally observed in heterogeneous system where grains, grain boundaries and electrode effect contribute to conductivity [81]. The value of ε' for x = 0 sample at 1MHz is found to be 15

at 300 K which is nearly comparable to the reported value by *Larsen* et al. [157] and it is found to increase upto 750 at 573 K. The value of ε' is found to decrease with increase in Mn-concentration (i.e., from 15 for x = 0 to 10 for x = 0.2) due to possible reduction in conduction contribution and decrease in grain size. The substitution of Mn is expected to disrupt the Fe^{2+}-Fe^{3+} networks in oxygen off stoichiometric YIG.

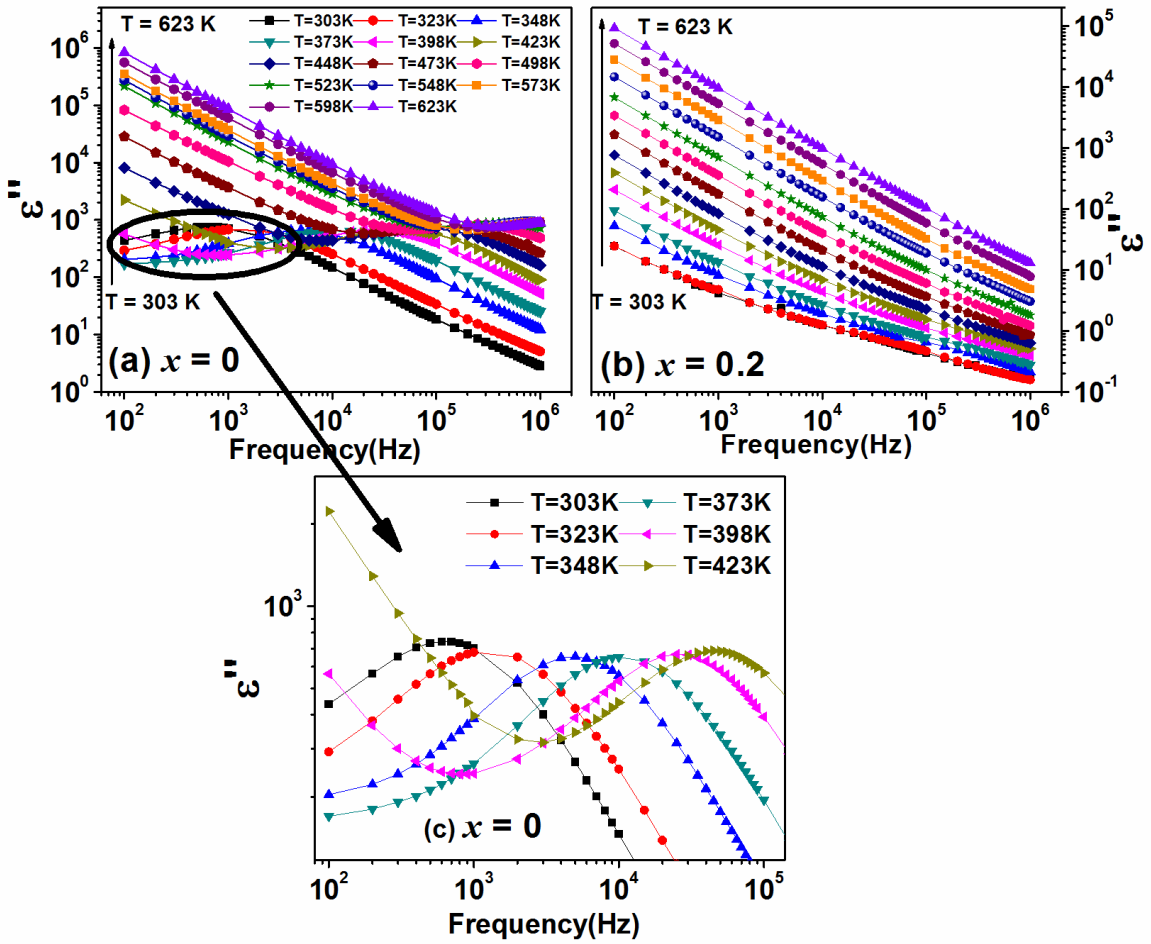

Figure 4.26: Imaginary (ε") components of complex dielectric constant as a function of frequency in logarithmic scale at different temperatures (T = 300 K to 623 K) for (a) x = 0 and (b) x = 0.2 samples. (c) ε" versus frequency of x = 0 sample for T ≤ 423 K (expanded scale).

Figure 4.26(a) and (b) show the frequency variation of ε" in logarithmic scale for Y-(Fe, Mn)-O samples with x = 0 and 0.2 at different temperatures (T = 300 K to 623 K). For x = 0, it is observed that ε" exhibits a relaxation peak for the measurements carried out in the temperature range of 300 K to 423 K, i.e., 600 Hz at T = 300 K and 45000 Hz at T = 423 K as shown in the expanded scale in Figure 4.26(c). The relaxation peak is found to shift towards higher frequency with increase in temperature and it suggests the presence of

thermally activated relaxation process. At higher temperature (T > 448 K), ε" exhibits a linear behaviour with a large value in the low frequency region and it is attributed to the conduction loss due to long-range movement of charge carriers across GB. The conduction loss may occur due to leakage current that depends upon vacancies and space charge accumulation across GB. The ε" versus frequency plots of Mn-substituted samples show the linear behaviour in the entire measured temperature range and it suggests the predominant conduction loss across GB and follow the typical power-law response known as Universal Dielectric Response (UDR) [73]. The value of ε" increases with increase in temperature due to increase in the thermally induced charge carriers and hence the conductivity. Such enhancement in ε" due to increase in conductivity has been reported in parent and substituted YIG [81,158]. The lack of relaxation peak in Mn-substituted samples can be ascribed to the presence of dominance of conduction loss across GB.

4.3 Conclusion

Polycrystalline samples of $Y_3Fe_{5-x}Cr_xO_{12}$ for x = 0 to 0.5 were prepared in single-phase form having cubic crystal structure. The analysis of XRD patterns reveals that the lattice constant value and unit cell volume decrease with increase in Cr-concentration and it is due to the substitution of smaller Cr^{3+} ions at Fe^{3+} site at octahedral site. Microstructural images show that the average grain size increases with Cr concentration. The analysis of *M-T* plots showed the FIM transition and its T_C, is found to decrease from 547 K for x = 0 to 494 K for x = 0.5 due to the weakening of superexchange interaction in $Fe^{3+}(a)$-O^{2-}-$Fe^{3+}(d)$ networks. The analysis of *M–H* loops show that saturation magnetization value increases from 24.8 emu/g for x = 0 to 26.6 emu/g at x = 0.5 due to the preferential occupation of Cr^{3+} ions at octahedral site of Fe^{3+} ions. The asymmetric and depressed nature of Nyquist plots suggests that, the relaxation of charge carriers is of non-Debye type. They were fitted by choosing appropriate equivalent circuit involving the contributions from grains and grain boundaries resistance, capacitance across grain boundaries and constant phase element. Both grains and grain boundaries are found to contribute towards relaxation process but grain boundaries contribution is found to be dominated at higher temperature due to the long-range hopping of charge carriers. The frequency dispersion of complex dielectric constant is explained in terms of Havriliak–Negami equations. The dielectric constant is found to increase (from 20 for x = 0 to 52 for x = 52 at T= 300 K, f = 1 MHz) due to the increase in number of hopping of charge carriers. The ac conductivity data

estimated from the dielectric constant measurement show increasing trend with increase in Cr concentration and the estimated frequency exponent (n) value is found to increase with temperature. It suggests that the small polaron model plays a role in the conduction process. The estimated activation energy values due to conduction process within the grains and across the grain boundaries suggest that they are governed by hopping of charge carriers across Fe^{2+}-Fe^{3+} centres and ionization of oxygen vacancies respectively.

Besides Cr-substitution, we have prepared $Y_3Fe_{5-x}Mn_xO_{12}$ (x = 0, 0.1 and 0.2) ceramic samples by sol-gel method and studied their magnetic and dielectric properties. These samples are in single-phase form with cubic crystal structure. The lattice parameter decreases with Mn-substitution due to the possible formation of Mn^{4+} ions having smaller ionic radii than that of Fe^{3+} ions. The temperature variation of magnetization of all the samples exhibit FIM transition with T_C in the range of 550 to 539 K. No appreciable variation has been observed in the saturation magnetization value and it is ~25emu/g. The impedance spectroscopy of the parent (YIG) compound is explained based on charge carrier relaxation across G and GB. However, the impedance spectra of x = 0.1 and 0.2 samples are explained by considering only the GB contribution. The Arrhenius plots of relaxation time showed an anomaly in the vicinity of FIM transition temperature, which highlights the presence of magneto-electric coupling. The dielectric constant is found to decrease with increase in Mn-concentration, which is attributed to the decrease in grain size.

Chapter 5

Ferrimagnetic and Relaxor Ferroelectric Properties in Gd-Fe-O Series

Among RIGs, the Gadolinium iron garnet (GIG) exhibits interesting magnetic and dielectric properties due to the presence of magnetic rare earth element (Gd) and its weak interaction with the net ferrimagnetic moment of Fe ions [43,120,121]. Such interaction gives rise to magnetic compensation around 286 K. Similar magnetic compensation has been reported in other RIGs (R = Er, Dy, Ho and Tb) and spinel ferrites [42,43]. Alternatively, some of the RIGs exhibit negative magnetization below T_{comp}, such as Bi-substituted $Tb_3Fe_5O_{12}$ and $Ho_3Fe_5O_{12}$, [16,53]. The tuning of magnetic and dielectric properties of mixed RIGs having Gd and other rare earth elements such as Y, Sm, Bi, La, Nd and Ce are studied by a few authors [101,122,159,160]. Generally, the large dielectric constant coexists with large dielectric loss in many materials. Ferroelectric materials, like $BaTiO_3$ and $BiFeO_3$ are known to exhibit large dielectric constant ($\varepsilon' > 15$) as a result of their permanent dipoles [158,161]. However, non-ferroelectric $CaCu_3Ti_4O_{12}$ and Sr_2SbMnO_6 are also known to exhibit a colossal dielectric constant due to the presence of Maxwell-Wagner type polarization [149,162]. Polycrystalline $Sm_3Fe_5O_{12}$ exhibits large dielectric constant as well as low dielectric loss in a broad temperature and frequency range [103]. Improved FIM T_C and dielectric constant have been reported in Bi-substituted YIG [18,104,135]. *Rajan* et al. [126] have reported that Bi-substitution at Gd site gives rise to enhanced dielectric constant and bigger grain size in GIG series. On the other hand, $Bi_3Fe_5O_{12}$ exhibits a magnetoelectric effect at room temperature as per the observation of *Popova* et al. [163]. Therefore, the detailed investigation of magnetic and electrical properties of GIG is required, and the prime motivation behind this study of Sm and Bi-substitution at Gd site is to tune the structural, magnetic, as well as electrical properties. Such substitution can give rise to an increase in saturation magnetization along with negative magnetization behaviour. In addition, it may lead to multiferroic behaviour with typical relaxor ferroelectric behaviour.

5.1 Sm-Substituted $Gd_3Fe_5O_{12}$

Polycrystalline $Gd_{3-x}Sm_xFe_5O_{12}$ [(Gd, Sm)-Fe-O] samples with x = 0, 0.5, 1.0, 2.0 and 3.0 were synthesized by the solid-state reaction method as described in chapter 2 (section 2.2.1). Starting materials such as Gd_2O_3, Sm_2O_3 and Fe_2O_3 (purity > 99 %) were weighed as per their stoichiometric ratio and mixed thoroughly in acetone medium. The pre-sintering was carried out at 1073 K for 12 hours. The presintered powder was ground and kept for final sintering at 1673 K for 8 hours in cylindrical pellet form with intermediate grinding.

5.1.1 Structural Studies

Figure 5.1 illustrates the XRD patterns of (Gd, Sm)-Fe-O samples for x = 0, 0.5, 1.0, 2.0 and 3.0. All the patterns were Rietveld refined using $Ia\bar{3}d$ (O_h^{10}) space group and they confirm the single-phase nature of samples. Figure 5.2 shows the Rietveld refined XRD pattern (solid line) for x = 0, 1.0, 2.0 and 3.0 samples. The lattice constant a, and the unit cell volume V, determined from the above analysis are given in Table 5.1. As per the above analysis, the a and V values are increasing with Sm-concentration and they are consistent with larger Sm^{3+} (1.02 Å) ions substituting at Gd^{3+} (1.01 Å) site. The site occupation values of various cations determined from the above analysis are also consistent with starting composition as shown in Table 5.1. As per the Rietveld analysis, the bond length across Fe(a)-Fe(d) ions, Gd(c)-Fe(d) ions and Gd(c)-Fe(a) ions and bond angles of Fe(a)-O-Fe(d), Gd(c)-O-Fe(d) and Gd(c)-O-Fe(a) networks as a function of x are illustrated in Figure 5.3. It is observed that the obtained bond length values increase with Sm-concentration in accordance with the substitution of larger Sm^{3+} ions at the Gd^{3+} site and the related stretching of interatomic distance. The Fe(a)-O-Fe(d) bond angle is found to be increased from 126.2^o (x = 0) to 127.8^o (x = 3.0), which influences the magnetic properties as discussed later. The bond length and the bond angle values of the parent compound (x = 0) are comparable with the literature [119]. The pictorial view of different ions (Gd/Sm and Fe) for x = 0 and x = 2.0 sample were generated using visualization of electronic and structural analysis (VESTA) software, and they are shown in Figure 5.4**.**

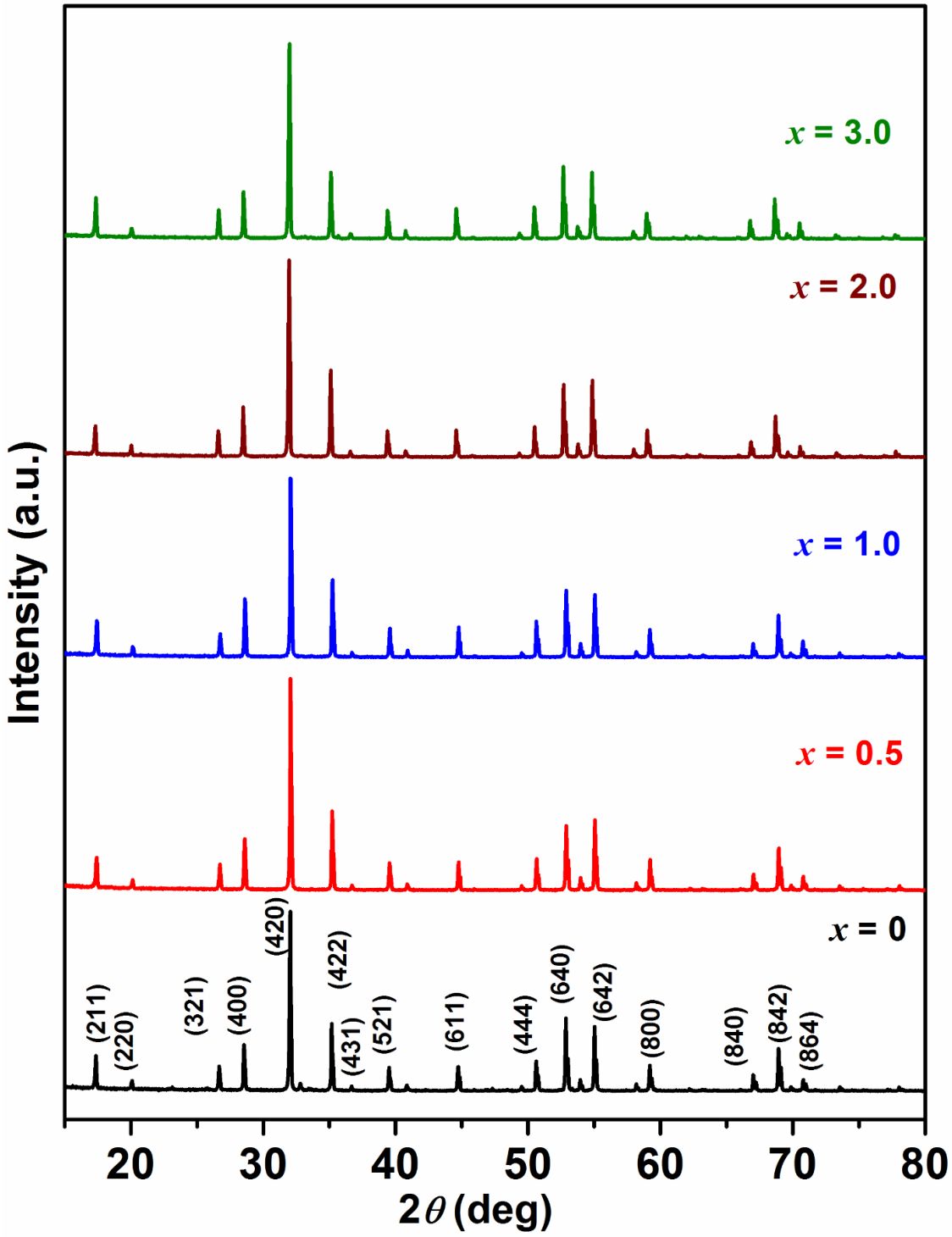

Figure 5.1: XRD patterns of (Gd, Sm)-Fe-O samples with x = 0 to 3.0.

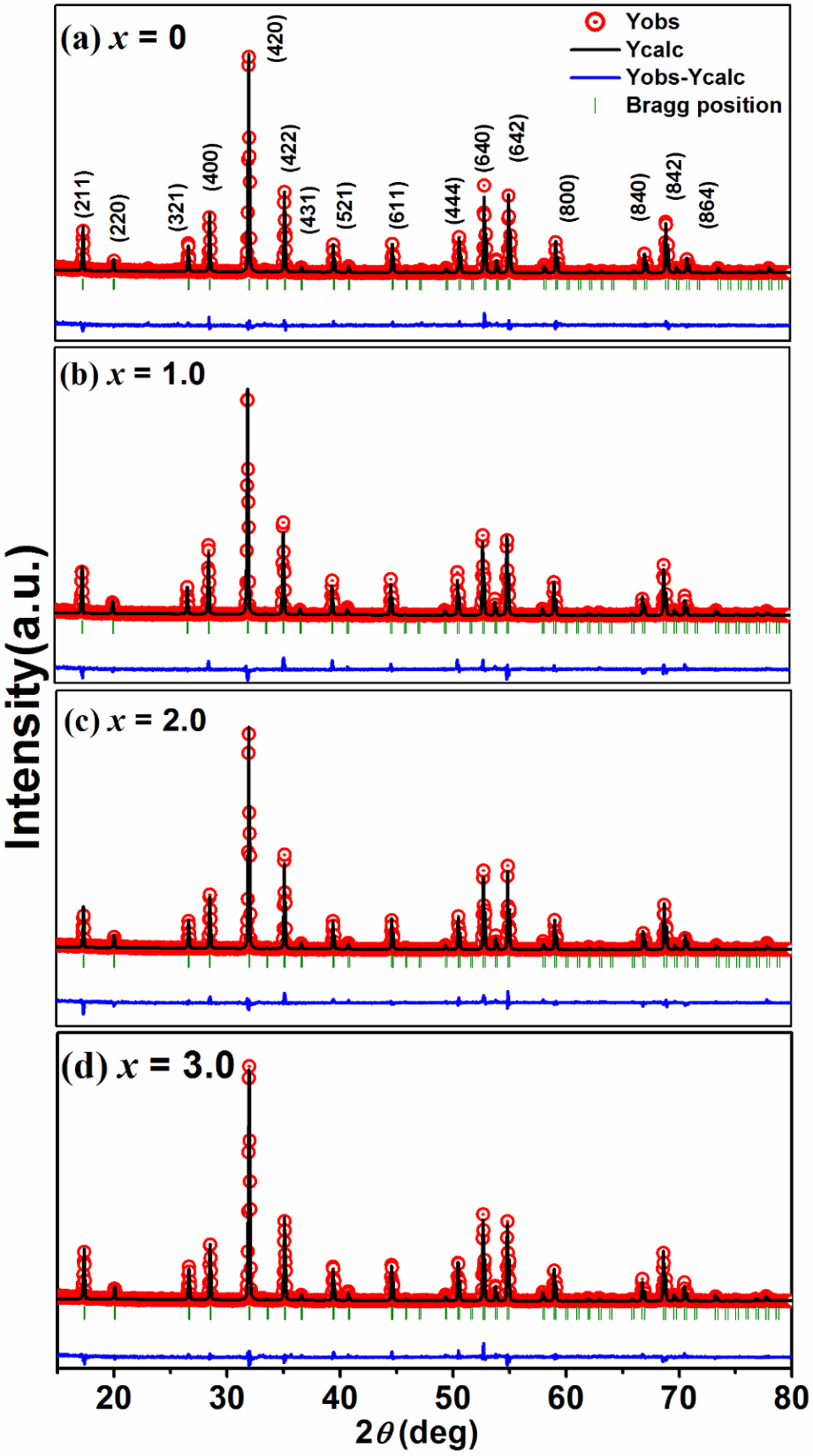

Figure 5.2: Rietveld refined (black solid line) XRD patterns along with the recorded data (red circle) for (a) x = 0, (b) x = 1.0, (c) x = 2.0 and (d) x = 3.0 samples.

Table 5.1: Structural (*a*, *V*) and reliability parameters (R_p, R_{exp}, R_F, R_{Bragg}, χ^2) along with cationic occupancy values obtained from the Rietveld refinement of XRD patterns of (Gd, Sm)-Fe-O samples with x = 0 to 3.0.

x	**0**	**0.5**	**1.0**	**2.0**	**3.0**
Space group	$Ia\bar{3}d$	$Ia\bar{3}d$	$Ia\bar{3}d$	$Ia\bar{3}d$	$Ia\bar{3}d$
***a* = *b* = *c* (Å)**	12.4624(5)	12.4726(5)	12.4835(6)	12.4985(5)	12.5211(5)
***V* (Å^3)**	1935.6	1940.3	1945.4	1952.4	1963.0
R_p (%)	8.77	8.87	10.4	8.99	9.75
R_{exp} (%)	7.25	7.53	7.23	7.85	9.83
R_f (%)	5.97	5.20	5.57	6.58	5.92
R_{Bragg} (%)	4.27	3.97	6.26	4.48	4.53
χ^2	3.21	3.26	3.71	3.68	3.67
Occupancy **Gd**	2.97	2.48	1.97	0.98	0.00
Sm	0.00	0.48	0.97	1.98	2.98
Fe	4.98	4.97	4.99	4.97	4.98

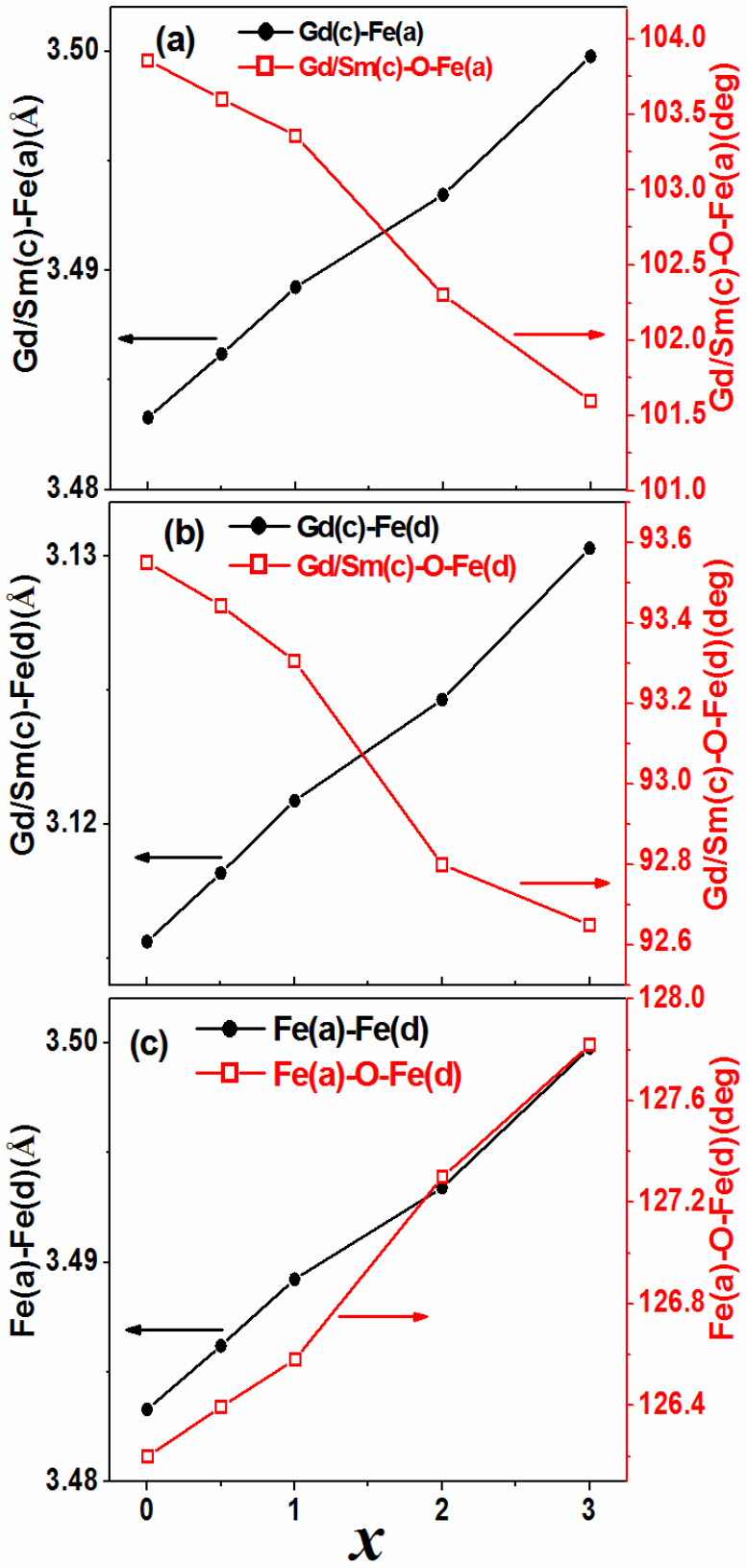

Figure 5.3: Various bond lengths (solid black circle) and bond angles (open blue square) as a function of *x*.

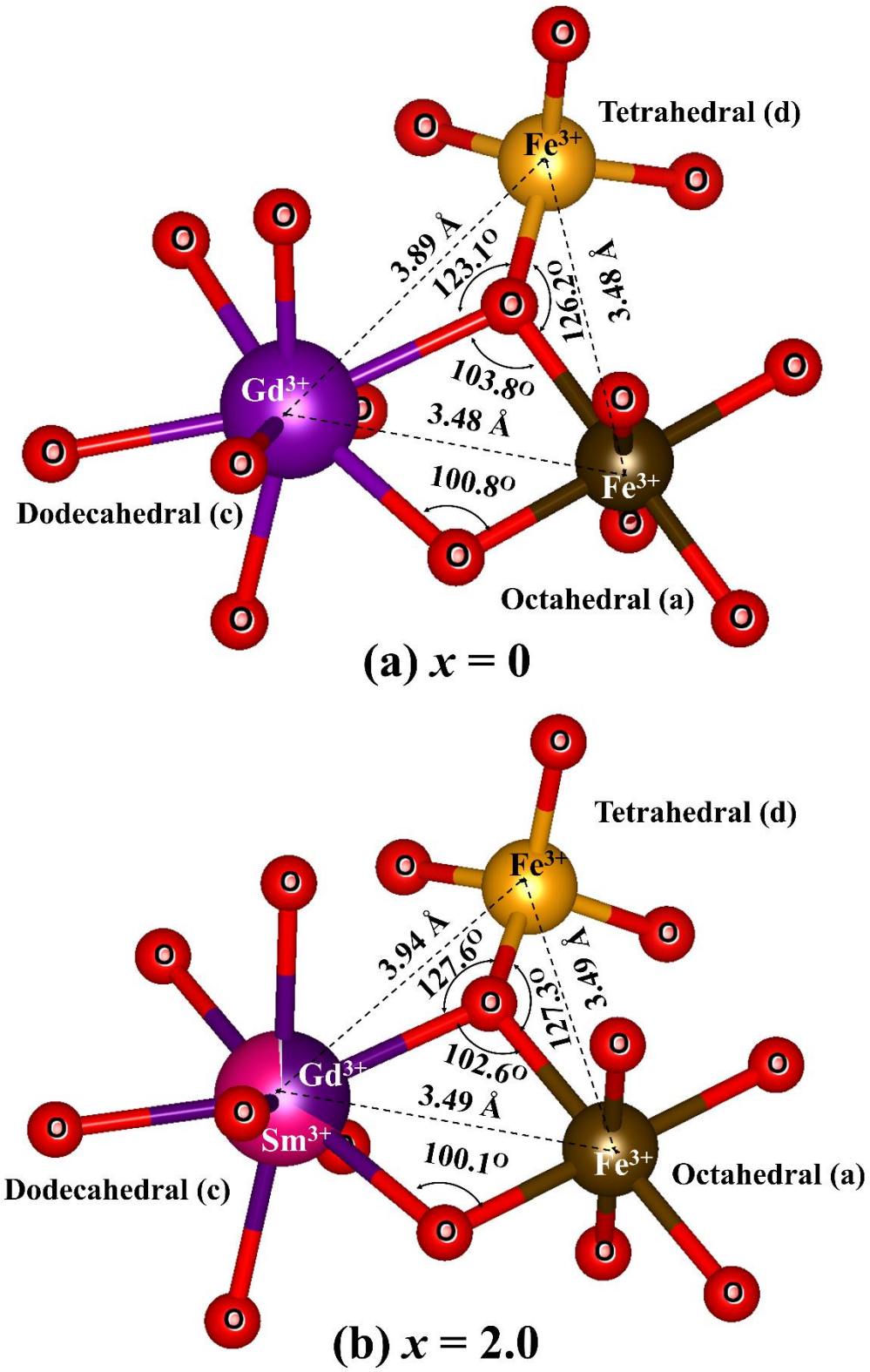

Figure 5.4: Pictorial view of Gd/Sm and Fe ions along with bond lengths and bond angles using VESTA software.

Figure 5.5(a-d) shows typical microstructural images of x = 0, 0.5 2.0 and 3.0 samples. The average grain size values are 3.4, 4.2, 4.7, 5.8 and 7.2 μm for x = 0, 0.5, 1.0, 2.0 and 3.0, respectively. The possible reason for grain growth due to Sm-substitution is the reduction in melting point and hence, better mobility of grain boundaries leading to a larger grain size [138]. The presence of Gd/Sm and Fe elements has been witnessed as per the typical EDS spectra (Figure 5.5(e, f)) of x = 0.5 and 2.0 samples. The chemical composition of the prepared samples is consistent with the nominal starting composition (Table 5.1). For example, cationic ratio Gd:Sm:Fe = 2.47:0.48:4.99 and 0.98:1.97:4.98 for x = 0.5 and 2.0, respectively. The density value of the prepared pellets determined from the Archimedes' principle; they lie in the range of 80% to 90% of theoretical density.

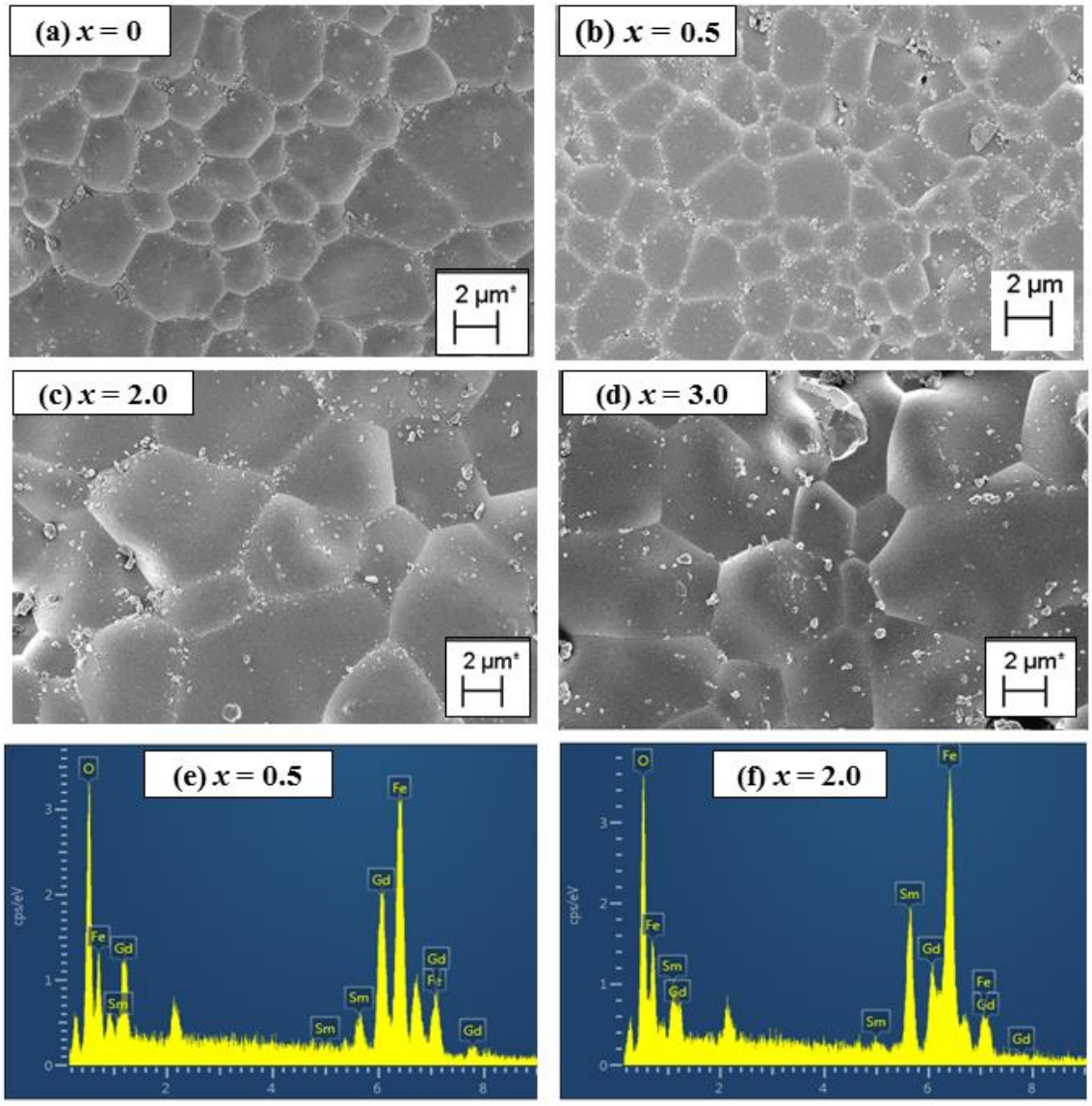

Figure 5.5: FESEM micrographs for (a) x = 0, (b) x = 0.5, (c) x = 2.0 and (d) x = 3.0 along with the EDX spectra for (e) x = 0.5 and (f) x = 2.0 samples of (Gd, Sm)-Fe-O.

The X-ray photoelectron (XPS) spectra for (Gd, Sm)-Fe-O with x = 1.0 and 2.0 are displayed in Figure 5.6(a-d). The XPS data were recorded [Versa Probe II (PHI 500), FEI Inc.] with Al Kα source. The binding energy peaks corresponding to $4d_{3/2}$ and $4d_{5/2}$ levels of Gd^{3+} and Sm^{3+} ions can be seen in Figure 5.6(a, b). Moreover, the binding energy peak corresponding to Sm^{3+} ions is found to increase with Sm-concentration. The binding energy peaks corresponding to both $2p_{3/2}$ and $2p_{1/2}$ levels of Fe ions are observed around 710.6 eV and 725.2 eV, respectively, as shown in Figure 5.6(c, d). The broad and asymmetric nature of peaks is explained by taking the contribution from Fe^{3+} and Fe^{2+} ions as per the profile fitting and their resolved binding energy values are 709 eV and 711 eV respectively for Fe-$2p_{3/2}$ level for x = 1.0 sample. The obtained binding energy values are comparable to those of respective elements [103,164,165].

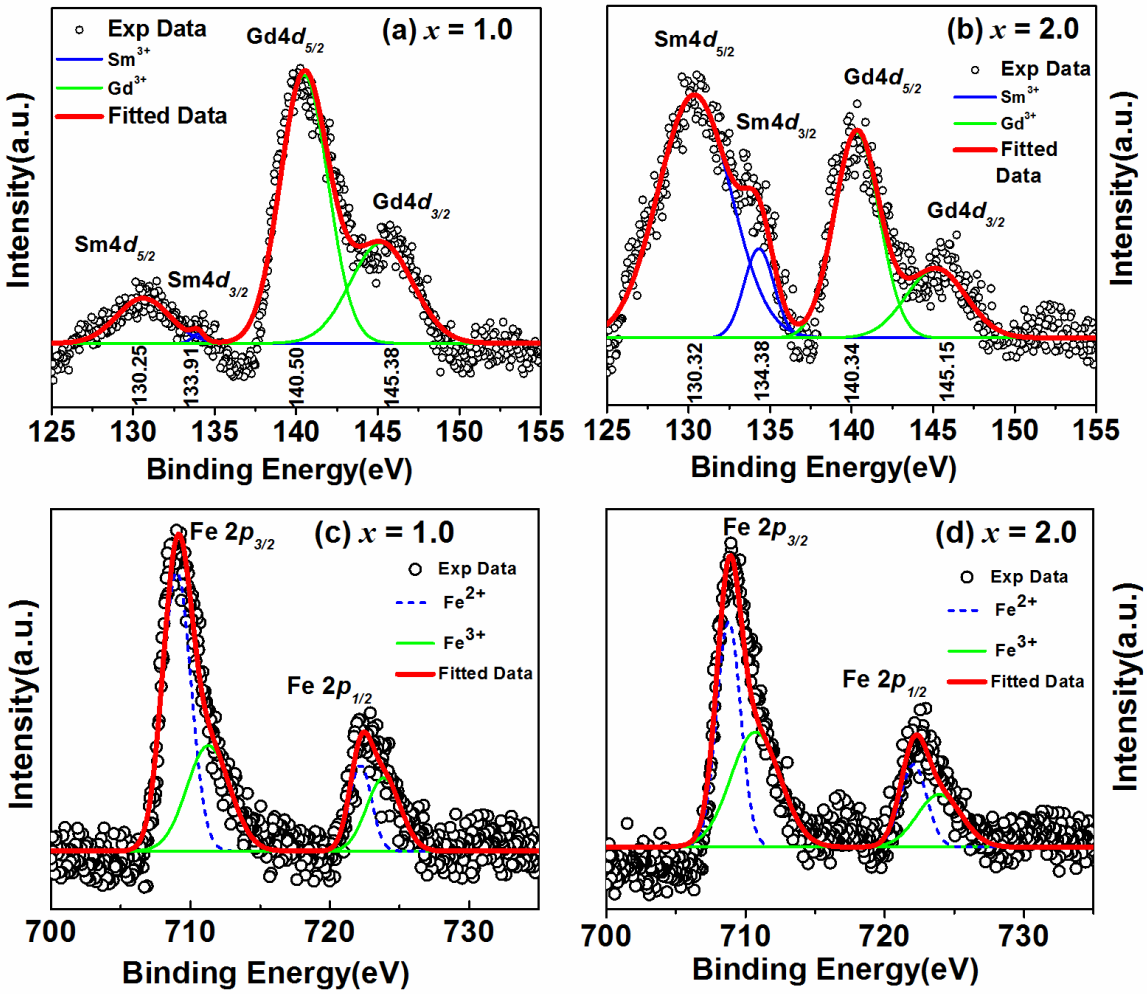

Figure 5.6: XPS spectra for x = 1.0 (a, c) and x = 2.0 (b, d) showing the oxidation state of Gd, Sm and Fe ions.

5.1.2 Magnetic Studies

The temperature (T) variation of magnetization (*M*) data were measured at an applied field of 200 Oe in the temperature range 25 K to 800 K as shown in Figure 5.7(a)**.** They all undergo ferrimagnetic (FIM) transition with increase in T_C from 567 K (x = 0) to 575 K (x = 3.0) as estimated from *dM/dT* versus T plots (Figure 5.7(b)). The estimated values of T_C are given in Table 5.2**.** The strengthening of superexchange interaction across $Fe^{3+}(a)$-O^{2-}-$Fe^{3+}(d)$ networks leads to increase in T_C, which is in accordance with the XRD analysis result. For x = 0, as the sample is cooled below T_C, the magnetization initially increases to a broad maximum value occurring at 450 K, and on further cooling, its value gradually approaches towards zero and reaching a magnetic compensation at T_{Comp} = 293 K. At T = T_{Comp}, it is expected that, $|3M_{Fe}(d)| = |2\mathrm{M}_{Fe}(a) + 3\mathrm{M}_{Gd}(c)|$. Here, the enhanced PM moment of Gd^{3+} refers to the weak exchange-coupled magnetic moment of Gd^{3+} ions with Fe^{3+} ions at the octahedral (*a*) site. However, for T < T_{Comp}, the magnetization starts increasing. The above observed trend along with T_C and T_{Comp} values in x = 0 sample is comparable with the literature [43,118]. A similar trend is observed for Sm-substituted samples; however, the T_{Comp} is found to be decreased drastically from 296 K (x = 0) to 70 K (x = 2.0) as mentioned in Table 5.2. For x = 3.0 sample, T_{Comp} is not observed due to small moment of Sm^{3+} ions, which cannot drive the system into magnetic compensation within the measured temperature limit. So here, two important observations, such as decrease in T_{Comp} and increase in peak magnetization value, can be ascribed to the Sm^{3+}-substituted ions having a smaller moment ($0.71\,\mu_B$) at Gd^{3+} site ($7\,\mu_B$). Such substitution gives rise to the reduction in moment at Gd site. So, it leads to the shifting of T_{Comp} towards lower temperature and hence, the enhanced peak magnetization. On the other hand, the flipping of the magnetic spin of each sublattice due to the relatively small anisotropic constant gives rise the secondary increase in magnetization for T < T_{Comp}.

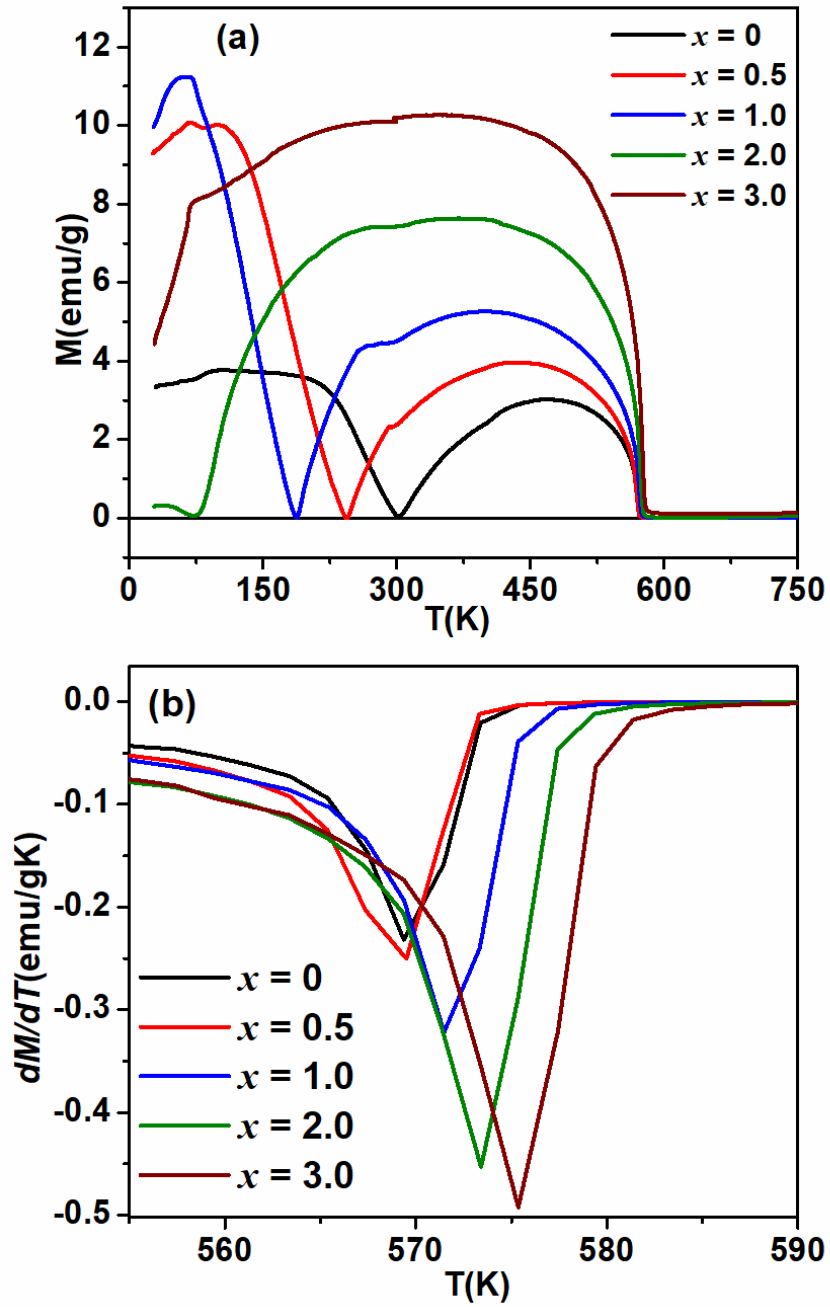

Figure 5.7: (a) *M-T* plots (b) *dM/dT* versus T plots of (Gd, Sm)-Fe-O samples for ZFC condition with H = 200 Oe.

We have also performed the *M-T* measurements under field-cooled (FC) condition for H_{FC} = 200 Oe in the temperature range of 25 K to 300 K, as shown in Figure 5.8. For *x* = 0, 0.5 and 1.0 samples, no noticeable change in magnetization is observed under FC condition, as the temperature is lowered, barring some irreversibility for T<100 K. However, for *x* = 2.0 sample, a novel negative magnetization or magnetization reversal is observed (Figure 5.9) for the first time in GIG series as the temperature is lowered below

T_{Comp}. This can be understood in terms of relatively large magnetic anisotropy introduced by Sm^{3+} ions. According to *Pearson* [166], $Sm_3Fe_5O_{12}$ exhibits larger magnetic anisotropy at lower temperature**.** No magnetic compensation and hence no negative magnetization is observed for x = 3.0 sample (Figure 5.8(d)) due to significantly smaller value of moment within the square bracket in the equation; $M_{net} = 3M_{Fe}(d) - [2M_{Fe}(a) + 3M_{Sm}(c)]$, such that it cannot compensate the tetrahedral sublattice moment [$3M_{Fe}(d)$]. One cannot rule out the shifting of T_{Comp} below the measured temperature limit of 25 K. Generally, the negative magnetization is quantitatively estimated from the ratio of minimum (M_{min}, negative) and maximum (M_{max}, positive) values of magnetization, i.e., $\left(\frac{M_{min}}{M_{max}}\right)$, and it is found to be 0.7. The value of $\frac{M_{min}}{M_{max}}$ is known to be in the range of 2 to 9 for rare earth orthochromites [45,167,168] and it lies in the range of 0.1 to 5 in some spinels and intermetallic alloys [42,61,62,169,170]. The relative irreversible magnetization, $\frac{\Delta M}{M_{ZFC}} = \frac{M_{Fc} - M_{ZFC}}{M_{ZFC}}$ was estimated and it is found to -11 at 25 K for H = 200 Oe as shown in the inset of Figure 5.9.

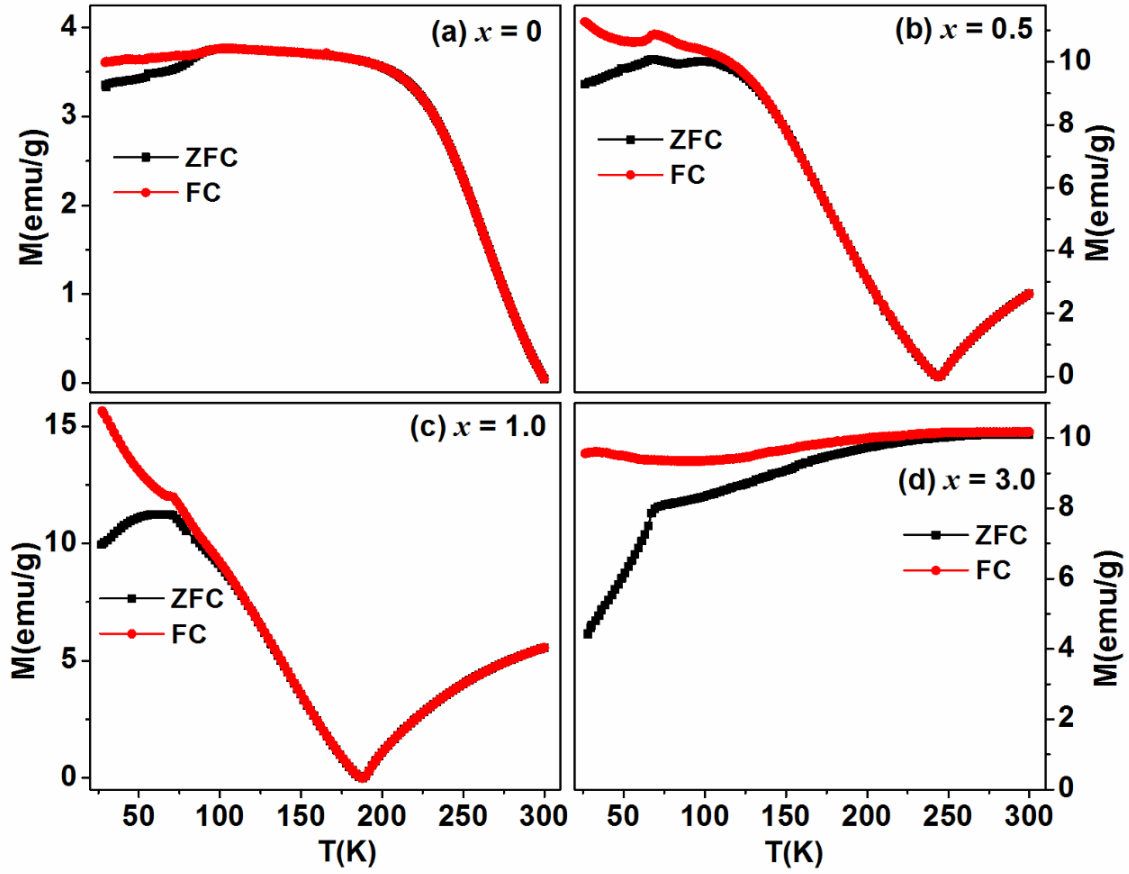

Figure 5.8: ZFC and FC M-T plots for (a) x = 0, (b) x = 0.5, (c) x = 1.0 and (d) x = 3.0 samples for H = 200 Oe.

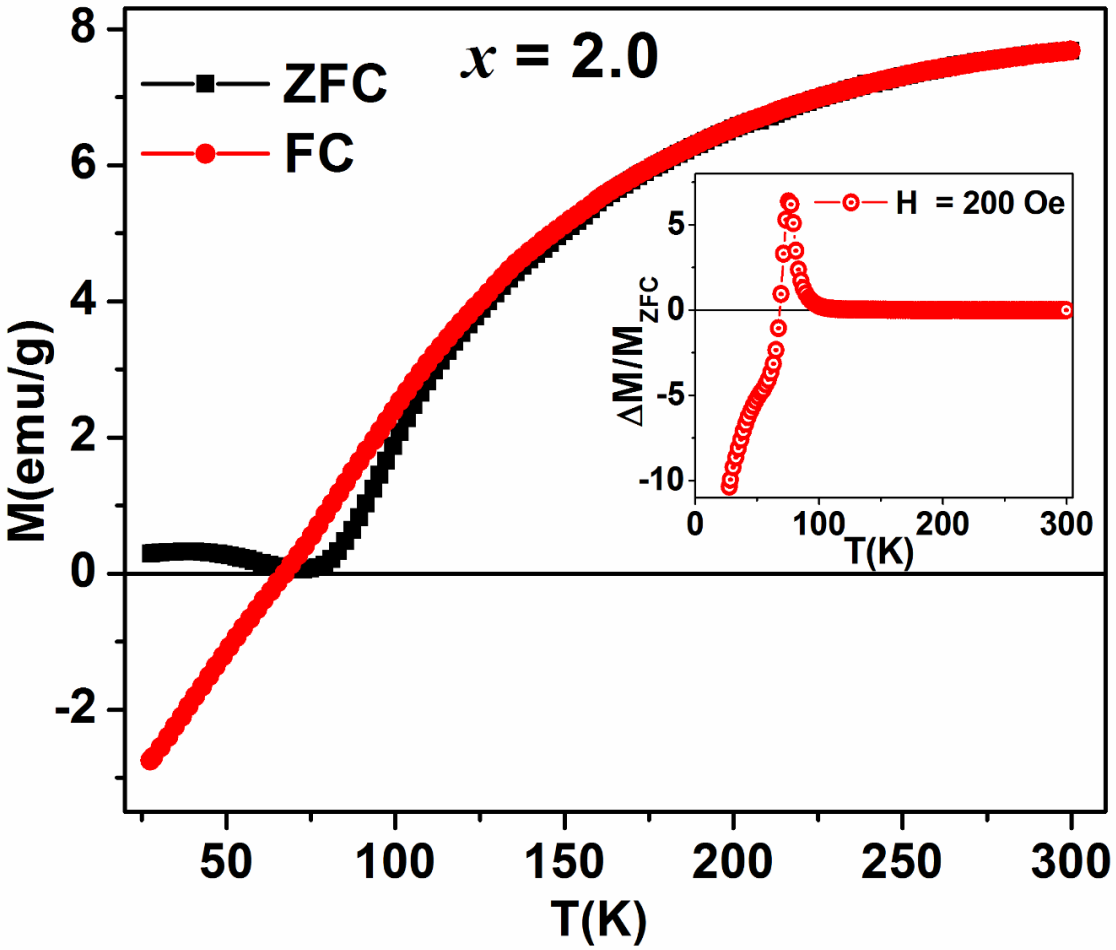

Figure 5.9: ZFC and FC *M-T* plots for x = 2.0 sample. The inset shows the irreversible magnetization versus T plot.

In order to further confirm that the negative magnetization is not due to any experimental artefact or residual magnetization, we have performed the *M-T* measurements for both H_{FC} = +200 Oe and -200 Oe using PPMS in the temperature range of 10 K to 300 K as shown in Figure 5.10(a) for x = 2.0 sample. We can evidently see that magnetization reversals in both cases, i.e., a mirror image of *M-T* plots for $H_{FC} = \pm 200$ Oe, and it confirms the presence of negative magnetization in x = 2.0 sample. We have also measured the FC *M-T* data by varying H_{FC} from 100 Oe to 600 Oe as depicted in Figure 5.10(b). The T_{Comp} is found to shift towards lower temperature with increase in $H_{FC,}$ and they are 70 K, 68 K, 65 K, 51 K for H_{FC} = 100, 200, 300 and 400 Oe, respectively. For $H_{FC} \geq 500$ Oe the magnetization passes through a magnetic compensation followed by a secondary rise in magnetization for $T<T_{Comp}$ similar to other samples in this series, i.e., without undergoing negative magnetization. Therefore, under this condition, the system overcomes the anisotropy energy and flip the sublattice magnetic spin.

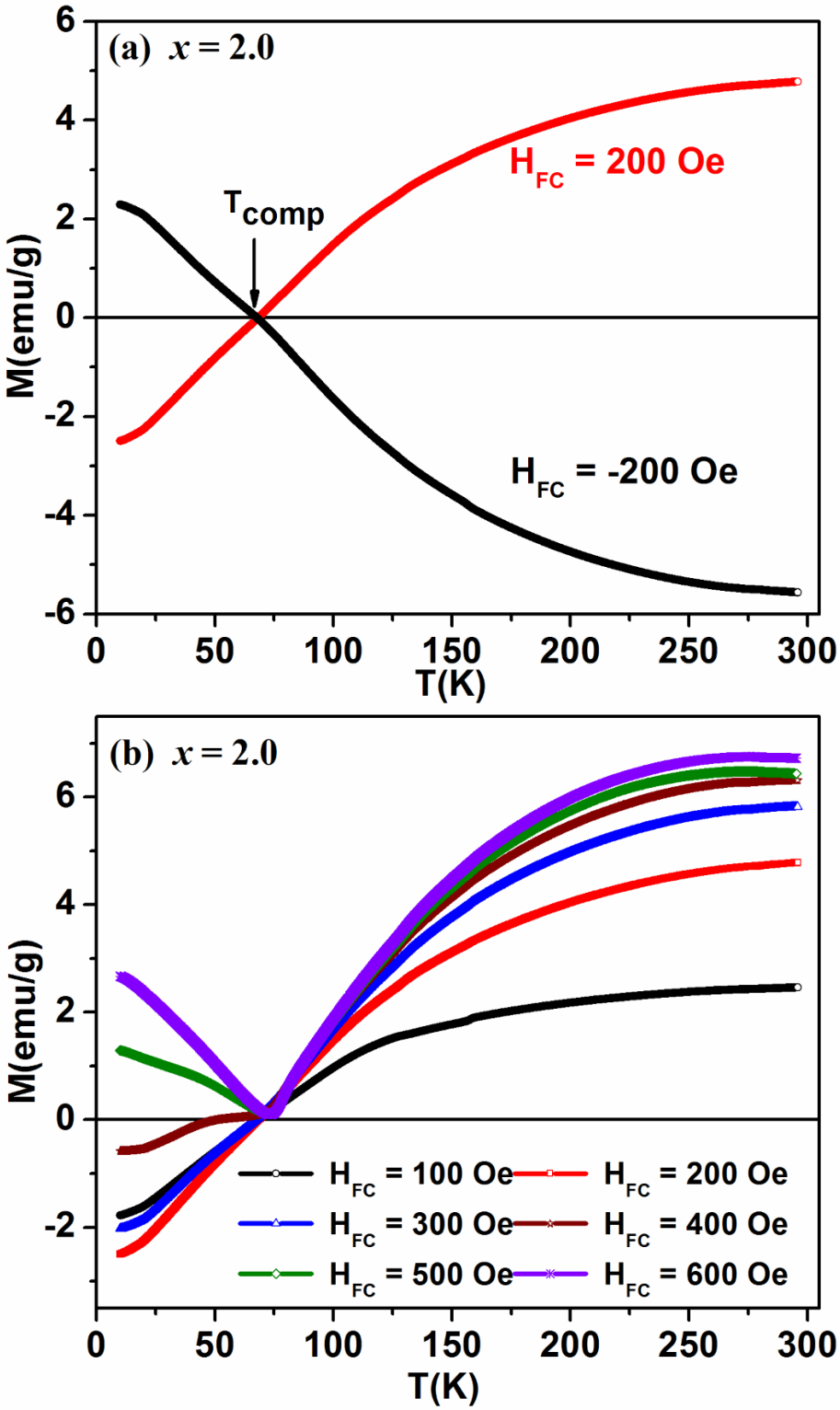

Figure 5.10: FC *M-T* plots of x = 2.0 sample for (a) H_{FC} = ± 200 Oe and (b) for different HFC values.

Figure 5.11(a) depicts the magnetic hysteresis loops (*M-H*) recorded at room temperature (300 K) for (Gd, Sm)-Fe-O samples. All Sm-substituted samples exhibit magnetic saturation as expected in a typical ferrimagnetic material. However, for x = 0, the

measured temperature being close to T_{Comp}, the measured magnetization is quite a small with a considerable linear contribution (inset of Figure 5.11(a)). Here, the exchange enhanced paramagnetic (PM) moment of Gd^{3+} ions almost compensate the ferrimagnetic moment of Fe^{3+} ions. The saturation magnetization (M_S) was determined by using law of approach to saturation (LAS) model fitted to the initial magnetization curve (Figure 5.11(b)).

$$M = M_S\left(1 - \frac{b}{H^2}\right) + cH,\ b = \frac{8K_1^2}{105\mu_0^2 M_S^2} \tag{5.1}$$

Here K_1 and the term cH indicate the effective anisotropy constant and forced magnetization respectively. The forced magnetization is generated especially at higher magnetic fields through linear increment in the spontaneous magnetization. However, the data of x = 0 sample do not follow the LAS equation, because its *M-H* plot is recorded near the magnetic compensation temperature and shows linear contribution at higher field. So here, the linear behaviour of *M-H* data in the high field region was analyzed based on the relation, $M = M_S + cH$, i.e., with b = 0 in equation (5.1). However, for other samples, the *M-H* data were fitted to equation (5.1). The M_S value at RT increases from 0.19 emu/g (x = 0) to 19.54 emu/g (x = 3.0). The net magnetic moment in (Gd, Sm)-Fe-O is basically attributed to the three different magnetic sublattices, viz., Gd^{3+}/Sm^{3+}(c), Fe^{3+}(a) and Fe^{3+}(d) ions. The total magnetic moment is represented as:

$$M_{net} = 3M_{Fe}(d) - [2M_{Fe}(a) + (3-x)M_{Gd}(c) + xM_{Sm}(c)] \tag{5.2}$$

Sm^{3+} (0.71 μ_B) ions substituting the Gd^{3+} (7 μ_B) ions having smaller magnetic moment at the 'c' site resulted in increase in net magnetization value at 300 K, as per the above empirical relation (5.2). It is noticed that the estimated value of K_1 increases from (6.85±0.03)×10^3 erg/cm^3 (x = 0.5) to (1.65±0.05)×10^5 erg/cm^3 (x = 3.0), which is also consistent with the explanation given for the negative magnetization in x = 2.0 sample. The coercivity (H_C) of x = 0 sample is 330 ± 10 Oe, while for other samples, they are in the range of 14 to 23 Oe. These obtained values suggest that Sm-substituted samples are magnetically soft. Since, the T_{Comp} value for x = 0 sample is in the vicinity of 300 K, it can lead to the relatively large value of H_C. The values of M_S and H_C are given in Table 5.2 for various samples.

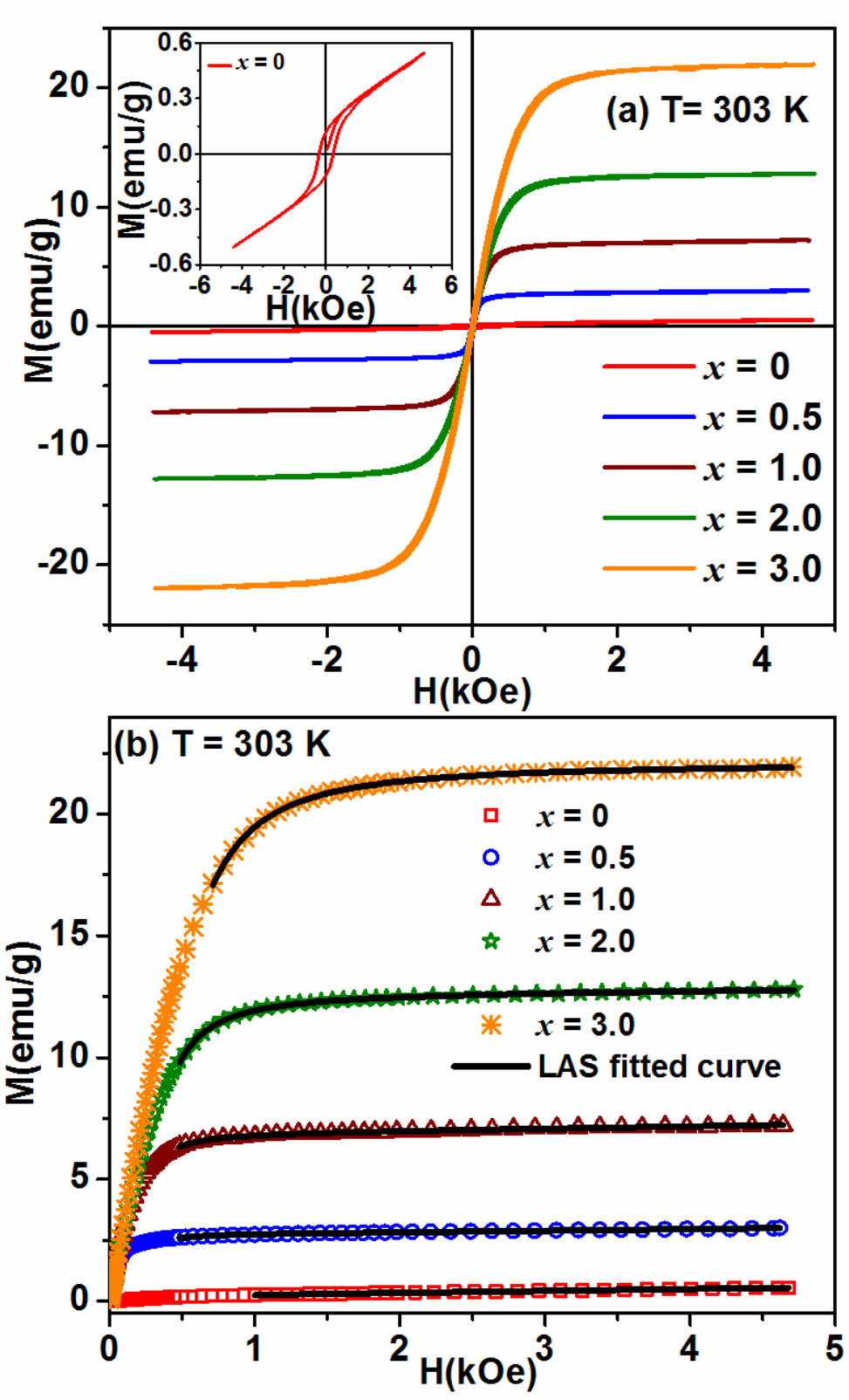

Figure 5.11: (a) *M-H* loops at RT, (b) observed initial magnetization data (open symbol) along with the fitted data (solid line) using LAS model for (Gd, Sm)-Fe-O samples. Inset shows the enlarged view of *M-H* plot of $x = 0$ sample.

Table 5.2: The estimated values of magnetic parameters for (Gd, Sm)-Fe-O samples.

x	**0**	**0.5**	**1.0**	**2.0**	**3.0**
T_{Comp} **(K)**	293	244	187	70	-
T_C **(K)**	567	568	568	573	575
M_S **(emu/g)**	0.19	2.71	6.83	12.52	21.91
K_1 **(erg/cm$^{3)}$)**	-	6.85×10^{3}	2.12×10^{4}	6.52×10^{4}	1.65×10^{5}
H_C **(Oe)**	330	14	16	20	23

5.1.3 Complex Impedance Spectroscopy Studies

RT data of real and imaginary (Z' and -Z") components of impedance as a function of frequency are shown in Figure 5.12(a) and (b), respectively. Relatively sharp fall in Z' value is observed for all samples as the frequency is increased up to 10^3 Hz and beyond that, it displays plateau-like behaviour. -Z" is observed to decrease linearly up to 10^5 Hz. Such a fall in Z' and the linear behaviour in -Z" in the low frequency region are mainly attributed to space-charge polarization. The frequency independent behaviour of Z' at higher frequency is due to the release of space charge polarization [142]. At a given frequency (100 Hz) Z' increases with Sm-concentration, i.e., from 100 kΩ for x = 0 to 300 kΩ for x = 3.0 sample.

Figure 5.13(a-d) shows the similar impedance spectra for x = 0, 1.0, 2.0 and 3.0 samples in the temperature range of T = 448 K to 623 K. For x = 0 sample, a wide peak in the low frequency region, i.e., at f_{max} = 300 Hz is observed at 473 K. This peak shifts towards higher f_{max} with rise in temperature, which is the manifestation of thermally activated charge carriers. These relaxation peaks in the low frequency region with large relaxation time varying from $5\text{x}10^{-4}$ sec at 473 K to $3\text{x}10^{-6}$ sec at 623 K, are attributed to relaxation across grain boundaries (GB). Similar behaviour is observed in Sm-substituted samples, but at lower f_{max} compared to that of x = 0 sample at a given temperature. For example, at 623 K, f_{max} values for x = 0, 1.0, 2.0 and 3.0 samples are found to be 60 kHz, 10 kHz, 20 kHz and 1 kHz, respectively. Such reduction in f_{max} value in Sm-substituted samples is consistent with their larger grains having fewer GB.

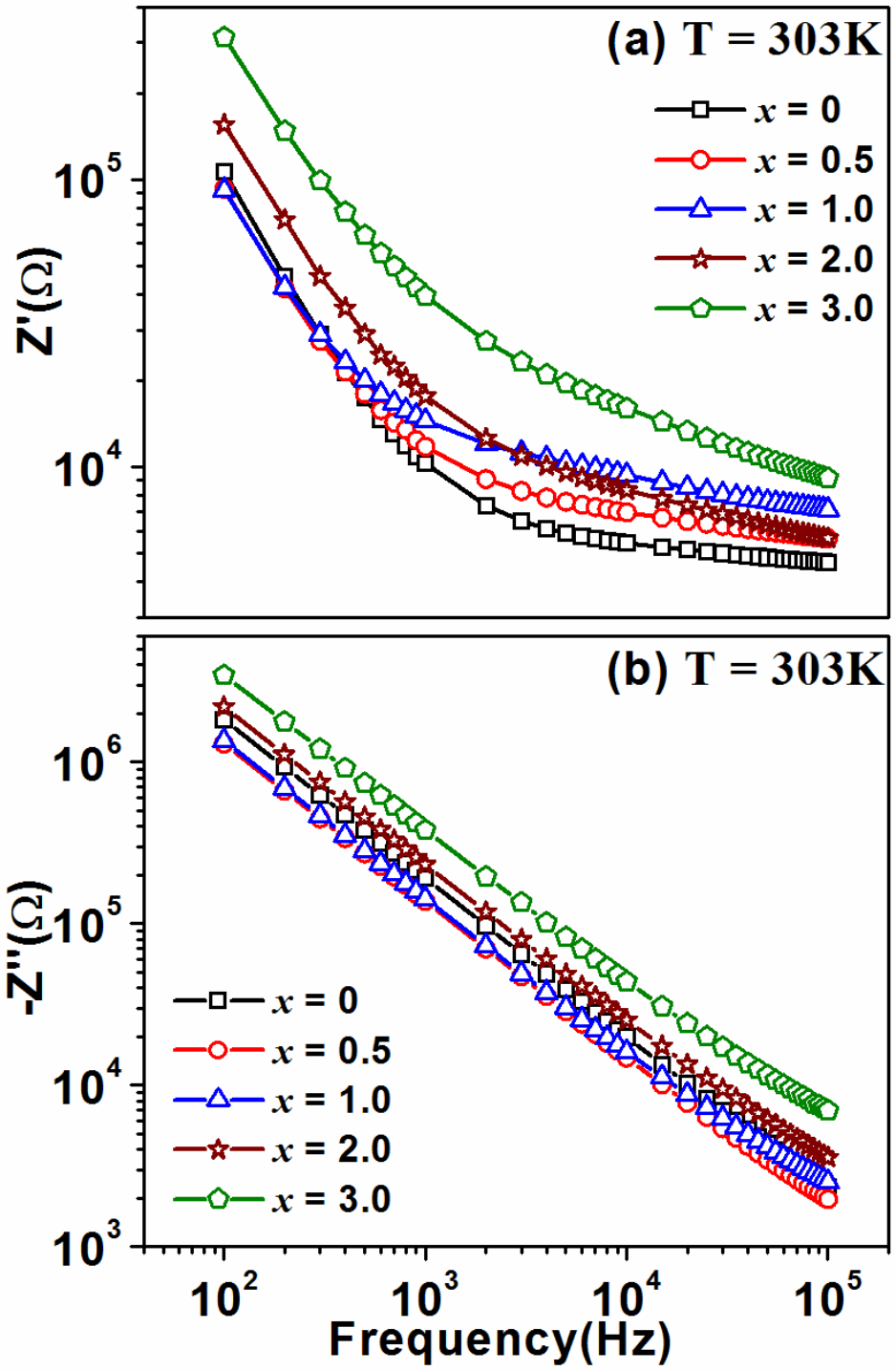

Figure 5.12: Frequency variation of (a) Z' and (b) -Z" at RT.

The complex impedance plane plots (-Z" versus Z': Nyquist plots) for different (Gd, Sm)-Fe-O samples are shown in Figure 5.14(a-c). We have analyzed the semicircular arc using ZSimpwin 3.21 software in the temperature range from 523 K to 623 K. The radius of semi-circular arc decreases with rise in temperature indicating the negative temperature coefficient of impedance. The semi-circular arcs are found to be suppressed and

asymmetric with its centre falling below the Z' axis and it implies the non-Debye type relaxation. The Nyquist plots were fitted (shown as solid lines in Figure 5.14) by choosing a model circuit shown in Figure 5.14(e). Here, R_g and R_{gb} refer to the grains and grain boundaries resistance, while Q_{gb} accounts for capacitance due to constant phase element (CPE) having impedance $Z_{CPE} = \frac{1}{A}(j\omega)^{-m}$ and C_{gb} represents the capacitance across GB. The exponent (m) associated with GB is in the range of 0.4 to 0.8. The plot of obtained value of R_{gb} as a function of Sm-concentration at different temperature are shown in Figure 5.14(d). It can be seen that the value of R_{gb} increases with Sm-concentration and it may be due to the decrease in the number of charge carriers across GB. However, it decreases with increase in temperature and it suggests the negative temperature coefficient of resistance (NTCR).

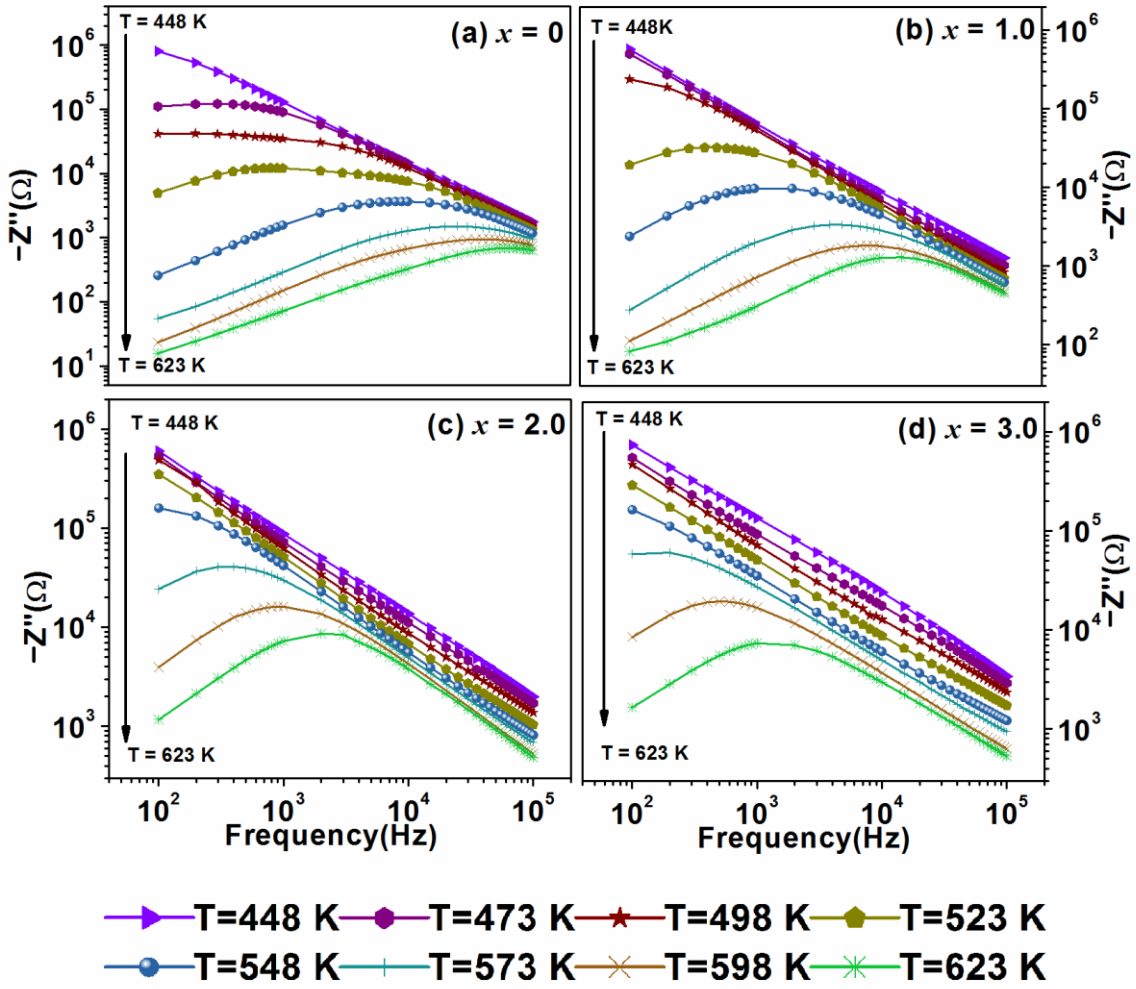

Figure 5.13: (a-d) -Z'' versus frequency for (Gd, Sm)-Fe-O samples in a wide temperature range (448 K to 623 K).

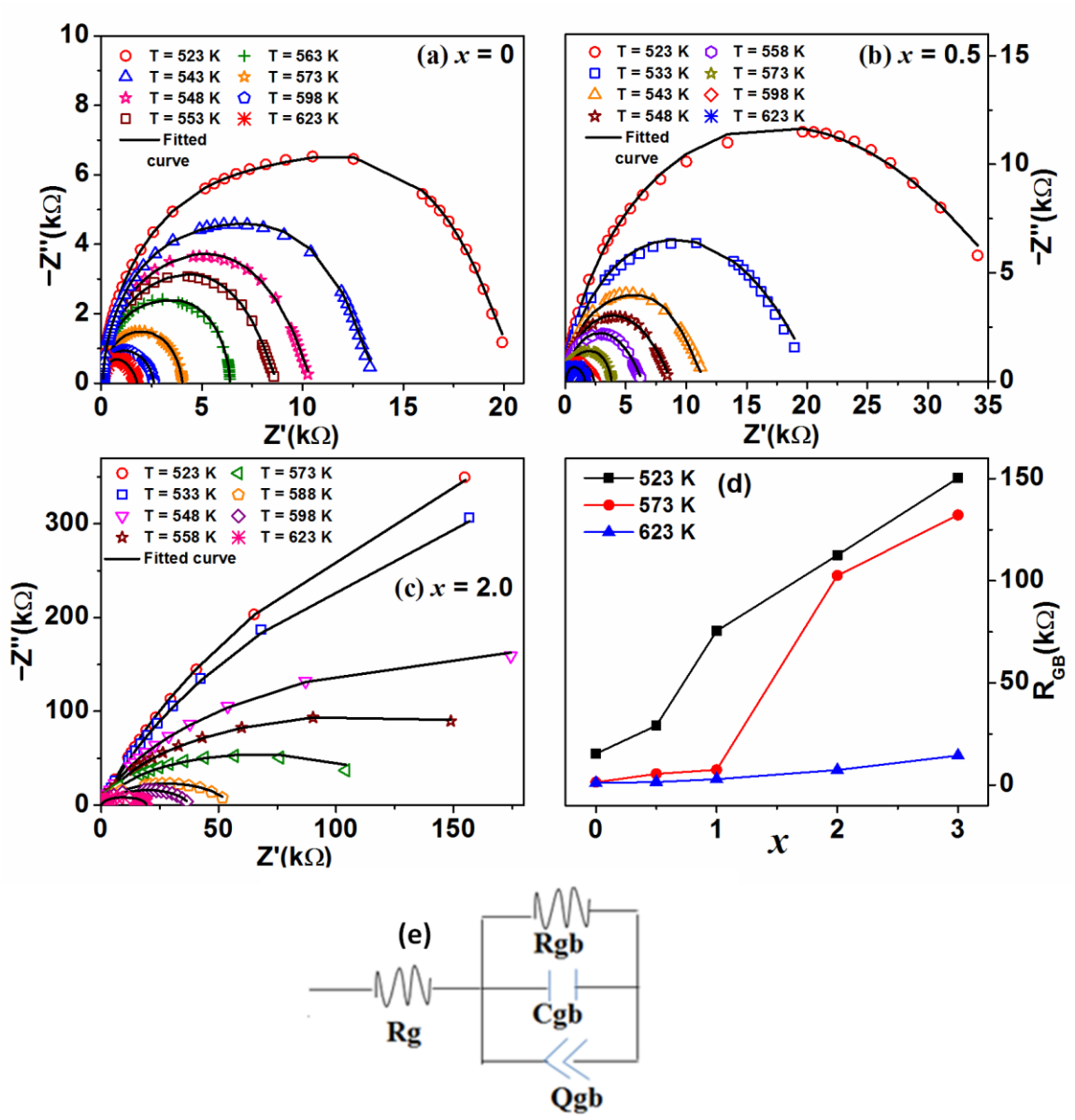

Figure 5.14: (a-c) Nyquist plots in the temperature range of 523 K ≤ T ≤ 623 K typically for x = 0, 0.5 and 2.0 samples, (d) the variation of R_{gb} with Sm-concentration at different temperature and (e) the equivalent modelled circuit for all the samples.

5.1.4 Relaxation Time

The relaxation time τ (=$1/2\pi f_{max}$) obtained from the above impedance spectra was plotted as a function of inverse temperature (10^3/T) (Figure 5.15). They all exhibit a linear behaviour and follow the Arrhenius law with a change of slope in the temperature range of 560 K to 570 K for all samples. In x = 0 sample, the change of slope occurs at around T = 560 K, which happens to be near the FIM T_C as per the discussion in magnetic properties (Table 5.2), and it highlights the existence of magneto-electric coupling. The activation energy (E_a) values obtained by fitting the data to Arrhenius relation in both paramagnetic

(PM: T > T_C) and ferrimagnetic (FIM: T < T_C) regions are given in Table 5.3. They are found to be in the range of 0.41 eV to 0.71 eV in the FIM region and 0.91 eV to 1.19 eV in the PM region. These E_a values in the FIM region are comparable with singly ionized oxygen vacancies, while the values in the PM regions are comparable with doubly ionized oxygen vacancies [150].

Table 5.3: The estimated values of activation energy (E_a) as per the analysis of Arrhenius plots of relaxation time obtained from the impedance spectra.

x	**0**	**0.5**	**1.0**	**2.0**	**3.0**
FIM (eV)	0.41±0.02	0.58±0.04	0.71±0.03	-	-
PM (eV)	0.91±0.06	1.04±0.12	1.09±0.10	1.13±0.12	1.19±0.15

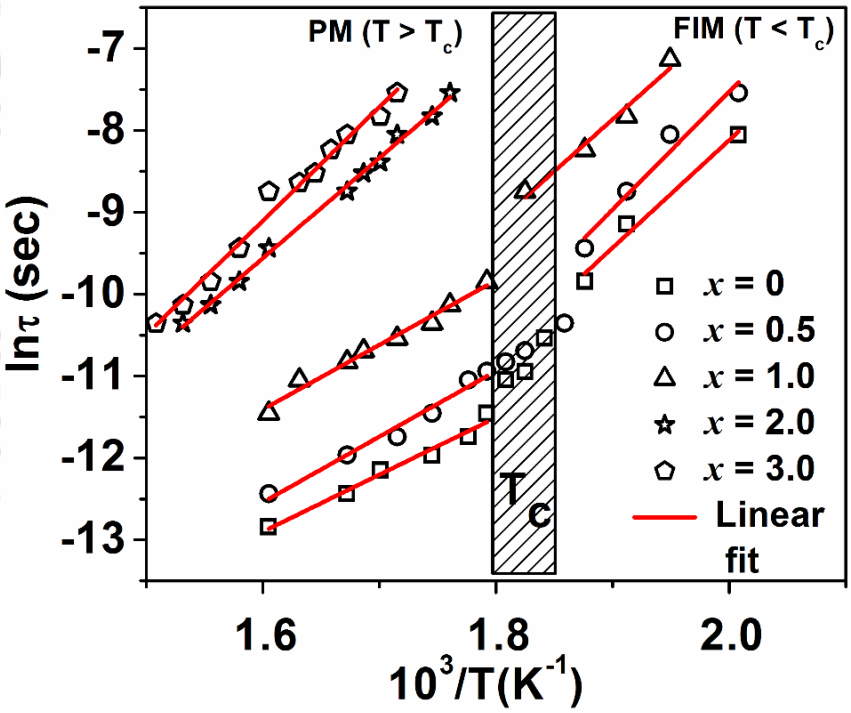

Figure 5.15: Arrhenius plots of relaxation time due to GB contribution.

5.2 Bi-Substituted $Gd_3Fe_5O_{12}$

In this section, we have described the preparation of Bi-substituted GIG samples using solid-state reaction method and study of their magnetic and electrical properties. Bi-substitution reduced the sintering temperature and shows ferroelectric relaxor type behaviour as well.

GIG with bismuth (Bi) substitution ($Gd_{3-x}Bi_xFe_5O_{12}$: (Gd, Bi)-Fe-O) for x = 0, 0.5 and 1.0 were synthesized by following the standard solid-state route as explained in section 2.2.1. The final sintering was carried out at 1673 K (24 hours), 1373 K (6 hours) and 1273 K (2 hours) respectively for x = 0, 0.5 and 1.0 samples.

5.2.1 Structural Studies

The Rietveld refined XRD patterns of polycrystalline samples are displayed in Fig 5.16. They were analyzed using cubic space group $Ia\bar{3}d$ having 8 number of formula units per unit cell. The XRD patterns (open circles) of x = 0, 0.5 and 1.0 samples of (Gd, Bi)-Fe-O and the Rietveld refined data (black solid line) follow each other as shown in Figure 5.16. All the prepared samples are found to be in the single-phase form as all the observed peaks are indexed with the goodness of fit less than 4. The lattice parameters such as lattice constant (a), unit cell volume (V) along with the R_p, R_{exp}, R_{Bragg}, R_F and χ^2 factors obtained from the Rietveld refinement are mentioned in Table 5.4. Bi-substitution increases the lattice constant and such increase in lattice constant with Bi-substitution has been reported in YIG [104,135] due to larger ionic size of Bi (1.03 Å) compared to Y (0.94 Å) and Gd (1.01Å) ions. The lattice constant (12.4624 Å) of undoped GIG is also comparable with the literature [119]. The Fe(a)-Fe(d), Gd/Bi(c)-Fe(a), Gd/Bi(c)-Fe(d) bond lengths and Fe(a)-O-Fe(d), Gd/Bi(c)-O-Fe(a), Gd/Bi(c)-O-Fe(d) bond angles determined from the Rietveld analysis are shown in Figure 5.17 as a function of Bi concentration (x). They are found to increase with Bi concentration. Here, Gd/Bi(c), Fe(a) and Fe(d) refer Gd/Bi at dodecahedral site, Fe ions at octahedral and tetrahedral sites, respectively.

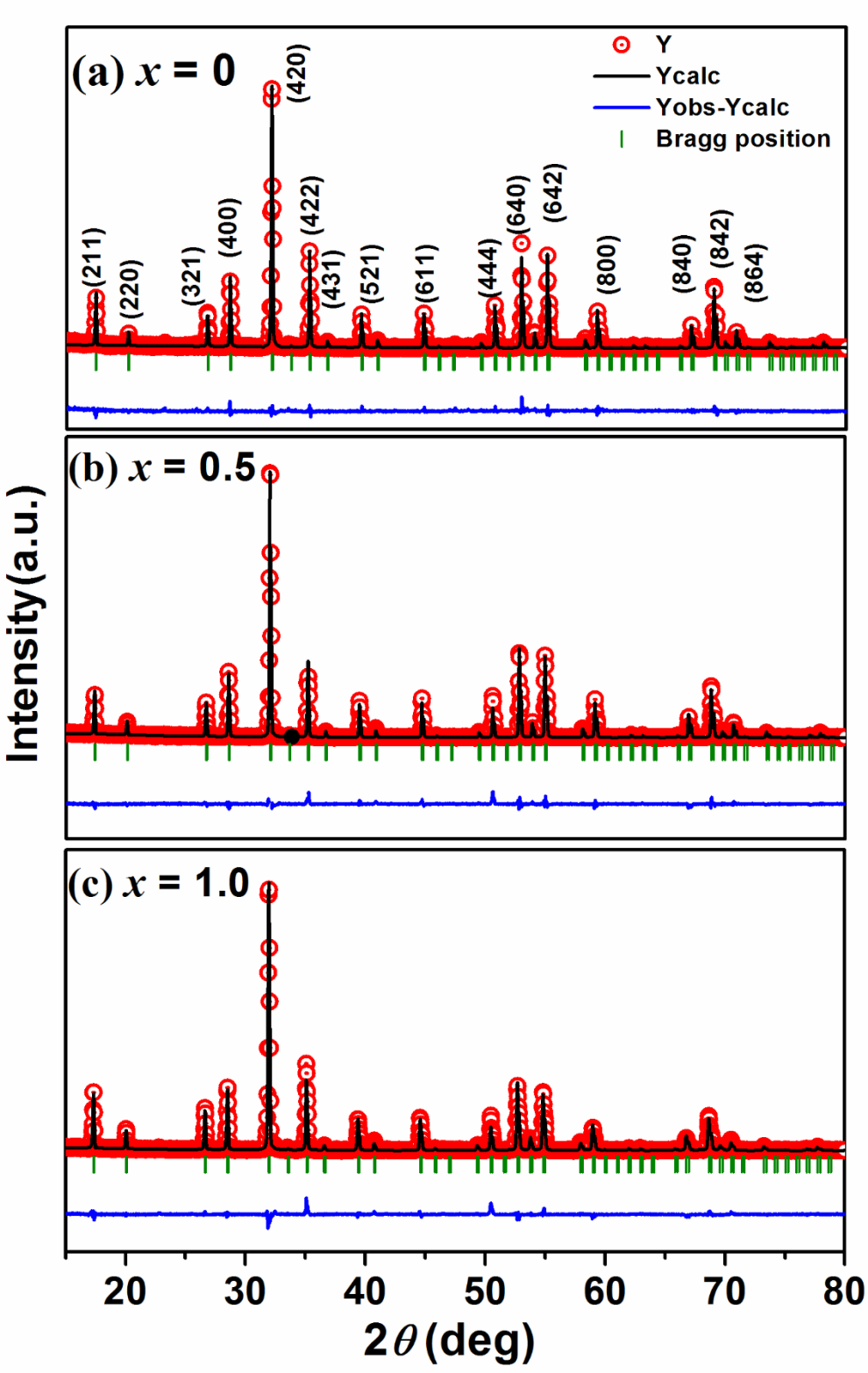

Figure 5.16: Rietveld refined XRD data for (Gd, Bi)-Fe-O samples.

Table 5.4: Structural and reliability parameters obtained from the Rietveld refinement of XRD patterns of (Gd, Bi)-Fe-O samples with x = 0 to 1.0.

x		**0**	**0.5**	**1.0**
Space group		$Ia\bar{3}d$	$Ia\bar{3}d$	$Ia\bar{3}d$
$a = b = c$ **(Å)**		12.4624(5)	12.4899(4)	12.5156(6)
V		1935.6	1948.4	1960.4
R_p		8.77	9.42	10.5
R_{exp}		7.81	7.56	7.45
R_f		4.97	5.19	5.45
R_{Bragg}		4.88	4.97	4.44
χ^2		3.46	3.81	3.82
Occupancy	**Gd**	2.98	2.47	1.96
	Bi	0.00	0.47	0.97
	Fe	4.98	4.96	4.97

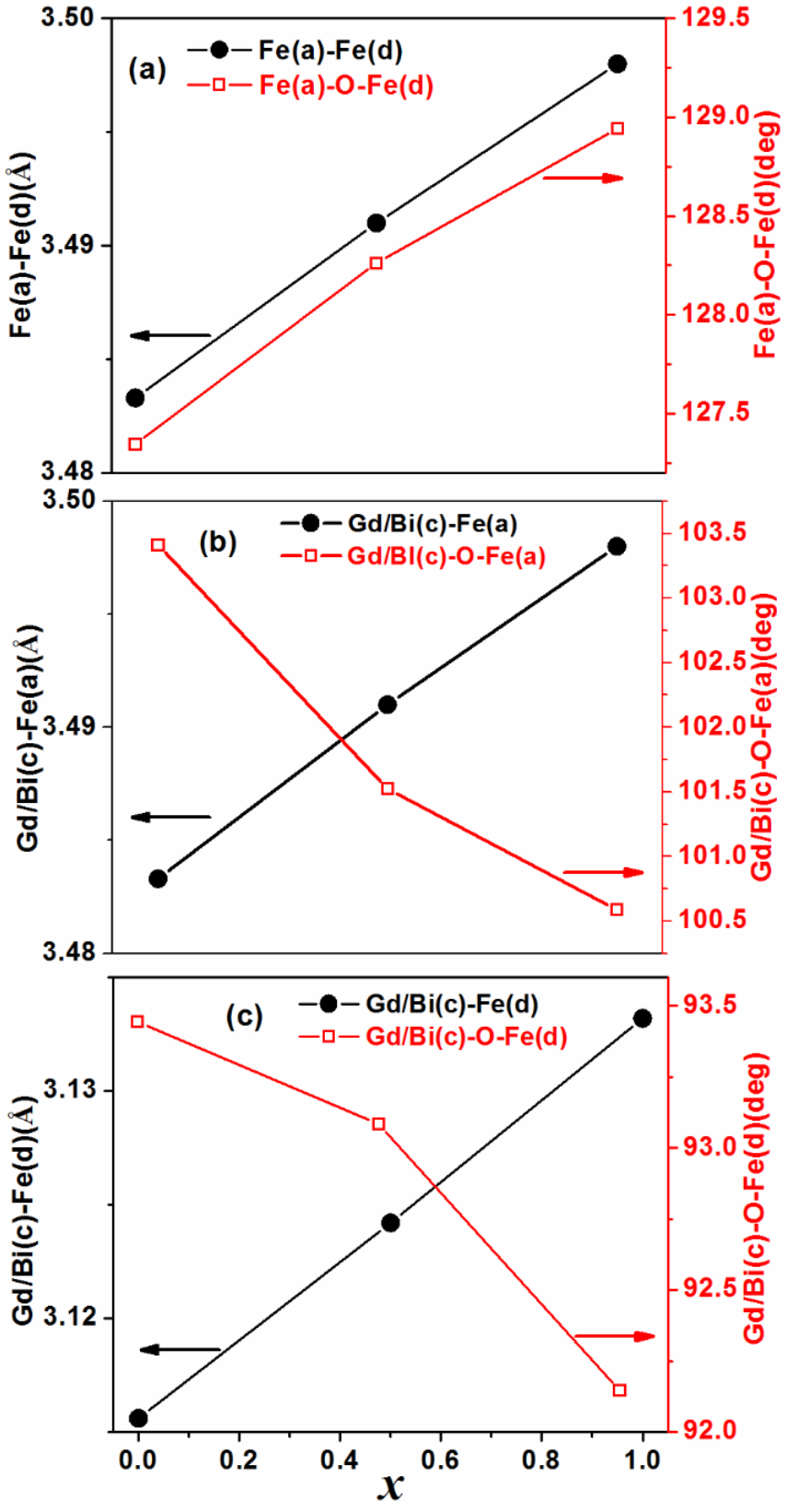

Figure 5.17: Various bond lengths and bond angles as a function of Bi-concentration (*x*).

FESEM micrographs of (Gd, Bi)-Fe-O samples along with a typical EDX spectrum of x = 0.5 sample are shown in Figure 5.18. Both grains and grain boundaries are clearly visible with the reduction in grain size with increase in Bi concentration. The average grain size values are found to be 4.5 μm, 2.7 μm and 2.1 μm for x = 0, 0.5 and 1.0 samples, respectively with a maximum error of ±0.2 μm. The observed smaller grain size in Bi substituted samples can be attributed to relatively lower sintering temperature and sintering duration chosen for these samples to avoid Bi loss due to its lower melting point. The sample density values are found to be 6.40, 6.62 and 6.70 g/cm^3 for x = 0, 0.5 and 1.0, respectively. The EDX spectrum (Figure 5.18(d)) shows the presence of Bi in addition to host elements such as Gd and Fe. The typical sample compositions obtained from the EDX spectra for x = 0.5 and 1.0 samples are Gd: Bi: Fe = 2.47: 0.48: 4.97 and 1.98: 0.97: 4.97 respectively and they are in agreement with the nominal starting composition.

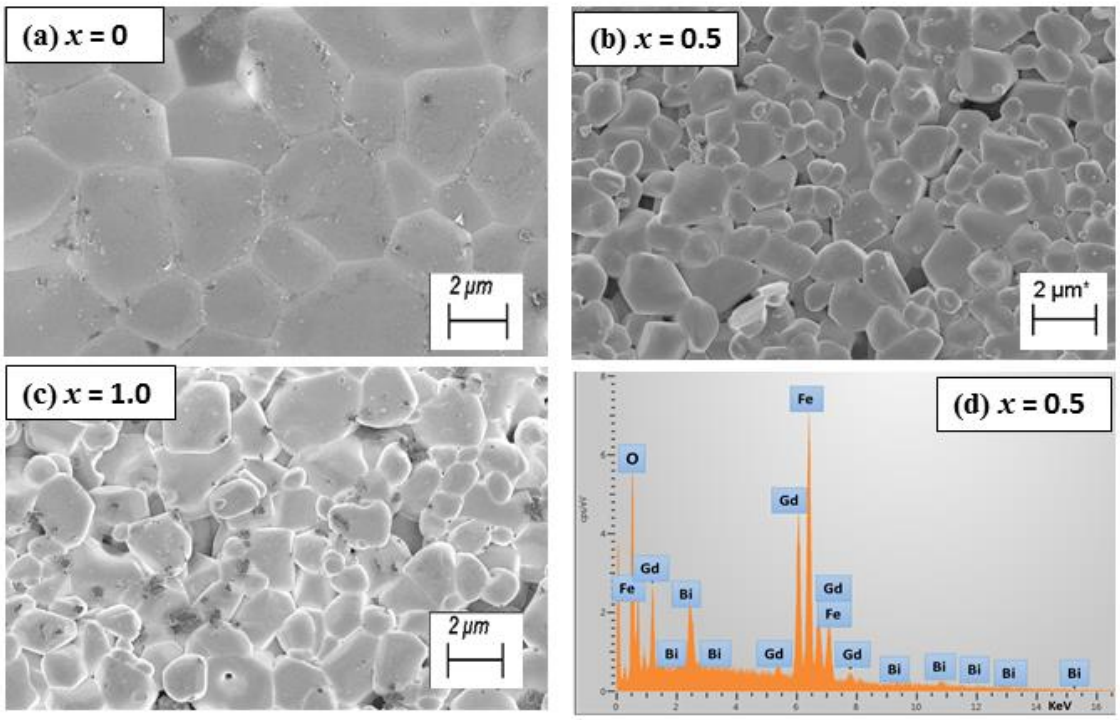

Figure 5.18: (a-c) FESEM micrographs of x = 0, 0.5 and 1.0 samples and (d) the EDX spectrum for x = 0.5 sample.

5.2.2 Magnetic Studies

Temperature variations of magnetization (*M-T*) measured under zero field cooled (ZFC) condition for H = 200 Oe in the low temperature (25 K to 300 K) as well as in the high temperature (300 K to 800 K) regions are shown in Figure 5.19(a) and (b),

respectively. All these samples undergo ferrimagnetic (FIM) transition with considerable increase in transition temperature (T_C) with Bi-substitution. The FIM transition is followed by a magnetic compensation at low temperature, i.e., below 300 K. The FIM T_C was determined from the plots of first order derivative of magnetization with respect to temperature (*dM/dT* versus T) and it is found to increase from 567 K for x = 0 to 596 K for x = 1.0 as given in Table 5.5. The FIM T_C of the parent compound (x = 0) is comparable with that of reported value by *Nguyet* et al. [118]. On the other hand, $Bi_3Fe_5O_{12}$ is known to exhibit higher FIM T_C > 600 K [75] and it is comparable with the present work for x = 1.0. The increase in FIM T_C can be attributed to the strengthening of superexchange interaction in $Fe^{3+}(a)$-O^{2-}-$Fe^{3+}(d)$ networks due to the larger bond angle as observed from XRD analysis. Such enhanced bond angle is known to improve the superexchange interactions through oxygen ions due to better overlapping of electronic orbitals [34]. Similar increase in FIM T_C is reported in Bi substituted YIG [104,135].

In addition to FIM transition, these samples undergo magnetic compensation as shown in Figure 5.19(a). The magnetic compensation temperature (T_{Comp}) value for x = 0 sample is found to be 296 K and is comparable with the reported value [43]. However, upon Bi-substitution it is found to decrease as given in Table 5.5. The observed magnetic compensation in RIGs having magnetic rare earth element is due to the weak exchange coupling of magnetic moment of rare earth ion (M_{Gd}) with the resultant magnetic moment of Fe^{3+} ions at '*a*' and '*d*' sites as we have already discussed in section (5.2.2). With the decrease in temperature below the FIM T_C of 567 K, the Gd sublattice moment increases sharply and hence the combination of M_{Gd} and the magnetic moment of two $Fe^{3+}(a)$ ions ($2M_{Fe}(a)$) overcome that of three $Fe^{3+}(d)$ ($3M_{Fe}(d)$) ions leading to a magnetic compensation at 296 K, i.e., $|3M_{Fe}(d)| = |2M_{Fe}(a) + 3M_{Gd}(c)|$. The decrease in T_{Comp} value with Bi-concentration can be understood based on the above empirical relation, where M_{Gd} is reduced due to the substitution of non-magnetic Bi at Gd site and as a result, T_{Comp} is shifted to lower temperature.

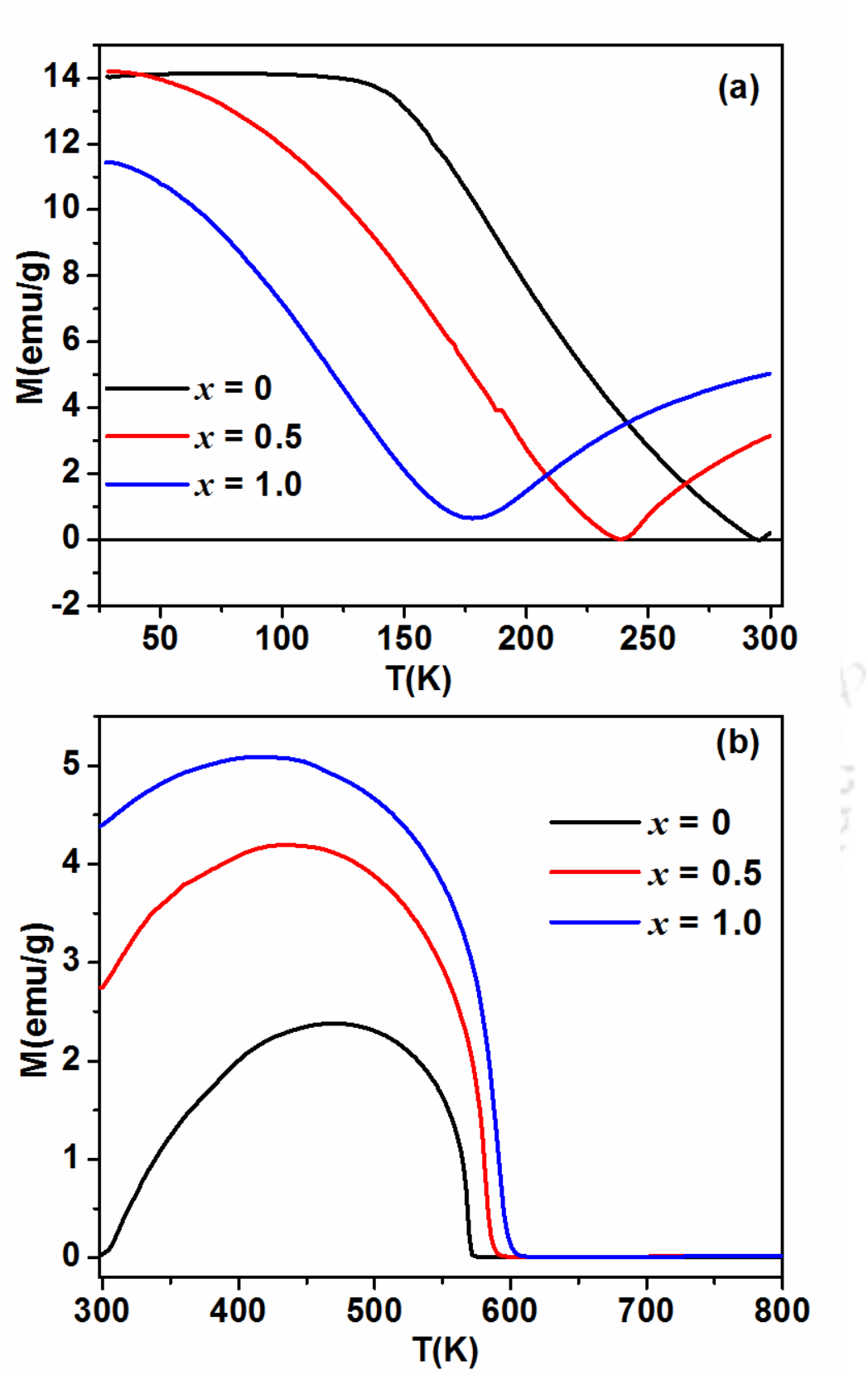

Figure 5.19: *M-T* plots in the temperature range of (a) 25 K to 300 K (b) 300 K to 800 K were recorded with an applied magnetic field of 200 Oe under ZFC condition.

Figure 5.20(a) shows the magnetic field (*H*) variation of magnetization (*M*) in the field range of 5 kOe to -5 kOe at room temperature. We have analyzed the initial magnetization curves to determine the value of saturation magnetization (M_S) for (Gd, Bi)-Fe-O samples using the LAS model (equation 5.1) [139]. The *M-H* data of x = 0 sample were analyzed based on the linear relation: $M = M_S + cH$, i.e., with b = 0 as explained in section (5.1.2). Here, the PM moment of Gd^{3+} ions almost compensate the ferrimagnetic moment of Fe^{3+} ions. However, it is observed that x = 0.5 and 1.0 follow the LAS model. Figure 5.20(b) shows fitted data to LAS model along with the observed data of initial magnetization for all the (Gd, Bi)-Fe-O samples. The room temperature M_S value is found to increase from 0.20 emu/g for x = 0 to 6.89 emu/g for x = 1.0. The rather small value of M_S for x = 0 sample is mostly due to the chosen temperature which is close to the magnetic compensation temperature. Nevertheless, the increasing trend of M_S value with Bi-substitution can be explained based on the empirical relation:

$$M_{net} = 3M_{Fe}(d) - 2M_{Fe}(a) - [(3-x)M_{Gd}(c) - xM_{Bi}(c)] \qquad (5.3)$$

Since Bi is non-magnetic in nature so, the net moment in the rare earth site or the term within the square bracket in the above relation decreases, which leads to net increase in M_S value as per the above relation. The value of K_1 is found to increase with Bi concentration and it is in agreement with the increase in M_S value. The obtained values of K_1, M_S and coercivity (H_C) are given in Table 5.5. However, the value of K_1 for x = 0 at room temperature could not be estimated due to the chosen linear relation with b = 0. The observed higher H_C value for x = 0 sample as compared to other samples may be due to the measurement, which was carried out in the vicinity of T_{Comp}. The plot of *dM/dH* versus *H* as shown in the inset of Figure 5.20(a) shows a single peak and indicates quite narrow particle size distribution with predominant ferrimagnetic behaviour without any magnetic frustration.

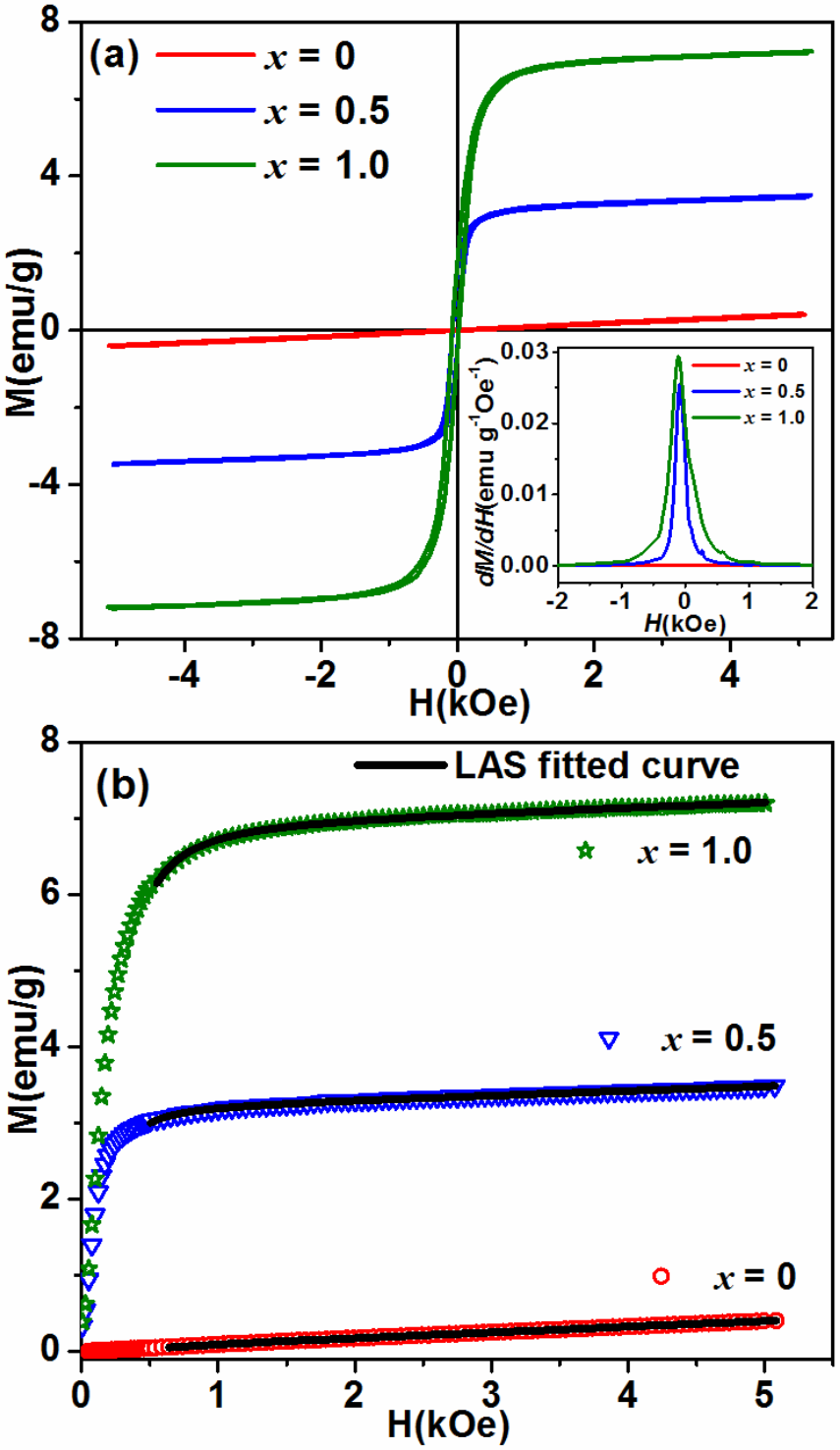

Figure 5.20: (a) *M-H* loops of (Gd, Bi)-Fe-O samples. Inset shows *dM/dH* versus H plots. (b) Initial magnetization data along with fitted data to LAS model for x = 0, 0.5 and 1.0 samples.

Table 5.5: The values of T_{Comp}, T_C, M_S, H_C and K_1 obtained from the magnetization data of (Gd, Bi)-Fe-O samples.

x	**0**	**0.5**	**1.0**
T_{Comp} **(K)**	296	240	176
T_C **(K)**	567	581	596
M_S **(emu/g)**	0.18	3.18	6.89
H_C **(Oe)**	150.0	16.0	36.0
K_1 **(erg/cm^3)**	-	9.97×10^3	3.11×10^4

5.2.3 Complex Impedance Spectroscopy Studies

Figure 5.21(a) and (b) show the frequency variations of Z' and -Z" for all the (Gd, Bi)-Fe-O samples at room temperature. It is observed that both Z' and -Z" values decrease gradually with the increase in frequency without any signature of relaxation process at room temperature. This can be also attributed to the lack of mobility of charge carriers due to relatively low thermal energy at room temperature. The values of both Z' and -Z" are found to increase with Bi concentration. For example, Z' at 100 Hz is found to be 0.1, 11.0 and 22.0 MΩ for x = 0, 0.5 and 1.0 samples respectively. The increase in both Z' and -Z" values with increase in Bi concentration can be attributed to reduced grain size as well as reduction in oxygen vacancies and associated charge carriers.

The impedance spectrum (-Z" versus f) was recorded by rising the set temperature in a step size of 10-15 K. As the temperature is raised to 558 K a clear relaxation behaviour is observed for x = 0 sample as shown in Figure 5.21(c). As the temperature is further raised, the relaxation peak is found to shift towards higher frequency. Such peak shifting highlights that relaxation process is thermally activated. Similar relaxation peaks are observed for x = 0.5 and 1.0 samples. For x = 1.0 sample, the relaxation peak is observed for T ≥ 523 K as shown in Figure 5.21(d). Since the relaxation process is observed only at higher temperature, it can be easily attributed to the relaxation across grain boundaries, i.e., in the long-range scale. The observed relaxation peaks were analyzed based on Arrhenius law:

$$\tau = \tau_0 \exp\left(\frac{-E_a}{k_B T}\right) \tag{5.4}$$

Here, relaxation time $\tau(=1/2\pi f_{max})$ is obtained from the peak frequency f_{max} at each temperature and E_a represents the activation energy. Figure 5.22(a-c) shows the Arrhenius

plots of (Gd, Bi)-Fe-O samples. They follow the linear behaviour and the obtained values of E_a are found to be 0.92(5), 0.98(4) and 1.08(8) eV for x = 0, 0.5 and 1.0 samples, respectively and these E_a values are assigned to the doubly ionized oxygen vacancies [150]. Since, Bi-substitution reduces the sintering temperature so, the number of Fe^{2+} and Fe^{3+} ions become less, thus lead to less electron hopping. The reduction in electron hopping may lead to increase in activation energy.

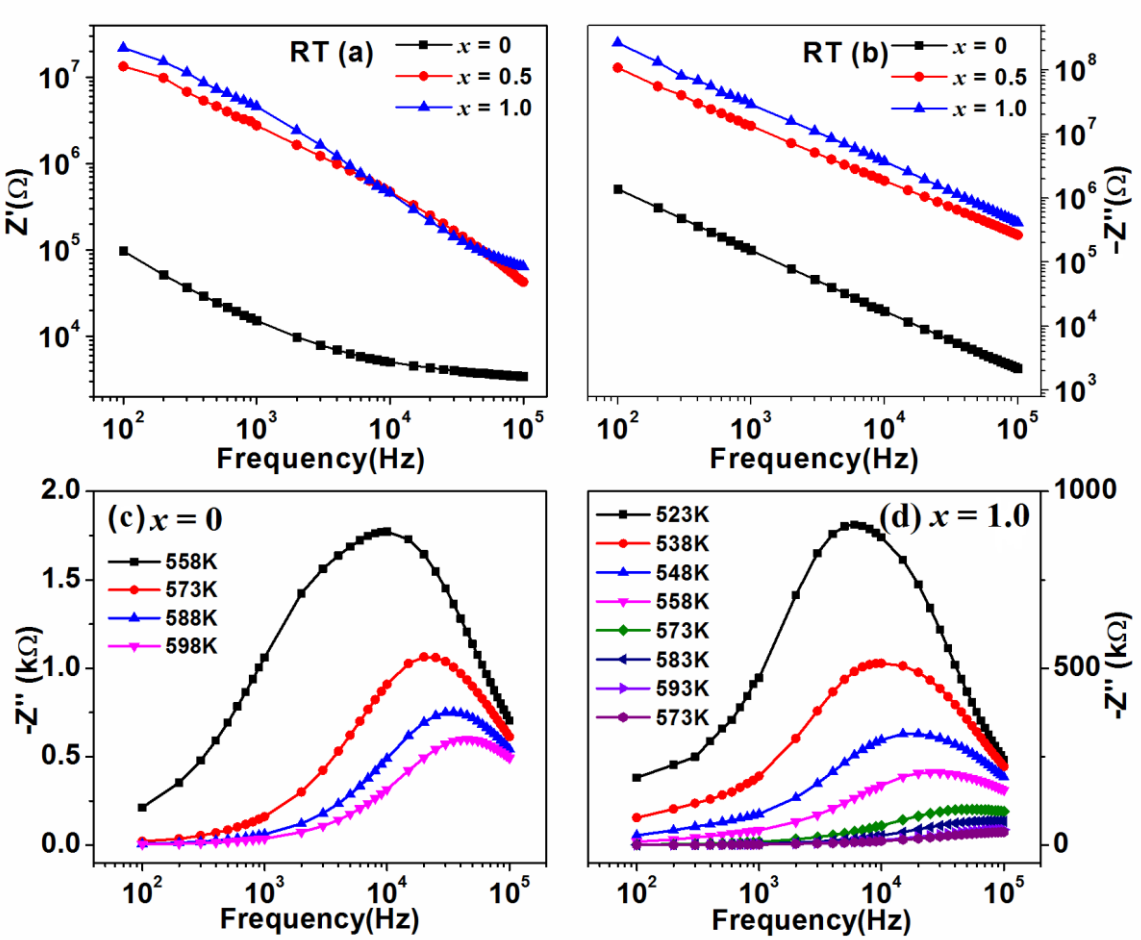

Figure 5.21: (a) Z' and (b) -Z" as a function of frequency for (Gd, Bi)-Fe-O samples at room temperature, (c, d) -Z" versus frequency at different temperatures for x = 0 and 1.0 samples.

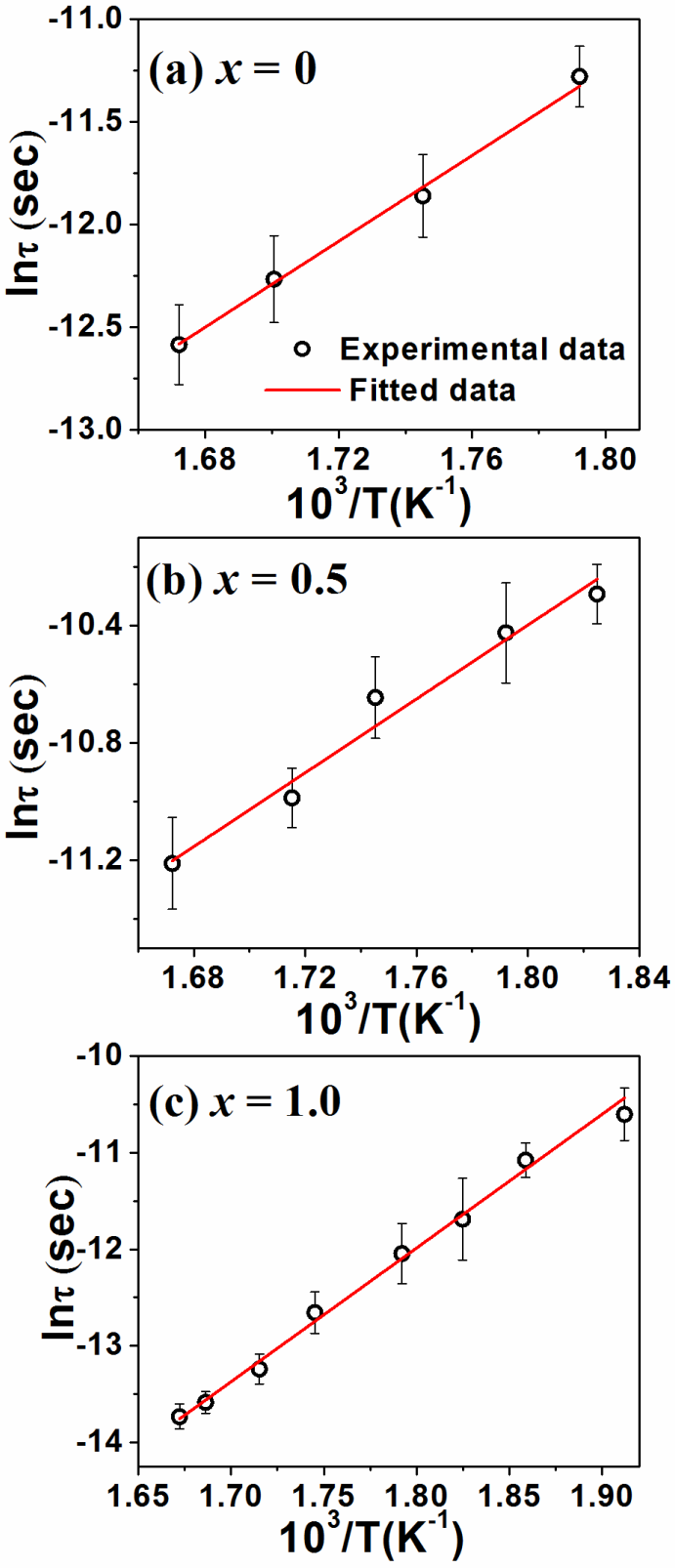

Figure 5.22: Arrhenius plots of relaxation time for (a) x = 0, (b) x = 0.5 and (c) x = 1.0 samples along with fitted data using Arrhenius equation.

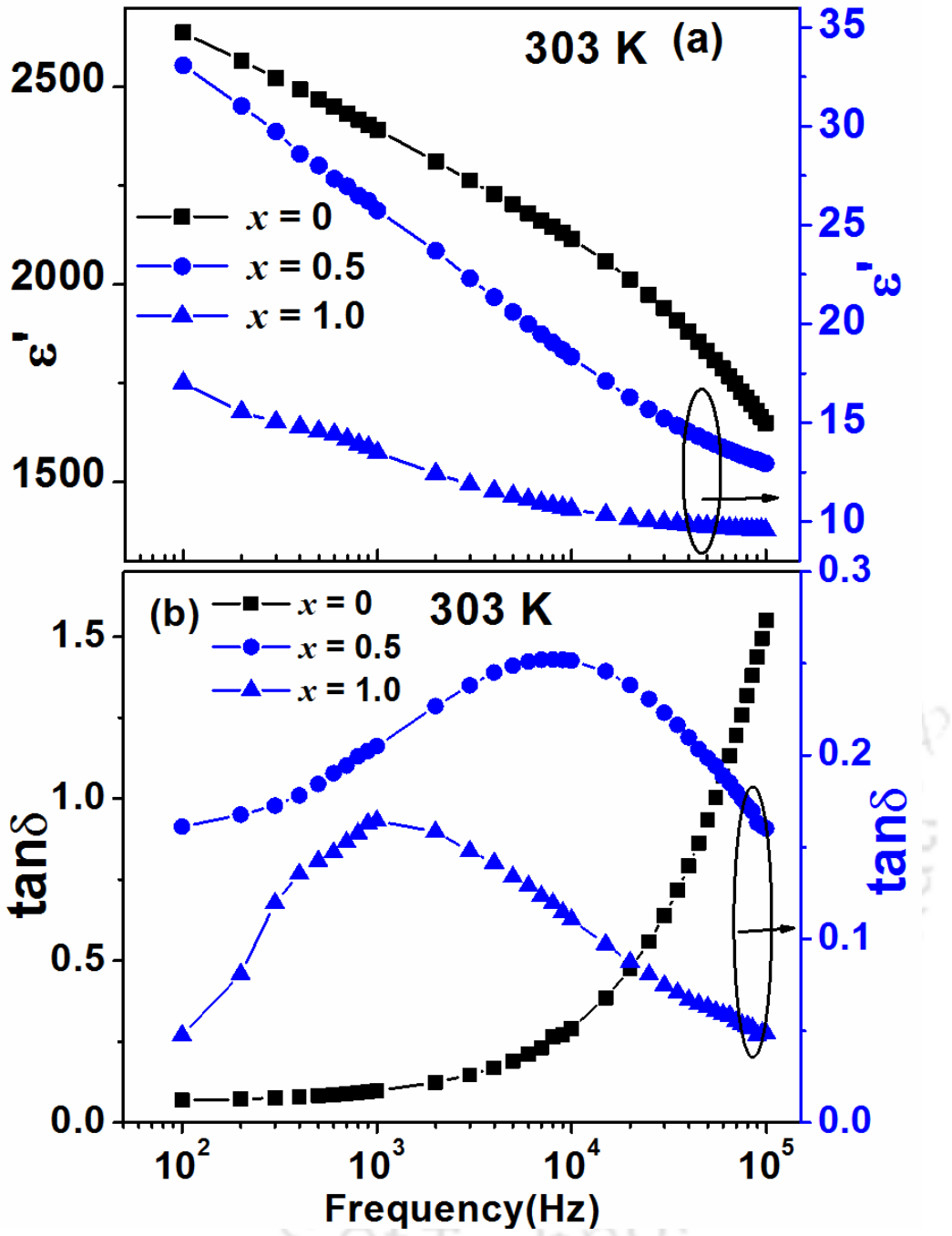

Figure 5.23: Frequency variations of (a) ε' and (b) tanδ for (Gd, Bi)-Fe-O samples at room temperature.

The frequency variations of the real component of dielectric constant (ε') and the loss tangent (tanδ) are shown in Figure 5.23. ε' is found to decrease monotonously with increase in frequency with a relaxation like behaviour for $f > 10^4$ Hz in $x = 0$ sample. The corresponding tanδ versus f plot of $x = 0$ sample shows small value upto around 10^4 Hz and beyond that it rises sharply. This behaviour can be attributed to relaxation peak falling above the measured frequency range. The ε' versus f plots of $x = 0.5$ and 1.0 samples exhibit

similar trend as that of x = 0 sample, but their values are suppressed strongly by about two orders of magnitude. Such sharp reduction in ε' value of Bi-substituted samples can be attributed to lack of charge carriers due to reduction in oxygen vacancies as these samples are annealed at lower temperature compared to the parent compound. However, tanδ values are smaller by an order of magnitude compared to the parent compound. Moreover, tanδ versus f plots of x = 0.5 and 1.0 samples show relaxation peaks within the measured frequency spectrum. The peak frequency (f_{max}), i.e., the frequency at which tanδ versus f plots exhibit a peak is found to be shifted towards lower frequency with increase in Bi-concentration. Such shifting of f_{max} value can be attributed to reduction in mobility of charge carriers due to enhanced grain boundaries volume.

The plots of temperature dependence of ε' and tanδ in the high temperature (T) range of 450 K to 600 K are shown in Figure 5.24 for x = 0 and 1.0 samples. The above measurements were repeated for different frequencies in the range of 100 Hz to 100 kHz. The ε' versus T plots show a broad peak for each frequency and as the frequency is increased the peak is found to be shifted towards higher temperature. Moreover, with increase in frequency the peak ε' value (ε'_{max}) is found to be suppressed. The tanδ data are found to increase with temperature with a step like behaviour in the vicinity of peak observed in ε' versus T plot. The RIG exhibits centrosymmetric structure and hence no ferroelectric transition is expected. However, the observed broad peak can be attributed to the relaxor ferroelectric transition due to local distortion in the crystal structure in the nano-region. Such behaviour is reported in Bi-substituted YIG [124]. The structurally distorted polar nano-region generally appears in the para-electric region, i.e., above the transition temperature due to short-range interactions in the local polar states (Fe^{2+}-Fe^{3+}). *Uchino* and *Nomura* [171] has explained the dielectric constant for relaxor ferroelectric using the modified Curie-Weiss law of diffused phase transition. It can be expressed in terms of power relation as following:

$$\left(\frac{1}{\varepsilon'} - \frac{1}{\varepsilon'_m}\right) = \frac{(T-T_m)^\gamma}{C} \qquad \text{for, } T > T_m \tag{5.5}$$

Here T_m and ε'_m represent the temperature at which broad peak is observed in ε' versus T plots and the corresponding ε' value, i.e., ε' (T_m). γ and C represent the temperature independent diffuseness exponent and Curie constant respectively. The value of γ gives the degree of diffuseness in the sample and lies in the range of 1 to 2. In a normal ferroelectric material γ is close to 1, whereas for an ideal relaxor ferroelectric material it would be close

to 2. The values of ε'_m and T_m at 100 Hz, 1 kHz and 10 kHz are given in Table 5.6. Figure 5.25 shows the typical plot of $ln\left(\frac{1}{\varepsilon'}-\frac{1}{\varepsilon'_m}\right)$ versus $ln(T-T_m)$ for x = 0 sample at f = 200 Hz in the temperature range of 523 K to 598 K. It is found to follow a linear behaviour and the fitted data as per equation 2 are shown as solid line. The fitted parameters C and γ are found to be 2.11x10^8 K and ~ 2.16 (±0.21) respectively for x = 0, and it highlights the relaxor type ferroelectric behaviour. Similar kind of behaviour is observed for Bi substituted GIG samples with smaller C values of the order of 10^6 K and the γ values are close to 2.0. Thus, all (Gd, Bi)-Fe-O samples exhibit relaxor type of ferroelectricity. Similar kind of relaxor ferroelectric behaviour has been reported in $Y_2BiFe_5O_{12}$ compound with the γ value of 2.014 (±0.15) [124].

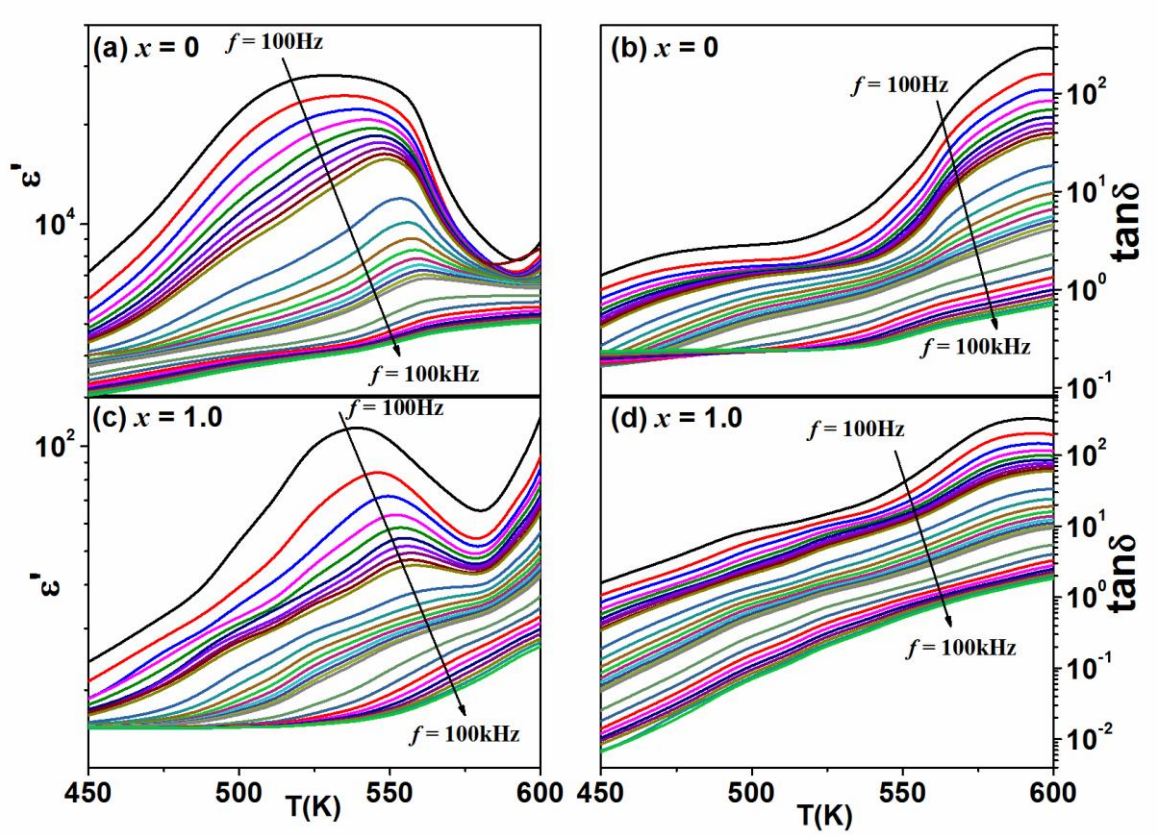

Figure 5.24: (a, c) ε' and (b, d) tanδ as a function of T for different applied frequencies (100 Hz to 100 kHz) for x = 0 and 1.0 samples.

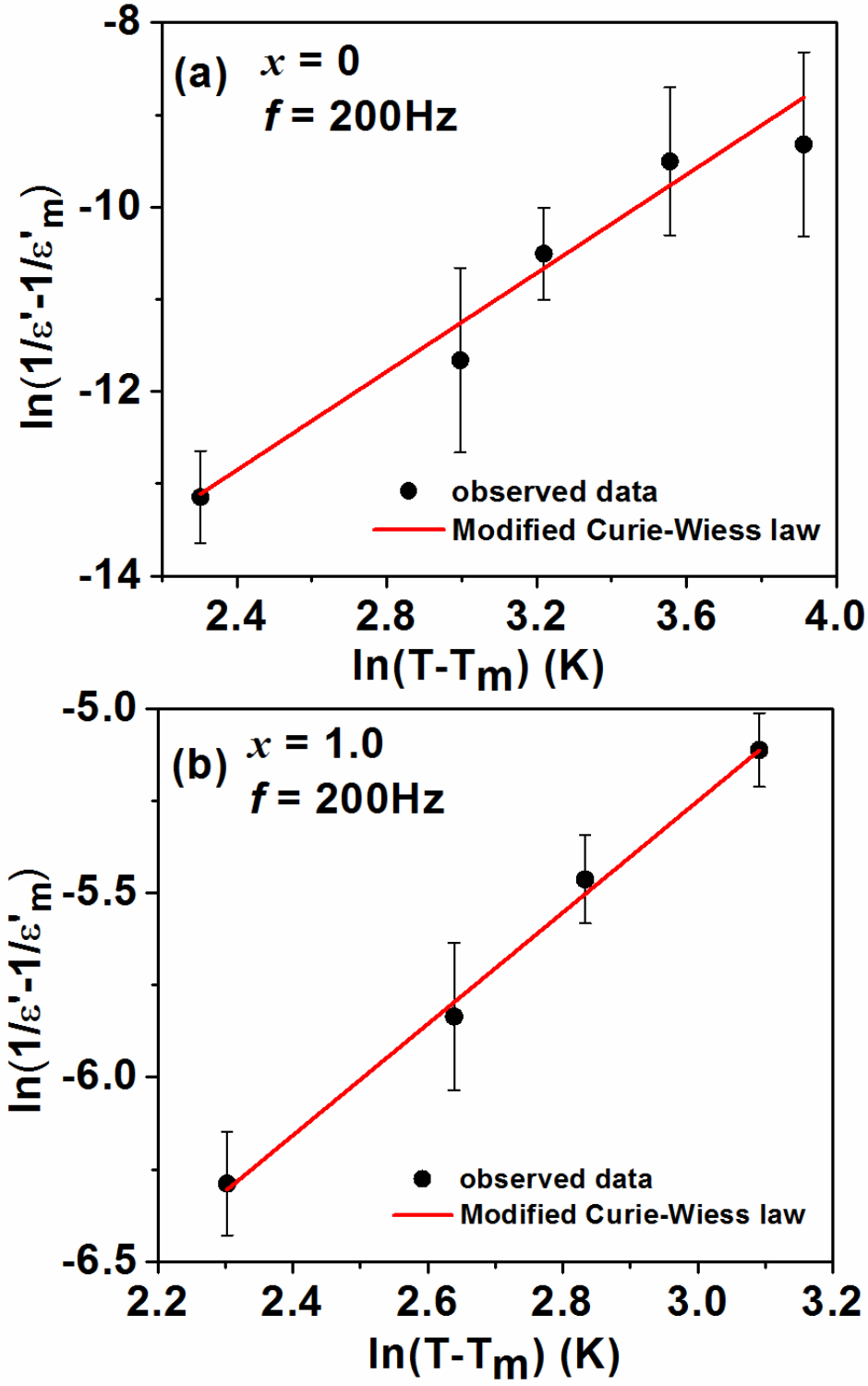

Figure 5.25: The plot of $ln\left(\frac{1}{\varepsilon'}-\frac{1}{\varepsilon'_m}\right)$ versus $ln(T-T_m)$ in the temperature range of 523 K to 598 K at f = 200 Hz for x = 0 and 1.0 samples along with fitted data using equation (5.5).

Table 5.6: T_m and ε'_m data for (Gd, Bi)-Fe-O samples at different frequencies.

x	***f* = 100 Hz**		***f* = 1 kHz**		***f* = 10 kHz**	
	T_m (K)	ε'_m	T_m (K)	ε'_m	T_m (K)	ε'_m
0	523	28253	548	16323	563	6888
0.5	530	3762	558	945	558	46
1.0	538	116	568	661	-	-

5.3 Conclusion

Sm-substituted polycrystalline gadolinium iron garnet ($Gd_{3-x}Sm_xFe_5O_{12}$) with compositions x = 0, 0.5, 1.0, 2.0 and 3.0 were prepared in pure-phase form by solid-state reaction method. These samples were Rietveld refined using (cubic) space group $Ia\bar{3}d$. The substitution of larger Sm^{3+} ions at Gd^{3+} site gives rise to considerable increase in lattice constant, i.e., from 12.4624 Å (x = 0) to 12.5211 Å (x = 3.0). We have carried out magnetization measurements (*M-T*) under zero field cooled (ZFC) condition in the temperature range of 25 K to 700 K with an applied field of 200 Oe. Sm-substitution leads to stronger $Fe^{3+}(a)$-O^{2-}-$Fe^{3+}(d)$ superexchange interaction and larger ferrimagnetic T_C, i.e., from 567 K (x = 0) to 575 K (x = 3.0). In addition, these samples exhibit magnetic compensation with decrease in T_{Comp} value, i.e., from 293 K (x = 0) to 70 K (x = 2.0). No T_{Comp} is observed for x = 3.0 sample in the measured temperature range. Sm-substitution enhances magnetic anisotropy thereby, an interesting negative magnetization is introduced in x = 2.0 sample below T_{Comp}. In order to confirm the negative magnetization, we have carried out the FC measurement under H_{FC} = -200 Oe and observed the opposite behaviour as that of H_{FC} = 200 Oe (mirror image). We have also demonstrated an improvement in saturation magnetization at room temperature upon substitution of Sm at Gd site. The increase in M_S value can be understood in terms of Sm^{3+} (0.71 μ_B) ions having smaller magnetic moment substituting the Gd^{3+}(7 μ_B) ions at the '*c*' site. The estimated value of anisotropy constant is found to increase from (1.39± 0.03)×10^3 erg/cm^3 for x = 0 to (1.65± 0.05)×10^4 erg/cm^3 for x = 3.0 and is in agreement with the explanation given for negative magnetization in x = 2.0 sample. The Nyquist plots (-Z" vs Z') were analyzed using an equivalent circuit comprised of resistance, capacitance and constant phase element in

parallel with a series resistance. The depressed and asymmetric nature of Nyquist plots show that the relaxation departs from the ideal Debye type and it has been controlled by thermal activation of charge carriers. The relaxation time was analyzed by Arrhenius law and they show an anomaly in the vicinity of ferrimagnetic transition temperature, which highlights the presence of magneto-electric coupling. The activation energy for charge carriers varies from 0.41 eV to 0.71 eV in the FIM region and 0.91 eV to 1.19 eV in the PM region.

In addition to (Gd, Sm)-Fe-O compounds, we have discussed about the Bi-substituted GIG ($Gd_{3-x}Bi_xFe_5O_{12}$ for x = 0, 0.5 and 1.0) samples, synthesized using solid-state route. These samples are found to be crystallized in cubic structure with $Ia\bar{3}d$ space group. The lattice constant, Fe(a)-Fe(d) bond length, Fe(a)-O-Fe(d) bond angle values are found to increase with Bi-concentration. The magnetization versus temperature measurements, show that all (Gd, Bi)-Fe-O samples undergo FIM transition followed by magnetic compensation (T_{Comp}). The transition temperature (T_C) is found to increase from 567 K for x = 0 to 596 K for x = 1.0 and it is explained in terms of strengthening of superexchange interaction across Fe^{3+}(a)-O^{2-}-Fe^{3+}(d) networks due to favourable bond angle in these networks. The T_{Comp} value is found to decrease from 296 K to 176 K with Bi concentration. This can be attributed to the reduction in magnetic moment at rare earth site due to the substitution of non-magnetic Bi^{3+} ions. The substitution of non-magnetic Bi^{3+} ions at Gd^{3+} site leads to increase in the value of saturation magnetization, i.e., from 0.02 emu/g to 6.89 emu/g. Bi-substitution gives rise to larger impedance due to the lack of oxygen vacancies and the associated reduction in charge carriers, as per the impedance spectra analysis. We have observed a sharp reduction in ε' value in Bi-substituted samples, which can be attributed to lack of Fe^{2+} and Fe^{3+} ions due to reduction in oxygen vacancies as these samples were annealed at lower temperature compared to the parent compound. However, tanδ values are found to be smaller by an order of magnitude compared to the parent compound, i.e., from 1.5 for x = 0 to 0.5 for x = 1.0. The ε' versus T measurements show a broad peak for each frequency, and as the frequency is increased the peak is found to be shifted to higher temperature. Moreover, with increase in frequency the peak ε' value (ε'_{max}) is found to be suppressed. Since, the RIGs exhibit centrosymmetric structure and hence no ferroelectric transition is expected. So, the observed broad peak is attributed to the relaxor ferroelectric transition due to local distortion in the crystal structure in the polar Nano-region. The ε' versus T plots were analyzed in terms of modified Curie-Weiss law, and they show the relaxor ferroelectrics behaviour with diffuseness exponent close to 2.

Chapter 6

Magnetic and Dielectric Studies in Gd-(Fe, Cr)-O Series

Gadolinium iron garnet (GIG) exhibits cubic crystal structure with $Ia\bar{3}d$ space group having 8 formula units per unit cell. GIG undergoes ferrimagnetic transition at 560 K due to the strong magnetic coupling of Fe^{3+}(*a*) and Fe^{3+}(*d*) ions [119]. However, a weak coupling of Gd ions located at dodecahedral site with the net ferrimagnetic moment of Fe ions leads to magnetic compensation around 286 K [118,120,121]. Other RIGs (R = Dy, Ho, Tb and Er) having magnetic rare earth element also undergo magnetic compensation at lower compensation temperature compared to that of GIG [43]. *Geller* et al. [172] have reported the reduction in transition temperature (T_C) from 560 K to 30 K with Al-substitution in GIG at Fe(d) site. On the other hand, the substitution of Sc at Fe(a) site reduces the T_{comp} upto 128 K. *Ilanchezhiyan* et al. [173] have reported the cobalt-substituted GIG nano-garnet for the application of magneto-optical and spintronic devices. The substitution of smaller (larger) ions occupy tetrahedral (octahedral) site of Fe^{3+} ions in RIGs. However, Cr^{3+} ions ($3d^3$) having smaller ionic size, preferentially occupy the octahedral site based on crystal field theory (CFT) [105]. As per our literature survey, the detailed study of magnetic and dielectric properties of Cr-substituted GIG is still lacking. Hence, the primary motivation of the present work is to tune the magnetic and dielectric properties by Cr-substitution.

Polycrystalline samples of $Gd_3Fe_{5-x}Cr_xO_{12}$ (Gd-(Fe, Cr)-O) for x = 0 to 0.3 were synthesized through standard solid-state reaction process. The oxides of Gd, Cr and Fe were taken as starting compounds (purity > 99%). The stoichiometric amounts of initial precursors were mixed homogeneously under the acetone medium for approximately 3 hours. The resultant mixture was pre-sintered at 873 K for 12 hours. Thereafter, the powder was pressed into cylindrical pellets of 10 mm diameter and 1.5 mm thickness and finally sintered at 1673 K for 24 hours.

6.1 Structural Studies

Room temperature (RT = 300 K) XRD patterns of Gd-(Fe, Cr)-O samples are shown in Figure 6.1. These patterns were Rietveld refined based on $Ia\bar{3}d$ (O_h^{10}) space group using Fullprof program [129] and, as per the analysis the samples are found to be in single-phase form. The experimental and Rietveld refined data closely follow each other with goodness of fit, $\chi^2 \approx 3.25$. As per the Rietveld refinement analysis, the structural parameters such as lattice constant (*a*), unit cell volume (*V*), Fe(*a*)-Fe(*d*) bond length and Fe(*a*)-O-Fe(*d*) bond angle are found to be 12.4729(8) Å, 1946 Å^3, 3.48 Å and 129.4° respectively for $x = 0$ sample, and these values are comparable with the literature [119]. The variations of *a* and *V* with Cr-concentration along with reliability factors and cationic occupancy are given in Table 6.1. The values of the bond length and the bond angle for Gd-(Fe, Cr)-O samples are also given in Table 6.1. These parameters are found to decrease with increase in Cr concentration and it is attributed to the preferential occupation of smaller Cr^{3+} (0.615 Å) ions at the octahedral site of Fe^{3+} (0.645 Å) ions.

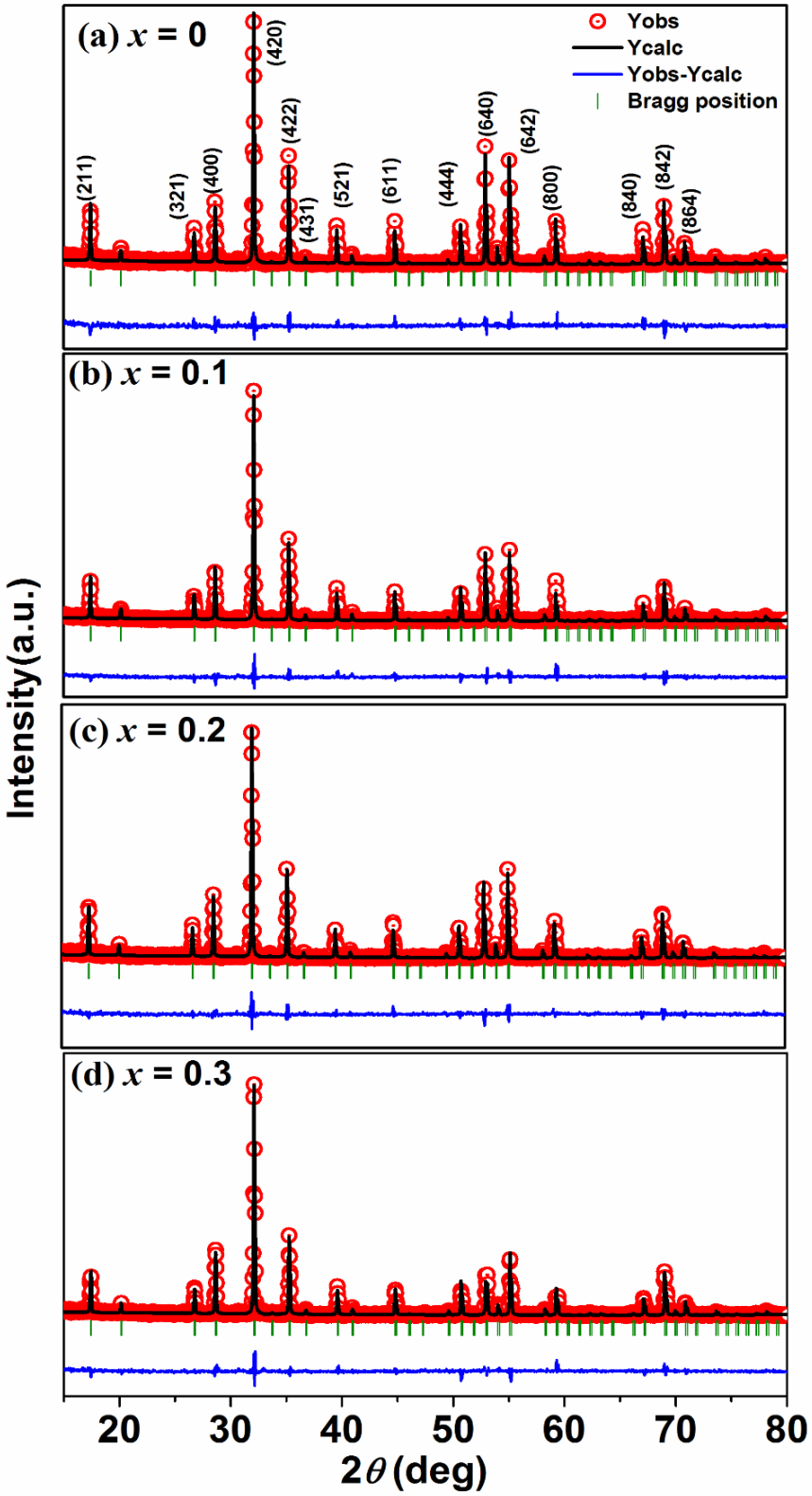

Figure 6.1: (a-d) Rietveld refined (black line) XRD patterns along with experimental data (red circle) for x = 0, 0.1, 0.2 and 0.3 samples.

Table 6.1: Structural and reliability parameters obtained from the Rietveld refinement of XRD patterns and FESEM micrographs of Gd-(Fe, Cr)-O samples with x = 0 to 0.3.

x	**0**	**0.1**	**0.2**	**0.3**
Space group	$Ia\bar{3}d$	$Ia\bar{3}d$	$Ia\bar{3}d$	$Ia\bar{3}d$
$a = b = c$ **(Å)**	12.4729(8)	12.4663(8)	12.4652(8)	12.4621(8)
V **(Å^3)**	1940.4	1937.3	1936.8	1935.4
R_p **(%)**	8.71	9.07	9.15	9.31
R_{ezp} **(%)**	8.00	8.14	8.83	8.72
R_f **(%)**	7.50	6.84	7.12	7.84
R_{Bragg} **(%)**	5.25	5.11	5.16	5.92
χ^2	3.25	3.17	3.32	3.31
Occupancy **Gd**	2.98	2.97	2.97	2.96
Fe	4.96	4.88	4.76	4.65
Cr	0	0.08	0.18	0.26
Fe/Cr(*a*)-Fe(*d*) (Å)	3.4862 (2)	3.4844 (3)	3.4841 (5)	3.4834 (3)
Fe/Cr(*a*)-O-Fe(*d*) (deg)	129.4 (6)	128.5 (5)	126.9 (7)	125.4 (5)
Average grain size (μm)	5.1 (3)	5.3 (7)	8.4 (4)	9.9 (5)

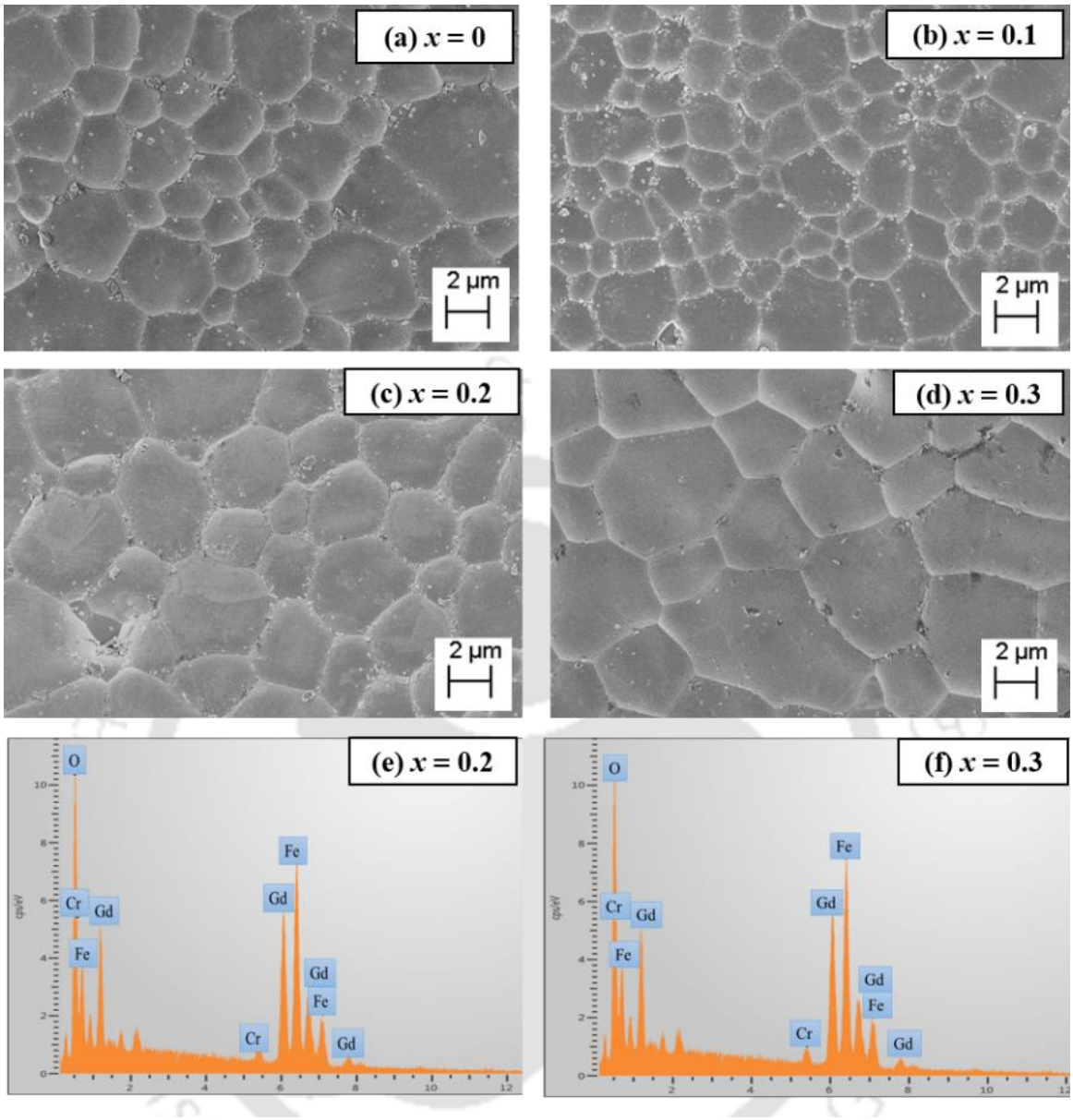

Figure 6.2: (a-d) Typical FESEM micrographs of Gd-(Fe, Cr)-O with x = 0 to 0.3 samples, (e, f) EDX spectra for Gd-(Fe, Cr)-O sample with (a) x = 0.2 and (b) x = 0.3.

Figure 6.2(a-d) shows the FESEM micrographs of Gd-(Fe, Cr)-O for x = 0 to 0.3. It can be seen that; these samples are dense in nature with well separated grains through grain boundaries. The estimated values of average grain size are given in Table 6.1. It is observed that the Cr-substitution leads to grain growth, and it may be due to the enhanced grain boundary mobility due to smaller ionic size of substituted Cr^{3+} ions compared to host cations [138]. Archimedes' principle was used to estimate the relative sample density and it is found to be in the range of 85 to 92 % of the theoretical density. The EDX spectra (Figure 6.2(e, f)) show the presence of Cr ions in addition to host Gd and Fe ions. The

obtained chemical compositions as per the EDX analysis are found to be comparable to the nominal stating composition for Gd-(Fe, Cr)-O samples.

6.2 Magnetic Studies

The thermomagnetic (*M-T*) measurements were carried out under zero field cooled (ZFC) condition in the temperature range of 25 K to 650 K for an applied field of H = 200 Oe. Figure 6.3 shows the *M-T* plot in the low temperature range of 25 K to 300 K (Figure 6.3(a)) and in the high temperature range of 300 K to 650 K (Figure 6.3(b)) for Gd-(Fe, Cr)-O samples. All these samples undergo magnetic compensation below 300 K as shown in Figure 6.3(a). The magnetic compensation is explained based on the competition between the magnetic moment of three Fe ions at the tetrahedral (*d*) site and the sum of magnetic moment due to two Fe ions at the octahedral (*a*) site and the weakly interacted magnetic moments of three Gd ions at the dodecahedral (*c*) site, i.e., $|3M_{Fe}(d)| = |2M_{Fe}(a) + 3M_{Gd}(c)|$. The inset of Figure 6.3(a) shows the magnified view of *M-T* plots near T_{Comp}. It is observed that, Cr^{3+} substitution leads to decrease in compensation temperature (T_{Comp}), i.e., from 294 K for x = 0 to 265 K for x = 0.3 as given in Table 6.2. The reduction in T_{Comp} value can be attributed to the domination of '*d*' sublattice magnetization due to the occupation of substituted Cr^{3+} ions in the '*a*' sublattice. Furthermore, in addition to magnetic compensation, all the Gd-(Fe, Cr)-O samples undergo ferrimagnetic (FIM) transition and the transition temperature (T_C) was determined from the plots of *dM/dT* versus T as shown in the inset of Figure 6.3(b). The FIM T_C is found to decrease from 569 K for x = 0 to 518 K for x = 0.3 (Table 6.2) and such decreasing trend is associated to the weakening of superexchange interaction across Fe^{3+}(*a*)-O^{2-}-Fe^{3+}(*d*) networks due to Cr-substitution induced decrease in bond angle as per the XRD analysis.

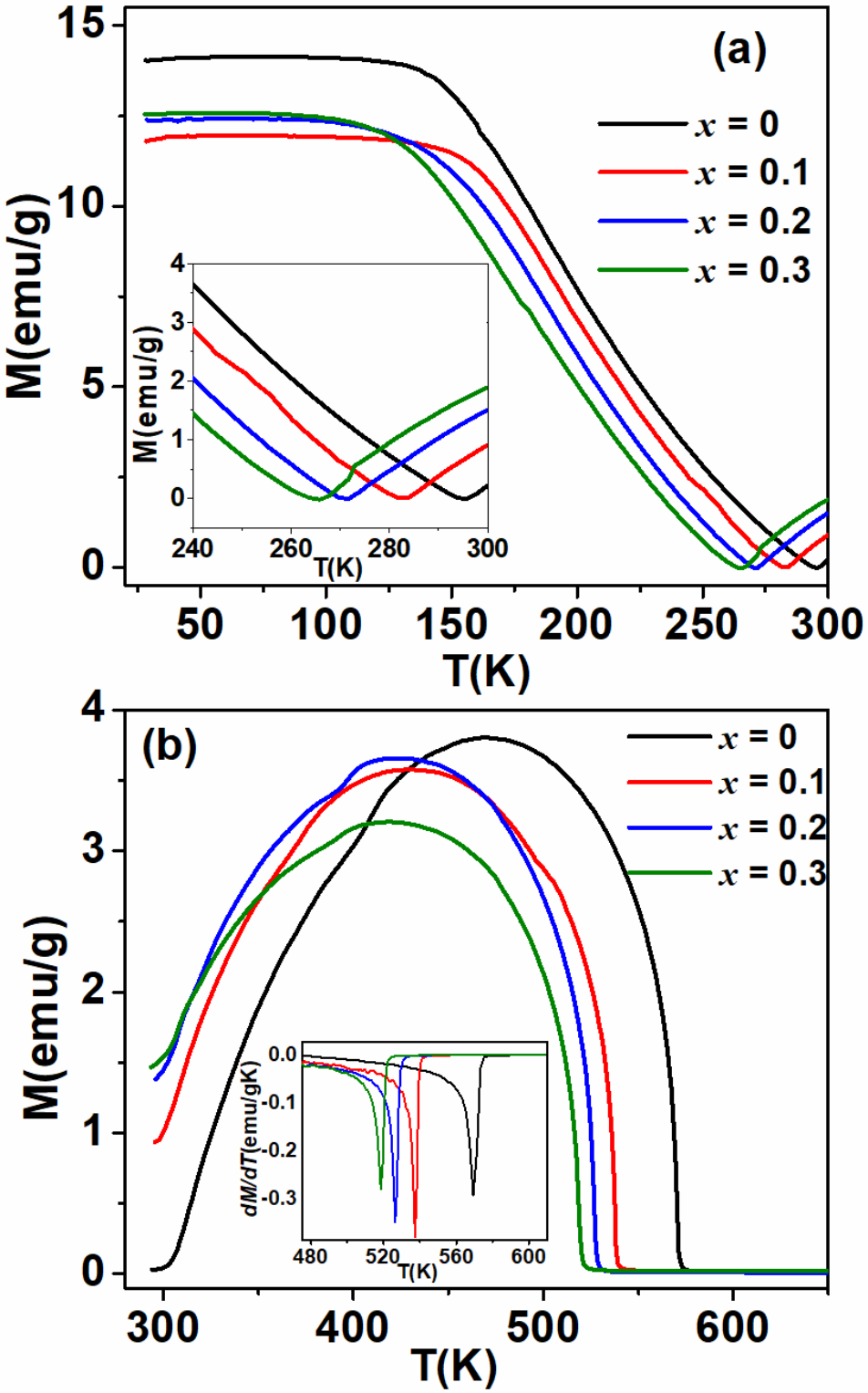

Figure 6.3: *M* versus T plots in two different temperature regions (a) T = 25 K to 300 K, (b) T = 300 K to 650 K at H = 200 Oe under ZFC condition. Insets show the enlarged view of *M-T* plots in the vicinity of T_{Comp} and *dM/dT* versus T plots respectively.

Figure 6.4(a) shows the isothermal magnetization (*M* versus *H*) plots, recorded at room temperature (RT = 300 K) for Gd-(Fe, Cr)-O samples. The saturation magnetization, M_S and anisotropy constant K_1 were estimated by analyzing the initial magnetization data using the law of approach to saturation (LAS) [139].

$$M = M_S\left(1 - \frac{b}{H^2}\right) + cH,\ b = \frac{8K_1^2}{105\mu_0^2 M_S^2} \tag{6.1}$$

Here *cH* indicates the forced magnetization. LAS model is not applicable for $x = 0$ sample, because its *M-H* plot is recorded near the magnetic compensation temperature and shows linear contribution at higher field. So here, the linear behaviour of *M-H* data in the high field region can be analyzed based on the relation, $M = M_S + cH$, i.e., with b = 0 in equation (6.1). Hence, magnetization data of $x = 0$ sample were analyzed based on the above linear relation. For $x > 0$, the magnetization data are fitted to the LAS model. The initial magnetization data along with the fitted data to LAS model are shown as symbols and black solid line respectively in Figure 6.4(b). The obtained value of M_S at room temperature is found to increase with Cr-substitution, i.e., from 0.56 emu/g for $x = 0$ to 2.29 emu/g at $x = 0.3$, and they are given in Table 6.2. The increase in M_S value with Cr concentration can be understood as per the empirical formula:

$$M_{net} = 3M_{Fe}(d) - [(2-x)M_{Fe}(a) - xM_{Cr}(a)] - 3M_{Gd}(c) \tag{6.2}$$

The major contribution towards magnetization comes from the ferrimagnetic ordering of Fe^{3+} ions at '*d*' and '*a*' site. Thus, the substitution of Cr^{3+} ions having smaller magnetic moment ($3\ \mu_B$) at the (down spin) octahedral site of Fe^{3+} ions having larger magnetic moment ($5\ \mu_B$) gives rise to net increase in magnetic moment as per the above empirical relation 6.2. The coercivity (H_C) values are found to be 98 Oe, 16 Oe, 20 Oe and 34 Oe for $x = 0$, 0.1, 0.2 and 0.3 samples respectively. The observed relatively large value of H_C for $x = 0$ is primarily due to the measurement carried out near the magnetic compensation temperature. However, the H_C value is found to increase as the Cr-concentration is increased above $x > 0.1$.

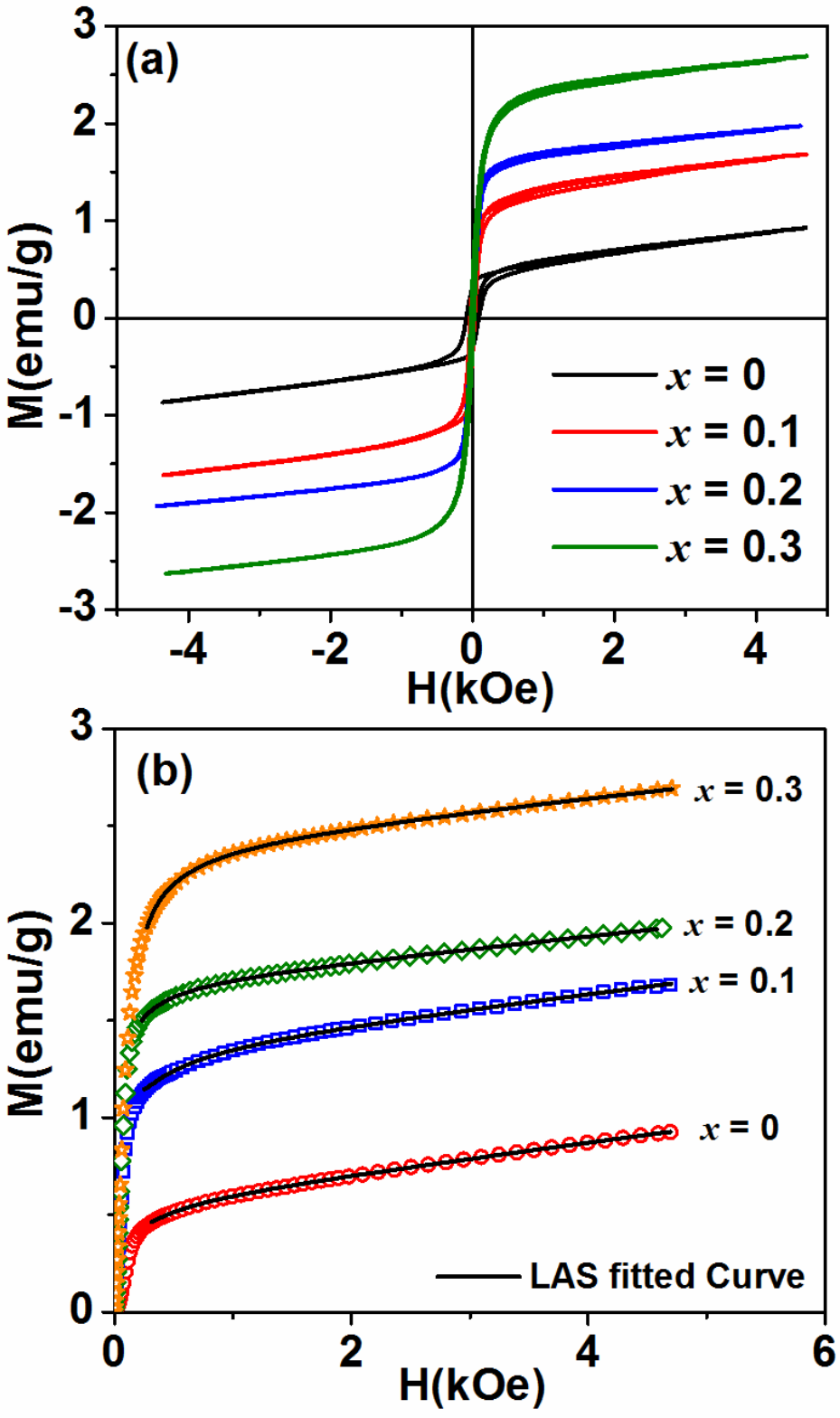

Figure 6.4: (a) Magnetization versus field (*M-H*) loops at 300 K (b) LAS fitted data (black line) along with experimental initial magnetization data (open symbols).

Table 6.2: The obtained values of T_{Comp}, T_C and M_S value for Gd-(Fe, Cr)-O samples.

x	**0**	**0.1**	**0.2**	**0.3**
T_{Comp} **(K)**	293	244	187	80
T_C **(K)**	569	537	526	518
M_S **(emu/g)**	0.569	1.36	1.63	2.29
K_1 **(erg/cm^3)**	-	2.84×10^3	2.91×10^3	6.02×10^3

6.3 Complex Dielectric Spectroscopy Studies

The real and the imaginary components of complex dielectric constant, ε' and ε'' as a function of frequency (*f*) are shown in Figure 6.5 for samples $x = 0$ and 0.3. Here, the plots are shown for different measuring temperature in the range of 473 K to 623 K. At a given temperature, a gradual decrease in ε' value in the low frequency region ($< 10^3$ Hz) followed by a dispersion in the middle frequency range (10^3 to 10^5 Hz) has been observed in $x = 0$ sample for $T \geq 548$ K. As the temperature is increased, the dispersion is found to shift towards higher frequency. The merging of ε' at higher frequency is associated to the non-alignment of dipoles in the direction of electric field, i.e., diploes do not follow the electric field and hence, the polarization contribution is negligible, leading to a static ε' value. Similar behaviour is observed in $x = 0.3$ sample but dispersion is clearly observed for $T \geq 473$ K. In general, the dispersion behaviour in ε' contributes towards relaxation peak in ε'' versus *f* plot, but in our case, the lack of clear peaks and the dominant linear behaviour in ε'' plots can be attributed to the dominant dc conduction loss. Substitution of Cr at Fe site leads to increase in the value of ε' at room temperature, i.e., from 15 for $x = 0$ to 27 for $x = 0.3$ at $f = 1$ MHz, which is attributed to the increase in the concentration of charge carriers. The values of ε' and ε'' are found to increase with rise in temperature due to the increase in thermal energy and hence the concentration of charge carriers. Minor signature of relaxation peak is observed for $x = 0.3$ sample in the middle frequency range however, the dc conduction of charge carriers continues to dominate, leading to increase in ε'' value at lower frequency.

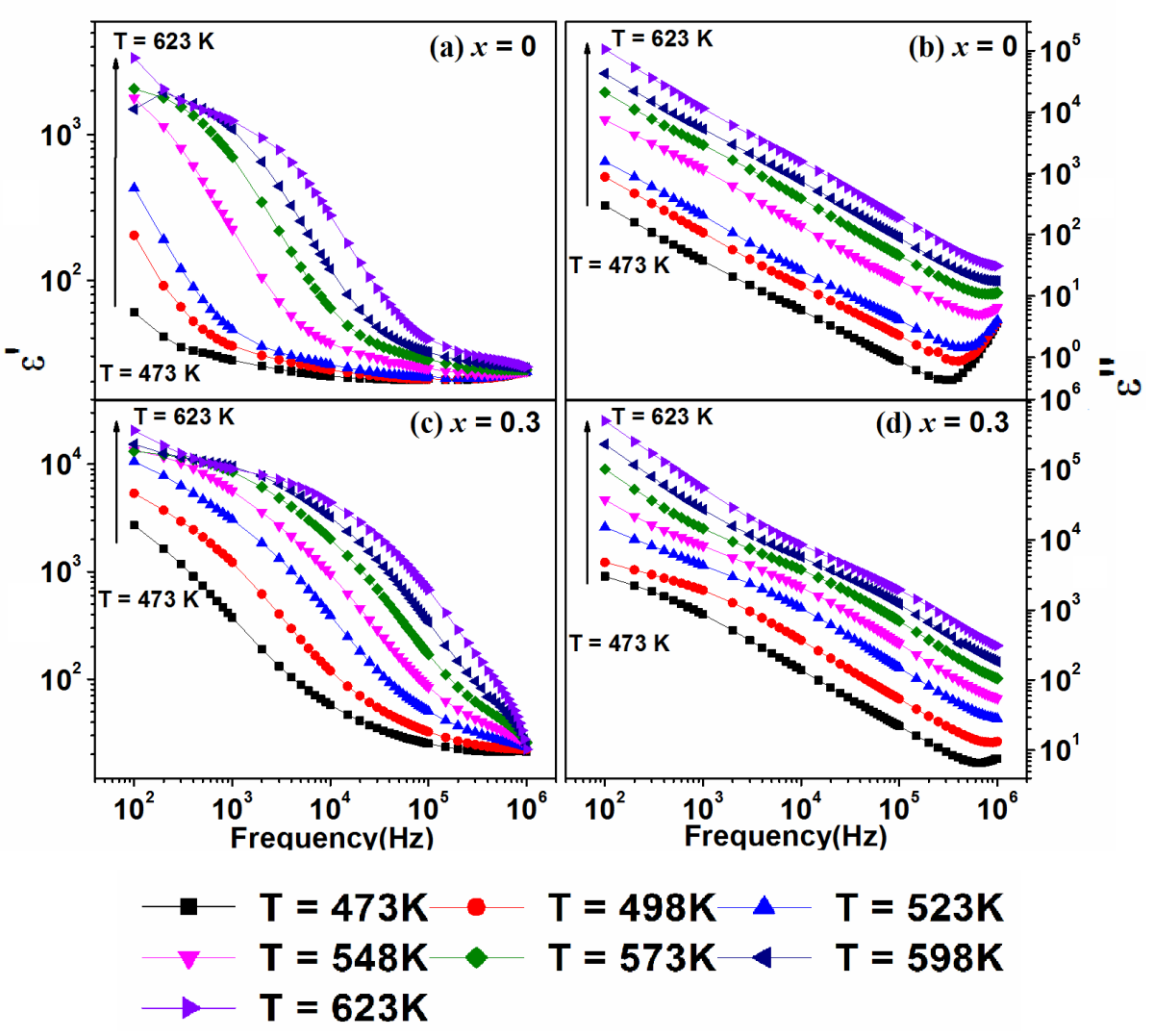

Figure 6.5: Frequency variation of ε' (a, c) and ε'' (b, d) in logarithmic scale at different temperatures for Gd-(Fe, Cr)-O samples with x = 0 and 0.3.

We have also studied modulus spectra to analyze electrical response of polycrystalline materials. It can distinguish between grains (G) and grain boundaries (GB) contributions while suppressing the electrode effect [144]. The grains effect is dominant in modulus spectrum due to its smaller capacitance as compared to that of grain boundaries. As the modulus is inverse of permittivity so, the dominant conductivity effect of ε'' is suppressed in M'' spectrum.

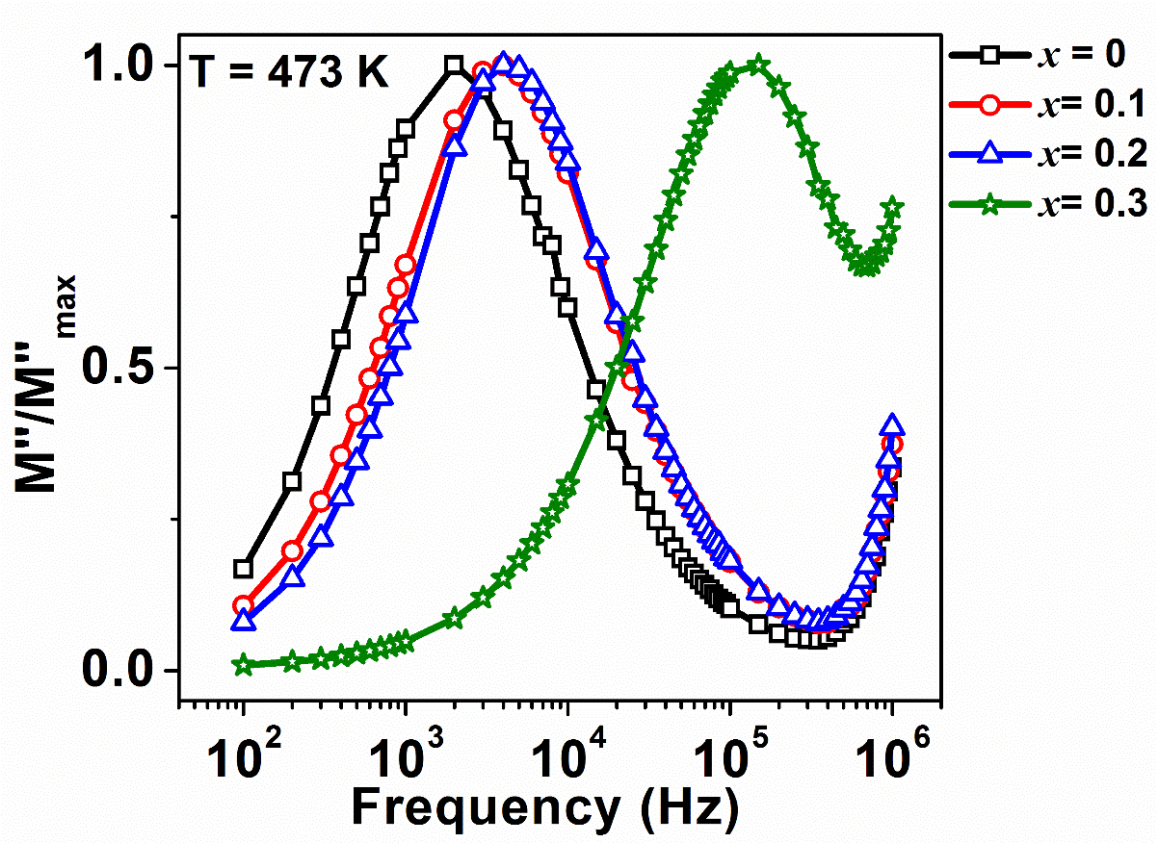

Figure 6.6: Normalized plots of imaginary component of modulus (M") versus *f* at (a) T = 473 K for Gd-(Fe, Cr)-O samples.

The plots of normalized modulus (M''/M''_{max}) as a function of frequency at T = 473 K are shown in Figure 6.6. It can be seen that all the samples show clear relaxation peak. The peak frequency reflects the transition point from the long-range movement of charge carriers at low frequency ($f < f_{max}$) to short-range movement of charge carriers at higher frequency ($f > f_{max}$) [174]. The relaxation peak is found to shift towards higher frequency side with increase in Cr concentration, i.e., from 10^3 Hz for $x = 0$ to 10^5 Hz for $x = 0.3$. The above shift in the relaxation frequency upon Cr-substitution, can be attributed to the increase in charge carrier concentration as well as due to the effective reduction in bond length between Fe ions at '*a*' and '*d*' site and hence smaller relaxation time.

Figure 6.7 and 6.8 show the normalized modulus spectra of M" (M''/M''_{max}) for x = 0, 0.1, 0.2 and 0.3 samples at different temperatures. With rise in temperature, the relaxation peak is found to shift towards higher frequency side suggesting the relaxation dynamics are thermally activated with different time constant. The merger of M" spectra at lower frequency with values close to zero indicates the suppression of electrode effect. The separation between the relaxation peaks of normalized modulus spectra indicates that the

relaxation process is dominated by short-range motion of charge carriers, i.e., within grains [71,144]. Moreover, the capacitance value of these Gd-(Fe, Cr)-O samples lies in the range of 10^{-11} F to 10^{-12} F in the entire frequency range, which also suggests that relaxation process is dominated by grains. These modulus spectra were analyzed on the basis of Bergman function explained by Kohlrausch-Williams-Watts (KWW) formula [175,176] written as:

$$M'' = \frac{M''_{max}}{1-\beta+\left(\frac{\beta}{1+\beta}\right)\left[\beta\left(\frac{f_{max}}{f}\right)+\left(\frac{f}{f_{max}}\right)^{\beta}\right]} \quad (6.3)$$

Where M''_{max} represents the peak value of M" and f_{max} is the corresponding frequency. β ($0 \leq \beta \leq 1$) is an exponent which is a measure of broadness of the spectra. The obtained f_{max} value is temperature dependent and follows Arrhenius law:

$$f_{max}(T) = f_0 \exp\left(\frac{-E_a}{k_B T}\right) \quad (6.4)$$

Here E_a is the activation energy, k_B is the Boltzmann constant and f_0 is the prefactor. Figure 6.9(a) shows the Arrhenius plots, which closely follow the linear behaviour. The obtained value of activation energy is found to marginally decrease with Cr concentration, i.e., from 1.14(8) eV for $x = 0$ to 0.98(5) eV for $x = 0.3$ sample. The obtained activation energy value is comparable to that predicted for doubly ionized oxygen vacancies and the charge transport across the vacancies [150]. The estimated β value is found to be temperature dependent and decreases with increase in temperature as shown in Figure 6.9(b). The above temperature variation of β suggests the wider distribution of relaxation frequency, i.e., departing from the ideal Debye type behaviour [71]. It is found that the β value is decreasing with increase in Cr concentration at T = 473 K, i.e., from 0.75 for $x = 0$ to 0.56 for $x = 0.3$.

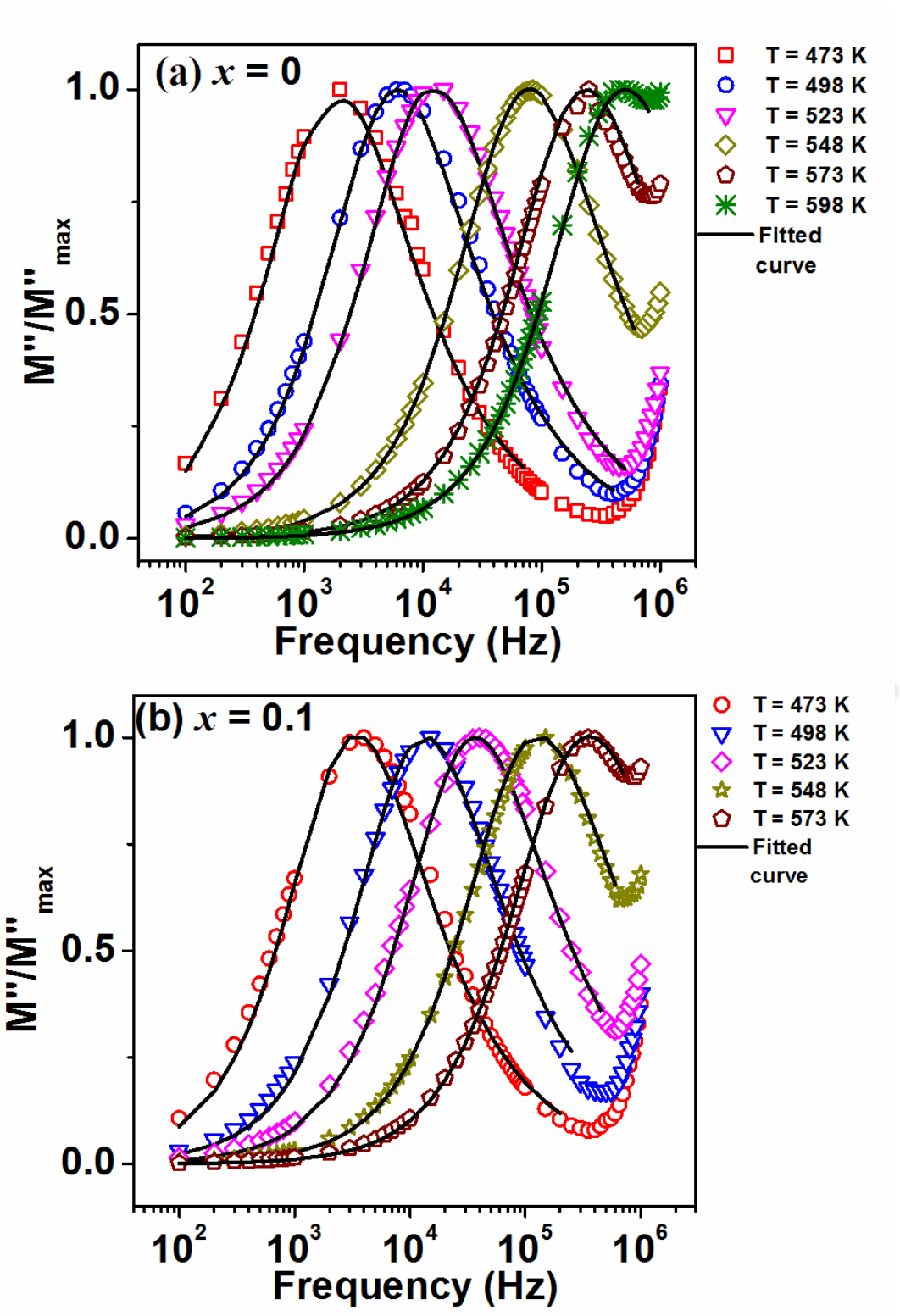

Figure 6.7: M''/M''$_{max}$ versus *f* plots at different temperatures for (a) $x = 0$ and (b) $x = 0.1$ samples.

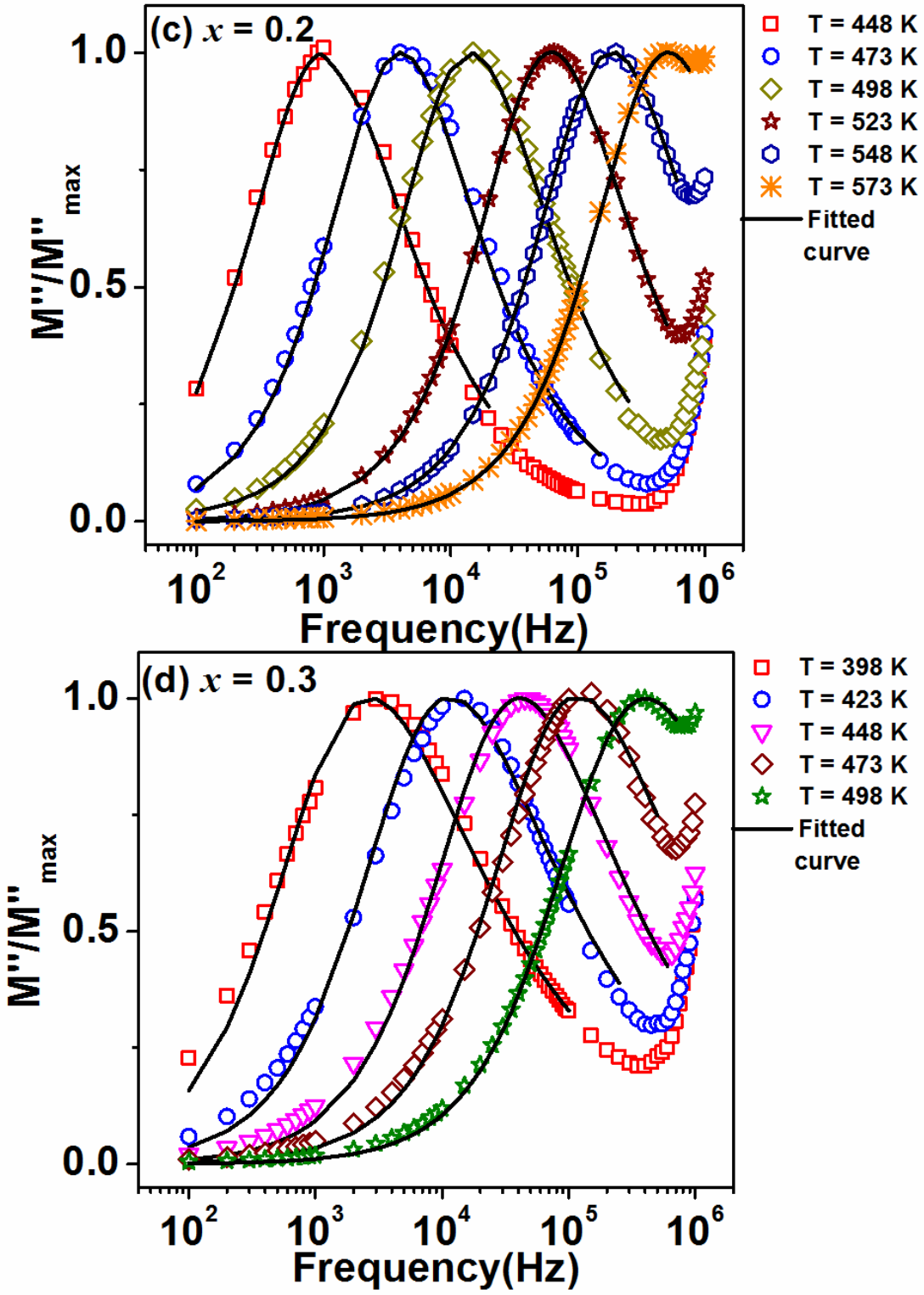

Figure 6.8: M''/M''$_{max}$ versus *f* plots at different temperatures for (a) x = 0.2 and (b) x = 0.3 samples.

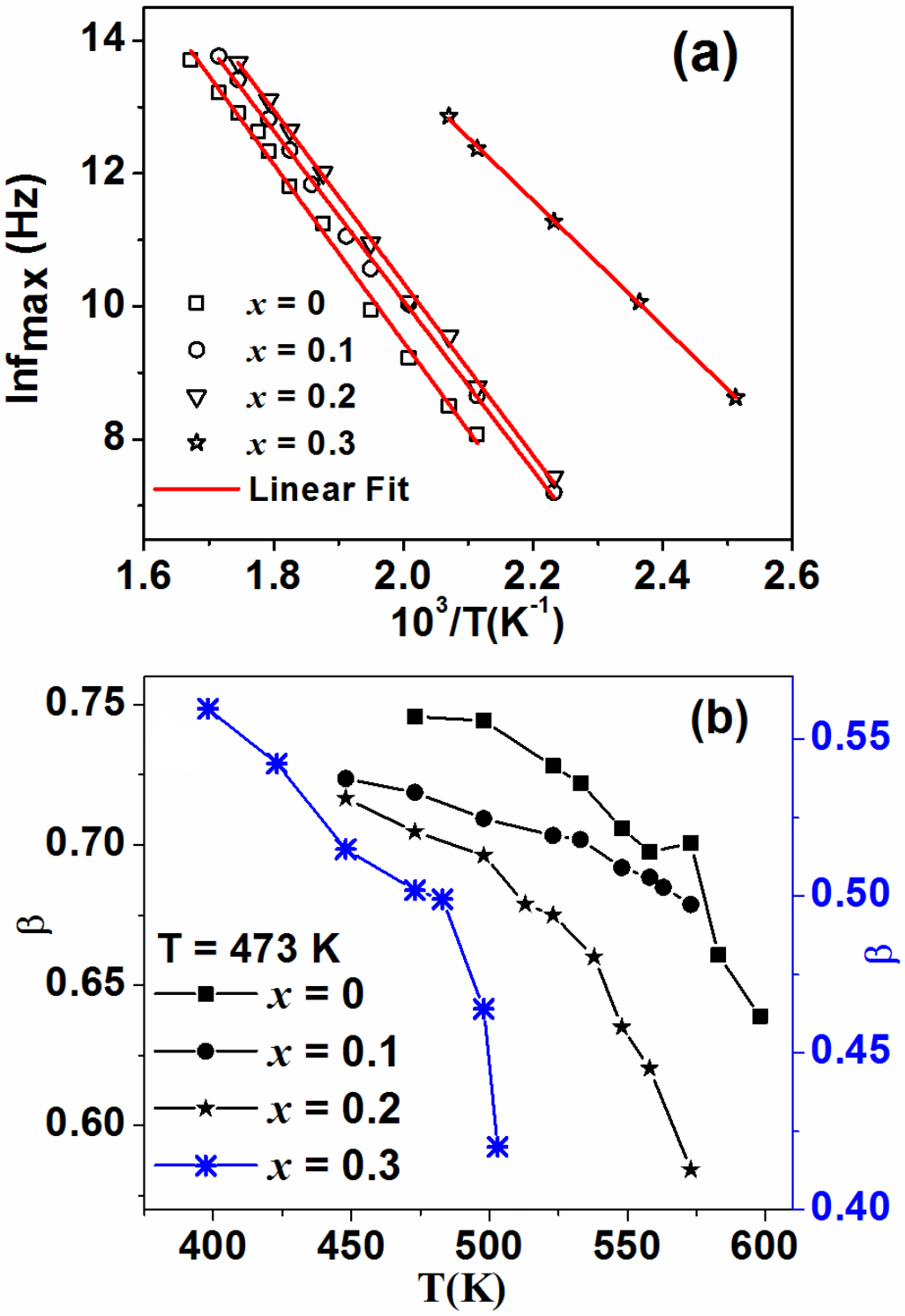

Figure 6.9: (a) Arrhenius plot of $\ln f_{max}$ versus 10^3/T and (b) β versus T plots for all Gd-(Fe, Cr)-O samples.

6.4 Conclusion

We have prepared polycrystalline samples of Cr substituted gadolinium iron garnets ($GdFe_{5-x}Cr_xO_{12}$ with x = 0 to 0.3) by solid-state reaction method. The phase purity of the samples was examined using Rietveld refinement based on $Ia\bar{3}d$ space group. The lattice constant, bond length and bond angle values are found to decrease with increase in Cr-concentration. Temperature variation of magnetization measurements show that all samples undergo FIM transition followed by magnetic compensation. The systematic decrease in T_C value with Cr-substitution, i.e., from 569 K for x = 0 to 518 K for x = 0.3 is mainly due to the decrease in superexchange interaction in $Fe^{3+}(a)$-O^{2-}-$Fe^{3+}(d)$ networks. The compensation temperature (T_{Comp}) varies from 294 K for x = 0 to 265 K for x = 0.3. Saturation magnetization (M_S) value at room temperature is found to increase with increase in Cr concentration, i.e., from 0.59 emu/g for x = 0 to 2.29 emu/g for x = 0.3 and it is attributed to the preferential occupation of Cr^{3+} ions at Fe^{3+} ions situated at octahedral site. The room temperature dielectric constant is found to increase from 15 for x = 0 to 27 for x = 0.3 at f = 1MHz. Moreover, modulus spectra were analyzed using Kohlrausch-Williams-Watts (KWW) function, which confirms the short-range movement of charge carriers associated to grains. The exponent β suggests that the relaxation dynamics is of non-ideal Debye type. The analysis of relaxation frequency using Arrhenius plots indicates that the doubly ionized oxygen vacancies are responsible for the relaxation process.

Chapter 7

Conclusion

Substitution plays an essential role and can reflect changes in the physical properties of the material for technological advancements. This chapter summarizes the result and discussion of structural, magnetic and dielectric properties of the Y and Gd based rare earth iron garnets. Six different series of compounds were prepared such as Sm, Cr and Mn-substituted YIG and, Sm and Cr-substituted GIG.

Polycrystalline samples of Sm-substituted YIG **($Y_{3-x}Sm_xFe_5O_{12}$: (Y, Sm)-Fe-O)** were successfully synthesized in single-phase form using solid-state reaction method. These samples are found to form in cubic structure with space group $Ia\bar{3}d$. The structural parameters such as lattice constant and unit cell volume increase with Sm-concentration due to the larger ionic size of Sm^{3+} ions as compared to those Y^{3+} host ions. The incorporation of Sm^{3+} ions at Y^{3+} site is confirmed from the shifting of Raman mode (F_{2g} = 271.4 cm^{-1}) towards lower wavenumber side and is consistent with increase in Y/Sm(*c*)-O-Fe(*a*) bond angle upon Sm-substitution.

The temperature dependent magnetization data showed the ferrimagnetic (FIM) to paramagnetic (PM) transition with increase in transition temperature (T_C) from 550 K for x = 0 to 573 K for x = 3.0 sample. Such increase in T_C is due to the strengthening of superexchange interaction between Fe^{3+} ions at octahedral (*a*) and tetrahedral (*d*) sites through O^{2-} ions. The saturation magnetization (M_S) value at room temperature was obtained by analyzing the initial magnetization data using the law of approach to saturation (LAS) method.

The complex impedance spectra (Z', -Z") measured in the frequency (*f*) range of 100 Hz to 1 MHz show relaxation behaviour. These relaxation behaviours are observed in terms of peak in -Z" versus *f* plots for T > 448 K. These relaxation peaks are attributed to grain boundaries contribution and they are shifting towards higher frequency side with rise in temperature due to the thermal activation process of charge carriers. The complex impedance spectra (Nyquist plots) measured at different temperature were analyzed by using two different equivalent circuits for T ≤ 448 K and T > 448 K, respectively. For T ≤ 448 K, both grains and grain boundaries contribution are observed and this is explained

based on equivalent circuit comprising of series combination of two parallel circuits consisting of resistor and a constant phase element. However, for T > 448 K, the grain boundaries contribution dominates over that of grains and such behaviour is modelled to an equivalent circuit of parallel arrangement of resistance (R_{gb}), capacitance (C_{gb}), and a constant phase element (Q_{gb}) of grain boundaries. The values of grains resistance (R_g) and grain boundaries resistance (R_{gb}) are found to decrease with increase in temperature and they are attributed to the increase in number of oxygen vacancies. Such trend suggests the negative temperature coefficient of resistance. The depressed and asymmetric nature of Nyquist plots signify the deviation of relaxation behaviour from the ideal Debye type. The dielectric constant increases from 12 for x = 0 to 29 for x = 3.0 at 1 MHz upon Sm-substitution, and it is ascribed to the increase in the concentration of Fe^{2+} and Fe^{3+} ions, which results in increase in polarization. The analysis of ac conductivity as a function of frequency at various temperatures was carried out using Jonscher power law (JPL) and suggests that conduction mechanism is governed by both small polaron hopping and large polaron hopping models.

Single-phase samples of Cr-substituted YIG (**$Y_3Fe_{5-x}Cr_xO_{12}$: Y-(Fe, Cr)-O**) were prepared by solid-state reaction method. The structural parameters such as lattice constant (12.3775 Å for x = 0 to 12.3560 Å for x = 0.5) and unit cell volume are found to decrease upon Cr-substitution. Such decrement is due to the preferential occupation of smaller Cr^{3+} (0.615 Å) ions at octahedral site of Fe^{3+} (0.645 Å) ions. The bond length [Fe(*a*)-Fe(*d*)] and bond angle [Fe(*a*)-O-Fe(*d*)] are found to decrease with Cr-concentration and it leads to shifting of F_{2g} Raman mode towards higher frequency side (271.4 cm^{-1} to 277.4 cm^{-1}) without any structural deformation.

The magnetization versus temperature (*M-T*) measurements were carried out for H = 200 Oe. These *M-T* plots show ferrimagnetic (FIM) transition with decrease in transition temperature (T_C) from 547 K for x = 0 to 494 K for x = 0.5. The weakening of superexchange interaction in Fe^{3+}(*a*)-O^{2-}-Fe^{3+}(*d*) networks results in decrease in T_C. Besides, isothermal magnetization plots (*M-H*) show the increase in saturation magnetization (M_S) upon Cr-substitution. It is explained based on the preferential occupation of doped Cr^{3+} ions at the octahedral site of Fe^{3+} (5 μ_B) ions.

The complex impedance measurements show that Cr-substitution gives rise to reduction in impedance value due to the possible increase in charge carriers. They all show relaxation behaviour with contributions from grains and grain boundaries. However, at

higher temperature, the relaxation across grain boundaries is found to be quite dominant. The Nyquist plots were explained by considering the equivalent circuit involving resistance and capacitance of grains and grain boundaries. The radius of semicircle in Nyquist plot decreases with increase in temperature and the plots are asymmetric in nature indicating the deviation from the ideal Debye type relaxation. The dielectric constant values were estimated using impedance data. The ε' and ε'' data as a function of frequency were analyzed using Havriliak – Negami (HN) equations including the contribution of dc conductivity to the dielectric response. The dielectric constant increases upon Cr-substitution from 20 to 52 at room temperature for f = 1 MHz, and it is ascribed to the increase in number of oxygen vacancies, hence, increase in the concentration of Fe^{2+} and Fe^{3+} networks. The ac conductivity spectra at various temperatures follow the Jonscher power law (JPL). The obtained frequency exponent n lies in the range of 1 to 2, and it is found to increase with temperature and such trend signifies the existing small polaron hopping induced conductivity.

Polycrystalline samples of Mn-substituted YIG (**$Y_3Fe_{5-x}Mn_xO_{12}$: Y-(Fe, Mn)-O**) were synthesized by sol-gel route. They are all found to be in single-phase form with decrease in lattice constant with increase in Mn-concentration. The substituted Mn ions possibly taking the Mn^{4+} (0.530 Å) state having smaller ionic radius compared to host Fe^{3+} (0.645 Å) ions leads to decrease in lattice constant. The decrease in FIM T_C from 550 K for x = 0 to 539 K for x = 0.2 has been observed with increase in Mn-concentration. The Nyquist plots of Mn-substituted samples were fitted to the parallel combination of resistance, capacitance and constant phase element associated to grain boundaries for higher temperature. The ε' and ε'' versus frequency plots show the presence of dispersion and relaxation peak, respectively. At higher temperature, the observed linear behaviour at lower frequency is associated to the dominance of dc conduction loss. The dielectric constant decreases due to Mn-substitution, i.e., from 15 to 10 at 1 MHz and T = 300 K.

Polycrystalline samples of Sm-substituted GIG (**$Gd_{3-x}Sm_xFe_5O_{12}$: (Gd, Sm)-Fe-O**) were prepared successfully in single-phase form using solid-state reaction method. Sm-substitution gives rise to increase in lattice constant from 12.4624 Å for x = 0 to 12.5212 Å for x = 3.0, which is due to its larger ionic size as compared to Gd ions. The bond length (Fe(a)-Fe(d)) and bond angle (Fe(a)-O-Fe(d)) increase with Sm-substitution. The temperature dependent magnetization (M-T) data were studied in both zero field-cooled (ZFC) and field-cooled (FC) conditions for (Gd, Sm)-Fe-O samples. M-T plots under ZFC undergo ferrimagnetic (FIM) transition with increase in transition temperature (T_C) from

567 K for x = 0 to 575 K for x = 3.0, due to strong superexchange interaction between Fe ions at octahedral and tetrahedral site. Below the FIM T_C, they exhibit magnetic compensation with decrease in compensation temperature (T_{Comp}) from 293 K for x = 0 to 70 K for x = 2.0. We have observed a novel negative magnetization below T_{Comp} for x = 2.0 sample for the first time in this series under FC condition. The negative magnetization is mainly attributed to the strong magnetic anisotropy induced by Sm-substitution. The strong magnetic anisotropy does not allow magnetic spins to flip along H for T < T_{Comp} and results in negative magnetization. The field dependent magnetization (*M*-*H*) plots were analyzed using the law of approach to saturation (LAS) model. The M_S value at room temperature (RT) is obtained from the LAS model and it is found to increase with increase in Sm-concentration, i.e., from 0.19 emu/g for x = 0 to 19.54 emu/g at x = 3.0. Sm^{3+} (0.71 μ_B) ions having smaller magnetic moment substituting the Gd^{3+} (7 μ_B) ions leads to increase in M_S value. The estimated value of anisotropy constant is found to increase from 6.85×10^3 erg/cm^3 for x = 0.5 to 1.65×10^5 erg/cm^3 for x = 3.0 and is in agreement with the explanation given for negative magnetization in x = 2.0 sample.

The plots of -Z" versus frequency show the relaxation behaviour at higher temperature. The relaxation frequency is shifting towards the lower frequency side with increase in Sm-concentration, i.e., from 60 kHz to 1 kHz and it is due to the reduction in grain boundaries concentration due to increase in grain size. The Nyquist plots (-Z" versus Z') were analyzed by fitting them to an equivalent circuit comprised of resistance, capacitance and constant phase element of grain boundaries in parallel configuration. The depressed and asymmetric nature shows that the relaxation behaviour deviates from the ideal Debye type and it is controlled by thermal activation of charge carriers.

Bi-substituted GIG (**$Gd_{3-x}Bi_xFe_5O_{12}$: (Gd, Bi)-Fe-O**) samples were prepared by solid-state reaction method. All the samples are found to be phase-pure as per the Rietveld refinement using $Ia\bar{3}d$ space group. The substitution of larger Bi ion at Gd site increases the lattice constant and volume.

The thermo-magnetization (*M*-*T*) plots show the presence of both ferrimagnetic transition and magnetic compensation above and below the room temperature respectively. The ferrimagnetic transition temperature increases with Bi-substitution, i.e., from 567 K for x = 0 to 596 for x = 1.0. Such increase in T_C is due to the strengthening of superexchange interaction followed by the increase in bond angle (Fe(*a*)-O-Fe(*d*)) as per the XRD analysis. However, the compensation temperature reduces from 296 K for x = 0 to 176 K for x = 1.0.

The substitution of non-magnetic Bi^{3+} ion at Gd site increases the saturation magnetization from 0.19 emu/g for $x = 0$ to 6.89 emu/g for $x = 1.0$ due to the reduction in magnetic moment at Gd site.

The analysis of impedance spectra at room temperature and at higher temperature shows that Bi-substitution gives rise to larger impedance due to the lack of oxygen vacancies and the associated reduction in charge carriers. At room temperature Z' is found to be 0.1, 11.0 and 22.0 MΩ for $x = 0$, 0.5 and 1.0 samples, respectively. Bi-substitution reduces the ε' value sharply and it is attributed to the reduction in oxygen vacancies and hence reduction in Fe^{2+} - Fe^{3+} networks. The dielectric loss also reduces from 1.5 for $x = 0$ to 0.5 for $x = 1.0$. The temperature variations of ε' show maxima at certain temperature for each frequency. The peak is found to shift towards higher temperature along with a reduction in peak intensity as the frequency is increased. These plots were analyzed in terms of modified Curie-Weiss law. The obtained values of the diffuseness exponent are close to 2, which suggest that they exhibit the relaxor ferroelectrics behaviour.

Cr-substituted GIG **($Gd_3Fe_{5-x}Cr_xO_{12}$: Gd-(Fe, Cr)-O)** samples were prepared by solid-state reaction method. The samples are found to be in single-phase form with considerable reduction in lattice constant. The ferrimagnetic transition temperature is found to decrease with Cr-concentration, i.e., from 569 K for $x = 0$ to 519 K for $x = 0.3$ sample. Such reduction is due to the weakening of superexchange coupling between Fe ions. Moreover, the magnetic compensation temperature is reduced from 294 K for $x = 0$ to 265 K for $x = 0.3$. The substitution of Cr^{3+} ions having smaller magnetic moment (3 μ_B) at the octahedral site of Fe^{3+} ions having larger magnetic moment (5 μ_B) gives rise to net increase in magnetic moment, i.e., from 0.56 emu/g for $x = 0$ to 2.29 emu/g at $x = 0.3$. The samples exhibit soft ferrimagnetic nature with small coercivity value in the range of 16 Oe for $x =$ 0.1 to 34 Oe for $x = 0.3$. Frequency dispersion of modulus (M") spectrum shows relaxation peak which is associated to the grains. The peaks are shifting towards higher frequency side with increase in temperature implying the thermal activation of relaxation dynamics. The relaxation peak was analyzed based on Kohlrausch-Williams-Watts (KWW) function, which confirms the short-range movement of charge carriers. The deviation of exponent β from the unit value suggests that it is tending towards non-ideal Debye type relaxation. The relaxation frequency follows Arrhenius law and the obtained value of activation energy is found to vary from 1.14(8) eV for $x = 0$ to 0.98(5) eV for $x = 0.3$ sample.

Thus, in the present thesis work, we have successfully tuned magnetic and dielectric properties in YIG and GIG compounds by substituting Sm, Bi and transition elements (Cr

and Mn). Cr-substitution reduces the FIM T_C value (494 K) quite sharply while the Bi-substituted GIG samples show larger T_C even close to 600 K. Interesting magnetization reversal is observed for the first time in GIG series due to Sm-substitution with $x = 2.0$ and it makes them useful for thermally assisted magnetic recording applications. On the other hand, Bi-substituted GIG samples exhibit relaxor ferroelectric behaviour at high temperature due to the possible inclusion of nano-polar regions, which leads them towards the multiferroic applications. Besides relaxor ferroelectric behaviour, Bi-substitution reduces the dielectric loss thereby making them useful for possible microwave and electronic devices. Dielectric constant enhances with Sm and Cr-substitution with the highest value of 52 observed in $Y_3Fe_{4.5}Cr_{0.5}O_{12}$ sample at room temperature for 1 MHz frequency.

Future scope of studies:

The following are the future scope in this area

1. Thin film growth of Sm and Bi-substituted YIG and GIG to study the negative magnetization, exchange bias and bipolar switching of magnetization for potential application in memory storage devices.
2. The substitution of divalent and tetravalent cations at rare earth (R) and Fe site may lead to tune the magnetic and dielectric properties. Such substitution may also lead to distorted non-centrosymmetry crystal structure leading to ferroelectric behaviour.
3. The magneto-caloric effect can be studied in these samples.
4. The presence of magneto-electric and magneto-dielectric coupling can be further studied by tuning the electric polarization by applying the magnetic field.
5. Other rare earth iron garnet such as $Bi_3Fe_5O_{12}$ can be studied for the purpose of multiferroic and magneto-electric properties near room temperature.
6. The effect of particle size on the magnetic and dielectric properties can be studied by preparing the above series of materials in nanocrystalline form.

References

[1] M. Fiebig, T. Lottermoser, D. Fröhlich, A. V Goltsev, R. V Pisarev, Observation of coupled magnetic and electric domains, Nature. 419 (2002) 818.

[2] D.I. Khomskii, Multiferroics: Different ways to combine magnetism and ferroelectricity, J. Magn. Magn. Mater. 306 (2006) 1–8.

[3] W. Eerenstein, N.D. Mathur, J.F. Scott, Multiferroic and magnetoelectric materials, Nature. 442 (2006) 759.

[4] D. Khomskii, Trend: Classifying multiferroics: Mechanisms and effects, Physics. 2 (2009) 20.

[5] D.K. Nagesha, B.D. Plouffe, M. Phan, L.H. Lewis, S. Sridhar, S.K. Murthy, Functionalization-induced improvement in magnetic properties of Fe_3O_4 nanoparticles for biomedical applications, J. Appl. Phys. 105 (2009) 07B317.

[6] J. Ma, J. Hu, Z. Li, C.W. Nan, Recent progress in multiferroic magnetoelectric composites: from bulk to thin films, Adv. Mater. 23 (2011) 1062–1087.

[7] N. Sharma, A. Das, S.K. Mishra, C.L. Prajapat, M.R. Singh, S.S. Meena, Magnetic and dielectric behaviour in $YMn_{1-x}Fe_xO_3$ ($x \leq 0.5$), J. Appl. Phys. 115 (2014) 213911.

[8] L. Néel, Magnetic properties of ferrites: ferrimagnetism and antiferromagnetism, Ann. Phys. 3 (1948) 137–198.

[9] R.W. Grimes, A.B. Anderson, A.H. Heuer, Predictions of cation distributions in AB_2O_4 spinels from normalized ion energies, J. Am. Chem. Soc. 111 (1989) 1–7.

[10] A.P. Alivisatos, Semiconductor clusters, nanocrystals, and quantum dots, Science (80-.). 271 (1996) 933–937.

[11] E.P. Wohlfarth, Ferromagnetic materials: A handbook on the properties of magnetically ordered substances, North Holland, (1982).

[12] J. Su, X. Lu, C. Zhang, J. Zhang, H. Sun, C. Ju, Z. Wang, K. Min, F. Huang, J. Zhu, Study on dielectric and magnetic properties of $Ho_3Fe_5O_{12}$ ceramics, Phys. B Condens. Matter. 407 (2012) 485–488.

[13] J. Su, X. Lu, J. Zhang, H. Sun, C. Zhang, Z. Jiang, C. Ju, Z. Wang, F. Huang, J. Zhu, The effect of Fe^{2+} ions on dielectric and magnetic properties of $Yb_3Fe_5O_{12}$ ceramics, J. Appl. Phys. 111 (2012) 14112.

[14] K. Praveena, S. Srinath, Effect of Gd^{3+} on dielectric and magnetic properties of $Y_3Fe_5O_{12}$, J. Magn. Magn. Mater. 349 (2014) 45–50.

[15] E.E. Anderson, J.R. Cunningham Jr, G.E. McDuffie, Magnetic properties of the mixed garnets $(3-x)Y_2O_3 \cdot xGd_2O_3 \cdot 5Fe_2O_3$, Phys. Rev. 116 (1959) 624.

[16] I.J. Park, K.U. Kang, C.S. Kim, Temperature-dependent magnetic properties of bismuth substituted terbium–iron garnets, IEEE Trans. Magn. 42 (2006) 2882–2884.

[17] M.H. Phan, M.B. Morales, C.N. Chinnasamy, B. Latha, V.G. Harris, H. Srikanth, Magnetocaloric effect in bulk and nanostructured $Gd_3Fe_5O_{12}$ materials, J. Phys. D. Appl. Phys. 42 (2009) 115007.

[18] Y.J. Wu, T. Zhang, J. Li, X.M. Chen, Effects of bi-substitution on dielectric and ferroelectric properties of yttrium iron garnet ceramics, Ferroelectrics. 458 (2014) 25–30.

[19] B.J.H. Stadler, T. Mizumoto, Integrated magneto-optical materials and isolators: a review, J. IEEE Photonics 6 (2013) 1–15.

[20] E.J.J. Mallmann, A.S.B. Sombra, J.C. Goes, P.B.A. Fechine, Yttrium iron garnet: properties and applications review, Solid State Phenom. 20 (2013) 65–96.

[21] S. Geprägs, A. Kehlberger, F. Della C., Z. Qiu, E.-J. Guo, C. Schulz T.and Mix, S. Meyer, A. Kamra, M. Althammer, others, Origin of the spin seebeck effect in compensated ferrimagnets, Nat. Commun. 7 (2016) 10452.

[22] N.B. Ibrahim, A.Z. Arsad, Investigation of nanostructural, optical and magnetic properties of cerium-substituted yttrium iron garnet films prepared by a sol gel method, J. Magn. Magn. Mater. 401 (2016) 572–578.

[23] G. Menzer, Die Kristallstruktur der Granate, Zeitschrift Für Krist. Mater. 69 (1928) 300–396.

[24] F. Bertaut, F. Forrat, Structure of ferrimagnetic rare earth ferrites, CR Acad. Sci. 242 (1956) 382.

[25] S. Geller, M.A. Gilleo, The crystal structure and ferrimagnetism of yttrium-iron garnet, $Y_3Fe_2(FeO_4)_3$, J. Phys. Chem. Solids. 3 (1957) 30–36.

[26] G.P. Espinosa, Crystal chemical study of the rare earth iron garnets, J. Chem. Phys. 37 (1962) 2344–2347.

[27] S. Blundell, Magnetism in condensed matter, Oxford University Press, (2001).

[28] R.G. Burns, Crystal field effects in chromium and its partitioning in the mantle, Geochim. Cosmochim. Acta. 39 (1975) 857.

[29] B.D. Cullity, C.D. Graham, Introduction to magnetic materials, John Wiley & Sons, 2011.

[30] H.A. Kramers, L'interaction entre les atomes magnétogènes dans un cristal paramagnétique, Physica. 1 (1934) 182–192.

[31] J.C. Slater, Quart. Progr. Rep. MIT, July 15, 1; Oct. 15 (1953) 1.

[32] J.B. Goodenough, Theory of the role of covalence in the perovskite-type manganites [La, M(II)]MnO_3, Phys. Rev. 100 (1955) 564.

[33] J.B. Goodenough, A.L. Loeb, Theory of ionic ordering, crystal distortion, and magnetic exchange due to covalent forces in spinels, Phys. Rev. 98 (1955) 391.

[34] M.A. Gilleo, Superexchange interaction energy for Fe^{3+}-O^{2-}-Fe^{3+} linkages, Phys. Rev. 109 (1958) 777.

[35] C. Zener, Interaction between the d-shells in the transition metals. II. Ferromagnetic compounds of manganese with perovskite structure, Phys. Rev. 82 (1951) 403.

[36] C. Zener, Interaction between the d shells in the transition metals, Phys. Rev. 81 (1951) 440.

[37] P.W. Anderson, H. Hasegawa, Considerations on double exchange, Phys. Rev. 100 (1955) 675.

[38] I. Dzyaloshinsky, A thermodynamic theory of "weak" ferromagnetism of antiferromagnetics, J. Phys. Chem. Solids. 4 (1958) 241–255.

[39] T. Moriya, Anisotropic superexchange interaction and weak ferromagnetism, Phys. Rev. 120 (1960) 91.

[40] N.A. Spaldin, Magnetic materials: fundamentals and applications, Cambridge University Press, 2010.

[41] C.D. Graham Jr, Some magnetic properties of Gd single crystals, J. Appl. Phys. 34 (1963) 1341–1342.

[42] J. Barman, S. Ravi, Sign reversal of magnetization and exchange bias in $Ni(Cr_{1-x}Al_x)_2O_4$ (x=0 – 0.50), J. Magn. Magn. Mater. 426 (2017) 82–88.

[43] J.S. McCloy, B. Walsh, Sublattice magnetic relaxation in rare earth iron garnets, IEEE Trans. Magn. 49 (2013) 4253–4256.

[44] N.S. Akulov, Über das magnetische quadrupolmoment des eisenatoms, Zeitschrift Für Phys. 57 (1929) 249–256.

[45] K. Yoshii, Magnetic properties of perovskite $GdCrO_3$, J. Solid State Chem. 159 (2001) 204–208.

[46] H. Adachi, H. Ino, A ferromagnet having no net magnetic moment, Nature. 401 (1999) 148.

[47] J. Nogués, I.K. Schuller, Exchange bias, J. Magn. Magn. Mater. 192 (1999) 203–232.

[48] I.L. Prejbeanu, M. Kerekes, R.C. Sousa, H. Sibuet, O. Redon, B. Dieny, J.P. Nozières, Thermally assisted MRAM, J. Phys. Condens. Matter. 19 (2007) 165218.

[49] R. Medapalli, I. Razdolski, M. Savoini, A.R. Khorsand, A.M. Kalashnikova, A. Tsukamoto, A. Itoh, A. Kirilyuk, A. V Kimel, T. Rasing, The role of magnetization compensation point for efficient ultrafast control of magnetization in $Gd_{24}Fe_{66.5}Co_{9.5}$ alloy, J. Eur. Phys. B. 86 (2013) 183.

[50] A. Kumar, S.M. Yusuf, The phenomenon of negative magnetization and its implications, Phys. Rep. 556 (2015) 1–34.

[51] A. Budkowski, A. Szytu, D. Rodic, R. Duraj, J. Mayer, J. Sciesinski, V. Spasojevic, The compensation point in reig and some of its properties, J. Magn. Magn. Mater. 78 (1989) 226–236.

[52] Y.G. Chukalkin, V.R. Shtirts, Peculiairities of magnetic properties of the garnet $Y_{2.25}Gd_{0.75}Fe_5O_{12}$ irradiated by fast neutrons, Phys. Status Solidi. 173 (1999) 459–465.

[53] I.J. Park, C.S. Kim, Structural and magnetic characteristics of bismuth substituted holmium iron garnet, Phys. Status Solidi. 244 (2007) 4562–4565.

[54] N. Menyuk, K. Dwight, D.G. Wickham, Magnetization reversal and asymmetry in cobalt vanadate (IV), Phys. Rev. Lett. 4 (1960) 119.

[55] V.K. Lakhani, B. Zhao, L. Wang, U.N. Trivedi, K.B. Modi, Negative magnetization, magnetic anisotropy and magnetic ordering studies on Al^{3+}-substituted copper ferrite, J. Alloys Compd. 509 (2011) 4861–4867.

[56] J. Barman, P.D. Babu, S. Ravi, Exchange bias and magnetization reversal in $Ni(Cr_{1-x}Fe_x)_2O_4$ (x= 0 – 0.20), J. Magn. Magn. Mater. 418 (2016) 300–305.

[57] T. Bora, S. Ravi, Study of magnetization reversal in $LaCr_{1-x}Fe_xO_3$ compounds, J. Appl. Phys. 114 (2013) 33906.

[58] D. Delmonte, F. Mezzadri, C. Pernechele, G. Calestani, G. Spina, M. Lantieri, M. Solzi, R. Cabassi, F. Bolzoni, A. Migliori, others, Thermally activated magnetization reversal in bulk $BiFe_{0.5}Mn_{0.5}O_3$, Phys. Rev. B. 88 (2013) 14431.

[59] T. Bora, S. Ravi, Sign reversal of magnetization and tunable exchange bias field in $NdCr_{1-x}Fe_xO_3$ (x= 0.05 – 0.2), J. Magn. Magn. Mater. 386 (2015) 85–91.

[60] B.B. Dash, S. Ravi, Sign reversal of magnetization in Mn substituted $SmCrO_3$, J. Magn. Magn. Mater. 405 (2016) 209–213.

[61] X.H. Chen, K.Q. Wang, P.H. Hor, Y.Y. Xue, C.W. Chu, Anomalies at the compensation temperature in the zero-magnetization ferromagnet (Sm, Gd)Al_2, Phys. Rev. B. 72 (2005) 54436.

[62] P.D. Kulkarni, A. Thamizhavel, V.C. Rakhecha, A.K. Nigam, P.L. Paulose, S. Ramakrishnan, A.K. Grover, Magnetic compensation phenomenon and the sign reversal in the exchange bias field in a single crystal of $Nd_{075}Ho_{0.25}Al_2$, EPL (Europhysics Lett. 86 (2009) 47003.

[63] K.C. Kao, Dielectric phenomena in solids, Elsevier, 2004.

[64] E. Barsoukov, J.R. Macdonald, Impedance spectroscopy: theory, experiment, and applications, John Wiley & Sons, 2018.

[65] D.J. Griffiths, Introduction to electrodynamics, Prentice Hall, New Jersey, 1999.

[66] G.G. Raju, Dielectrics in electric fields, CRC press, Florida, USA, 2017.

[67] S. Havriliak, S. Negami, A complex plane representation of dielectric and mechanical relaxation processes in some polymers, Polymer (Guildf). 8 (1967) 161–210.

[68] N.G. McCrum, B.E. Read, G. Williams, Anelastic and dielectric effects in polymeric solids, Wiley, New York, 1967.

[69] H. Wagner, R. Richert, Thermally stimulated modulus relaxation in polymers: method and interpretation, Polymer (Guildf). 38 (1997) 5801–5806.

[70] R. Kohlrausch, Theorie des elektrischen Rückstandes in der Leidener Flasche, Ann. Phys. 167 (1854) 179–214.

[71] R. Bergman, General susceptibility functions for relaxations in disordered systems, J. Appl. Phys. 88 (2000) 1356–1365.

[72] K. Funke, Jump relaxation in solid electrolytes, Prog. Solid State Chem. 22 (1993) 111–195.

[73] A.K. Jonscher, The 'universal'dielectric response, Nature. 267 (1977) 673.

[74] F. Bertaut, R. Pauthenet, Crystalline structure and magnetic properties of ferrites having the general formula $5Fe_2O_3 \cdot 3M_2O_3$, Proc. IEEE, Conv. Ferrites, London. 104 (1957) 261–264.

[75] T. Okuda, T. Katayama, H. Kobayashi, N. Kobayashi, K. Satoh, H. Yamamoto, Magnetic properties of $Bi_3Fe_5O_{12}$ garnet, J. Appl. Phys. 67 (1990) 4944–4946.

[76] T. Okuda, T. Katayama, K. Satoh, H. Yamamoto, Preparation of polycrystalline $Bi_3Fe_5O_{12}$ garnet films, J. Appl. Phys. 69 (1991) 4580–4582.

[77] L. Guo, K. Huang, Y. Chen, G. Li, L. Yuan, W. Peng, H. Yuan, S. Feng, Mild hydrothermal synthesis and ferrimagnetism of $Pr_3Fe_5O_{12}$ and $Nd_3Fe_5O_{12}$ garnets, J. Solid State Chem. 184 (2011) 1048–1053.

[78] L. Guo, L. Yuan, K. Huang, M. Shang, W. Peng, H. Yuan, S. Feng, Ferrimagnetism corresponding spin state transition in $Nd_3Fe_5O_{12}$ garnet, J. Appl. Phys. 110 (2011) 83921.

[79] S. Geller, H.J. Williams, R.C. Sherwood, J.P. Remeika, G.P. Espinosa, Magnetic study of the lighter rare earth ions in the iron garnets, Phys. Rev. 131 (1963) 1080.

[80] S. Geller, J.P. Remeika, R.C. Sherwood, H.J. Williams, G.P. Espinosa, Magnetic study of the heavier rare earth iron garnets, Phys. Rev. 137 (1965) A1034.

[81] Y.J. Wu, Y. Gao, X.M. Chen, Dielectric relaxations of yttrium iron garnet ceramics over a broad temperature range, Appl. Phys. Lett. 91 (2007) 92912.

[82] P. Manimuthu, M. Manikandan, M.M. Selvi, C. Venkateswaran, Multiferroic $Lu_3Fe_5O_{12}$ for magneto-dielectric applications, AIP Conf. Proc., 2012: pp. 1205–1206.

[83] G. Velleaud, B. Sangare, M. Mercier, G. Aubert, Magnetoelectric properties of yttrium iron garnet, Solid State Commun. 52 (1984) 71–74.

[84] N. Hur, S. Park, S. Guha, A. Borissov, V. Kiryukhin, S.W. Cheong, Low-field magnetodielectric effect in terbium iron garnets, Appl. Phys. Lett. 87 (2005) 42901.

[85] Y. Kohara, Y. Yamasaki, Y. Onose, Y. Tokura, Excess-electron induced polarization and magnetoelectric effect in yttrium iron garnet, Phys. Rev. B. 82 (2010) 104419.

[86] K.M. Song, Y.A. Park, K.D. Lee, B.K. Yun, M.H. Jung, J. Cho, J.H. Jung, N. Hur, Magnetodielectric effect via a noncollinear-to-collinear spin reorientation in rare earth iron garnets, Phys. Rev. B. 83 (2011) 12404.

[87] Y.J. Wu, C. Yu, X.M. Chen, J. Li, Magnetodielectric effects of $Y_3Fe_{5-x}Ti_xO_{12+x/2}$ ceramics, Appl. Phys. Lett. 100 (2012) 52902.

[88] K.N. Belov, E. V Talalaeva, L.A. Chernikova, V.I. Ivanovskii, T. V Kudryavtseva, Magnetocaloric effect in rare earth iron garnets, Pisma Redaktsiiu. 9 (1969) 671.

[89] R.D. McMichael, J.J. Ritter, R.D. Shull, Enhanced magnetocaloric effect in $Gd_3Ga_{5-x}Fe_xO_{12}$, J. Appl. Phys. 73 (1993) 6946–6948.

[90] D. Rodić, Z. Tomkowicz, L. Novaković, A. Szytula, M.L. Napijalo, The initial magnetic susceptibilities of $Gd_3Fe_5O_{12}$ and $Tb_3Fe_5O_{12}$ in the compensation point region, Solid State Commun. 73 (1990) 243–246.

[91] D.D. Stancil, A. Prabhakar, Spin waves: Theory and applications, Springer, 2009.

[92] S.M. Rezende, R.L. Rodríguez-Suárez, J.C.L. Ortiz and A. Azevedo, Thermal properties of magnons and the spin seebeck effect in yttrium iron garnet/normal metal hybrid structures, Phys. Rev. B. 89 (2014) 134406.

[93] H. Asada, A. Kuwahara, K. Sueyasu, T. Ishibashi, Q. Liu, G. Lou, K. Kishimoto, T. Koyanagi, Longitudinal spin seebeck effect in Bi-substituted neodymium iron garnet on gadolinium gallium garnet substrate prepared by MOD method, Phys. Procedia. 75 (2015) 932–938.

[94] K. Uchida, J. Ohe, T. Kikkawa, S. Daimon, D. Hou, Z. Qiu, E. Saitoh, Intrinsic surface magnetic anisotropy in $Y_3Fe_5O_{12}$ as the origin of low-magnetic-field behaviour of the

spin seebeck effect, Phys. Rev. B. 92 (2015) 14415.

[95] H. Kidoh, A. Morimoto, T. Shimizu, Synthesis of ferromagnetic Bi-substituted yttrium iron garnet films by laser ablation, Appl. Phys. Lett. 59 (1991) 237–239.

[96] C. Jiang, Neutron irradiation of czochralski and temperature gradient technique grown YAG crystals, Phys. B Condens. Matter. 373 (2006) 42–45.

[97] E.E. Anderson, Some electrical and magnetic Pproperties of garnets, J. Appl. Phys. 30 (1959) S299–S300.

[98] E.E. Anderson, Molecular field model and the magnetization of YIG, Phys. Rev. 134 (1964) A1581.

[99] H. Zhao, J. Zhou, Y. Bai, Z. Gui, L. Li, Effect of Bi-substitution on the dielectric properties of polycrystalline yttrium iron garnet, J. Magn. Magn. Mater. 280 (2004) 208–213.

[100] T.C. Mao, J.C. Chen, Influence of the addition of CeO_2 on the microstructure and the magnetic properties of yttrium iron garnet ceramic, J. Magn. Magn. Mater. 302 (2006) 74–81.

[101] Z. Cheng, H. Yang, L. Yu, W. Xu, Saturation magnetic properties of $Y_{3-x}Re_xFe_5O_{12}$ (Re: Gd, Dy, Nd, Sm and La) nanoparticles grown by a sol–gel method, J. Mater. Sci. Mater. Electron. 19 (2008) 442–447.

[102] H. Wu, F. Huang, T. Xu, R. Ti, X. Lu, Y. Kan, X. Lv, W. Zhu, J. Zhu, Magnetic and magnetodielectric properties of $Y_{3-x}La_xFe_5O_{12}$ ceramics, J. Appl. Phys. 117 (2015) 144101.

[103] S. Huang, L.R. Shi, H.G. Sun, C.L. Li, L. Chen, S.L. Yuan, High temperature dielectric response in $Sm_3Fe_5O_{12}$ ceramics, J. Alloys Compd. 674 (2016) 341–346.

[104] Y.J. Wu, C. Yu, X.M. Chen, J. Li, Magnetic and magnetodielectric properties of Bi-substituted yttrium iron garnet ceramics, J. Magn. Magn. Mater. 324 (2012) 3334–3337.

[105] M.A. Gilleo, S. Geller, Magnetic and Crystallographic Properties of Substituted Yttrium-Iron Garnet, $3Y_2O_3 \cdot xM_2O_3 \cdot (5 – x)Fe_2O_3$, Phys. Rev. 110 (1958) 73.

[106] E.M. Gyorgy, F.J. Schnettler, Induced anisotropy in YIG with Si and Mn additions, J. Appl. Phys. 35 (1964) 1067–1068.

[107] C.S. Kim, B.K. Min, S.J. Kim, S.R. Yoon, Y.R. Uhm, Crystallographic and magnetic properties of $Y_3Fe_{5-x}Al_xO_{12}$, J. Magn. Magn. Mater. 254 (2003) 553–555.

[108] W. Jiaqian, Y. Jian, J. Yulong, Q. Tai, Effect of manganese addition on the microstructure and electromagnetic properties of YIG, J. Rare Earths. 29 (2011) 562–566.

[109] Y.J. Wu, C. Yu, X.M. Chen, J. Li, Effects of Al substitution on dielectric response and magnetic behaviour of yttrium iron garnet ceramics, J. Am. Ceram. Soc. 95 (2012) 1671–1675.

[110] S.R. Naik, A. V Salker, Enhancement in the magnetic moment with Cr^{3+} doping and its effect on the magneto-structural properties of $Ce_{0.1}Y_{2.9}Fe_5O_{12}$, Phys. Chem. Chem. Phys. 14 (2012) 10032–10040.

[111] S. Khanra, A. Bhaumik, Y.D. Kolekar, P. Kahol, K. Ghosh, Structural and magnetic studies of $Y_3Fe_{5-5x}Mo_{5x}O_{12}$, J. Magn. Magn. Mater. 369 (2014) 14–22.

[112] Z. Zhang, F. Chen, J. Li, Z. Feng, Y. Nie, Effect of Sn doping on the room temperature magnetodielectric properties of yttrium iron garnet, J. Appl. Phys. 118 (2015) 154102.

[113] V.D. Murumkar, K.B. Modi, K.M. Jadhav, G.K. Bichile, R.G. Kulkarni, Magnetic and electrical properties of aluminium and chromium co-substituted yttrium iron garnets, Mater. Lett. 32 (1997) 281–285.

[114] K. Bouziane, A. Yousif, H.M. Widatallah, J. Amighian, Site occupancy and magnetic study of Al^{3+} and Cr^{3+} co-substituted $Y_3Fe_5O_{12}$, J. Magn. Magn. Mater. 320 (2008) 2330–2334.

[115] A.O. Imaddin A, S. Ralph, D.J. SellmyerMagnetic Properties of $Y_{3-2x}Ca_{2x}Fe_{5-x}V_xO_{12}$ Garnets, Adv. Mater. Phys. Chem. 2012 (2012).

[116] L. Wang, Z. Huang, H. Zhang, R. Yu, Phase and magnetic properties evolutions of $Y_{3-x}(CaZr)_xFe_{5-x}O_{12}$ by the sol–gel method, J. Magn. Magn. Mater. 395 (2015) 73–80.

[117] T. Ramesh, R.S. Shinde, S.R. Murthy, Nanocrystalline gadolinium iron garnet for circulator applications, J. Magn. Magn. Mater. 324 (2012) 3668–3673.

[118] D.T.T. Nguyet, N.P. Duong, T. Satoh, L.N. Anh, T.D. Hien, Magnetization and coercivity of nanocrystalline gadolinium iron garnet, J. Magn. Magn. Mater. 332 (2013) 180–185.

[119] J.E. Weidenborner, Least squares refinement of the structure of gadolinium-iron garnet $Gd_3Fe_2Fe_3O_{12}$, Acta Crystallogr. 14 (1961) 1051–1056.

[120] G.F. Dionne, Molecular field and exchange constants of Gd^{3+}-substituted ferrimagnetic garnets, J. Appl. Phys. 42 (1971) 2142–2143.

[121] J.C. Waerenborgh, D.P. Rojas, A.L. Shaula, V. V Kharton, F.M.B. Marques, Defect formation in $Gd_3Fe_5O_{12}$- based garnets: a Mössbauer spectroscopy study, Mater. Lett. 58 (2004) 3432–3436.

[122] A.A. Sattar, H.M. Elsayed, A.M. Faramawy, Comparative study of structure and magnetic properties of micro-and nano-sized $Gd_xY_{3-x}Fe_5O_{12}$ garnet, J. Magn. Magn. Mater. 412 (2016) 172–180.

[123] D. Bahadur, O.M. Parkash, D. Kumar, Electron transport in hot pressed $Y_{3-x}Gd_xFe_5O_{12}$, Bull. Mater. Sci. 3 (1981) 325–331.

[124] A. Durán, C. Ostos, O. Arnache, J.M. Siqueiros, M. García-Guaderrama, Multiferroic properties of the $Y_2BiFe_5O_{12}$ garnet, J. Appl. Phys. 122 (2017) 134101.

[125] Q.I. Mohaidat, M. Lataifeh, S.H. Mahmood, I. Bsoul, M. Awawdeh, Structural, Mössbauer effect, magnetic, and thermal properties of gadolinium erbium iron garnet system $Gd_{3-x}Er_xFe_5O_{12}$, J. Supercond. Nov. Magn. 30 (2017) 2135–2141.

[126] A. Rajan, S.L. Das, K.S. Sibi, G. Subodh, Influence of Bi Substitution on the Microstructure and Dielectric Properties of $Gd_3Fe_5O_{12}$ Ceramics, J. Electron. Mater. 48 (2019) 1133–1138.

[127] S.J.L. Kang, Sintering: densification, grain growth and microstructure, Elsevier, (2004).

[128] B.D. Cullity, Elements of X-ray diffraction: a practical approach, (1956).

[129] R.A. Young, The rietveld method, International union of crystallography, (1993).

[130] C.N. Banwell, E.M. McCash, Fundamentals of molecular spectroscopy, McGraw-Hill

New York, (1994).

[131] R. Kumar, Atomic and molecular physics, Campus Book International, (2009).

[132] S. Foner, Versatile and sensitive vibrating-sample magnetometer, Rev. Sci. Instrum. 30 (1959) 548–557.

[133] J. Saha, S. Chaudhary, P. Majumdar, B.K. Kuanr, S. Patnaik, High temperature magneto-electric effect in yittrium iron garnet (YIG), AIP Conf. Proc., (2016) 140056.

[134] K. Sadhana, S.R. Murthy, K. Praveena, Effect of Sm^{3+} on dielectric and magnetic properties of $Y_3Fe_5O_{12}$ nanoparticles, J. Mater. Sci. Mater. Electron. 25 (2014) 5130–5136.

[135] Y.J. Siao, X. Qi, C.R. Lin, J.C.A. Huang, Dielectric relaxation and magnetic behaviour of bismuth-substituted yttrium iron garnet, J. Appl. Phys. 109 (2011) 07A508.

[136] Y.J. Siao, X. Qi, Dielectric responses in polycrystalline rare earth iron garnets, J. Alloys Compd. 691 (2017) 672–682.

[137] E.A. Odo, Morphology and elemental study of silicon nanoparticles produced using a vibratory disc mill, Nanosci Nanotechnol. 5 (2015) 57–63.

[138] P.L. Chen, I.W. Chen, Grain growth in CeO_2: dopant effects, defect mechanism, and solute drag, J. Am. Ceram. Soc. (1996).

[139] J.F. Herbst, F.E. Pinkerton, Law of approach to saturation for polycrystalline ferromagnets: remanent initial state, Phys. Rev. B. 57 (1998) 10733.

[140] V. Nekvasil, Magnetocrystalline anisotropy of samarium garnets, Czechoslov. J. Phys. 34 (1984) 1052–1059.

[141] K. Kumari, A. Prasad, K. Prasad, Dielectric, Impedance/modulus and conductivity studies on $[Bi_{0.5}(Na_{1-x}K_x)_{0.5}]_{0.94}Ba_{0.06}TiO_3$, ($0.16 \leq x \leq 0.20$) leadfree ceramics, Am. J. Mater. Sci. 6 (2016) 1–18.

[142] S. Pattanayak, B.N. Parida, P.R. Das, R.N.P. Choudhary, Impedance spectroscopy of Gd-doped $BiFeO_3$ multiferroics, Appl. Phys. A. 112 (2013) 387–395.

[143] P.K. Larsen, R. Metselaar, Electric and dielectric properties of polycrystalline yttrium iron garnet: space-charge-limited currents in an inhomogeneous solid, Phys. Rev. B. 8 (1973) 2016.

[144] N. Ortega, A. Kumar, P. Bhattacharya, S.B. Majumder, R.S. Katiyar, Impedance spectroscopy of multiferroic $PbZr_xTi_{1-x}O_3/CoFe_2O_4$ layered thin films, Phys. Rev. B. 77 (2008) 14111.

[145] S.K. Patri, R.N.P. Choudhary, B.K. Samantaray, Dielectric anomaly in $Y_3Fe_5O_{12}$, Solid State Commun. 144 (2007) 441–444.

[146] B. Deka, S. Ravi, A. Perumal, D. Pamu, Effect of Mn doping on magnetic and dielectric properties of $YFeO_3$, Ceram. Int. 43 (2017) 1323–1334.

[147] R. Gangopadhyay, A. De, S. Das, Transport properties of polypyrrole–ferric oxide conducting nanocomposites, J. Appl. Phys. 87 (2000) 2363–2371.

[148] S. Nasri, M. Megdiche, M. Gargouri, DC conductivity and study of AC electrical conduction mechanisms by non-overlapping small polaron tunneling model in $LiFeP_2O_7$ ceramic, Ceram. Int. 42 (2016) 943–951.

[149] D. Capsoni, M. Bini, V. Massarotti, G. Chiodelli, M.C. Mozzatic, C.B. Azzoni, Role of doping and CuO segregation in improving the giant permittivity of $CaCu_3Ti_4O_{12}$, J. Solid State Chem. 177 (2004) 4494–4500.

[150] J. Wu, J. Wang, Ferroelectric and impedance behaviour of La-and Ti-codoped $BiFeO_3$ thin films, J. Am. Ceram. Soc. 93 (2010) 2795–2803.

[151] B. Ghosh, D. Bhattacharya, A.K. Raychaudhuri, S. Arumugam, Frequency dependence of dielectric anomaly around Néel temperature in bilayer manganite $Pr(Sr_{0.1}Ca_{0.9})_2Mn_2O_7$, J. Appl. Phys. 105 (2009) 123914.

[152] S. Kumari, N. Ortega, A. Kumar, S.P. Pavunny, J.W. Hubbard, C. Rinaldi, G. Srinivasan, J.F. Scott, R.S. Katiyar, Dielectric anomalies due to grain boundary conduction in chemically substituted $BiFeO_3$, J. Appl. Phys. 117 (2015) 114102.

[153] A. Goldman, Modern ferrite technology, Springer Science & Business Media, 2006.

[154] M.D. Abràmoff, P.J. Magãlhaes, S.J. Ram, Image processing with ImageJ, Biophotonics Int. 11 (2004) 36–42.

[155] P.B.A. Fechine, E.N. Silva, A.S. De Menezes, J. Derov, J.W. Stewart, A.J. Drehman, I.F. Vasconcelos, A.P. Ayala, L.P. Cardoso, A.S.B. Sombra, Synthesis, structure and vibrational properties of GdIGX: YIG1-X ferrimagnetic ceramic composite, J. Phys. Chem. Solids. 70 (2009) 202–209.

[156] R.D. Shannon, Revised effective ionic radii and systematic studies of interatomic distances in halides and chalcogenides, Acta Crystallogr. Sect. A Cryst. Physics, Diffraction, Theor. Gen. Crystallogr. 32 (1976) 751–767.

[157] P.K. Larsen, R. Metselaar, Electrical properties of yttrium iron garnet at high temperatures, Phys. Rev. B. 14 (1976) 2520.

[158] P. Lin, S. Cui, X. Zeng, H. Huang, S. Ke, Giant dielectric response and enhanced thermal stability of multiferroic $BiFeO_3$, J. Alloys Compd. 600 (2014) 118–124.

[159] D.S. Hung, Y.P. Fu, S.F. Lee, Y.D. Yao, F.B. Abdul Ahad, Relaxation behaviours of the bismuth-substituted yttrium iron garnet in the microwave range, J. Appl. Phys. 107 (2010) 09A503.

[160] M.N. Akhtar, A.B. Sulong, M. Ahmad, M.A. Khan, A. Ali, M.U. Islam, Impacts of Gd–Ce on the structural, morphological and magnetic properties of garnet nanocrystalline ferrites synthesized via sol–gel route, J. Alloys Compd. 660 (2016) 486–495.

[161] M.T. Buscaglia, M. Viviani, V. Buscaglia, L. Mitoseriu, A. Testino, P. Nanni, Z. Zhao, M. Nygren, C. Harnagea, D. Piazza, others, High dielectric constant and frozen macroscopic polarization in dense nanocrystalline $BaTiO_3$ ceramics, Phys. Rev. B. 73 (2006) 64114.

[162] K. Majhi, B.S. Prakash, K.B.R. Varma, Extreme values of relative permittivity and dielectric relaxation in Sr_2SbMnO_6 ceramics, J. Phys. D. Appl. Phys. 40 (2007) 7128.

[163] E. Popova, A. Shengelaya, D. Daraselia, D. Japaridze, S. Cherifi-Hertel, L. Bocher, A. Gloter, O. Stéphan, Y. Dumont, N. Keller, Bismuth iron garnet $Bi_3Fe_5O_{12}$: A room temperature magnetoelectric material, Appl. Phys. Lett. 110 (2017) 142404.

[164] G. Dufour, R.C. Karnatak, J.M. Mariot, C. Bonnelle, Atomic and chemical effects in Sm and Sm_2O_3 photoelectron spectra, Chem. Phys. Lett. 42 (1976) 433–436.

[165] K. Wandelt, C.R. Brundle, The interaction of oxygen with gadolinium: UPS and XPS

studies, Surf. Sci. 157 (1985) 162–182.

[166] R.F. Pearson, Magnetocrystalline anisotropy of rare earth iron garnets, Proc. Seventh Conf. Magn. Magn. Mater. (1962) 1236–1242.

[167] K. Yoshii, A. Nakamura, Y. Ishii, Y. Morii, Magnetic properties of $La_{1-x}Pr_xCrO_3$, J. Solid State Chem. 162 (2001) 84–89.

[168] N. Sharma, B.K. Srivastava, A. Krishnamurthy, A.K. Nigam, Magnetic behaviour of the orthochromite $La_{0.5}Gd_{0.5}CrO_3$, Solid State Sci. 12 (2010) 1464–1468.

[169] R. Padam, S. Pandya, S. Ravi, A.K. Nigam, S. Ramakrishnan, A.K. Grover, D. Pal, Magnetic compensation effect and phase reversal of exchange bias field across compensation temperature in multiferroic $Co(Cr_{0.95}Fe_{0.05})_2O_4$, Appl. Phys. Lett. 102 (2013) 112412.

[170] S. Venkatesh, U. Vaidya, V.C. Rakhecha, S. Ramakrishnan, A.K. Grover, Magnetic response in the vicinity of magnetic compensation: a case study in spin ferromagnetic $Sm_{1-x}Gd_xAl_2$ intermetallic alloys, J. Phys. Condens. Matter. 22 (2010) 496002.

[171] K. Uchino, S. Nomura, Critical exponents of the dielectric constants in diffused-phase-transition crystals, Ferroelectrics. 44 (1982) 55–61.

[172] S. Geller, H.J. Williams, R.C. Sherwood, G.P. Espinosa, Magnetic and crystallographic studies of substituted gadolinium iron garnets, J. Appl. Phys. 36 (1965) 88–100.

[173] P. Ilanchezhiyan, G.M. Kumar, C. Siva, A.M. Kumar, S.U. Yuldashev, Y.H. Kwon, T.W. Kang, Magnetic and optical property studies on cubic $Gd_3Fe_{5-x}Co_xO_{12}$ nanogarnets for spintronics, R. Chem. Soc. Cryst Eng Comm. 20 (2018) 2806–2811.

[174] C. Rayssi, S.El. Kossi, J. Dhahri, K. Khirouni, Frequency and temperature-dependence of dielectric permittivity and electric modulus studies of the solid solution $Ca_{0.85}Er_{0.1}Ti_{1-x}Co_{4x/3}O_3$ ($0 \leq x \leq 0.1$), RSC Adv. 8 (2018) 17139.

[175] S.K. Saha, D. Chakravorty, Inhomogeneous conductor model for relaxation behaviour in oxide glasses, Solid State Commun. 82 (1992) 715–720.

[176] S.R. Elliott, Frequency-dependent conductivity in ionically and electronically conducting amorphous solids, Solid State Ionics. 70 (1994) 27–40.

I. Paper Published in International Journals

(a) From Thesis work:

1. **Aakansha**, Bipul Deka, S. Ravi and D. Pamu,
   Impedance Spectroscopy and AC Conductivity Mechanism in Sm Doped Yttrium Iron Garnet
   Ceramic International **43** (2017) 10468-10477.
2. **Aakansha**, Bipul Deka and S. Ravi,
   Magnetic and Dielectric Properties of $Y_{3-x}Sm_xFe_5O_{12}$ (x = 0.0 to 3.0)
   Journal of Superconductivity and Novel Magnetism **31** (2018) 2121-2129.
3. **Aakansha** and S. Ravi
   Structural, Magnetic and Dielectric Properties of Cr Substituted Yttrium Iron Garnets
   Journal of American Ceramic Society **101** (2018) 5046.
4. **Aakansha** and S. Ravi
   Study of Dielectric and Impedance Spectroscopy in $Y_3Fe_{5-x}Mn_xO_{12}$ (x = 0 to 0.2)
   Journal of Material Science: Material in Electronics **30** (2019) 7815-7823.
5. **Aakansha** and S. Ravi
   Investigation of Magnetic and Relaxor Dielectric Properties of Polycrystalline Gadolinium Iron Garnet by Bi Substitution
   Applied Physics A. **125** (2019) 498.
6. **Aakansha** and S. Ravi
   Influence of Cr Substitution on Structural, Magnetic and Dielectric Properties of Gadolinium Iron Garnets
   Solid State Communication. **300** (2019) 113690.
7. **Aakansha** and S. Ravi
   Investigation of Negative Magnetization and Impedance Spectroscopy of Sm-Substituted Gadolinium Iron Garnets
   Material Research Express (Accepted).

(b) Outside the Thesis Work

1. M. Brahma, **Aakansha**, V. M Gaikwad, S. Ravi
   Investigation of Structural, Magnetic and Dielectric Properties of Al-doped Samarium Iron Garnet.

Applied Physics A **125** (2019) 333.

2. R. Hussain, **Aakansha**, B. Brahma, R.K. Basumatary, R. Brahma, S. Ravi, S.K. Srivastava

   Sperimagnetism in Perpendicularly Magnetized Co-Tb Alloy-Based Thin Films

   Journal of Superconductivity and Novel Magnetism **32** (2019) 4027 – 4031.

3. S. K. Srivastava, R. Brahma, S. Datta, S. Guha, **Aakansha**, S. S. Baro, B. Narzary, D. R. Basumatary, M. Kar and S. Ravi

   Effect of (Ni-Ag) co-doping on Crystal Structure and Magnetic Property of SnO_2

   Materials Research Express **6** (2019) 126107.

II. Participation and Paper Presentation

1. National workshop on "**Advance Probing Techniques in TEM**" held in Feb 2016 at IIT Guwahati, India.
2. **International conference on technologically advanced materials and Asian meeting on ferroelectricity** (**ICTAM-AMF 2016**) held during 7^{th} – 11^{th} Nov, 2016 at University of Delhi: Study of Dielectric Relaxation in $Y_3Fe_5O_{12}$ Above Room Temperature.
3. **International conference on Magnetic Materials and Applications** (**ICMAGMA-2017**) held during Feb 1^{st} – 3^{rd}, 2017 at DMRL Hyderabad: Magnetic and Dielectric Properties of $Y_{3-x}Sm_xFe_5O_{12}$.
4. **International conference on Sophisticated Instruments in Modern Research (ICSIMR-2017)** held during June 30^{th} – 1^{st} July 2017 at IIT Guwahati: Magnetic and Dielectric Properties of $Y_{3-x}Sm_xFe_5O_{12}$.
5. National workshop on "**Condensed Matter Days**" held during 29^{th} – 31^{st} August, 2017 at Tezpur University, India: Study of Structural and Magnetic Properties of $Y_3Fe_{5-x}Cr_xO_{12}$.
6. **International conference on condensed matter and applied physics (ICC-2017)** held during 24^{th} – 25^{th} Nov 2017 at Bikaner, Rajasthan: Magnetic and Dielectric Properties of Cr Substituted Yttrium Iron Garnets.
7. **Research conclave 2018** held during 8^{th} – 11^{th} March, 2018 at IIT Guwahati: Study of Dielectric and Impedance Spectroscopy in $Y_3Fe_{5-x}Mn_xO_{12}$ (x = 0 to 0.2).

8. **International conference on superconductivity and magnetism (ICSM-2018)** held during 29th April – 4th May 2018 at Antalya, Turkey: Study of Dielectric and Impedance Spectroscopy in $Y_3Fe_{5-x}Mn_xO_{12}$ (x = 0 to 0.2).
9. **6th National Seminar on Crystallography** held during 27th – 29th June, 2018 at NIMHANS: Bangalore, Structural Characterization of Samarium Substituted Gadolinium Iron Garnets.
10. **International Conference on Advanced Materials (ICAM 2019)** held during 12th – 14th June, 2019, Nirmalagiri College, Kannur, Kerala, India: Investigation of Magnetic and Dielectric Properties of Cr substituted $Gd_3Fe_5O_{12}$.

---------- *** ----------